Laboratory and in-situ studies on mechanical properties of volcanic soil embankment in cold region

March 2014

by

Satoshi Matsumura

TABLE OF CONTENTS

TABLE OF CONTENTS

CHAPTER 1 INTRODUCTION

1.1 General introduction

Recent big earthquakes and heavy rains have caused an enormous number of ground disasters all over Japan, and those have often led to the serious crises involving human lives. The geotechnical engineering has developed from such experience in a way, and a number of excellent findings have been made for the important design and construction. Accordingly, the geotechnical problems become more and more complicated and enlarged in the cycle of developing human activities, increasing natural disasters and highly-required studies. On the other hand, in constructing man-made earth structures such as embankment, for example, the reasonable construction procedure has been possibly focused on, while little is known about how compacted soils (or embankments) behave and lead to failures during seismic action and rainfall. Therefore, it is preferable to clarify the mechanical properties of compacted soils and collapsing phenomenon of embankments through experimental attempts.

In addition to the above, the geotechnical approach against the natural disasters may be equal to understanding the regional problems as represented by geological and climatological properties. Especially, some countries, located on plate boundaries and composed of a number of volcanoes, are forced to face not only the frequent earthquakes but also the geological diversity even in a small island such as Japan. Furthermore, in a cold region such as Hokkaido, Japan, freeze-thaw phenomenon and inflowing snowmelt in ground are considered to make the geotechnical problems more complicated.

Therefore, in order to prevent earthquake- and/or rainfall-induced ground disasters here in Japan,

to deal with the above problems will be strongly required. This thesis will treat the mechanical properties of compacted embankment especially focusing on the influences of possible compaction conditions, freeze-thaw sequence and finer content (or constitutive particle crushing). Moreover, it will attempt to reveal a failure mechanism of a full-scale embankment slope to predict slope failure risk beforehand.

1.2 Outline of present study

This thesis is mainly composed of four research contents as follows;

(1) Change in mechanical properties of compacted soil materials due to compaction conditions

(2) Change in mechanical properties of compacted soil materials due to freeze-thaw sequence

(3) Change in mechanical properties of compacted soil materials due to finer fraction (or constitutive particle crushing)

(4) Long-term monitoring of full-scale embankment slope and failure test

Regarding (1), as mentioned in *1.1*, recent big earthquakes and heavy rains have inflicted serious damage on many kinds of earth structures including embankment all over Japan. In constructing the embankment, its mechanical stability tends to be confirmed ordinarily based on some physical quantities such as dry density, degree of saturation and air content. Such indices, however, can be ambiguous in terms of ensuring required performance of the embankment. Therefore, understanding the mechanical characteristics of compacted soil under possible compaction conditions related to compactive effort, dry density and molding water content is of great importance. On the other hand, little is considered about seismic behavior inside the embankment, in particular liquefaction phenomenon, while the fact that the compacted embankment materials could be liquefied was recognized since Kushiro-oki earthquake, 1993. Keeping in mind the above, a series of laboratory tests was conducted to examine cyclic and monotonic compression strength-deformation behaviors, stiffness and permeability of compacted soils.

Secondly, in order to accomplish the above (2), a cyclic triaxial apparatus capable of simulating the freeze-thaw sequence was newly developed, and the effect of freeze-thawing on the compacted soil was examined. Hokkaido in Japan is located in a cold region where varieties of volcanic soils have widely deposited. The climatic condition of Hokkaido probably causes change in mechanical performance of soil structures. The fact is known with slope failures that frequently occur in a

snowmelt season and differential settlement resulting from frost heaving. From a geotechnical standpoint for disaster prevention in cold regions, some attempts to identify the freeze-thaw effects on mechanical characteristics have been conducted by many researchers as introduced in *CHAPTER 2*. However, cyclic deformation-strength characteristics including liquefaction behavior of the volcanic soils subjected to freeze-thaw sequence is hardly known. In this study, using the developed apparatus, a series of cyclic triaxial tests was performed with a compacted volcanic soil subjected to a freeze-thaw cycle. In this thesis, to examine the fundamental results of cyclic deformation-strength characteristics, the volcanic soils were applied cyclic loading under fully-saturated condition after freezing and thawing.

Subsequently, in Hokkaido, as mentioned above, many kinds of volcanic soils have widely deposited, and as a result those have been often used as useful embankment materials. According to previous researches, coarse-grained volcanic soils are constituted by porous and brittle particles, and those are prone to significant particle crushing even under low stress condition. Then, it is pointed out that the particle breakage can cause change in mechanical behavior leading to strength deterioration. In Hokkaido, the compaction and the freeze-thaw sequence mentioned above could be the causes of particle crushing in addition to consolidation and shearing stress history after construction. Thus, although the embankment is generally stabilized with the consolidation progressing, the fact does not always agree with the coarse-grained volcanic soil embankment. Therefore, that implies the importance of understanding the influence of particle crushing on the mechanical properties of compacted soil. Simulating the particle crushing, the above (3) will treat four coarse-grained volcanic soils gradation-controlled beforehand. A series of cyclic triaxial tests was conducted using those soils compacted under various compaction conditions as well as (1).

Finally, as a motivation for the above (4), recent heavy rains have triggered an enormous number of slope failures on the earth structures such as road embankments, cut slopes and dikes etc. In

Hokkaido, furthermore, the inflow of snowmelt can be concerned as the possible cause of slope failures because those occurrences tend to concentrate in the springtime. On the other hand, the mechanical behavior of volcanic soil embankments constructed in Hokkaido are considered exposed to the above influential factors such as the compaction conditions, freeze-thawing and particle crushability, which are complexly intertwined. Therefore, to clarify the mechanism of rainfall-induced slope failures, and simultaneously to develop reasonable prediction approach with some manageable parameter to evaluate the potential risk of slope failures have been increasingly required. The previous approaches to evaluate the slope stability depend differently on moisture content, displacement, pore pressure and rainfall intensity. In particular, the rainfall intensity has been mainly adopted as a leading methodology of the prediction in many cases so far. However, because the possible slope failure phenomenon must differ at each ground condition, the alternatives to the rainfall intensity based on some geotechnical indices will be necessary in the future. In this study, the full-scale embankment was constructed in-situ using a volcanic soil, and afterwards the mechanical properties inside the embankment have been long monitored with the embankment exposed to the natural environmental conditions such as freeze-thawing, rainfall and earthquake. Consequently, the monitoring attempt has lasted until the embankment reaches slope failure after supplying water inside the embankment. The testing results indicate the potential prediction of slope failure based on the moisture content.

In this thesis, two kinds of soil materials that had deposited in Hokkaido were employed for the laboratory element tests and the in-situ test. One is classified into “sandy-silt”, and the other is “volcanic coarse-grained soil” based on the classification mentioned in *CHAPTER 2*. The former material was used for each laboratory element test to examine the effect of compaction conditions regarding (1). In addition to the above attempts, using the latter material, the effects of freeze-thaw sequence and finer content F_c (%) on cyclic deformation-strength characteristics will be discussed.

Furthermore, the in-situ full-scale embankment was constructed by the same volcanic coarse-grained soil.

In *CHAPTER 2*, the brief reviews of previous researches and the significance of this study will be explained with regard to each study (1) ~ (4). Next, in *CHAPTER 3*, the two soil materials used in this study will be introduced with those physical properties. Further, *CHPATER 4* will treat a series of testing methods including testing apparatuses, specimen preparation, each triaxial test procedure and construction of the in-situ full-scale embankment. Finally, in *CHAPTER 5*, the testing results and discussions will be in detail stated, which will be briefly concluded in *CHAPTER 6*. At the end of this thesis, the tables of every laboratory element test conditions and fundamental results and of often used symbols will be additionally shown.

CHAPTER 2 REVIEW AND ITS RELATION WITH THIS STUDY

2.1 Compaction of geomaterial and its mechanical characteristics

Since compaction of soil was treated as a geotechnical problem by R.R. Proctor (1933), large numbers of researchers have attempted to clarify the structure of compacted soils and those mechanical characteristics such as permeability, compressibility and shear strength-deformation behavior. In this section, very limited previous studies on this can be introduced despite many other excellent approaches and findings to note.

First, one of the researches well-known would be with regard to the structure of compacted clay and its mechanical properties reported by Lambe (1958a and 1958b). In his study, the structures of compacted clay were identified on the basis of physicochemical analysis as schematically shown in Figure 2.1.1, which has been widely sustained by many researchers. According to his theory, the soil compacted dry of optimum at point A in the figure has insufficient water not to develop the diffuse double layer of soil colloids and to bring a high concentration of electrolyte, and it leads to a flocculated structure that has a low degree of particle orientation and low density. The molding water increased plays a role as “lubrication” to densify the soil up to the optimum of point B, but further increase lowers the density conversely resulting from the volume of added water as indicated by point C. He reported, moreover, the results of permeability test conducted with two kinds of clays soaked after compaction. It is apparent that the hydraulic conductivity of compacted clays tends to decrease with increasing the molding water content. Such behavior is confirmed as well by

Mitchell et al. (1965). In addition to the above, Mitchell et al. (1965) clarified the effects of some variables to influence mechanical properties of the compacted soil such as compactive effort, compaction method, thixotropy and degree of saturation on the permeability.

Around the same time, strength-deformation properties of compacted clays versus the compaction conditions were in detail examined, following the Lambe's idea of clay structure, by Seed et al. (1959). Very interesting results are that when as-compacted specimens was sheared under undrained and unconsolidated condition, the specimens compacted dry of optimum exerted higher strength than those compacted wet of optimum; however, when the compacted specimens were soaked and subsequently sheared with developing pore water pressure under undrained and consolidated condition, the shear stress and pore water pressure exhibited the each same value at around 20 % in axial strain regardless of the difference in the soil structure resulting from the molding water content, although the earlier stress-strain behavior was quite different. They argued, hence, that the above results would be misleading if the strengths of compacted soils were compared at a certain limiting strain.

On the other hand, Ahmed et al. (1974), Juang and Holtz (1986), Benson and Daniel (2000), Yamaguchi and Ikenaga (1992) and Watabe et al. (2000) attempted to depict the influence of compaction condition on the mechanical properties of compacted soils in terms of difference in pore size and its distribution. Ahmed et al. (1974), Juang and Holtz (1986) and Yamaguchi and Ikenaga (1992) evaluated the pore size distribution of compacted soils by the mercury porosimetry. They reported that the specimens compacted dry of optimum possessed larger size of pore; in contrast, the predominant pore size became smaller at wetter condition. It was concluded, as a result, that such behavior as observed by Lambe (1958b) and Mitchell et al. (1965) could occur for compacted soils, i.e., the permeability reduced with the molding water content increasing (Juang and Holtz 1986 and Yamaguchi and Ikenaga 1992). Ahmed et al. (1974) confirmed the same undrained-unconsolidated strength-deformation behavior of compacted clay as explained above (Seed et al. 1959). A direct

observation was conducted through scanning electron photomicrographs to identify compacted soil structures and pores (Benson and Daniel 2000 and Watabe et al. 2000). In addition, Watabe et al. (2000) evaluated the influence of pore size distribution of compacted soils on the hydraulic conductivity by means of analyzing suction measured in an apparatus.

Although compacted soils are ordinarily under unsaturated condition where the suction is acting on those mechanical properties, when losing the suction due mainly to rainfall and increasing water table, the compacted soils have often suffered from significant volume change. Therefore, to clarify the volume change of compacted soils resulting from soaking has been a principal objective for many researchers. Seed et al. (1962) conducted a series of laboratory tests soaking the clay specimens compacted at variable compaction conditions, i.e., the molding water content and the compactive effort, to predict swelling potential for the compacted clays. In contrast to such consideration as the swelling behavior of compacted soils, understanding a shrinking phenomenon of compacted earth structures has been attempted (Kamei and Enomoto 1994 and Kato 1998). This is because the embankments loosely constructed, especially in dry regions, often lead to serious settlement with absorbing water. On the other hand, the attempt of evaluating the mechanical properties of compacted soil relating with the suction have been seen in recent years with development and diversity of measurement techniques (Jotisankasa et al. 2009, Kimoto et al. 2011, Heitor et al. 2013, Alonso et al. 2013 and Sivakumar et al. 2013).

Thus, such mechanical characteristics as strength-deformation, volume change due to soaking, permeability have been in detail revealed by many researchers, but a study on dynamic properties such as liquefaction behavior and small strain stiffness for compacted soils is quite limited. This is considered owing to an erroneous thought that the liquefaction would not occur inside the compacted earth structures such as embankment. However, since the liquefaction phenomenon of the embankment materials causing enormous failures, was recognized in Kushiro-oki earthquake (Sasaki

2012), such a type of embankment failure has been pointed out after The 2011 off the Pacific coast of Tohoku Earthquake (2011) as well. Therefore, understanding the cyclic shear behavior of compacted soils will be increasingly of great importance in order to improve seismic performance of the embankment. On the other hand, because most of previous studies on the compacted soils have focused on the clay materials, there is little attempt of using a silt, sand or coarse-grained soil such as gravel (e.g. Magistris and Tatsuoka 2004, Kawajiri et al. 2011, Yokohama et al. 2012 and Matsumura et al. 2012). In this thesis, keeping in mind the above, the effect of compaction conditions, i.e., the molding water content, compactive effort and degree of compaction, on the dynamic properties of liquefaction and shear modulus at small strain, in addition to the monotonic compression and the permeation behaviors, will be discussed using a sandy silt and a coarse-grained volcanic soil, which have deposited in Hokkaido.

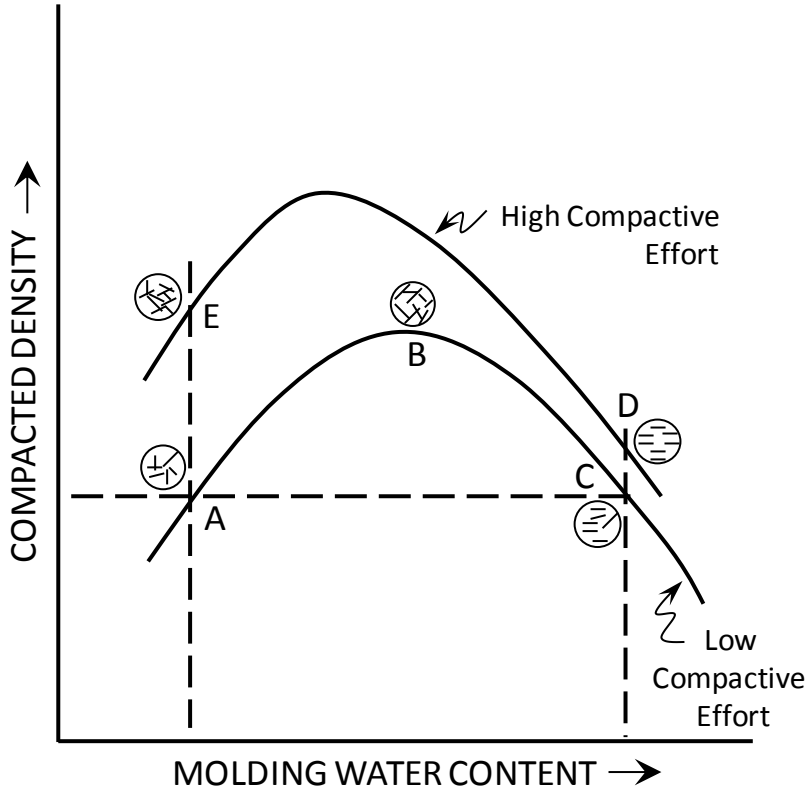

Figure 2.1.1 Structures of compacted clay (revision of Lambe 1958a)

2.2 Volcanic soils deposited in Hokkaido and its engineering properties

2.2.1 Volcanic activities in Hokkaido and classification of volcanic soil

Volcanic activities from the Neogene to the Quaternary, based on the geological timescale shown in Table 2.2.1 (revision of Miki 1997), are the origin of many kinds of volcanic soil deposited widely over the area of Japan. In particular, Hokkaido region is located on the intersection point of each arc of Tohoku-Nihon and Chishima, where a number of volcanic activities and earthquakes have been observed. More than 40 volcanoes were generated in the Quartenary, and those provided acres of tephra on Hokkaido. Those tephra are distinguished based on components, sedimentary structure, distributional area and degrees of weathering in a geotechnical purpose. In this section, the geotechnical definition of volcanic soils and the physical and mechanical properties of the ones that deposit in Hokkaido will be elaborated with the help of the Hokkaido branch of the Japanese Geotechnical Society (2010).

Table 2.2.2 introduces the technical terms regarding “tephra”, which are identical to pyroclastic materials: volcanic soil in a broad sense. Tephra correspond to volcanic ash and pumice which are solid constituents contained in volcanic gas provided with explosive eruption of volcanoes, and it is distinguished from lava. In addition, the tephra can be classified broadly into two groups; “tephra fall deposit” and “pyroclastic flow deposit”. The tephra fall deposit is the depositing product of the volcanic ash and the pumice carried on the wind with plinian eruption. The plinian eruption indicates the type of erupting with a volcanic column rising up over the volcano as shown in Figure 2.2.1. The volcanic ash and the pumice eructed and carried on the wind begin falling down to deposit on the ground when the gravity and the air resistance balance. Then, because each volcanic product has a variety of grain sizes and densities, those are selected to fall down related to the distance from the volcano. Hence, the tephra fall deposit has comparatively-uniform grain size distribution.

On the other hand, the pyroclastic flow deposit is provided by that the volcanic column containing the pumice, the volcanic ash and the scoria yields to the gravity action, and those products flow above the ground. Therefore, the pyroclastic flow deposit tends to be composed of well-grained soils.

Figure 2.2.2 shows the distribution chart of the tephra depositing in Hokkaido with those symbols, separating the tephra fall deposit and the pyroclastic flow deposit. In the figure, the sampling sites of soils used in this study are also plotted; Komaoka and Chiyoda districts, which will be discussed in detail later. From the figure, the tephra fall deposits spread especially eastward over wide areas due to the westerlies, while the pyroclastic flow deposits remain nearer from the volcanoes.

The Japanese Geotechnical Society, JGS additionally proposes the geotechnical classification of the volcanic soils depending on the finer content F_c (%) (< 75 μm) and the liquid limit w_L, etc. as shown in Table 2.2.3. In terms of the finer content, the research committee for the property and use of volcanic soil in Hokkaido (in Japanese) distinguished the volcanic soils of $F_c < 50$ % and $F_c \geq 50$ % as “volcanic coarse-grained soil” and “volcanic fine-grained soil”, respectively. In particular, the volcanic coarse-grained soil is primary sediment or secondary one generated by the volcanic ash, the pumice and the scoria, while the volcanic fine-grained soil indicates the weathered volcanic coarse-grained soil. Then, the primary sediment means the product that falls down and deposits after the eruption, and the secondary sediment is redeposit on the ground or in the water resulting from the primary sediment flowing in the gravity action or water flow. The volcanic soil used for this study will be discussed based on the above classification of JGS.

Table 2.2.1 Geological timescale (revision of Miki 1997)

Geological timescale				
Era / Group		*Period / System*		*Epoch / Series*
（×10^6 year age）				
Cenozoic	0.01	Quaternary		Holocene
				Pleistcene
	1.7	Tertiary	Neogene	Pleiocene
	5			Miocene
	34		Paleogene	Oligocene
	37			Eocene
	54			Paleocene
	64			
Mesozoic		Cretaceous		Late
	140			Early
		Jurassic		
	208	Trassic		
	242	Perimian		
Paleozoic	284	Carboniferous		Late
	360			Early
		Devonian		
	409	Silurian		
	436	Ordovician		
	500	Cambrian		
	564			
Proterozoic	2500±			
Archean	4500±			

Table 2.2.2 Technical terms regarding “tephra”

A cycle of volcanic product
- Tephra
  Pyroclastic material
  = Volcanic soil
  in a broad sense
  - Tephra fall deposit
    - Pumice fall deposit
    - Scoria fall deposit
    - Ash fall deposit
  - Pyroclastic flow deposit
    - Ash flow deposit*† (Large-scale)
    - Pumice flow deposit*† (Medium- to large-scale)
    - Nuée ardente deposit*† (Small-scale)
  - *Welded tuff, tuff
    † Ignimbrite
  - Pyroclastic surge deposit
    (Base surge, ash cloud surge)
  - Volcanic ash soil ; weathered product

Several cycles of volcanic product : Cluster of tephra*2; Volcanic soil, loam, red earth, black earth and andosol, etc.
*2 Possibly including alien or similar substances

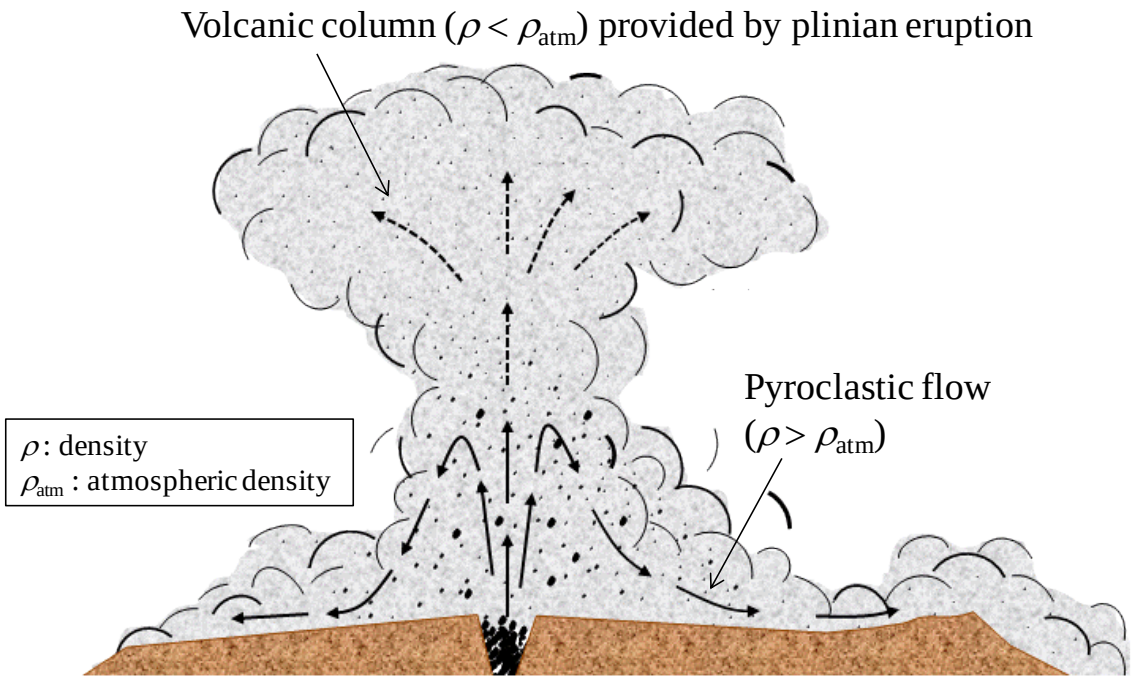

Figure 2.2.1 Schematic diagram of plinian eruption

Fall deposit	
Komagatake	Ko
Oshima-Oshima	Os
Otobe-sou	a
Hutoro-sou	b
Zenigamegawa-sou	Z-M
Yotei-san	Yo
Eniwa-dake	En
Tarumae-san	Ta
Shikotsu	Spfa
Usu-san	Us
Tokachi-dake	To
Mashu	Ma
Oakan	Oa
Meakan	Me
Rishiri-san	Ri

Flow deposit	
① Motomura	*1
② Komagatake	*2
③ Nigorikawa	*2
④ Kimobetsu	*1
⑤ Toya	*3
⑥ Kuttara	*2
⑦ Tarumae	*2
⑧ Shikotsu	*2
⑨ Tokachi	*1
⑩ Sounkyo Antaroma-gawa	*1
⑪ Muka	*1
⑫ Akan	*2
⑬ Kuccharo	*2
⑭ Mashu	*2
⑮ On-nebetsu	*3

*1 : welded tuff, tuff, ignimbrite
*2 : pumice flow deposit
*3 : pyroclastic flow deposit

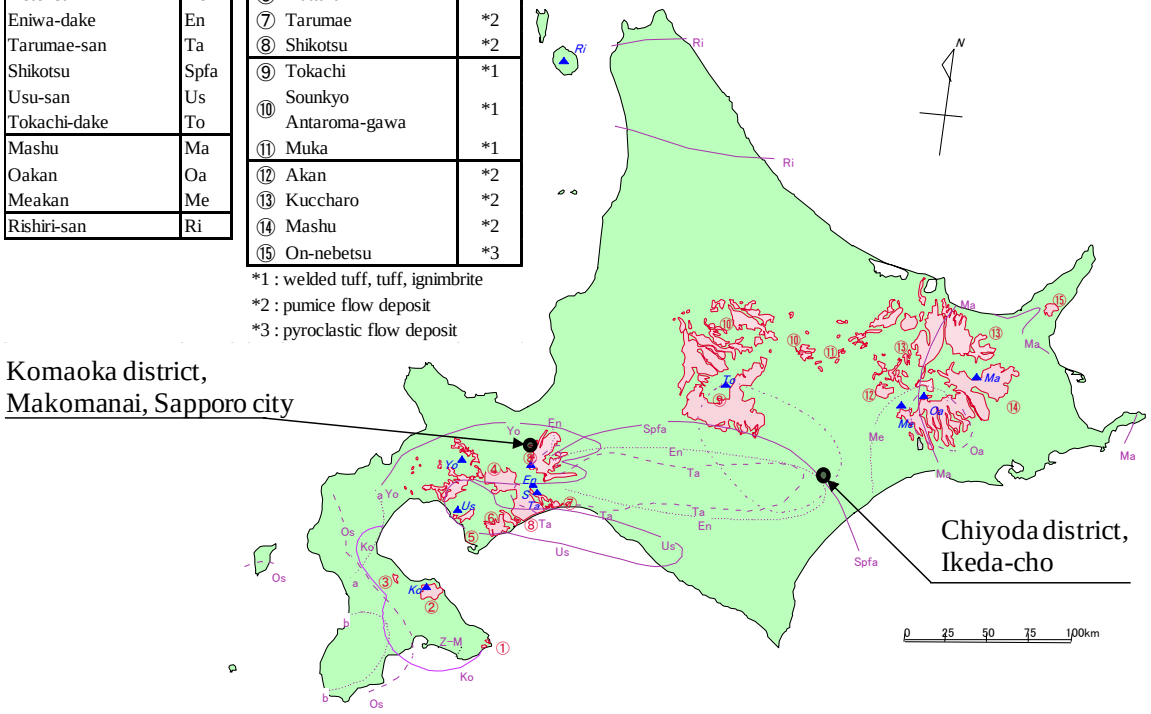

Figure 2.2.2 Distributions of volcanic soils deposited in Hokkaido

Table 2.2.3 Geotechnical classification for volcanic soils

★Fine-grained soil ($F_c \geq 50\%$)

Volcanic cohesive soil {V}

Low liquid limit(VL) ・・・・・・・・・・・・・・・・・ $50\% > w_L$

Type I(VH_1) ・・・・・・・・・・・・・・・・・・・・ $50 \leq w_L < 80\%$

Type II(VH_2) ・・・・・・・・・・・・・・・・・・・・ $w_L \geq 80\%$

Organic soil {O} ・・・・・・・・・・・・・・・・・・・・ Organic, dark-colored soil with organic smell

Organic-volcanic ash soil (OV) ・・・・・・・・・・・・ Organic-volcanic soil

★Coarse-grained soil ($F_c < 50\%$)

$F_c \geq 5\%$; Volcanic soil {V}

$5\% \leq F_c < 15\%$ (G-V, S-V)

$15\% \leq F_c < 50\%$ (GV, SV)

★Classification by Stratum, Unusual soil, Local soil, colloquial term

Shirasu (SV), Kanto loam (VH_1, VH_2), Hachinohe loam (VL)

2.2.2 Mechanical properties of volcanic soil

In Japan, a variety of volcanic soils deposits widely, and it is assumed that the depositing area reaches around 40 % of the soil, especially of Hokkaido. Therefore, the volcanic soil has been treated as a geomaterial for embankment and foundation ground. Accordingly, the recent big earthquakes have caused serious damage of volcanic soil ground in various regions in Japan from 1968 to 2008 as shown in Table 2.2.4 (Kazama et al. 2006a). Needless to say, the 2011 off the Pacific coast of Tohoku earthquake (2011) damaged many embankment structures and foundation ground including volcanic soil as well (e.g., Investigation group of Japanese Society of Civil Engineering for damage due to the 2011 off the Pacific coast of Tohoku Earthquake, 2011). On the other hand, it is pointed out that not only the earthquakes but also heavy rain and snowmelt water are the causes of volcanic soil slope failures (e.g., Kudo 2013). Hence, in order to reveal mechanical properties of volcanic soil, many studies have been performed with laboratory element and model tests and in-situ monitoring test. In this section, those findings will be introduced with a focus on the volcanic soils in Hokkaido.

The constitutive particles of volcanic coarse-grained soils have some features such as porosity and crushability more or less because those soils partially or wholly contain the unweathered pumice, and the peculiarities are considered to characterize the mechanical properties. Miura et al. (1996a) carried out the triaxial compression test in both drained and undrained conditions, the plane strain compression test and cyclic triaxial test using some volcanic soils that deposited in Hokkaido. They concluded that the crushable volcanic soils caused significant particle breakage in the stress path where the effective mean principal stress p' increased in shearing, compared with the liquefaction process where the p' value decreased. In addition, it was confirmed that the volcanic soils that had the stronger particle crushability tended to behave in stress-strain relation, depending strongly on the effective confining pressure. Furthermore, the importance of considering cementation and welding

effects and anisotropic behavior on the volcanic soils in natural soil deposits was pointed out by comparing the results of undisturbed samples with reconstituted ones. In the paper, on the other hand, the validity of the increment of finer content ΔF_c (%) as a crushability index was discussed. Miura et al. (1996b) and Miura and Yagi (1997) elucidated how the mechanical behavior of volcanic soils varied in a different stress or consolidation history, connecting with the particle crushability. Yagi and Miura (2001) performed the one-dimensional consolidation test and the cyclic triaxial test with the gradation-controlled volcanic soils, and examined change in the mechanical performance resulting from the increment of finer content. In the paper, they reported that the relation between F_c and the liquefaction strength was not uniform; i.e., the minimum value of the liquefaction strength appeared at a specific F_c condition. Regarding dynamic properties of the volcanic soils, Asonuma et al. (2002) and Sahaphol and Miura (2005) showed the shear modulus at small strain obtained from the cyclic triaxial test and the bender element test. Their attempts are very useful in terms of the findings that several volcanic soils in Japan were adopted, and the function of the shear modulus with the void ratio and the effective confining pressure for clean sand was applicable for the crushable volcanic soils. Moreover, in order to discuss the applicability of various in-situ tests for the volcanic soils, Miura et al. (2003) conducted various site investigations using standard penetration test (SPT), cone penetration test (CPT) and seismic cone penetration test (SCP). In these tests, SPT to require dynamic penetrations induces significant particle breakage, and that leads to underestimation of the N value. Thus, the above studies have indicated the deformation-strength characteristics of the crushable volcanic coarse-grained soils with each laboratory element test and site investigations.

Nakata and Miura (2007) attempted quantitative estimation of void structure and its change of the volcanic coarse-grained soil, focusing on the porosity and crushability of constitutive particles. In the paper, those particles containing void inside were modeled as shown in Figures 2.2.3 and 2.2.4. In addition, creep test in a triaxial cell was performed with those volcanic soils. From a series of

testing results, the volcanic coarse-grained soils in Hokkaido are composed of "opening intra-particle void" being exposed to the atmosphere (*see* Figures 2.2.3 and 2.2.4) at a high rate, which leads to significant particle breakage and peculiarity of creep performance, unlike Toyoura sand with no particle crushability.

On the other hand, in Hokkaido as a cold region, freeze-thaw sequence should be a non-negligible factor in determining the mechanical property of geomaterial including volcanic soils. Therefore, some researchers have revealed the freeze-thaw effect on deformation-strength characteristics and slope failure of volcanic coarse-grained soils as mentioned later (Yamaki et al. 2009, Ishikawa and Miura 2011 and Kawamura and Miura 2013a).

Finally, let us briefly look at some studies using volcanic soils that deposit in some areas different from Hokkaido. Kazama et al. (2006b) examined the effect of degree of saturation S_r (%) from 40 to 100 in liquefying on cyclic strength-deformation and excess pore water pressure behavior of the volcanic coarse-grained soils in Tohoku region. They successfully explained the liquefaction phenomenon in the unsaturated condition based on decreasing in effective stress in cyclic shearing. Kiyohara and Kazama (2008) performed long-term monitoring of volcanic soil model embankment in the field to know moisture movement and pore pressure behavior. Moreover, as some of studies on the typical volcanic soil, Shirasu that deposits in Kyushu region, Haruyama M. (1973), Takada et al. (1997), Takada et al. (1999) and Takada et al. (2001) are taken. They all conducted site investigations, SPT and CPT, and discussed the applicability for Shirasu with comparing the laboratory test results. Kitamura et al. (2007) constructed a model embankment using Shirasu in the laboratory to figure out the mechanism of rainfall-induced slope failure.

Table 2.2.4 Earthquake-induced damage of volcanic soil structures (revision of Kazama et al. 2006a)

Year	Month/Day	Earthquake, eq.	M	Place City (town)/prefecture	Epicentral distance (km)	Seismic intensity	damage type	Origin of Volcanic soil	Damaged structure
1968	2/21	Ebino eq.	6.1	Ebino-cho/Miyazaki	35	IV	Slope failure	Kakuto pyroclastic flow	Natural slope
							Liquefaction		Paddy
1968	5/16	Tokachi-oki eq.	7.8	Sannohe-machi/Aomori	200	V	Slope failure	Towada/Hakkoda pumice flow	Road embankment
				Gonohe-machi/Aomori	200	V	Slope failure		Natural slope
				Kiyota/Sapporo/Hokkaido	310	IV	Liquefaction	Shikotsu pumice flow	Housing ground
1978	1/14	Izu oshima kinkai eq.	7.0	Mitakairiya/Kawazu-cho/Shizuoka	20	V	Slope failure	Volcaniclastic material	Natural slope
1978	6/12	Miyagiken-oki eq.	7.4	Kotobukiyama/Shiroishi/Miyagi	140	IV	Slope failure	Pumice flow	Housing embankment with filling a valley
1984	9/14	Naganoken seibu eq.	6.8	Ontake-san/Otaki/Nagano	5	VI	Slope failure	Senbonmatsu pumice stratum	Natural slope
				Matsukoshi/Otaki/Nagano	1	VI	Slope failure	Ontake 3 pumice stratum	River terrace
1993	1/15	Kushiro-oki eq.	7.8	Shibecha-cho/Hokkaido	40	-	Slope failure	Pumice flow	Housing embankment with filling a valley
				Midorigaoka/Kushiro/Hokkaido	15	VI	Slope failure	Kussharo pumice flow	Housing embankment
1993	7/12	Hokkaido Nansei-oki eq.	7.8	Mori-cho/Hokkaido	145	-	Liquefaction	Komagatake pyroclastic flow	Housing ground, wharf, quay
1994	10/4	Hokkaido Toho-oki eq.	8.1	Shibecha-cho/Hokkaido	250	V	Slope failure	Pumice flow	Housing embankment
				Nakashibetsu-cho/Hokkaido	220	V	Liquefaction	Mashu pumice fall	Natural soil deposit
1994	12/28	Sanriku Haruka-oki eq.	7.5	Shingo/Aomori	230	VI	Slope failure	Towada/Hakkoda pumice flow	Embankment with filling a valley
1997	3/26	Kagoshimaken Hokuseibu eq.	6.2	Iriki-cho/Kagoshima	30	IV	Slope failure	Ito pyroclastic flow	Housing embankment
2003	5/26	Sanriku-minami eq.	7.1	Tateshita/Tsukidate/Miyagi	35	V	Slope failure	Onikobe pyroclastic flow	Embankment for agriculture with filling a valley
2003	9/26	Tokachi-oki eq.	8.0	Kyowa/Tanno-cho/Hokkaido	230	V	Slope failure	Kussharo pumice flow	Embankment for agriculture with filling a valley
				Utsukushigaoka/Sapporo/Hokkaido	255	IV	Liquefaction	Shikotsu pumice flow	Housing embankment
2008	6/14	Iwate・Miyagi Nairiku eq.	7.2	Kurihara (Hiyashizawa)/Miyagi	15	VI	Slope failure	Kurikoma pyroclastic flow pumice fall	Valley
				Tateshita/Tsukidate/Kurihara/Miyagi	35	VI	Slope failure	Onikobe pyroclastic flow	Embankment for agriculture with filling a valley

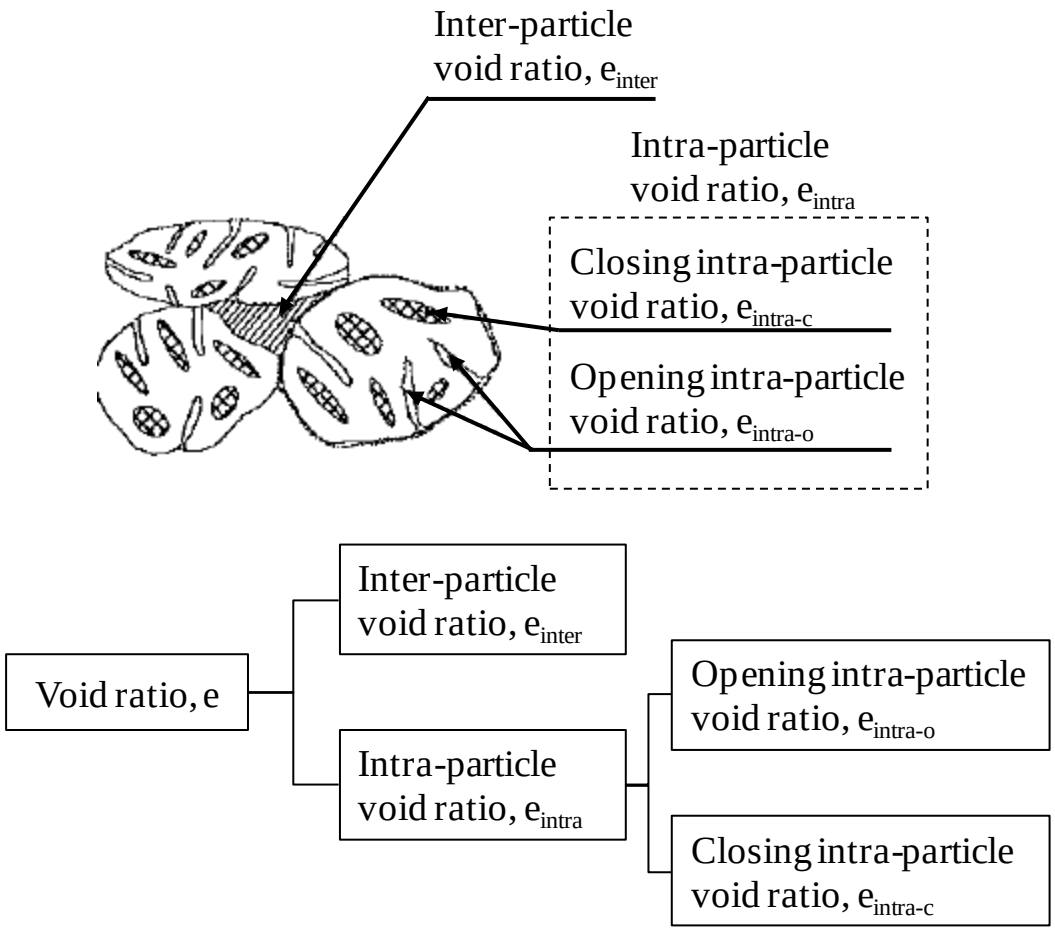

Figure 2.2.3 Model of volcanic porous particles (revision of Nakata and Miura 2007)

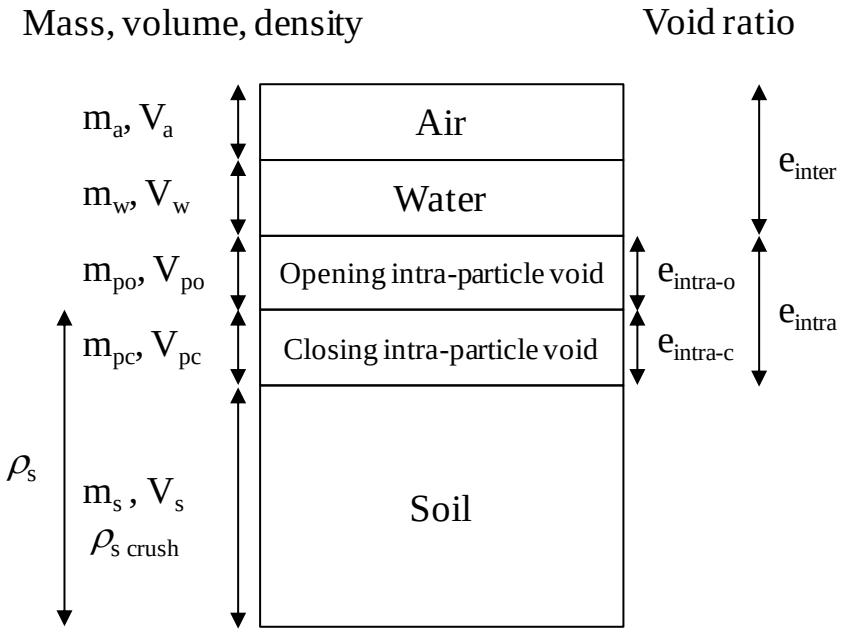

Figure 2.2.4 Physical quantities taking into account porosity of volcanic soil (revision of Nakata and Miura 2007)

2.3 Engineering application of frozen soil and geotechnical problems in cold regions

In terms of freeze-thawing on soil mechanics, a number of researches has addressed effect of freezing on liquefaction of clean sands, which it is difficult to sample without any disturbance, in order to discuss the validity of an in-situ freezing method as high-quality sampling. The researchers that began to examine such influence on liquefaction strength at the earlier time should be Walberg (1978), Yoshimi et al. (1978) and Ishihara et al. (1978). Walberg (1978) performed the cyclic triaxial test using the specimens reconstituted by Monterey No. 0 sand with or without freeze-thaw sequence, and reported no significant change in liquefaction strength due to freeze-thawing in the case that the specimens caused no expansion with drainage in freezing. Yoshimi et al. (1978) and Ishihara et al. (1978) actually conducted the sampling of saturated sands by freezing to clarify the mechanical properties of sand soil deposits with the triaxial compression test and the cyclic triaxial test, respectively. Furthermore, as the examples in which the freezing sampling was in-situ carried out, Hatanaka et al. (1985) and Goto et al. (1992) can be introduced. Hatanaka et al. (1985) especially discussed the applicability of the freezing method for liquefaction strength to the Shirasu grounds in the province of Kagoshima as well as the validity of SPT to estimate the liquefaction strength. They reported that the liquefaction strength of the in-situ sampled Shirasu by the freezing method became higher than that of the reconstituted Shirasu specimen in the laboratory, even though it was made at the same relative density. In addition, an interesting result displayed by them is that the prediction by SPT tends to underestimate the in-situ liquefaction strength compared with the above laboratory liquefaction strength with the frozen Shirasu samples. That is considered to occur to Shirasu from the same cause as to Hokkaido volcanic soils as mentioned in the previous section (Miura et al. 2003), i.e., constitutive particle crushing. Goto et al. (1992) applied the in-situ freezing method to gravel ground, and measured the stiffness, monotonic and cyclic strength. On the other hand, Singh and

Seed (1982) and Goto (1993) inspected the influence of freezing and thawing on the liquefaction strength of clean sands applied prior strain history, which was referred to as “seismic history” (Seed et al. 1982). Goto (1993), in addition, discussed the effect of finer content on the above results, and revealed that the effect of freezing and thawing on the liquefaction strength became remarkable as the finer content increased.

On the other hand, in cold regions where ground temperature falls below 0 °C, the freeze-thaw sequence can be often a non-negligible factor in determining the mechanical property of geomaterial so as to maintain every soil structures in required condition. The fact is easily understood from slope failures that frequently occur in a snowmelt season and differential settlement resulting from frost heaving. Therefore, many researchers have attempted to elucidate the influence of freeze-thawing as a geotechnical problem. Ishikawa and Miura (2011) conducted the monotonic compression triaxial test with some volcanic soils exposed to one-dimensional freeze-thaw sequence. They reported in the paper, the increment of finer content with the freeze-thaw cycle increased triggered critical deterioration of strength parameter. Yamaki et al. (2009) examined change in dynamic properties of a coarse-grained volcanic soil deposited in Hokkaido due to freeze-thawing to simulate the mechanical reduction of volcanic soil ground in a cold region. Ono et al. (2003) showed the experimental results of triaxial shear behavior of clay subjected to freeze-thaw under various consolidation conditions.

Furthermore, for the purpose to evaluate the freeze-thaw effect on hydraulic conductivity of compacted liner for earth dams or waste containers, a variety of freeze-thawing tests were developed using some clay material. Kim and Daniel (1992), Eigenbrod (1996), Viklander (1998) and Konrad (2010) all performed laboratory permeability tests for fine-grained soils subjected to freeze-thaw sequence, and reported reduction in imperviousness of the compacted clay resulting from freeze-thawing. Benson and Othman (1993) prepared the in-situ large-scale specimen, which was

reconstituted with glacial clay, of 0.91 m height and 0.3 m diameter, and examine the hydraulic conductivity of the soil subsequent to freeze-thaw cycles of two months in the field. They reported in the paper that although little change in the hydraulic conductivity was found when conducting the percolation through the entire specimen, each piece of sliced specimen reflected the effect of freeze-thaw sequence, i.e., increasing in hydraulic conductivity, as it was shallower part of the specimen from the upper surface.

Thus, while the mechanical characteristics such as monotonic shear behavior, stiffness and hydraulic conductivity of frozen and thawed soils have been focused on, little is known about the cyclic deformation-strength behavior including liquefaction, in particular, of crushable volcanic soils containing sufficient finer fractions subjected to freeze-thaw sequence. In this study, therefore, the aim is to manifest how the volcanic soil behaves in freezing and thawing, and it results in change in cyclic behavior, combining with the effect of compaction conditions discussed above.

2.4 Earthquake- and/or rainfall-induced slope failure

Recent earthquakes and heavy rains, in Japan, have triggered serious damage of natural grounds and earth structures in various ways, e.g., slope failure, debris flow, liquefaction, and differential settlement etc. In particular, the debris flow caused in a mountain area tends to lead to an extensive damage to involve human lives once it occurs, as recently experienced in Chugoku region (Japanese society of civil engineering, JSCE and JGS, 2013), and in Tohoku region (JGS 2013) in Japan; therefore, understanding of the mechanism and a possible countermeasure will be increasingly required. On the other hand, the above-mentioned damage of the man-made earth structures such as road embankment, cut slope, dyke and reclaimed land can have often a great impact on our society, even though those scales are limited. Thus, although it is desirable to simulate a wide variety of failure types that is induced by earthquake and/or rainfall, in this section, limited reviews about the damage of compacted embankment and related studies will be explained.

Road embankment and dyke embankment, although both constructed by compaction, have individual different feature and role as infrastructure. That is, fundamentally the road embankment should not cause a remarkable reduction of transportation system and the dyke must avoid overflow, after acceptable failure. Figures 2.4.1 show typical types of earthquake-induced failure of road embankment and dyke embankment, respectively (Japan road association 2010 and Sasaki 1980). As shown by type I in Figure 2.4.1 (a), when the embankment widened on a natural slope was subjected to seismic force, it might lead to large scale of slope failure with rising pore water pressure due to the inflow of water out of the ground. Type II indicates the embankment failure occurring on a landslide landform. The failure with significant settlement exhibited by type III results from that the loose saturated sand foundation is liquefied. Sliding failure of widening of embankment and self-weight settlement due to shaking displayed by types IV and V, respectively, are mostly attributed

to insufficient degree of compaction. On the other hand, as illustrated in Figure 2.4.1 (b), while type I' is prone to minor failure, the dyke embankments of type II' to IV' cause serious damage lowering the height of levee. Then, type III' can be triggered by either the liquefaction of ground or a slope failure involving the soft ground. Furthermore, the dam settlement of type IV' is considered the same phenomenon as mentioned by type V in Figure 2.4.1 (a). The dyke failures classified into type II' to IV', which were caused by a number of major earthquakes (eq.) earlier than 1980 (Noubi eq., Kanto eq., Fukui eq., Tokachi-oki eq. and Niigata eq. etc.), reach about 88 % (Sasaki 1980), compared with type I and no-damage case. Accordingly, the seismic performance has been widely investigated for the dyke embankments since, and those have been reinforced if desired (JGS 2009a). However, considering little has been changed on the thought of compaction control for the dyke, including the road embankment, it could be understood that the fundamental mechanical properties of compacted embankment are still uncertain.

In recent years, furthermore, a failure form of dyke embankment was newly confirmed in Kushiro-oki earthquake (1993), i.e., liquefaction phenomenon inside the embankment, which caused significant settlement. A mechanism of the liquefaction-induced settlement was explained by Sasaki (2012) as shown in Figure 2.4.2. In this case, it could be recognized that water had been widely distributed inside the dyke embankment due to appreciable settlement of peat layer depositing below the dyke after construction, as indicated by (I) in the figure. Subsequently, the strong motion of Kushiro-oki eq. caused the liquefaction at the saturated section inside the dyke. Then at the process of (II) to (IV), the liquefied sand tended to break through a freezing zone and to flow out with decreasing excess pore water pressure, and it resulted in caving of soil mass. Such phenomenon as liquefaction of compacted soil materials is not necessarily attributed to the specific ground condition as in the peat layer; that is, it is possible to occur for some embankment sufficiently saturated due to rainfall, inflow of water from ground or at below water level of river, and the suspected damage have

been detected in the failure of the dyke embankments by The 2011 off the Pacific coast of Tohoku Earthquake (Yamaguchi et al. 2012). Furthermore, although the embankment did not reach the liquefaction, there is a number of cases that the embankment saturated beforehand led to serious damage with increasing the pore water pressure in Mid Niigata prefecture eq. (2004), Noto Hanto eq. (2007), the Niigataken Chuetsu-oki eq. (2007) and Shizuoka-oki eq. (2009).

Accordingly, in recent years, the attempts of understanding compositive effect of rainfall and earthquake on mechanical properties and slope failure mechanism of embankments have been conducted by some researchers. Ichii (2005) reported the result of shaking table tests under 1G field for the model embankment constructed with a decomposed granite soil. In the tests, two model specimens were simultaneously applied vibration, when one had been subjected to simulated rainfall in advance. Hata and Ichii (2011) developed a seismic response analysis of an embankment slope incorporating the effect of rainfall, based on the above results (Ichii 2005). Nakamura et al. (2010) conducted a series of centrifuge model tests for understanding of water distribution effect on seismic performance of embankments on a sand ground and a cement-improved foundation. Mori et al. (2010) monitored the seismic behavior of a valley fill ground in a field, and discussed change in water distribution and seismic response due to rainfall.

On the other hand, recent heavy rains have solely caused a large number of the embankment slope failures in Japan. According to Yajima et al. (2008), the numbers of appreciable damage or failure of Japanese national roads that occurred within 15 years from 1990 to 2004 reached 1310, and the cases more than 90 % were induced by rainfall. An interesting fact is, in particular, that the rainfall-induced failures of 30 % resulted from cumulative rainfall less than 25 mm, which is considered not significant intensity of rainfall. The fact implies the limitation of predicting the risk of slope failure from the cumulative rainfall. Therefore, some studies on the rainfall-induced slope failure have been conducted related to seepage behavior of embankments. Kiyohara and Kazama

(2008) in-situ constructed a model embankment, and long monitored change in water distribution and suction using two volcanic soils deposited in Tohoku region throughout rainfall and freeze-thawing periods. Similarly, Kawamura et al. (2010) and Kawamura and Miura (2013a) evaluated the effect of freeze-thaw sequence on the slope stability and dilatancy behavior of Hokkaido volcanic soils by means of a laboratory model test under 1G field. Kitamura et al. (2007) observed the temporal change in pore pressure inside the slope constructed by Shirasu (the volcanic soil in Kyushu), due to simulated rainfall in the laboratory. From the above results, they discussed the applicability of water content (Kawamura and Miura 2013a) and pore pressure (Kitamura et al. 2007) as the useful indices of predicting the slope failure risk.

However, in terms of the limitation of applying the laboratory model test results to in-situ slope stability problems, in recent years, some studies on mechanical behavior of full-scale earth structures begin to be seen. Kawamura and Miura (2013b) constructed a full-scale volcanic soil embankment in a cold region, and reported a slope failure phenomenon induced by simulated rainfall. Danjo et al. (2012) examined the seepage-failure behavior of the embankment constructed by a decomposed granite soil, which had the scale of 5 m height, 4 m width and 40° slope gradient. Panayides et al. (2012) discussed the applicability of a constitutive model for structured clay on the basis of monitoring mechanical behavior of a full-scale embankment. Furthermore, Zwanenburg et al. (2012) constructed a trial embankment with 6 m high on peat and brought to failure, while examined shear behavior of the peat using direct simple shear testing. They reported the in-situ failure mechanism could be well explained by the obtained peat parameters. In addition, the automatic displacement monitoring system for the slope safety by means of GPS is expected as a promising technique (Iwasaki et al. 2012). Thus, from the point of view of establishing more accurate prediction for slope stability, such in-situ monitoring as introduced above will be increasingly required.

In this study, a full-scale embankment was built in-situ using a volcanic soil that had deposited in Hokkaido in order to monitor moisture content distribution, pore pressure, acceleration and temperature inside the embankment throughout rainfall, freezing and snowmelt periods. Consequently, the monitoring attempt had lasted until the embankment led to slope failure after supplying water inside the embankment.

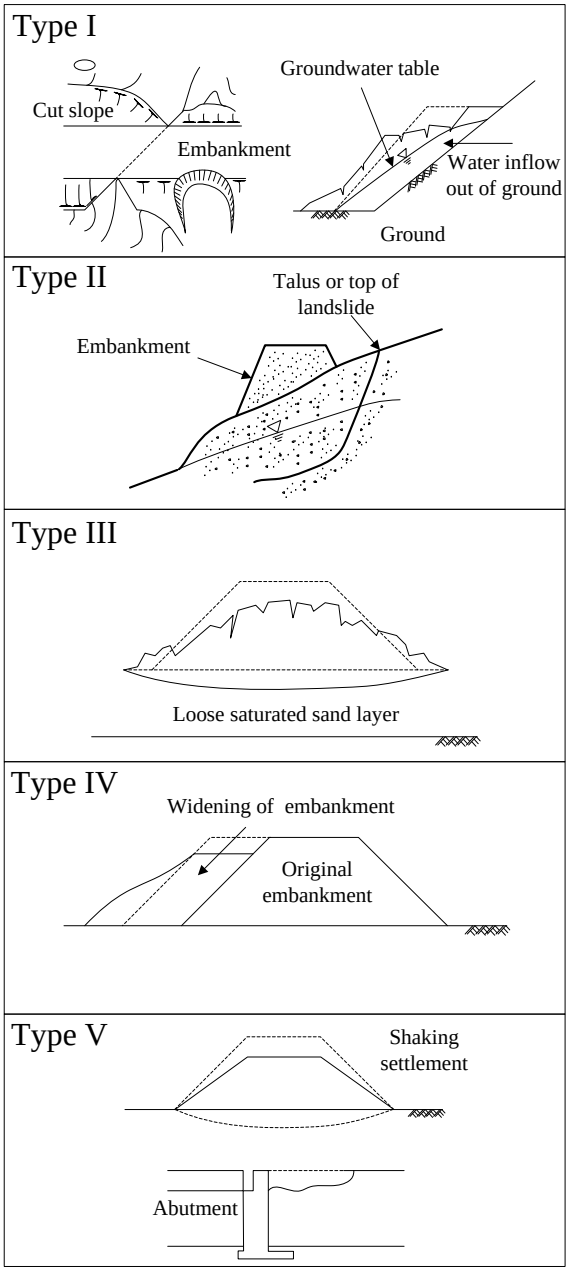

(a) Road embankment (revision of Japan Road Association, 2010)

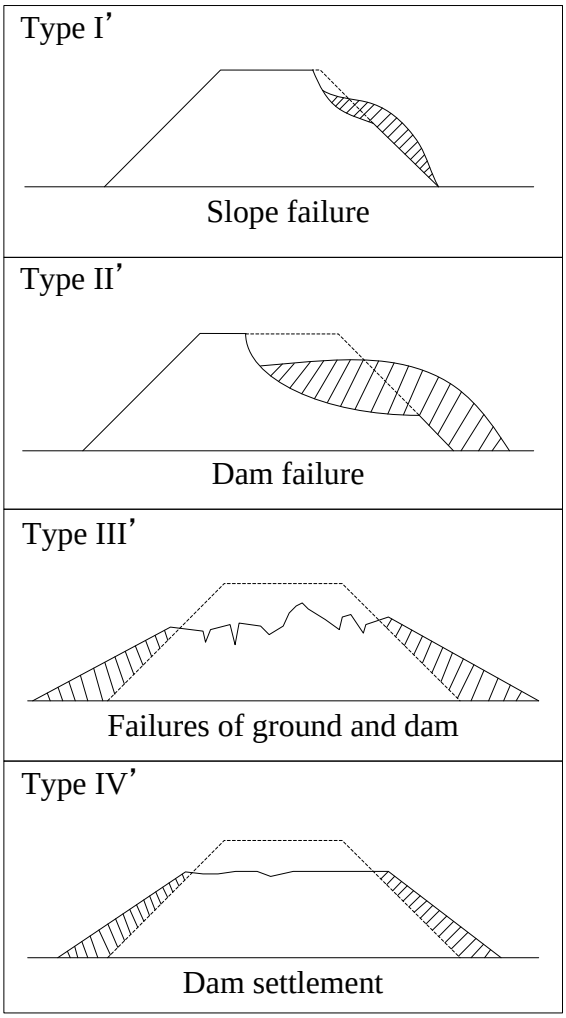

(b) Dyke embankment (revision of Sasaki, 1980)

Figures 2.4.1 Typical types of earthquake-induced failure

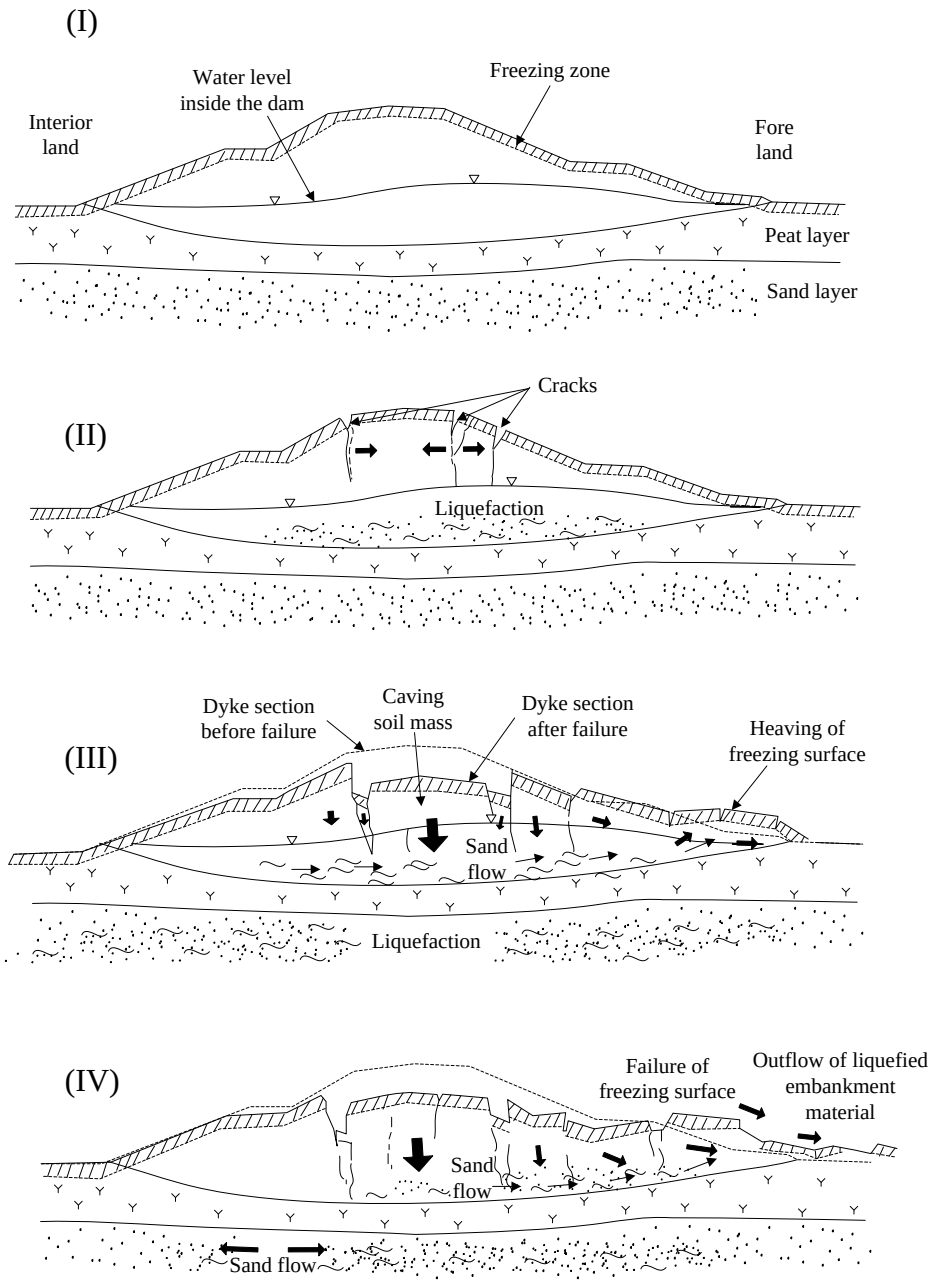

Figures 2.4.2 Mechanism of liquefaction-induced failure caused inside embankment, based on the occurrence in Kushiro-oki earthquake, 1993 (revision of Sasaki, 2012)

CHAPTER 3 SOIL MATERIALS

3.1 Sampling sites and soil materials used

3.1.1 Sandy silt

A sandy silt used for this study (called as Ikeda sandy silt) was sampled at Chiyoda district, Ikeda-cho in Hokkaido, which is located at latitude 42°58′26″ north and longitude 143°26′34″ east (*see* Figure 2.2.2). Figure 3.1.1 shows the subsurface geological map of Tokachi river basin (revision of Obihiro Development and Construction Department 2010). From the figure, it is seen that the volcanic deposits, especially the loam, widely deposit. Those are assumed to be the fall deposits provided by Tokachi-dake or Shikotsu based on Figure 2.2.2. Thus, although many kinds of volcanic weathered or unweathered occupy the Tokachi river basin, the sampling site for Ikeda sandy silt near the Toshibetsu river are considered to be composed of solidified deposits such as gravel, sand and clay, gsm as shown in Figure 3.1.1.

This soil had been used as a dike embankment material constructed in Ikeda-cho. Photograph 3.1.1 shows the borrow pit for the dike embankment material, where Ikeda sandy silt was actually sampled within 1 m below the ground surface. Photographs 3.1.2 (a) and (b) represent Ikeda sandy silt at natural water content w_n (%) and dry condition after oven-dried for 24 hours, respectively. From the photographs, it is seen that Ikeda sandy silt naturally has strongly aggregated structures although the maximum grain size of Ikeda sandy silt is 2.0 mm as explained later. Therefore, the aggregated structures were sufficiently crushed by a hammer before testing.

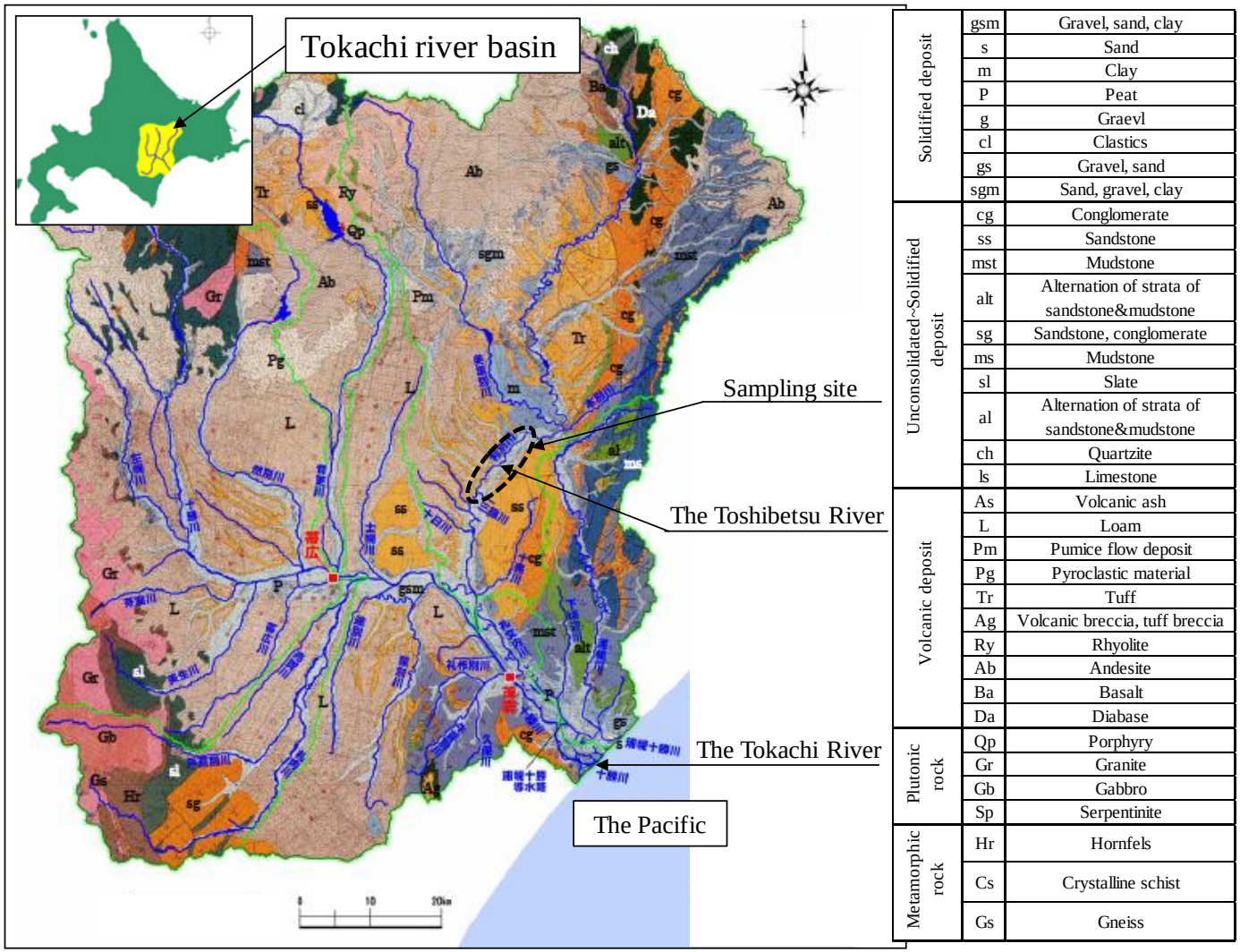

Solidified deposit	gsm	Gravel, sand, clay
	s	Sand
	m	Clay
	P	Peat
	g	Graevl
	cl	Clastics
	gs	Gravel, sand
	sgm	Sand, gravel, clay
Unconsolidated~Solidified deposit	cg	Conglomerate
	ss	Sandstone
	mst	Mudstone
	alt	Alternation of strata of sandstone&mudstone
	sg	Sandstone, conglomerate
	ms	Mudstone
	sl	Slate
	al	Alternation of strata of sandstone&mudstone
	ch	Quartzite
	ls	Limestone
Volcanic deposit	As	Volcanic ash
	L	Loam
	Pm	Pumice flow deposit
	Pg	Pyroclastic material
	Tr	Tuff
	Ag	Volcanic breccia, tuff breccia
	Ry	Rhyolite
	Ab	Andesite
	Ba	Basalt
	Da	Diabase
Plutonic rock	Qp	Porphyry
	Gr	Granite
	Gb	Gabbro
	Sp	Serpentinite
Metamorphic rock	Hr	Hornfels
	Cs	Crystalline schist
	Gs	Gneiss

Figure 3.1.1 Subsurface geological map of Tokachi river basin and sampling site of Ikeda sandy silt

Photograph 3.1.1 Borrow pit for Ikeda sandy silt

(a) Wet condition (water content =31.5%)

(b) Dry condition (oven-dried)

Photographs 3.1.2 Ikeda sandy silt, I soil

3.1.2 Volcanic coarse-grained soil

A volcanic coarse-grained soil used for this study (called as Komaoka volcanic soil) was sampled at Komaoka district, Makomanai, Sapporo city in Hokkaido, which is located at latitude 42°57′13″ north and longitude 141°21′46″ east (*see* Figure 2.2.2). The place is at the typical area where Shikotsu pumice flow deposit, denoted as "Spfl", widely deposits as understood in Figure 2.2.2. According to Miyaura et al. (2011), the homogeneous volcanic soil layer was verified to exist up to 5 m below the ground surface from boring investigation conducted at the site. In addition, no ground water was found within the depth of 5 m. This site was adopted to construct the full-scale embankment for the in-situ testing as well as sampling Komaoka volcanic soil for the laboratory element tests. Accordingly, the location and view of sampling site will be introduced in *CHAPTER 4* in detail.

Photographs 3.1.3 (a) and (b) show original Komaoka volcanic soil at natural water content and after oven-dried for 24 hours, respectively. Komaoka volcanic soil is composed of particles various in grain size, which turn whitish after dried. The fact should be because Komaoka volcanic soil contains relatively-high amount of finer fractions, and those cover coarse-grained particles. Therefore, when observing the soil particles washed and separated in several grain sizes, those could be understood to vary in shape and color as shown in Photographs 3.1.4 (a) ~ (i). In addition, the surfaces of some particles picked up from the grain size of 4.75 to 9.5 mm are shown in Photographs 3.1.5 (a) ~(c). From the photographs, it is found that a degree of porosity differs in each grain, and those are mixing in Komaoka volcanic soil. In particular, the degree of porosity seems to increase from (a) to (c) in order. Because the porosity and particle crushability are considered to characterize the mechanical properties of volcanic coarse-grained soil (Nakata and Miura 2007), it is important to evaluate such effect on the mechanical properties of Komaoka volcanic soil as well.

On the other hand, Shikotsu pumice flow deposit Spfl is known as the soil material liquefied at exactly the same area of Sapporo city by Tokachi-oki earthquakes in both 1968 and 2003 (*see* Table

2.2.4). Based on the prior occurrences, although Spfl can be distinguished into a well-grained soil containing some finer fractions as mentioned above, the material should be recognized to be readily liquefied in meeting liquefaction conditions such as pore water, strong oscillation and its duration. Therefore, Spfl has been an important object for volcanic soil research in geotechnical engineering. Table 3.1.1 shows the typical values of physical properties and permeability coefficient of Spfl (Hokkaido branch of JGS 2010). As some characteristic trends, the soil particle density is very variable, which leads to lower in-situ density and corresponding higher void ratio. That is supposed to result from containing porous pumice. Furthermore, Spfl indicates relatively-high permeability coefficient while including sufficient finer fractions.

Finally, Figure 3.1.2 represents the boring log obtained from Makomanai, Sapporo city, nearest to the sampling site of Komaoka volcanic soil (Hokkaido branch of JGS 2010). From the figure, Spfl exists over 10 m in depth, and the *N* value rapidly increases in the range as deeper.

(a) Wet condition (water content = 40.2%)

(b) Dry condition (oven-dried)

Photographs 3.1.3 Komaoka volcanic soil, $K_{original}$

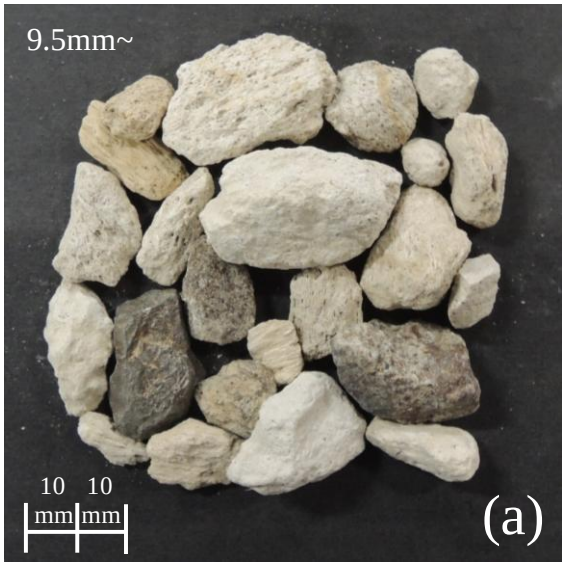
9.5mm~
10 10
mm mm
(a)


4.75~9.5mm
10 10
mm mm
(b)

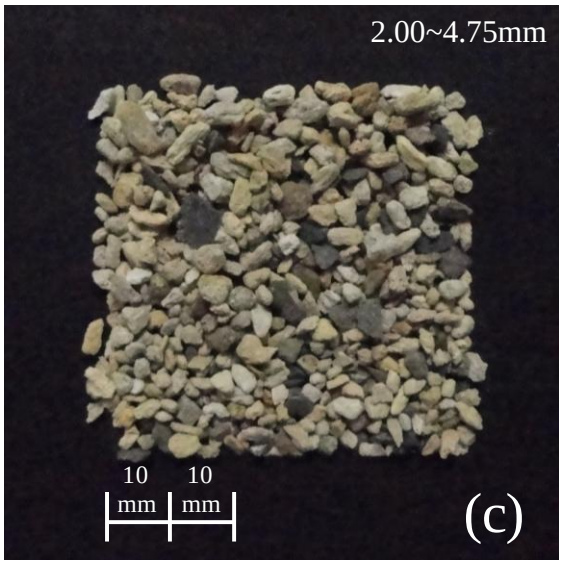
2.00~4.75mm
10 10
mm mm
(c)

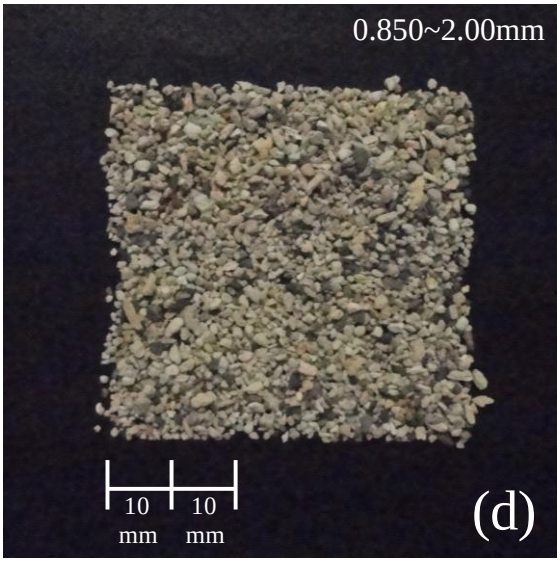
0.850~2.00mm
10 10
mm mm
(d)

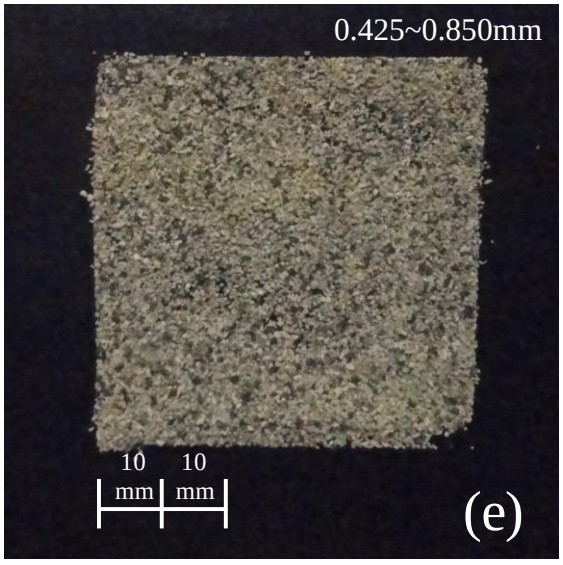
0.425~0.850mm
10 10
mm mm
(e)

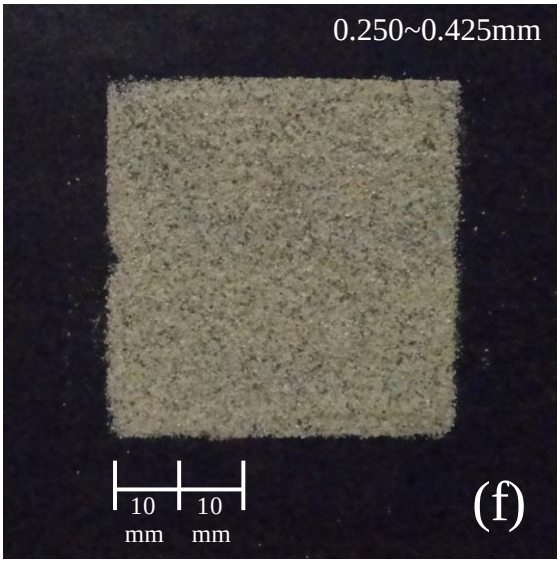
0.250~0.425mm
10 10
mm mm
(f)

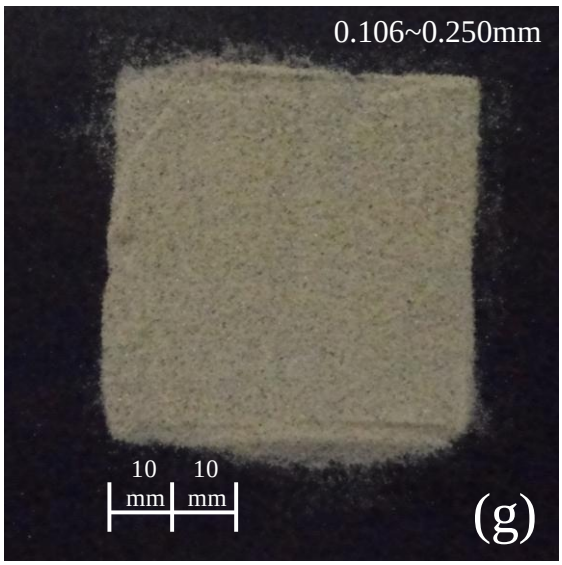

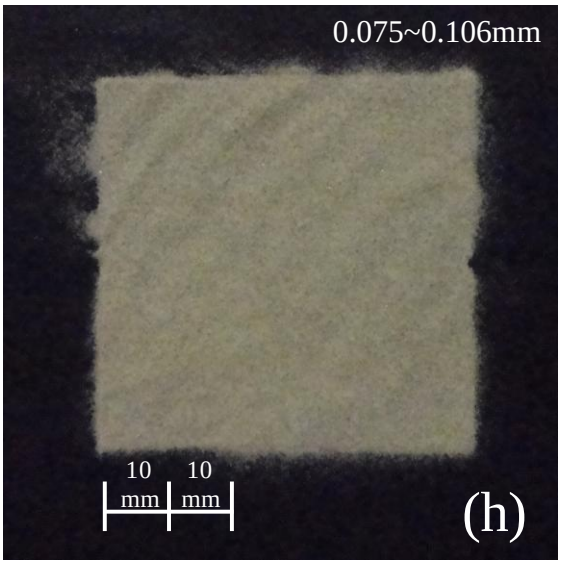

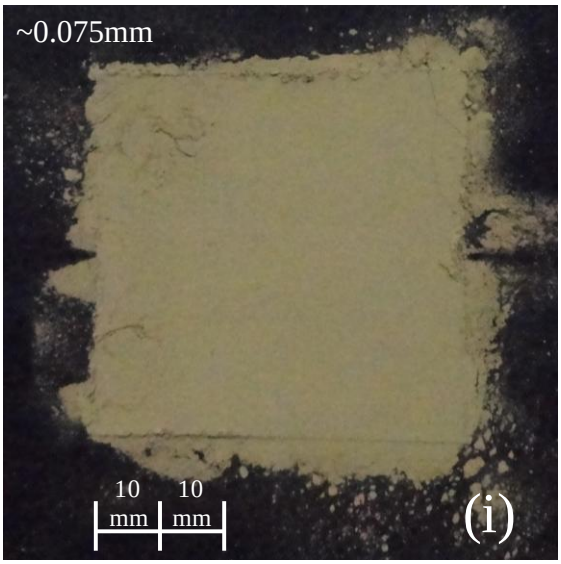

Photographs 3.1.4 Particle images in each grain size
(a) 9.5 mm ~
(b) 4.75 ~ 9.5 mm
(c) 2.0 ~ 4.75 mm
(d) 0.850 ~ 2.0 mm
(e) 0.425 ~ 0.850 mm
(f) 0.250 ~ 0.425 mm
(g) 0.106 ~ 0.250 mm
(h) 0.075 ~ 0.106 mm
(i) ~ 0.075 mm

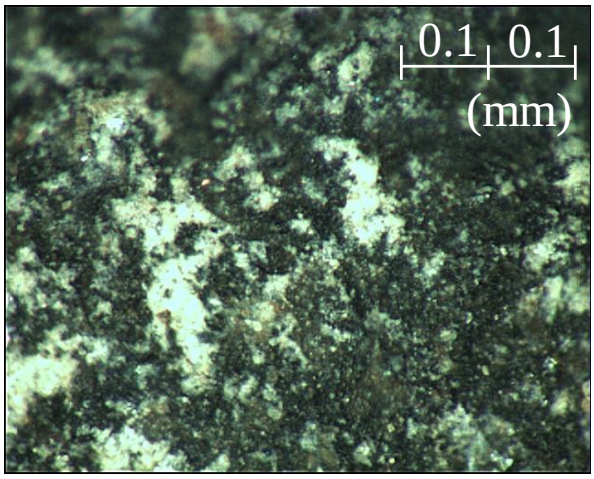

(a) Coarse particle with low porosity

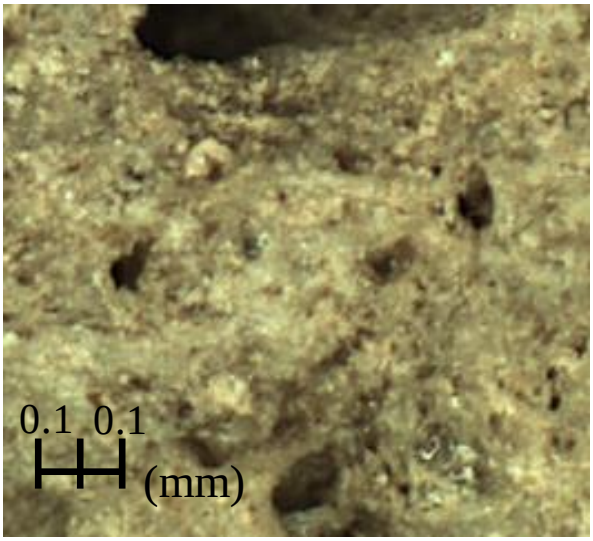

(b) Coarse particle with medium porosity

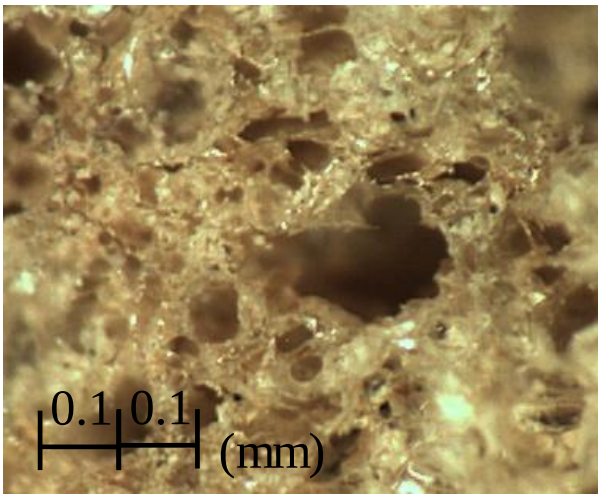

(c) Coarse particle with high porosity

Photographs 3.1.5 Particle images of Komaoka volcanic soil

Table 3.1.1 Typical physical properties of Spfl (JGS 2010)

Sample Name	Soil particle density	Grain size distribution		In-situ property			Compaction (A-c)		Permeability coefficient
	ρ_s	G_c	F_c	ρ_t	ρ_d	e	w_{opt}	ρ_{dmax}	k
	g/cm^3	%	%	g/cm^3		-	%	g/cm^3	(m/s)
Spfl	2.1~2.8	0~30	10~50	1.1~1.6	0.7~1.3	1.0~4.0	35~47	0.96 ~ 1.18	4.4×10^{-5} ~ 2.3×10^{-7}

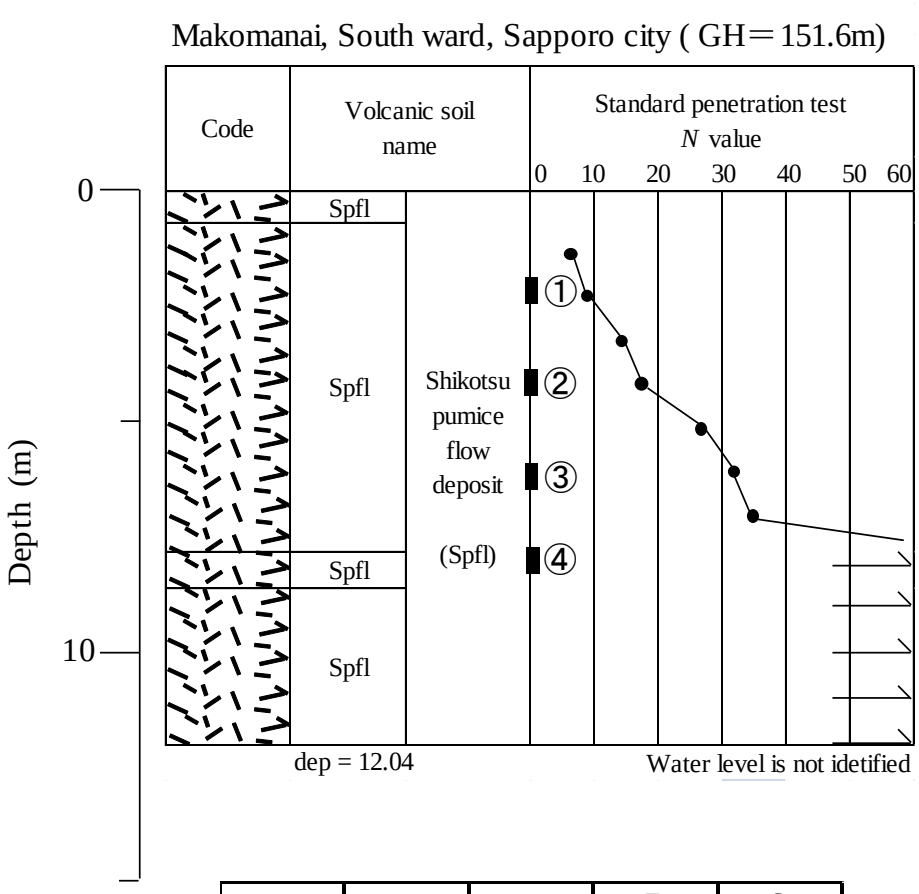

Location	w_n	ρ_s	F_c	G_c
	%	g/cm^3	%	%
①	37	2.48	28	22
②	35	2.40	31	15
③	32	2.36	35	11
④	34	2.28	32	12

Figure 3.1.2 Boring log in Makomanai, Sapporo city (revision of Hokkaido branch of JGS 2010)

3.2 Physical properties

3.2.1 List of physical properties

Tables 3.2.1 (a) and (b) and Figure 3.2.1 indicate the physical properties and grain size accumulation curves of Ikeda sandy silt and Komaoka volcanic soil obtained from “test method for particle size distribution of soils” (JGS 0131-2009), “test method for density of soil particles” (JGS 0111-2009), “test method for liquid limit and plastic limit of soils” (JGS 0141-2009) and “test method for soil compaction using a rammer” (JGS 0711-2009). In Table 3.2.1 (a) and Figure 3.2.1, the materials represented by I soil and $K_{original}$ have each original grain size distribution of Ikeda sandy silt and Komoaka volcanic soil, respectively. Therefore, the after-mentioned full-scale embankment was constructed using the $K_{original}$ material. K soil means the soil material composed of soil particles smaller than 9.5 mm in grain size obtained from $K_{original}$. This is because of the limitation of specimen size for laboratory element tests. Owing to the laboratory testing condition and that the amount of the soil particles > 9.5 mm is not high, Komaoka volcanic soil will be mainly discussed focusing on K soil. On the other hand, $K_{1.9}$, $K_{17.4}$ and $K_{48.2}$ are the gradation-controlled materials using K soil, prepared to evaluate the effect of finer fractions or particle crushability on cyclic strength characteristics. Then, $K_{1.9}$ was prepared washing the finer fractions from K soil on the sieve No.200 (75μm) to control the finer content F_c at 1.9 %. $K_{17.4}$ was controlled at F_c = 17.4 % by sieving the oven-dried K soil materials with the sieve No.200. In addition, $K_{48.2}$ was mixed with the finer fractions of the oven-dried K soil materials to K soil until the F_c value reached 48.2 %.

Because I soil has the maximum grain size of 2.0 mm, finer content F_c of 68.1 % and liquid limit < 50 %, it is regarded as lower plastic sandy-silt. On the other hand, K soil contains finer fractions of 31% in F_c. The finer fractions of K soil indicated non-plastic property, which is consistent with the

plasticity of $K_{1.9}$, $K_{17.4}$ and $K_{48.2}$.

Table 3.2.2 and Figure 3.2.2 present each density of soil particles separated in grain sizes (< 9.5 mm) shown in Photographs 3.1.4 (b) ~ (i). The densities could be understood to vary depending on the grain size. Furthermore, the soil particles larger than 0.425 mm tend to be higher densities. That should be because the soil particles with low-porosity as shown in Photograph 3.1.5 (a) that have higher density, are included more in the grain size range from 0.425 to 9.5 mm. The entire soil particle densities of $K_{1.9}$, $K_{17.4}$ and $K_{48.2}$ shown in Table 3.2.1 (b) are calculated based on Table 3.2.2 as follows;

$$\rho_s = \sum_{i=1}^{8} \rho_{si} \cdot x_i \tag{3.1}$$

where, ρ_{si} is each ρ_s value separated in grain size, and x_i is equal to content percentage of soil particles that have ρ_{si}. The i value includes 8 grain size ranges shown in Table 3.2.2.

Tables 3.2.3 and 3.2.4 show the compaction methods and the classifications of preparation methods and usage of compaction material, respectively (JGS 0711-2009). Because this study focused on filled up ground of embankment, the compaction method A in Table 3.2.3 was adopted. In addition, considering Komaoka volcanic soil causing significant particle breakage due to compaction as mentioned later, reuse of compaction material in a compaction test was not permitted following the b and c methods in Table 3.2.4. Accordingly, in Table 3.2.1 (b), the compaction test results with A-b and -c methods are shown. It is noted that the result with the compactive effort of 621.5 kJ/m^3 using I soil additionally is introduced, and will be mentioned in detail later.

Tables 3.2.1 Physical properties

(a) Grain size distributions

Sample Name	Gravel	Sand	Silt	Clay	F_c	D_{max}	D_{50}	U_c	Soil classification (symbol)	Remark
	%	%	%	%	%	mm	mm	-		
I soil	0	31.9	50.3	17.8	68.1	2.0	0.032	45	Sandy silt (ML)	Original grain size distribution
$K_{original}$	13.6	56.3	23.6	6.4	30.0	>9.5	0.197	45	(SFG)	Original grain size distribution
K soil	12.8	56.2	24.4	6.6	31.0	9.5	0.200	48	(SFG)	Cut grain size distiribution
$K_{1.9}$	23.3	74.8	-	-	1.9	9.5	0.598	5.5	(SG)	Controlled grain size distribution
$K_{17.4}$	18.9	63.7	11.3	6.1	17.4	9.5	0.381	58	(SFG)	Controlled grain size distribution
$K_{48.2}$	10.9	40.9	40.7	7.5	48.2	9.5	0.094	27	(SFG)	Controlled grain size distribution

(b) Soil particle density, plasticity and compaction (A-c method)

Sample Name	ρ_s	w_L	w_P	I_p	Compaction			
					A-c		A-b	
					w_{opt}	ρ_{dmax}	w_{opt}	ρ_{dmax}
	g/cm^3	%	%	%	%	g/cm^3	%	g/cm^3
I soil	2.578	46.8	34.5	12.3	28.2	1.405	25.0 (25.0)*	1.419 (1.446)*
K soil	2.512	46.7	Unavailable	NP	40.5	1.059	34.2	1.090
$K_{1.9}$	2.533				-	-	37.5	1.030
$K_{17.4}$	2.525				-	-	37.5	1.044
$K_{48.2}$	2.509				-	-	32.7	1.125

*Compactive effort of 621.5 kJ/m^3

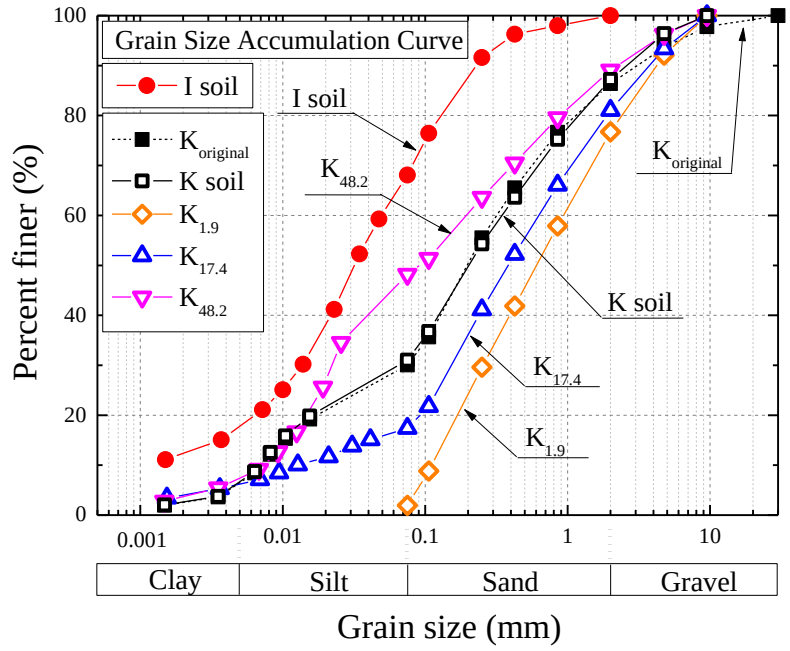

Figure 3.2.1 Grain size distributions of Ikeda sandy silt and Komaoka volcanic soils

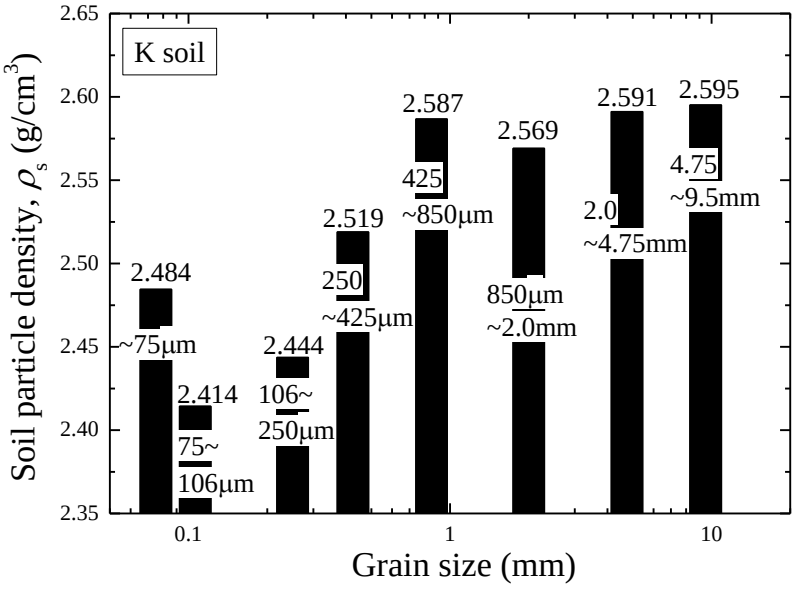

Figure 3.2.2 Soil particle densities in each grain size

Table 3.2.2 Soil particle densities in each grain sizes

Sample Name	Soil particle density, g/cm^3							
	4.75~9.5 mm	2.0~4.75 mm	0.850~2.0 mm	0.425~0.85 mm	0.25~0.425 mm	0.106~0.25 mm	0.075~0.106 mm	~0.075 mm
K soil	2.595	2.591	2.569	2.587	2.519	2.444	2.414	2.484

Table 3.2.3 Compaction methods (JGS 0711-2009)

Compaction method	Rammer weight	Mold inner diameter	Number of compaction layers	Number of blows per a layer	Permissible maximum grain size	Compactive effort
	kg	m	-	-	mm	kJ/m^3
A	2.5	10	3	25	19	550
B	2.5	15	3	55	37.5	550
C	4.5	10	5	25	19	2500
D	4.5	15	5	55	19	2500
E	4.5	15	3	92	37.5	2500

Table 3.2.4 Classification by preparation method and usage of compaction material(JGS 0711-2009)

Combination name of compaction method	Preparation method for compaction material	Reuse compaction material in a compaction work
a	Dry	Yes
b	Dry	No
c	Wet	No

3.2.2 Compaction properties

In this study, for the compaction test and specimen preparation, three kinds of compaction molds and two kinds of rammers were prepared. Tables 3.2.5 (a) and (b) and Figures 3.2.3 (a) and (b) show each size of compaction molds and rammers and their schematic diagrams, respectively. The compaction mold (a) was used for compaction tests by A-b and -c methods to determine compaction condition, while the compaction molds (b) and (c) were utilized for sample preparation by compaction. Those molds (b) and (c) are possible to split longitudinally so as not to disturb the specimen when it is taken out after compaction. Compaction with the compaction mold (c) was conducted using the rammer (ii) because of acceptable frame diameter of rammer smaller than 70 mm. In addition, the compaction mold (c) is height-adjustable to make specimens 140 or 170 mm in height.

First, let us discuss the compaction test results of Ikeda sandy silt, I soil. Figure 3.2.4 shows the compaction curves. In the figure, the circle and the triangle are the results with the compaction mold (a) in the A-b and -c methods, respectively. Then, the compactive effort is corresponding to 550 kJ/m^3. The square was obtained from the compaction with the compaction mold (b) in the A-b method. However, it is noted that because the compaction mold height was about 23 mm higher than the compaction mold (a), the compaction was conducted with 4 layers. The number of blows per a layer is 25 times as well. Accordingly, the compactive effort reaches 621.5 kJ/m^3. Comparing those results, the compaction curve with the higher compactive effort shifts at the upper left along the zero air void curve than the others with the lower compactive effort. Furthermore, it is seen that the compaction curve in A-b method tends to be located at the upper left of the one in A-c method even in the same compactive effort condition (550 kJ/m^3). In *CHAPTER 5*, the compaction curve with the compactive effort of 621.5 kJ/m^3 is adopted to determine compaction condition of triaxial specimens.

Subsequently, Figure 3.2.5 represents the compaction curves related to Komaoka volcanic soil.

All the results are obtained from the compaction with the compactive effort of 550 kJ/m^3. Focusing on the difference in compaction method, the relation tends to be similar to that with I soil; i.e., the compaction curve in A-b method shifts at the upper left of that in A-c method. As a possible reason for the phenomenon, the effect of the aggregated structure of I soil and the porosity of K soil may be presumed. That is, for A-b method, particles of K soil once oven-dried are considered to contain empties inside of the opening intra-particle void (*see* Figure 2.2.3) even after moisture-controlled again as shown in Figure 3.2.6. On the other hand, K soil particles that have been exposed to rain or ground water over the long term, are comparatively saturated. Then, because water acting on compaction condition should be at inter-particle voids, even if the volume of the influential water is exactly the same in both A-b and A-c methods, water content at compaction of A-c method can be higher than that in A-b method. Such effect is considered to agree with I soil that has aggregated structures. Then, each void inside of aggregated structures and between them should be corresponding to the opening intra particle void and the inter-particle void of K soil as shown in Figure 3.2.6. Keeping in mind the above, in the cases that volcanic coarse-grained soil or a fine-grained soil to form aggregated structures, the A-c method ought to be employed to determine a compaction property.

On the other hand, the optimum water content w_{opt} (%) and maximum dry density ρ_{dmax} (g/cm^3) of each Komaoka volcanic soil determined from Figure 3.2.5 are shown in Figures 3.2.7 (a) and (b), respectively, in terms of the relation with the finer content F_c before compaction. From the results in the A-b method, it is obvious that the w_{opt} and ρ_{dmax} values becomes lower and higher, respectively as the finer content increases. This tendency is similar to the relation of the compaction result in the A-a method with a crushable volcanic coarse-grained soil to those in A-b and -c methods (JGS, 2009b). That is, on the A-a method to permit reuse of compaction materials, the compacted specimen causes particle breakage to become denser as the compaction and reuse of soil materials progress.

Tables 3.2.5 Compaction molds and rammers used in this study

(a) Compaction mold sizes

Compaction mold	Inner diameter, D_m	Height, H_m	Volume, V_m
	mm	mm	cm^3
(a)	100	127	1000
(b)	100	150	1178
(c)	70	140 or 170	539 or 654

(b) Rammer sizes

Rammer	Diameter of weight	Dropping height	Diameter of frame
	mm	mm	mm
(i)	50	300	76
(ii)	50	300	60

Figures 3.2.3 Compaction molds and rammers used in this study (a)Compaction molds

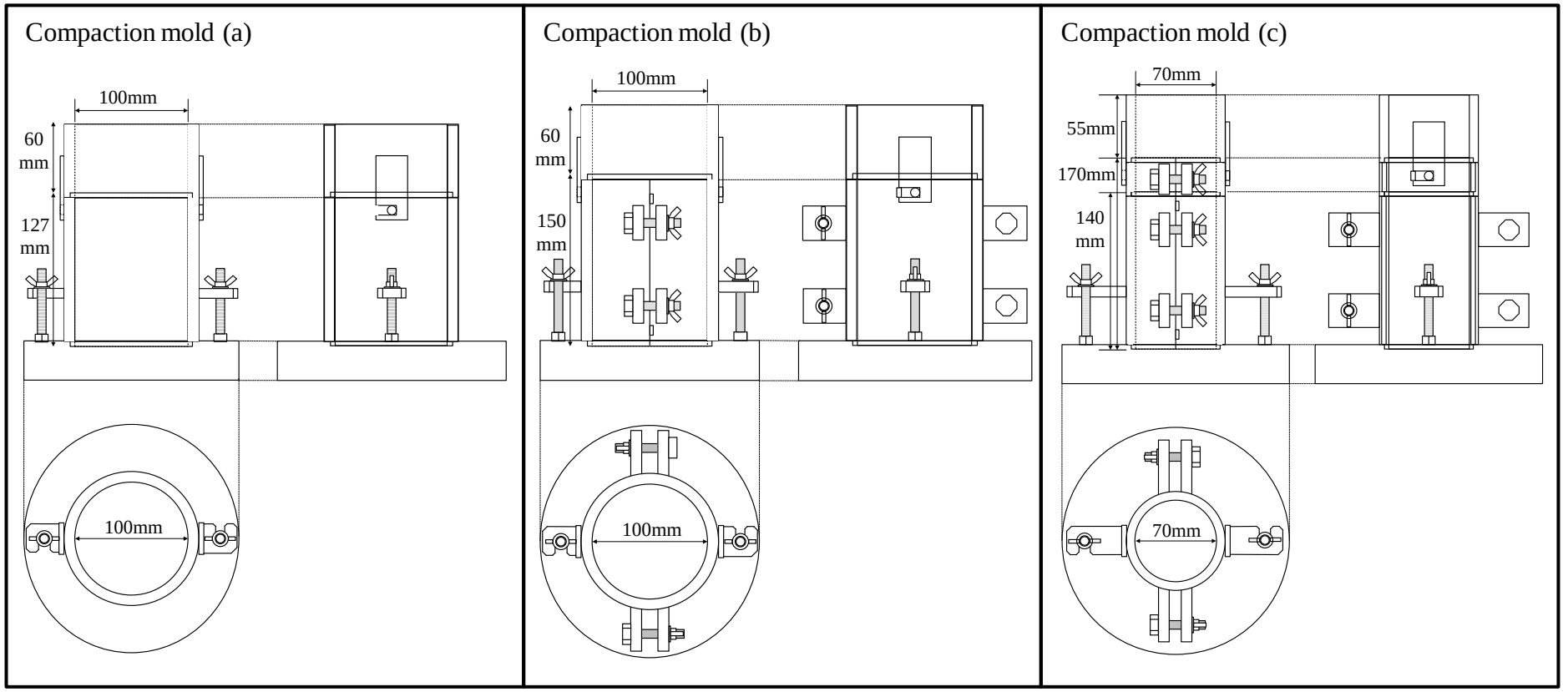

Figures 3.2.3 Compaction molds and rammers used in this study (b) Rammers

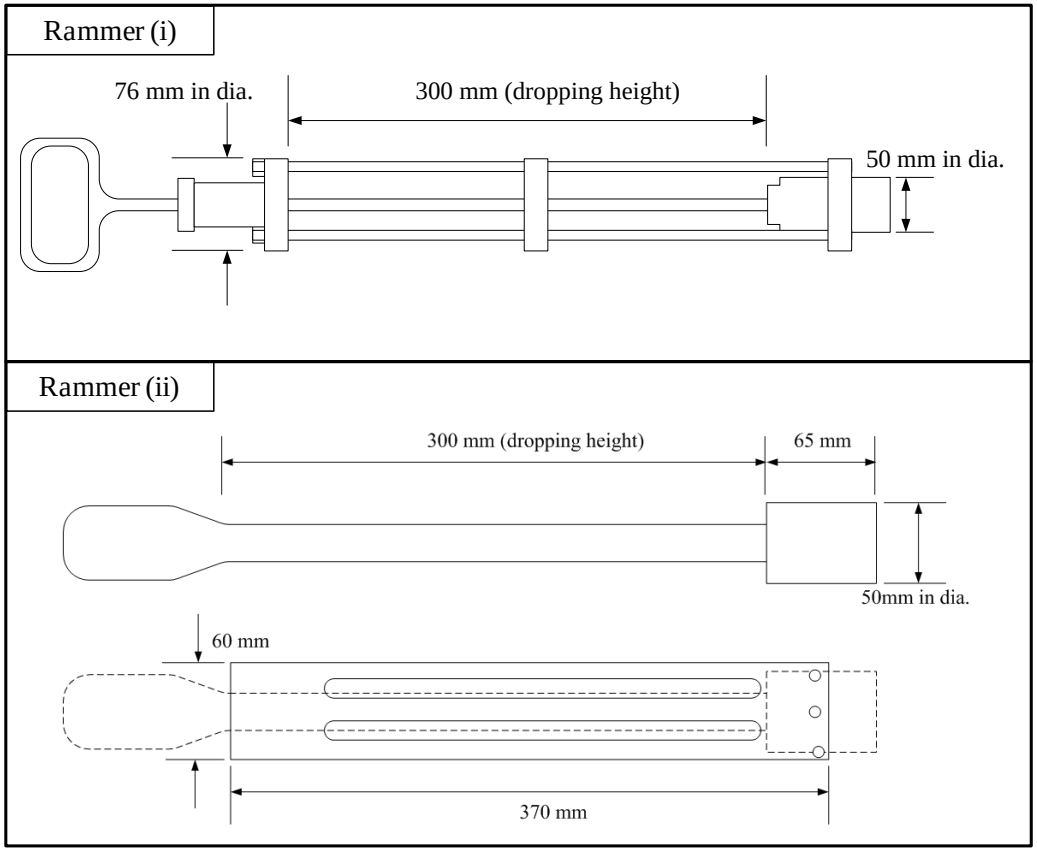

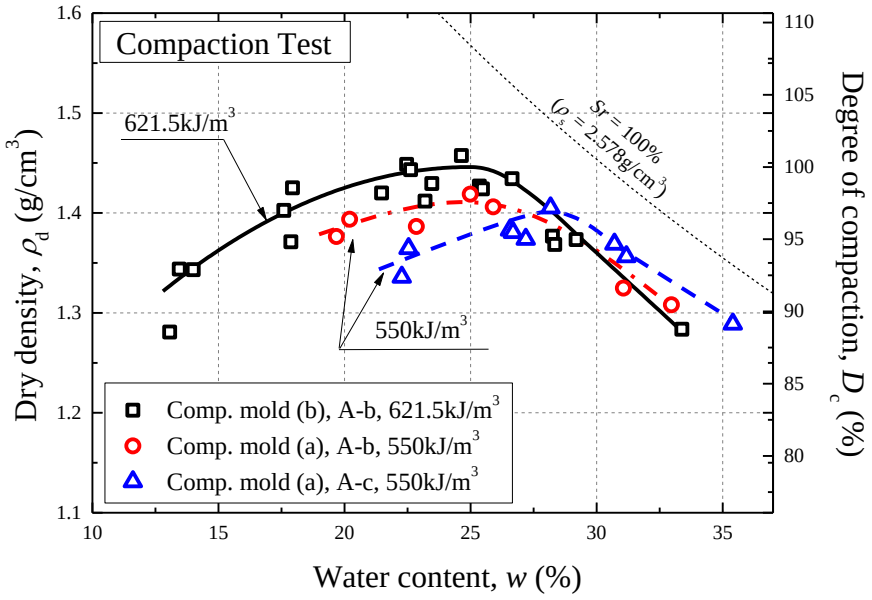

Figure 3.2.4 Compaction test results for I soil

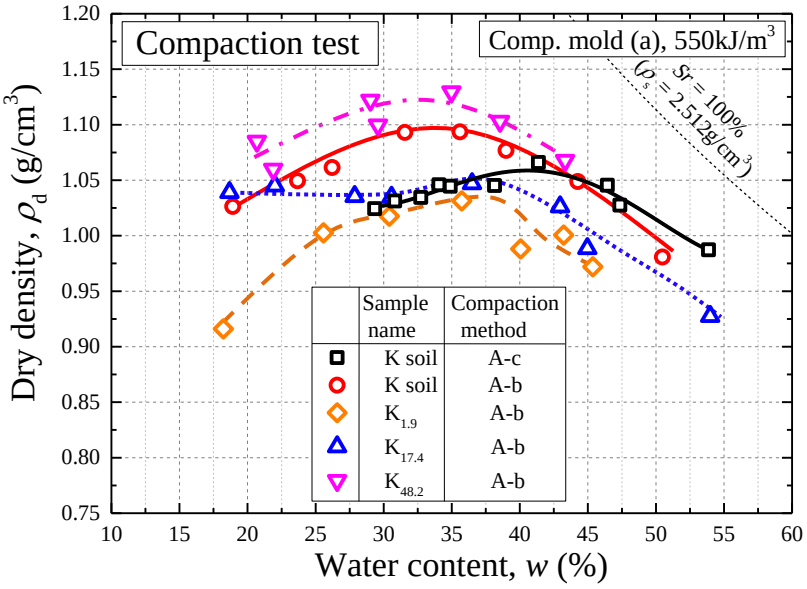

Figure 3.2.5 Compaction test results for Komaoka volcanic soils

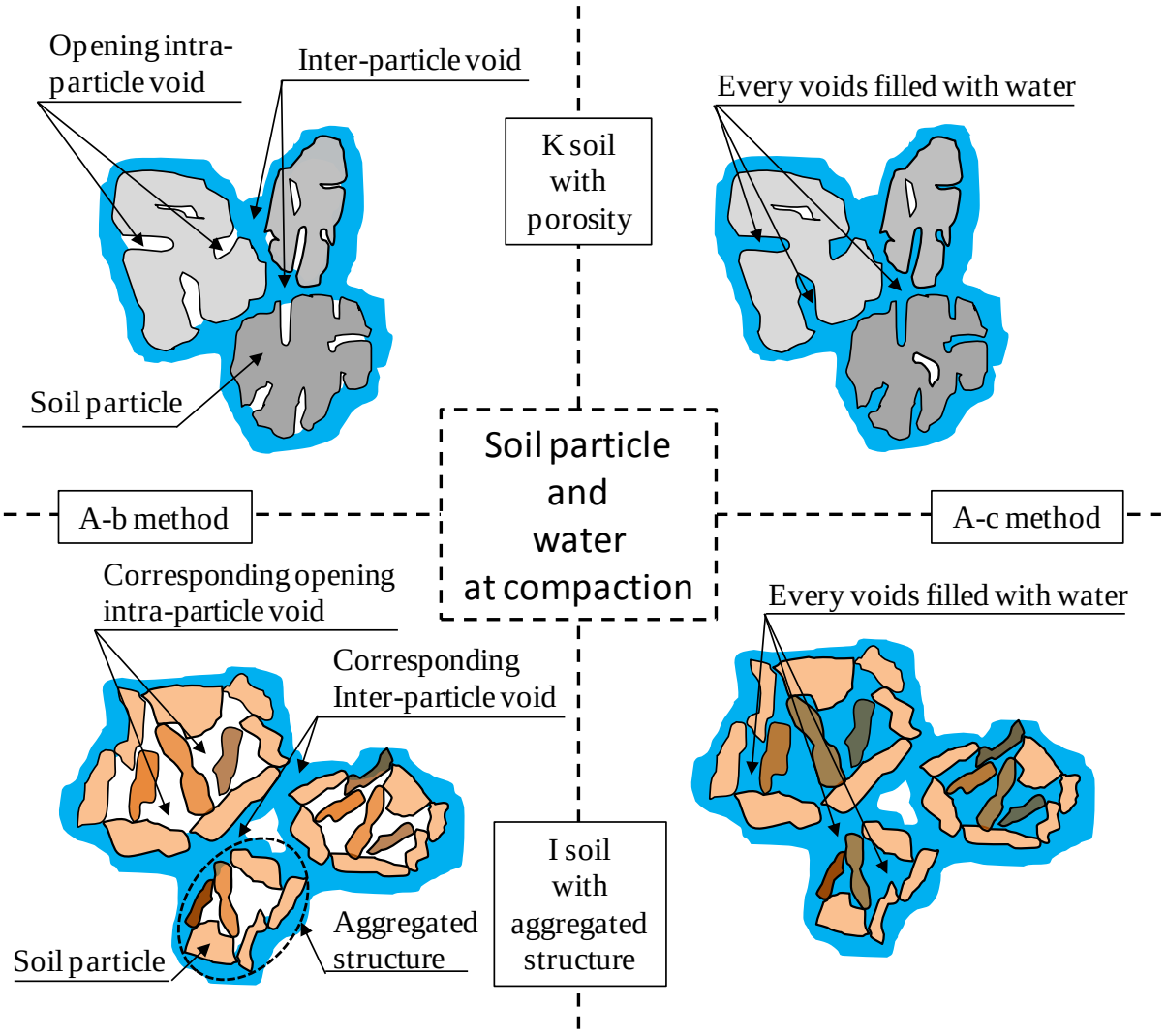

Figure 3.2.6 Water distribution in each particle or aggregated structure in compaction of A-b and -c methods

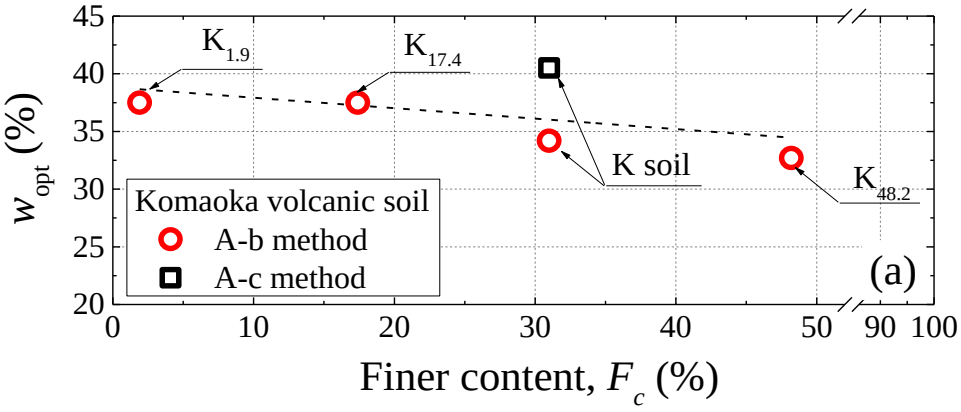

(a) Optimum water content

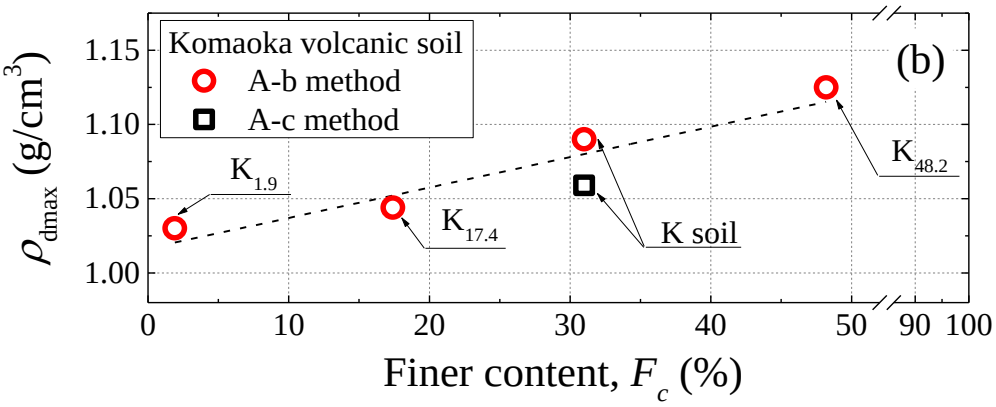

(b) Maximum dry density

Figures 3.2.7 Optimum conditions of $K_{1.9}$, $K_{17.4}$, K soil and $K_{48.2}$

3.2.3 Soil water retention characteristics of K soil

Figure 3.2.8 shows the soil-water characteristics curve (denoted as SWCC) of K soil examined by the pressure plate method in "test method for water retentivity of soils" (JGS 0151-2009). In the figure, the fitted curve is indicated by van Genuchten model (JGS 2006) shown in Equation (3.2).

$$S_e = [1+|\alpha\psi|^n]^{-(1-1/n)}$$
$$= (S_r - S_{r0})/(100 - S_{r0}) \quad (3.2)$$

where, S_e, ψ and S_{r0} are specific storage, pressure head and residual degree of saturation, respectively. The parameters a and n are coefficients for fitting. It is noted that the test was conducted with a triaxial apparatus which will be introduced in *4.1.2.1, CHAPTER 4*. The specimen was compacted at the water content at compaction w_i of 38.2 % with the compaction mold (c) shown in Figure 3.2.3. The specimen size is 70 mm in diameter and 140 mm in height, and its initial dry density ρ_{di} becomes 0.931 g/cm^3 (0.931 Mg/m^3), which corresponds to the initial degree of compaction D_{ci} of 88.0 % on the basis of ρ_{dmax} = 1.059 g/cm^3 (1.059 Mg/m^3). After the specimen was saturated at the degree of saturation S_r of 75 % in the triaxial cell, it was isotropically consolidated at the effective confining pressure σ_c' of 50 kPa. Afterward, desired suction values s (= $u_a - u_w$, kPa) were applied to drain and absorb pore water in the specimen in stages. Each pore pressure and the amount of drainage were monitored by means of a set of pore pressure transducers and a differential pressure transducer connected to a double tube burette thorough PC. The detail of the apparatus will be mentioned later. From the figure, it is clear that the hysteresis of SWCC appears. In the drying path, it could be understood that water begins to rapidly flow out of the specimen at s = 20 kPa. The suction value of 19.6 kPa was determined as the air entry value, AEV. Furthermore, the suction value tends to abruptly increase again as the degree of saturation decreases below 40%. In this case, therefore, the residual degree of saturation can be found as around 30%. On the other hand, in the wetting path, although very little change in S_r (%) is found up to s = 10 kPa, it is recognized that the specimen is

drastically saturated below 10 kPa in suction. Based on the fitting curve, the water entry value, WEV, should be 2.1 kPa.

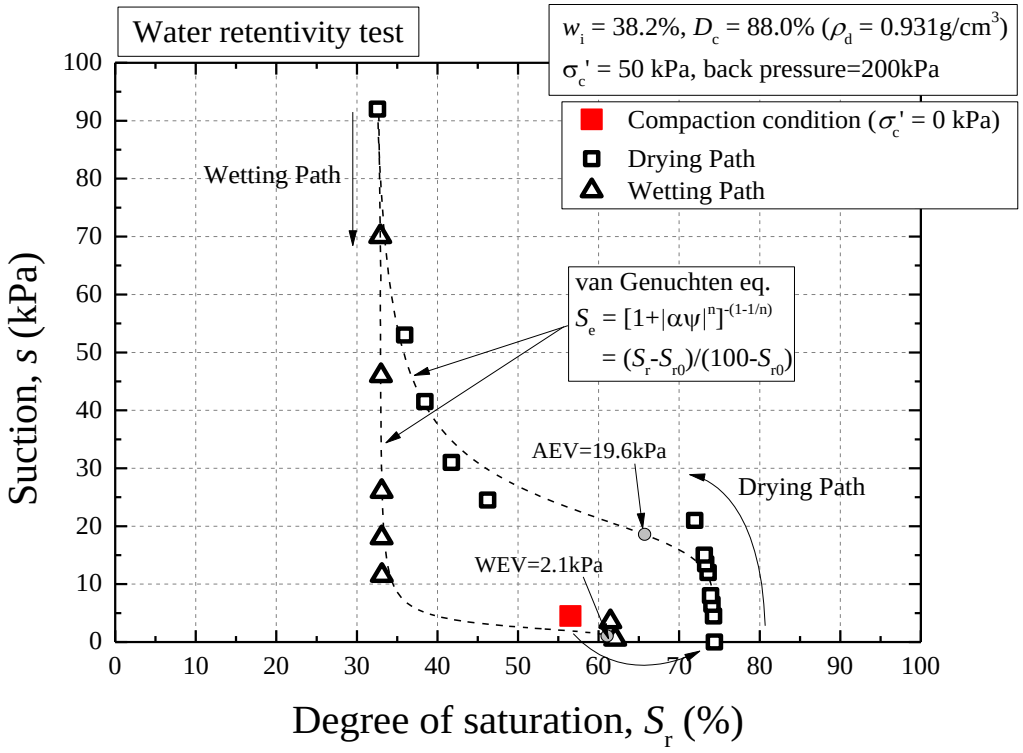

Figure 3.2.8 Soil water characteristics curve of K soil at w_i = 38.2 % and D_c = 88.0 %

3.2.4 Crushability of constitutive particles

3.2.4.1 Indices of particle breakage

In treating a crushability soil material, how to identify a degree of crushability adequately has been discussed by some researchers. Figure 3.2.9 shows some concepts of identifying the degree of crushability based on change in degradation (JGS 2009b). Marsal proposed the summation of change in residual percentage at each grain size between before and after testing. Lee and Farhoomand focused on 15 % diameter on the grain size diagram, while it is 10 % diameter on the grain size diagram in the case of Lade et al. Hardin evaluated the crushability index including all the grain sizes. On the other hand, Miura and Yagi established the crushability evaluation with the finer content increment ΔF_c (%) for volcanic soils. In the paper (Miura and Yagi 1997), the validity of the ΔF_c evaluation was discussed in detail. In this thesis, the ΔF_c evaluation was employed as the crushability index because of its simplicity and the attempt to clarify the effect of finer fractions on mechanical properties.

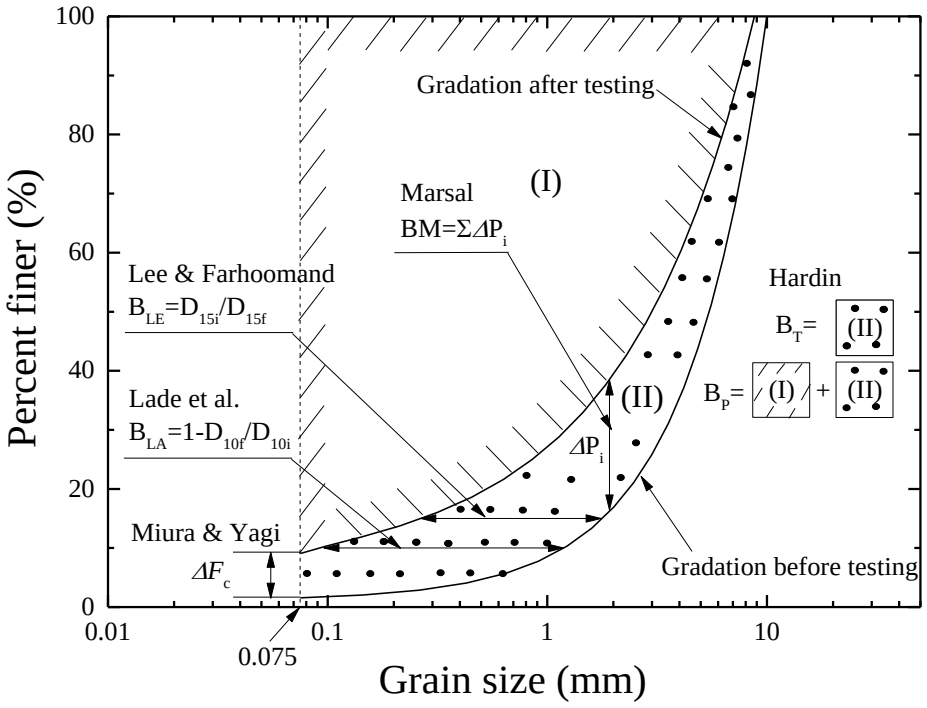

Figure 3.2.9 Indices of identifying particle breakage (JGS, 2009a)

3.2.4.2 Particle crushability of K soil due to compaction

Based on the finer content increment ΔF_c evaluation, the particle crushing behavior of K soil due to compaction was examined prior to a series of laboratory element tests. The compaction was conducted under various conditions of initial water contents w_i (%) and compactive efforts with the compaction mold (a) (*see* Figure 3.2.3). Those compaction conditions are plotted in Figure 3.2.10 with regard to each compactive effort E_c, which is defined as $1.0E_c$ = 550 kJ/m^3. In addition, the compaction conditions are classified into three groups based on the w_i / w_{opt} value normalized by the optimum water content of 40.5% ; drier, optimum and wetter conditions, which belong at $w_i / w_{opt} <$ 0.9, $0.9 \leq w_i / w_{opt} \leq 0.9$ and $1.1 \leq w_i / w_{opt}$, respectively.

Figure 3.2.11 shows the relations of ΔF_c with E_c and the dry density ρ_d (g/cm^3). From the figure, it could be understood that the ΔF_c value tends to uniquely increases with the compactive effort and corresponding dry density higher. That is, the compaction with higher compactive effort obviously stimulates stronger particle crushing. Furthermore, focusing on the effect of molding water content w_i, the particle breakage at the optimum condition is considered higher than at the drier and wetter conditions. The fact implies that the compactive effort can propagate to the soils most effectively. However, the difference in ΔF_c due to the molding water content condition reach about 1 % at most, and the additional study will be required to clarify the effect of compaction on the particle crushing.

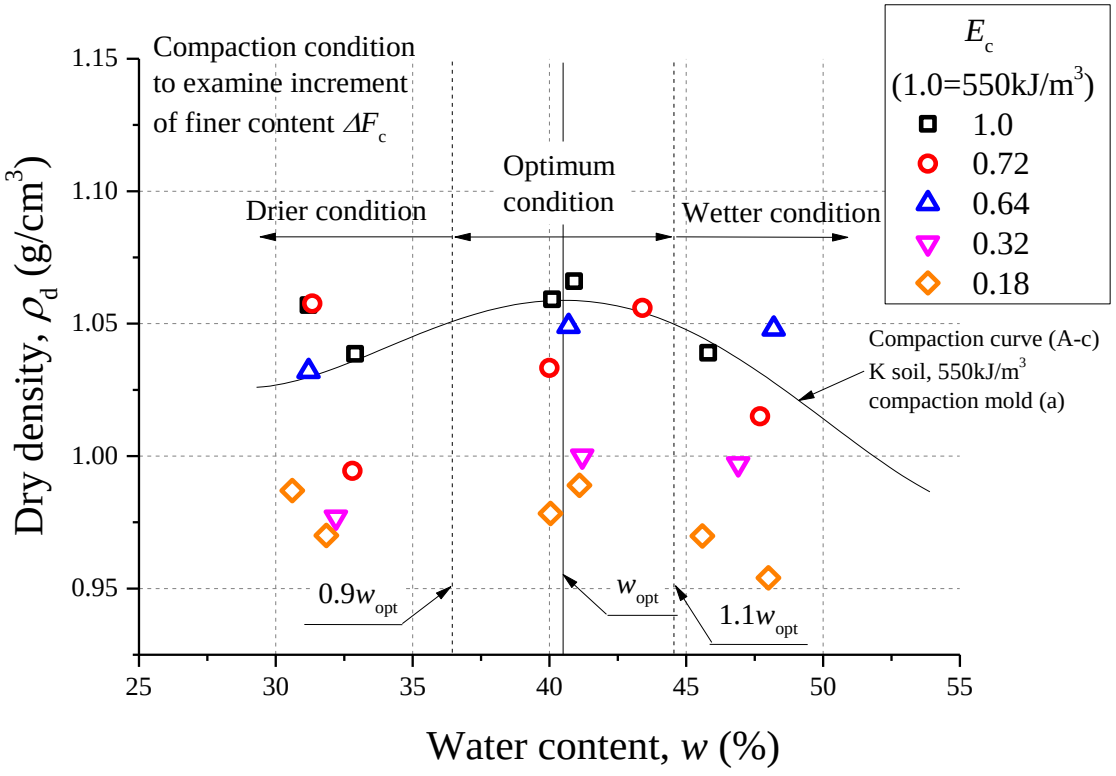

Figure 3.2.10 Compaction condition of specimens for sieving analysis to clarify increment of finer content due to compaction

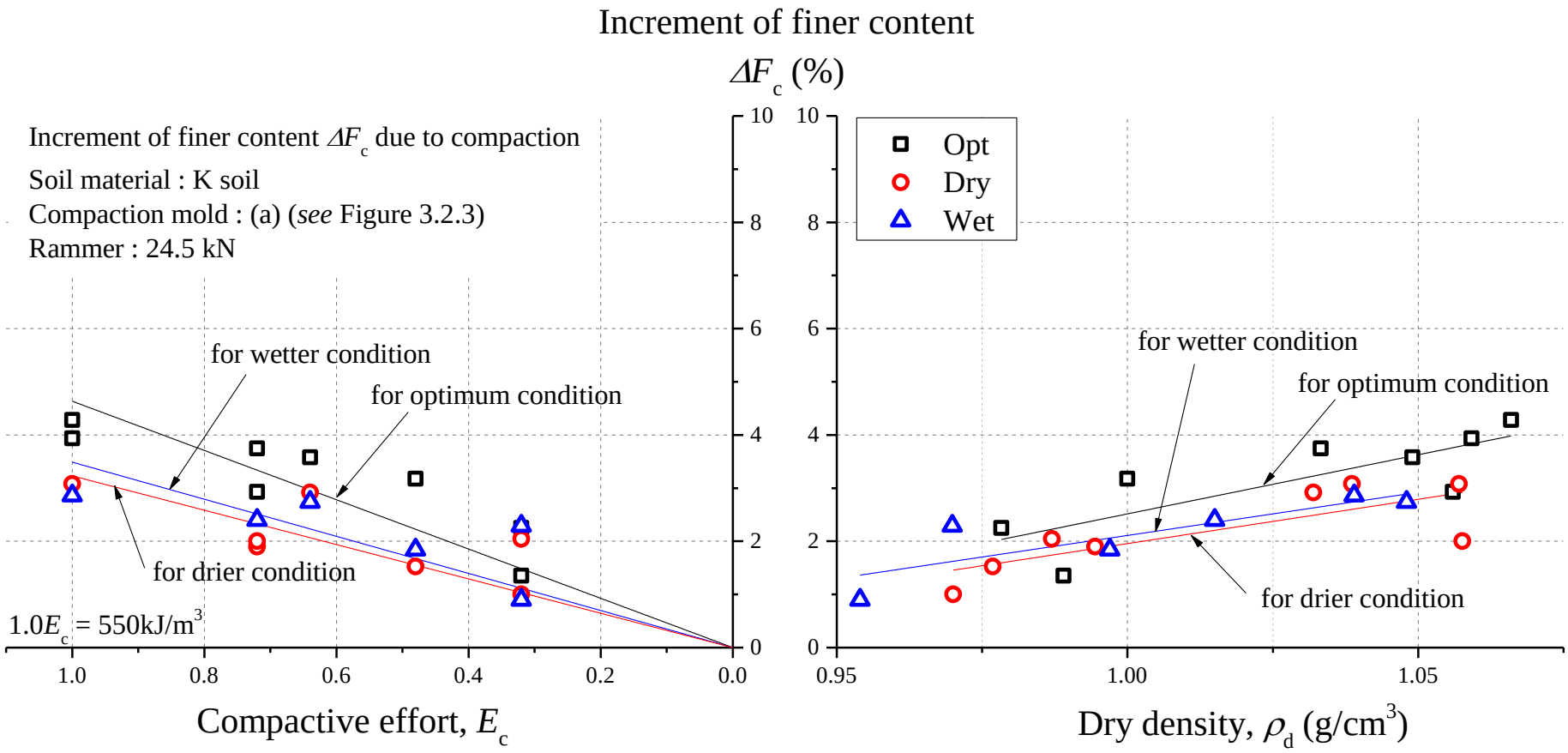

Figure 3.2.11 Relations of increment of finer content due to compaction with compactive effort and dry density

CHAPTER 4 TESTING METHOD

4.1 Laboratory tests

4.1.1 Introduction

The aim of laboratory element tests is to reveal mechanical characteristics of compacted embankment especially in a cold region, focusing mainly on effects of compaction condition, freeze-thaw sequence and finer fractions contained. Accordingly, many testing conditions were covered in terms of not only the above conditions but also various mechanical parameters and soil materials. Therefore, first, the summation of testing conditions will be briefly introduced with Table 4.1.1. In the table, the combinations among the conducted laboratory element tests, soil materials and specimen sizes adopted for those tests are shown. In addition, the compaction molds (b) and (c) used in preparing the specimens are noted, which were chosen in accordance with the applicable specimen sizes and difficulty in trimming coarse-grained soils.

Cyclic triaxial test (I) was conducted particularly to examine the effect of freeze-thaw sequence on cyclic shear behavior of K soil compacted in different compaction conditions. The f value in the row (0.005 Hz) means the frequency of cyclic loads applied to the specimens, which will be mentioned later. Cyclic triaxial test (II), which was conducted under the condition of f = 0.1 Hz, was performed for cyclic shear behavior varying in different compaction conditions and finer contents. Then, the gradation-controlled soils, $K_{1.9}$, $K_{17.4}$ and $K_{48.2}$, were used in addition to I soil and K soil.

Furthermore, compression triaxial test, bender element test and permeability test were carried out to examine the influence of compaction conditions with I soil and K soil.

Tables 4.1.2 ~ 4.1.4 show specifications of the equipment belonging to each triaxial test. In Tables 4.1.2 (a) ~ (c), each transducer, dynamic strain amplifier and function generator and oscilloscope for the bender element test are introduced. Table 4.1.3 indicates loading system for each testing apparatus. Then, in non-destructive tests such as the bender element test and the permeability test, loading system was used to keep no deviator stress in whole testing processes. In Table 4.1.4, the specifications of temperature bath for freeze-thawing test are summarized. Thus, although the testing conditions broadly vary depending on the objectives for each test as mentioned above, the fundamental structures of each triaxial apparatus are very similar. Therefore, in the following section, those testing apparatuses will be introduced with concentrating on some differences to note such as shearing, freeze-thawing and percolating system. In addition, specimen preparation method appropriate to soil materials and specimen sizes, and stress states in testing will be explained in detail.

Table 4.1.1 Laboratory element tests simulating effects of compaction condition, freeze-thaw sequence and finer content

Testing type		Compaction condition			Freeze-thaw sequence			Finer content (particle crushability)		
		Soil material	Compaction mold	$D_s \times H_s$ (mm)	Soil material	Compaction mold	$D_s \times H_s$ (mm)	Soil material	Compaction mold	$D_s \times H_s$ (mm)
Cyclic triaxial test	(I) f=0.005Hz				K soil	(c)	70×140			
	(II) f=0.1Hz	I soil	(b)	70×140				K soil, $K_{1.9}$, $K_{17.4}$, $K_{48.2}$	(c)	70×140
		K soil, $K_{1.9}$, $K_{17.4}$, $K_{48.2}$	(c)							
Compression triaxial test		I soil, K soil	(b)	100×150						
Bender element test		I soil	(b)	70×140						
		K soil	(c)	70×130~						
Permeability test		I soil, K soil	(b)	100×150~						

Table 4.1.2 (a) Specifications of triaxial apparatuses

Testing type		Load cell (Stress)			Dial gauge (Displacement)			Cell pressure transducer		
		Model	Brand	RC	Model	Brand	RC	Model	Brand	RC
Cyclic triaxial test	(I)	TU-BR5KN	TEAC	5kN	DTH-A-50	KYOWA	50mm	PG-10KU	KYOWA	10 kgf/cm^2
	(II)	DB-100K	SHOWA MEASURING INSTRUMENTS CO., LTD.	100kgf	9E08-D1	SAN-EI INSTRUMENT CO., LTD.	30mm	PG-10KU	KYOWA	10 kgf/cm^2
Compression triaxial test		TU-BR	TEAC	20kN	-	KYOWA	20mm	PG-10KU	KYOWA	10 kgf/cm^2
Bender element test		LCP-100L	ORIENTEC CORPORATION	100kgf	DT-30D	KYOWA	30mm	PG-5KU	KYOWA	5 kgf/cm^2
Permeability test		TU-200	SEIKEN INC.	200kgf	TR5730	SOHGOH KEISO	30mm	PG-5KU	KYOWA	5 kgf/cm^2

Testing type		Pore water pressure transducer			Dynamic strain amplifier		
		Model	Brand	RC	Model	Brand	RC
Cyclic triaxial test	(I)	PG-5KU	KYOWA	5 kgf/cm^2	DPM-611B	KYOWA	0~±5V
	(II)	PG-5KU	KYOWA	5 kgf/cm^2	DPM-305B	KYOWA	-
Compression triaxial test		PG-5KU	KYOWA	5 kgf/cm^2	AS1201 LC210	NEC UNIPULSE	-
Bender element test		PG-10KU	KYOWA	10 kgf/cm^2	DPM-601A LC-240	KYOWA UNIPULSE	0~±10V
Permeability test		PG-5KU	KYOWA	5 kgf/cm^2	DPM-601A LC-240	KYOWA UNIPULSE	0~±10V

Table 4.1.2 (b) Specifications of cyclic triaxial apparatus for freeze-thawing and unsaturated test

Testing type	Pore air pressure transducer			Differential pressure transducer for specimen volume change			Differential pressure transducer for water level change in double-tube burette		
	Model	Brand	RC	Model	Brand	RC	Model	Brand	RC
Cyclic triaxial test (I)	PG-5KU	KYOWA	5 kgf/cm^2	DP15-28-N-3-S-4-A	Validyne	5kPa	PD-100GA	KYOWA	10kPa

Table 4.1.2 (c) Specifications of bender element test apparatus

Testing type	Function generator				
	Model	Brand	Specifications		
			Output frequency range (sine wave)	Type of output wave	Frequency accuracy
Bender element test	SFG-2120	GWINSTEK	1Hz~20MHz	Sine Square Triangle	±20ppm

Testing type	Oscilloscope					
	Model	Brand	Specifications			
			Frequency range	Sampling rate	Vertical sensitivity	Horizontal time
Bender element test	GDS-1062A	GWINSTEK	60MHz	1GS/s (1ch)	2mV~10V/div (1-2-5 strep)	1ns~50s/div

Table 4.1.3 Loading systems of triaxial apparatuses

Testing type		Loading system		
		Model	Brand	RC
Cyclic triaxial test	(I)	FCD-100-144	Fujikura Ruber LTD.	0.01~0.7MPa
	(II)	FCD-80-108	Fujikura Ruber LTD.	0.01~0.7MPa
Compression triaxial test		AS0408FN031	NIPPON SEIKO K.K.	
Bender element test		FCD-80-108	Fujikura Ruber LTD.	0.01~0.7MPa
Permeability test		FCD-80-108	Fujikura Ruber LTD.	0.01~0.7MPa

Table 4.1.4 Specifications of temperature bath for freeze-thawing test

Model	Brand	Size (w×d×h)	Capacity	Specifications		
				Temperature	Precision	Gradient
NCB-3200	TOKYO RIKAKIKAI CO., LTD	393×511×793 (mm)	23 (Liter)	-30~80°C	+/-0.03°C	<0.9°C/min (Heating) <0.5°C/min (Cooling)

4.1.2 Apparatuses used

4.1.2.1 Development of cyclic triaxial apparatus applicable for freeze-thaw and unsaturated tests

In this study, a triaxial apparatus which is capable of simulating freeze-thaw cycles, several moisture contents, and cyclic loading was newly developed. Figures 4.1.1 (a) and (b) and Photograph 4.1.1 show the schematic diagrams and view of the triaxial apparatus, respectively. The main features are as follows; 1) to simulate a soil subjected to freeze-thaw sequence by controlling temperature, 2) to control several moisture contents and 3) to conduct the liquefaction test by applying stress-controlled cyclic loads.

In order that a sequence of freeze-thawing and cyclic loading can be carried out with temperature and stress conditions controlled arbitrarily, a set of cooling system was equipped with the conventional cyclic triaxial apparatus as shown in Figure 4.1.1 (b). An acrylic cylindrical cell (frost heave cell) fixed to the soil specimen covered with a membrane of 0.3 mm in thickness, constrains the lateral displacement throughout freezing and thawing to simulate a one-dimensional freeze-thawing phenomenon. The maximum of three temperature-controlled baths (T-C baths) to circulate non-freezing fluids independently through a cap, pedestal and outer cell, are capable of one-dimensionally cooling the specimen set up in the triaxial apparatus at a desired temperature gradient. In this study, as shown in Figure 4.1.1 (b), T-C bath (B) operates to cool the specimen from the bottom end through the pedestal while T-C bath (A) is keeping the cell water replaced with the non-freezing fluid constant at the temperature of 0 to 1 °C. The specifications of the T-C bath are shown in Table 4.1.4. At the same time, a set of platinum resistance thermometers installed into

both the cap and pedestal measures the temperatures at the top and bottom ends of the specimen, which is recorded in the data logger as shown in the figure. Moreover, the amount of drainage in freezing and thawing can be monitored by a double-tube burette connected with the low-capacity differential pressure transducer (A) in Figure 4.1.1 (a). On the other hand, this apparatus is available for unsaturated soil testing by using the appropriate equipment; 1) a set of transducers and pressure regulators to independently measure and control pore water pressure u_w and pore air pressure u_a of the specimen, 2) an inner cell and the differential pressure transducer (B) shown in Figure 4.1.1 (a) to measure volume change of the specimen and 3) the pedestal with a ceramic disk, which is free to be replaced with the one setting in a porous plate used in this study. The axial displacement is monitored using an external displacement transducer (dial gauge), and its stress is measured using a load cell inside of the outer cell. All the transducers of load, displacement and pressure are connected with the PC to monitor the measurements.

Figure 4.1.2 shows the arrangement of cooling, monitoring and water- and pressure-supply paths on the upper and lower plates applicable to freeze-thawing test and/or cyclic shearing under unsaturated condition in the triaxial cell. Although the inner cell installation position is shown in the figure, it differs from that for the frost heave cell. The frost heave cell can be placed with attached to the specimen to confine the radial strain. The schematic diagrams of those cells are represented in Figures 4.1.3 (a) and (b). The volume change of specimens during the unsaturated testing can be basically measured by the water level change at the cylindrical part of 85 mm in diameter in Figure 4.1.3 (a). The frost heave cell has the inner diameter of 71 mm, which is slightly larger than that of specimen, from Figure 4.1.3 (b).

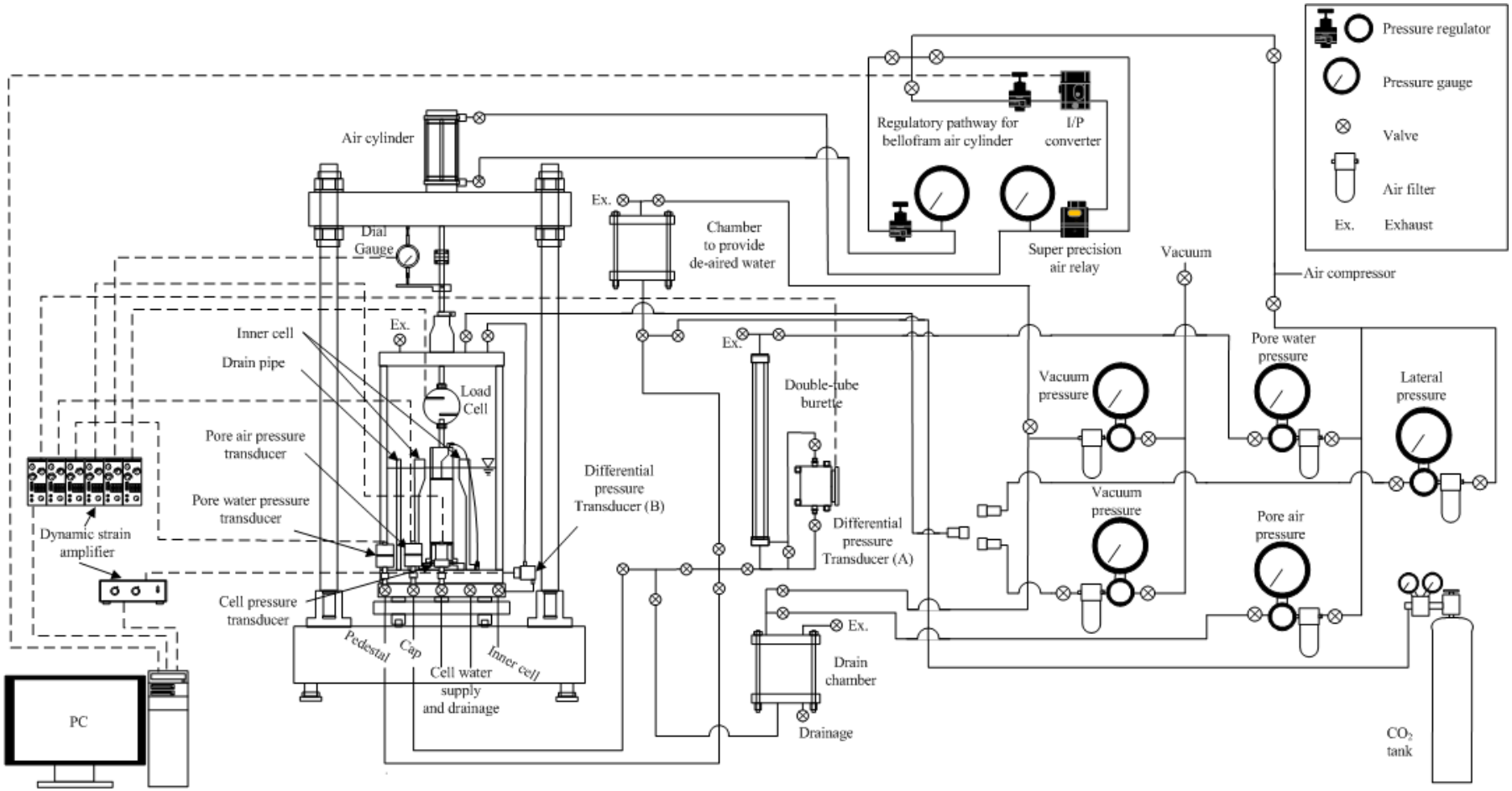

Figure 4.1.1 Cyclic triaxial apparatus capable of simulating freeze-thawing and unsaturated condition (a) Unsaturated test

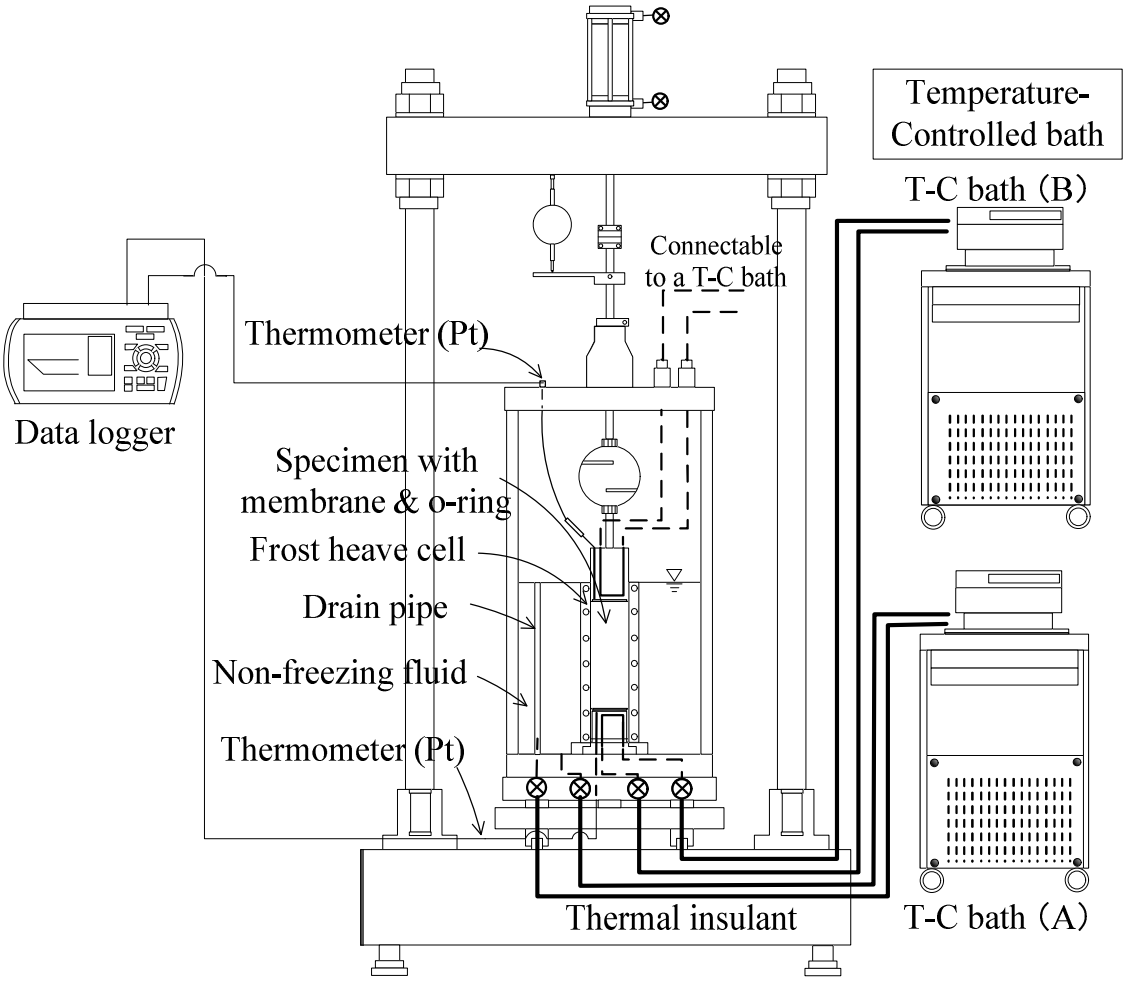

Figure 4.1.1 Cyclic triaxial apparatus capable of simulating freeze-thawing and unsaturated condition (b) Freeze-thawing test

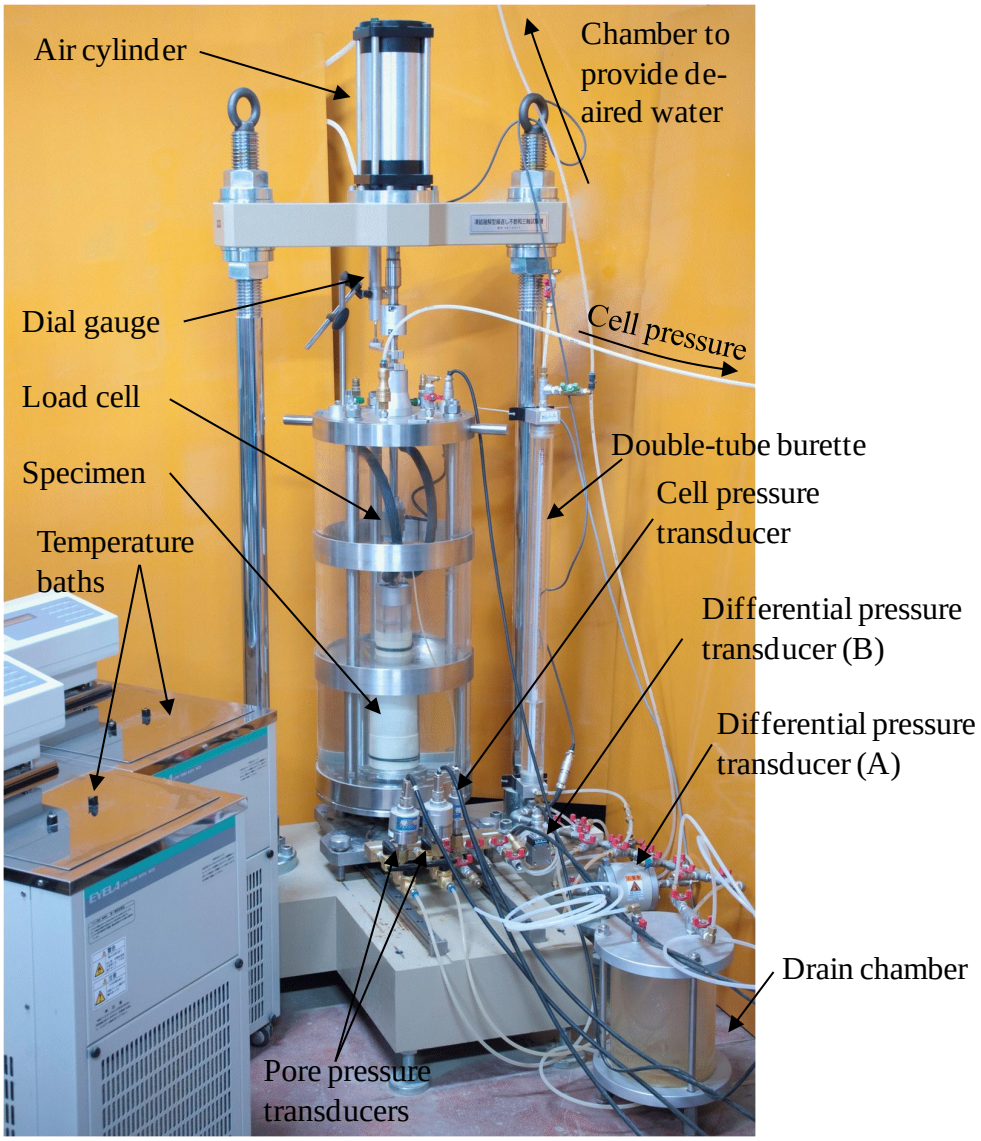

Photograph 4.1.1 Cyclic triaxial apparatus capable of simulating freeze-thawing and unsaturated condition

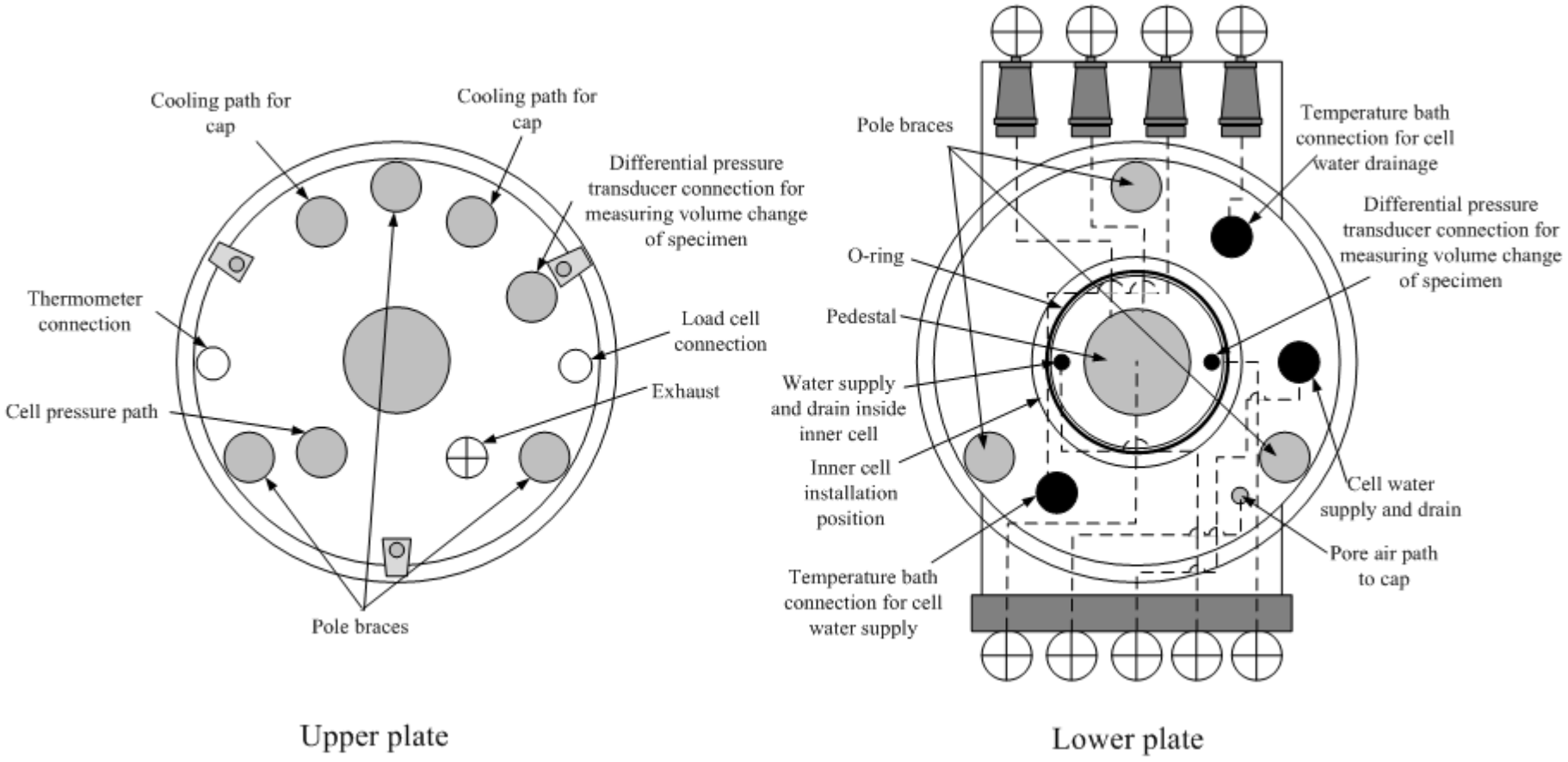

Figure 4.1.2 Arrangements of freeze-thawing, water and transducers' paths on upper and lower plates of freeze-thawing triaxial apparatus

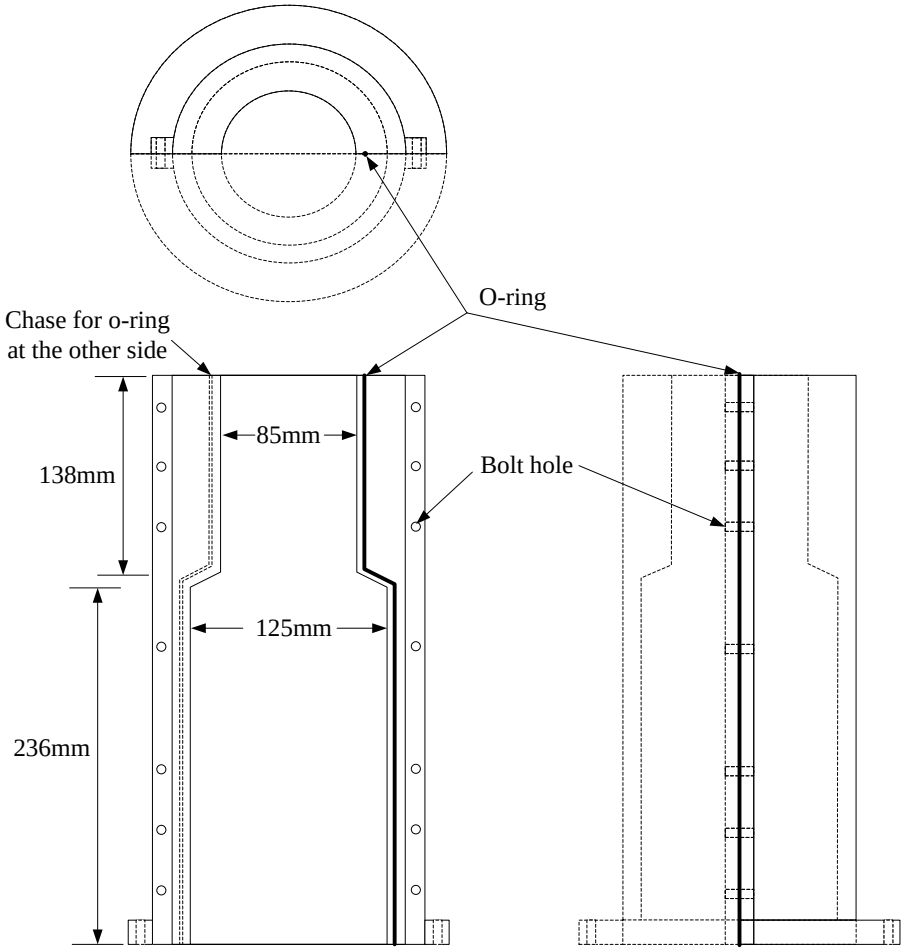

(a) For measuring volume change of specimen

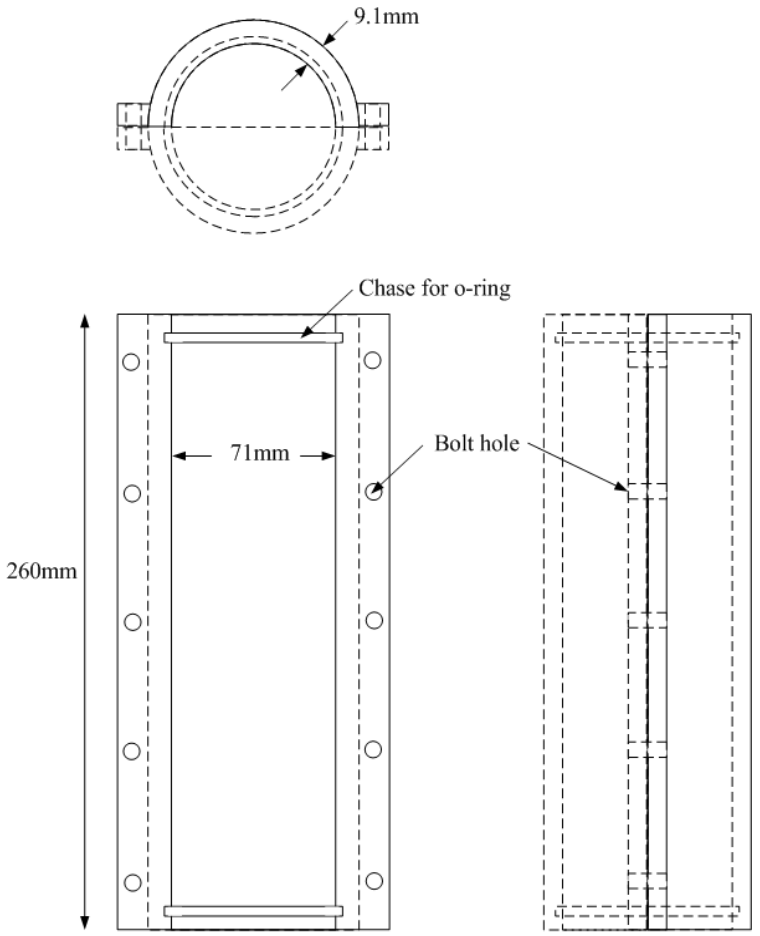

(b) Frost heave cell (Freeze-thawing test)

Figures 4.1.3 Inner cells for cyclic triaxial apparatus capable of simulating freeze-thawing and unsaturated condition

4.1.2.2 Cyclic triaxial test

Figure 4.1.4 shows the schematic diagram of the conventional cyclic triaxial apparatus used for this study. Although the view of the apparatus is omitted here, the fundamental testing system such as measuring and controlling the stress and pressure is almost exactly the same to that of the bender element test introduced later (*see* Figure 4.1.6 and Photograph 4.1.3). This testing is corresponding to the cyclic triaxial test (II) in Table 4.1.1. Axial stress, axial displacement, cell pressure and pore water pressure can be monitored in performing the cyclic test. Furthermore, the drainage due to consolidation was measured by the double-tube burette. The specimen diameter, D_s is 70 mm. For loading system, the air cylinder controlled by PC through an I/P converter is adopted. In shearing, cyclic loads are applied at the frequency *f* of 0.1 Hz.

4.1.2.3 Triaxial compression test

Figure 4.1.5 and Photograph 4.1.2 show the schematic diagram and view of the conventional compression triaxial apparatus used for this study. The axial stress is being controlled to keep constant with the direct-drive megatorque motor. After saturating and consolidating, the specimens are applied static compression load at the loading rate, $\dot{\varepsilon}_a$ = 0.1%/min. In the test, axial stress and axial displacement are measured by the load cell and dial gauge in Figure 4.1.5, respectively. In addition, cell pressure and pore water pressure are monitored by each transducer. The specimen size is basically 100 mm in diameter.

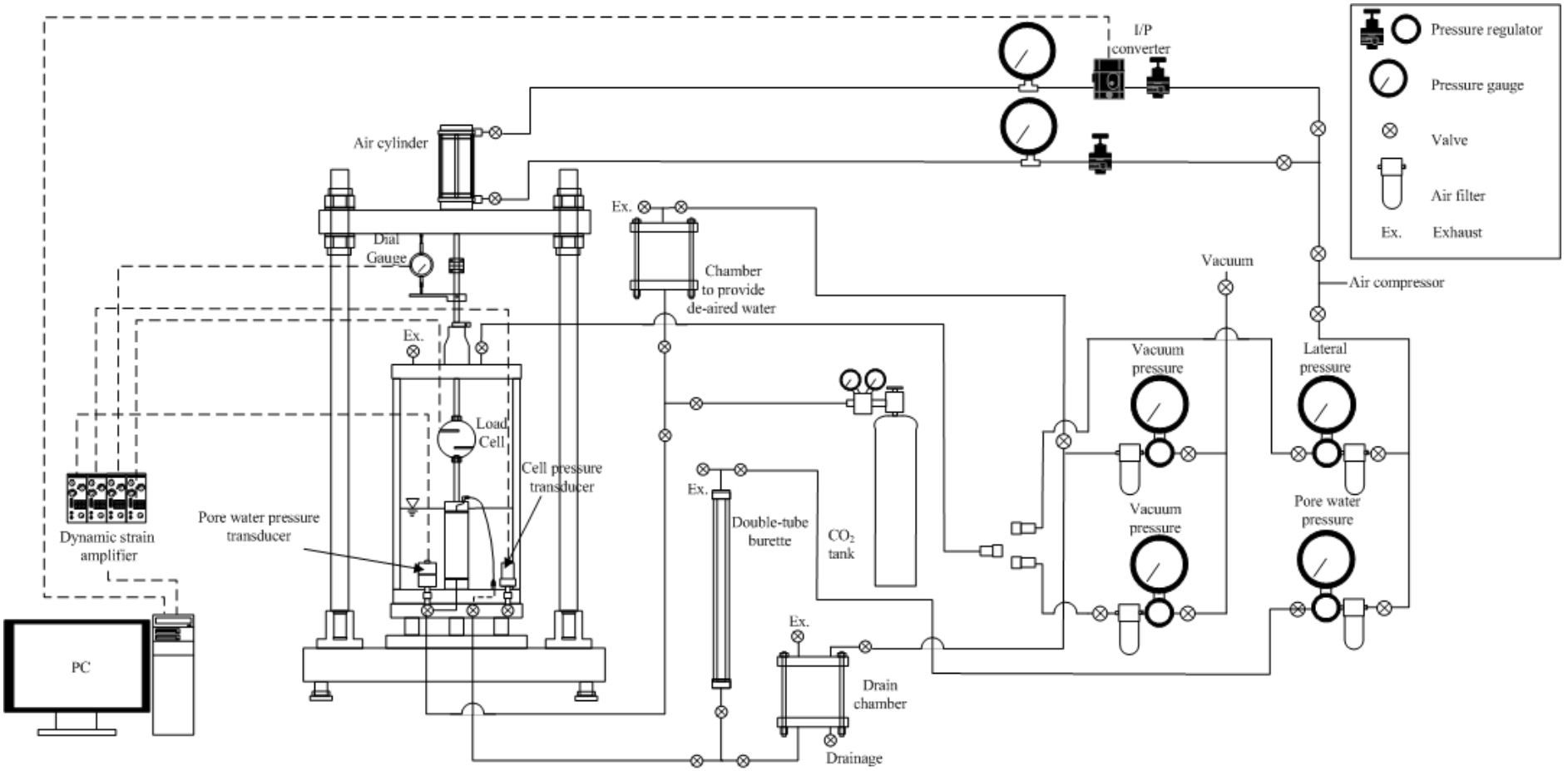

Figure 4.1.4 Cyclic triaxial apparatus

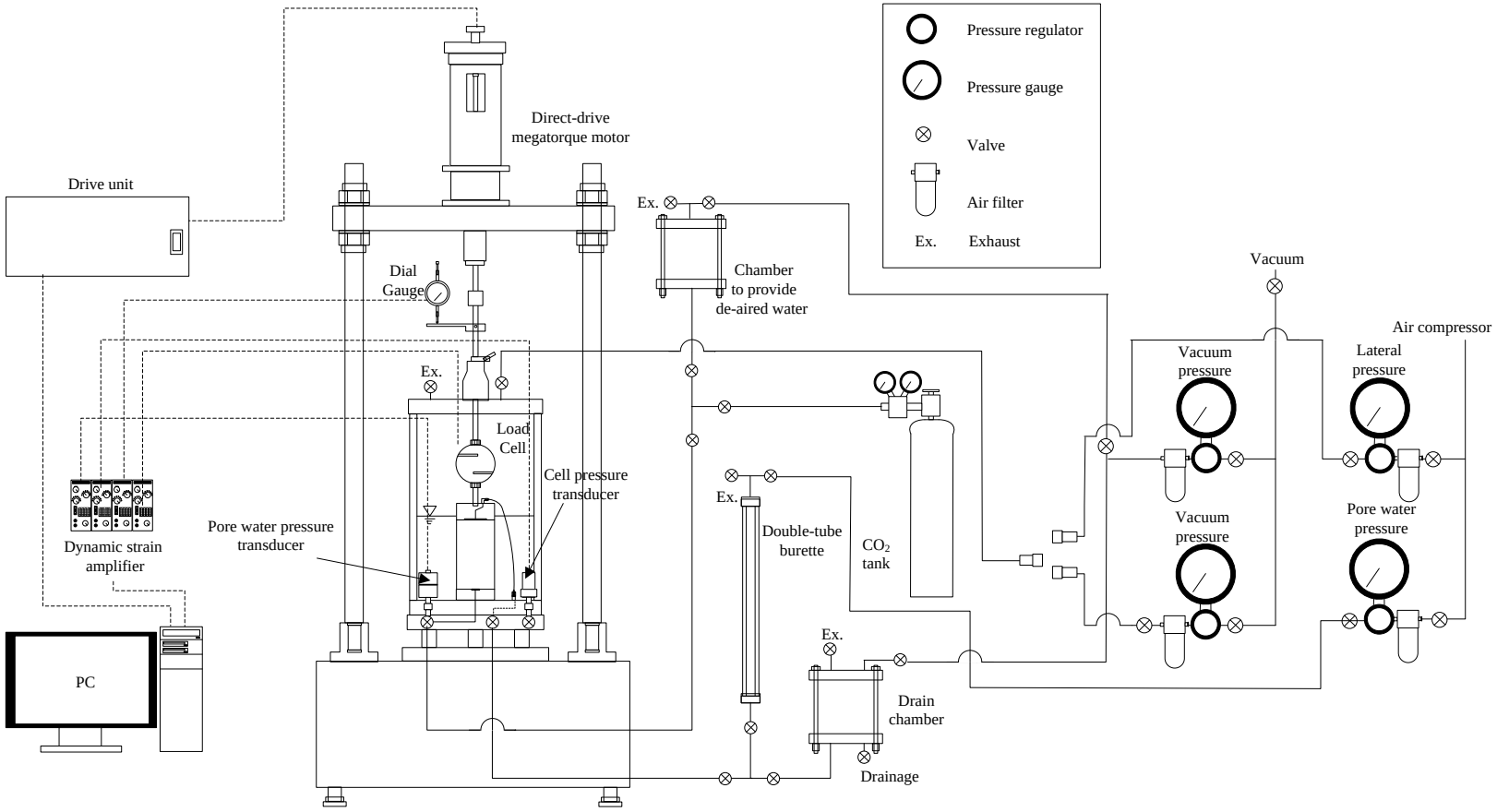

Figure 4.1.5 Monotonic triaxial compression test apparatus

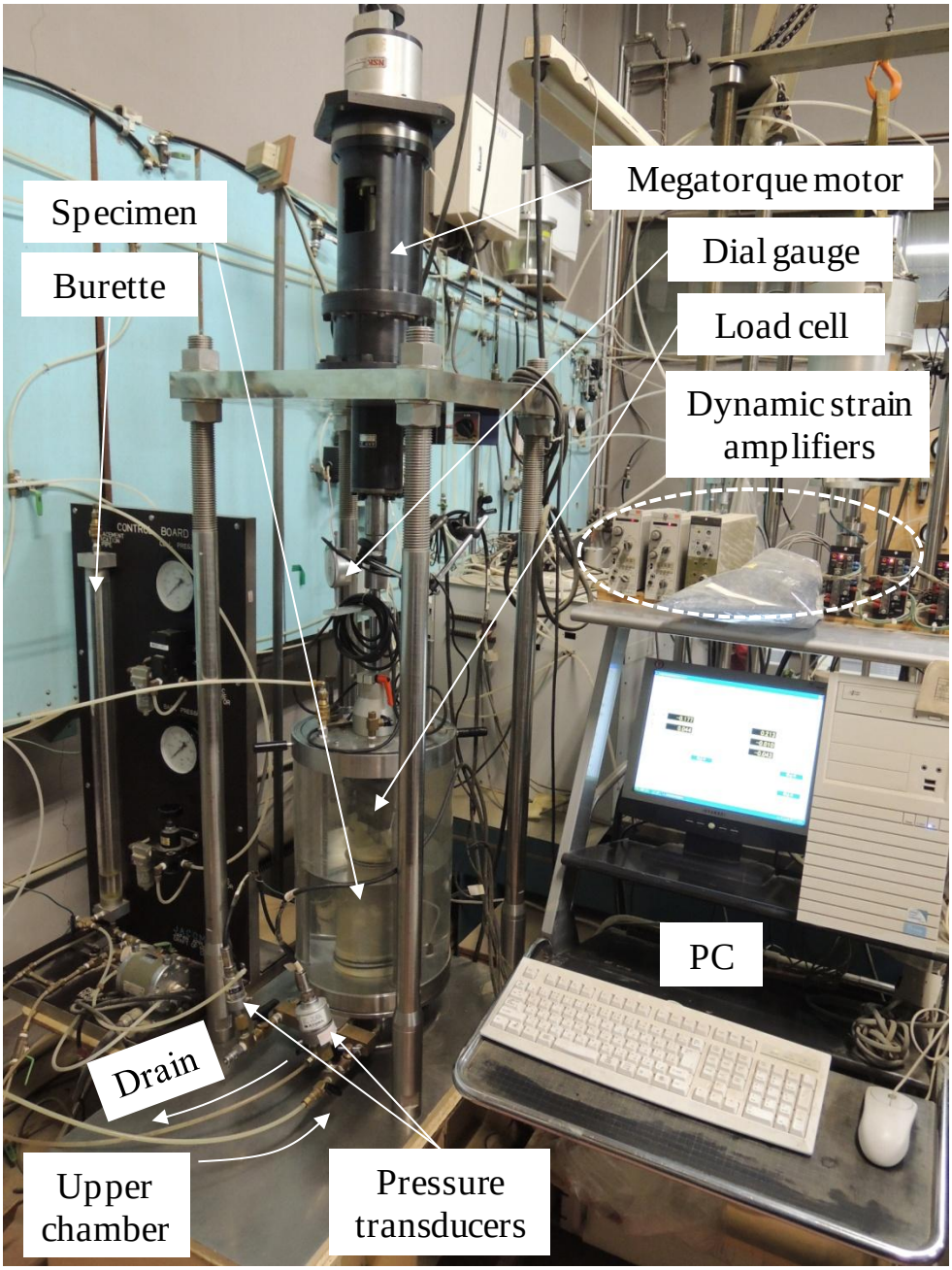

Photograph 4.1.2 Monotonic triaxial compression test apparatus

4.1.2.4 Bender element test

Figure 4.1.6 and Photograph 4.1.3 show the schematic diagram and view of the bender element test apparatus used for this study. The loading system by means of the air cylinder and the measuring system for axial stress, displacement and pore and lateral pressures are fundamentally the same to those of the cyclic triaxial test (II) apparatus shown in Figure 4.1.4. In the test, a pair of bender elements is installed into the cap and pedestal in the triaxial cell, which makes it possible to observe the shear modulus under desired isotropic stress condition. The bender element is made from a pair of piezoelectric elements, and that can transduce electric signal with physical deformation, and vice versa. Figure 4.1.7 indicates the diagram of a specimen with 70 mm in diameter put in the triaxial cell. The shear wave induced by the bender element in the cap connected with a function generator propagates thorough the specimen, and that is received by the other bender element in the pedestal. During testing, an oscilloscope receives the propagated shear wave. When the shear wave propagates for time Δt_{BE} over the length of L_{BE}, which corresponds to the distance between two bender elements as shown in Figure 4.1.7, shear wave velocity V_s and shear modulus G_{BE} can be expressed as follows;

$$V_s = L_{BE} / \Delta t_{BE} \tag{4.1}$$

$$G_{BE} = \rho_t \cdot V_s^{\,2} \tag{4.2}$$

where, ρ_t is the wet density of the specimen.

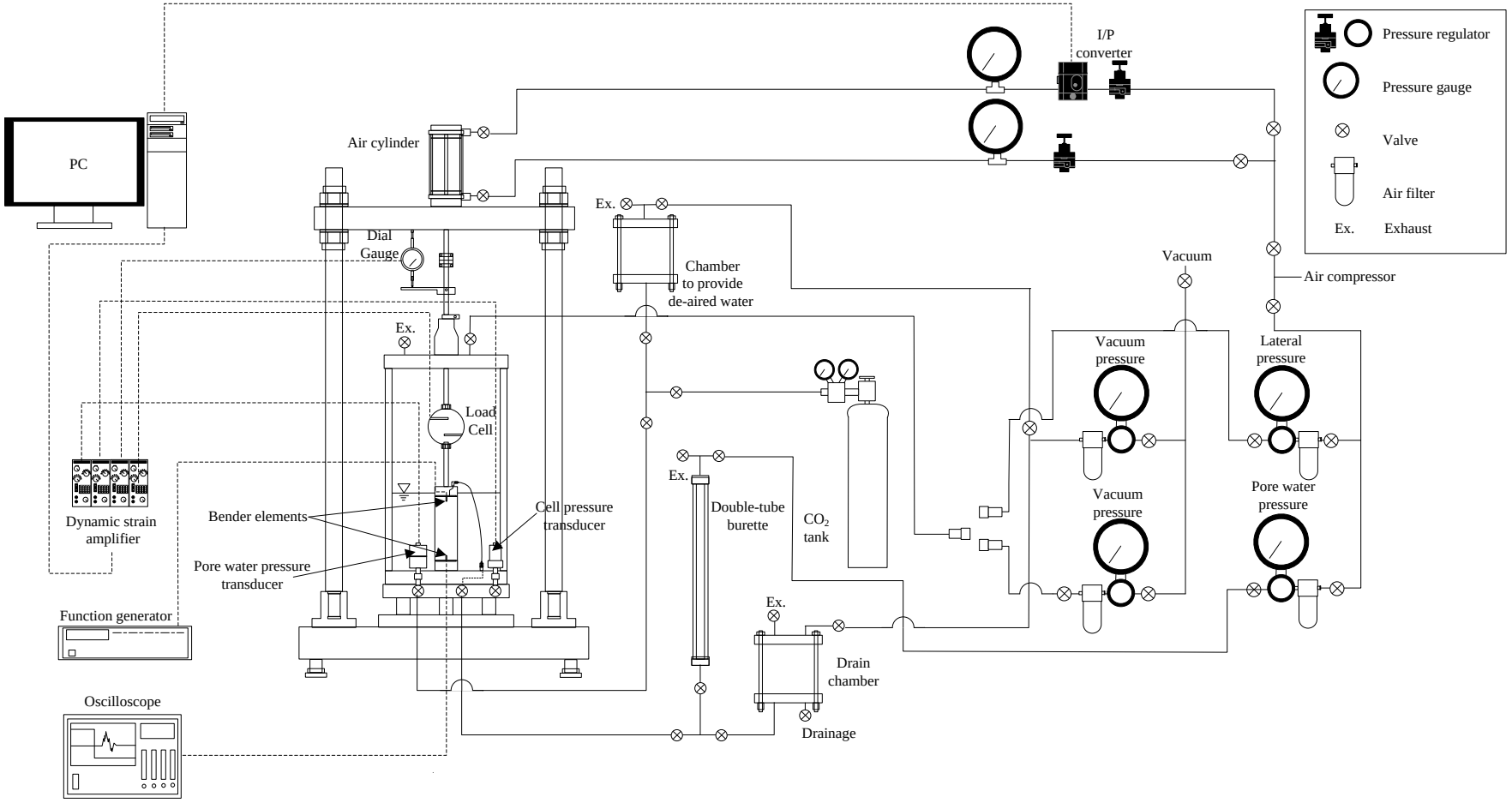

Figure 4.1.6 Bender element test apparatus

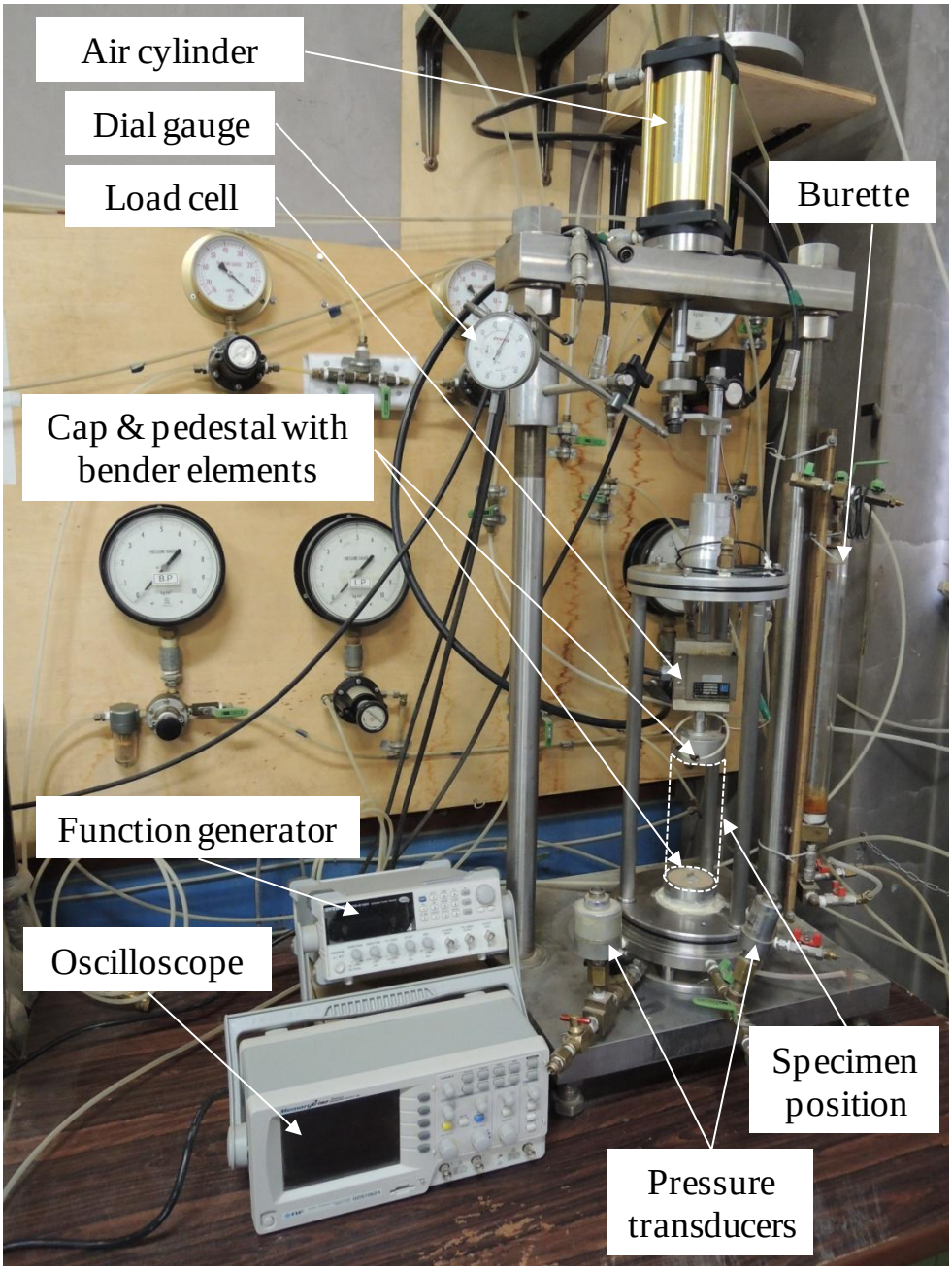

Photograph 4.1.3 Bender element test apparatus

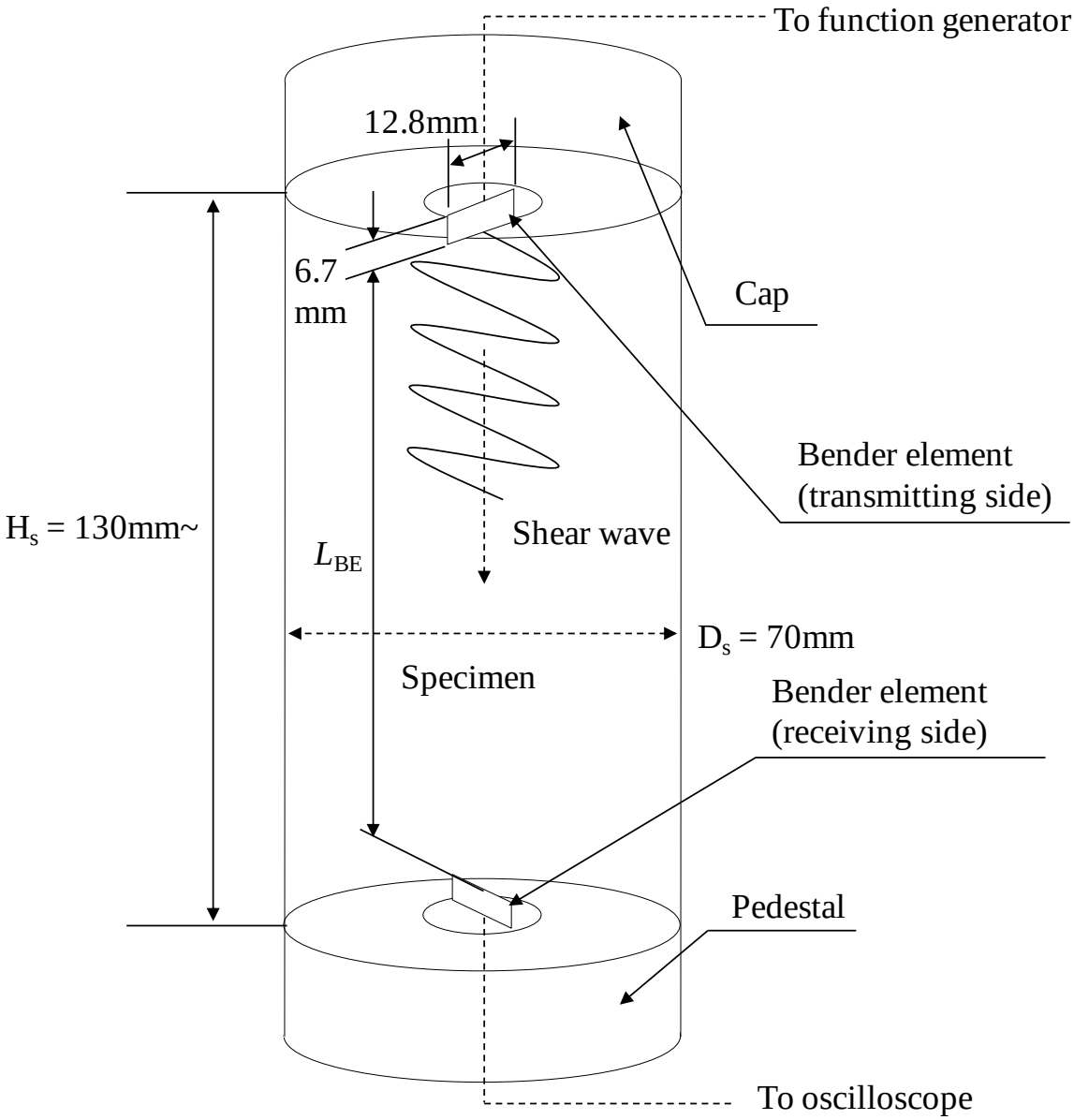

Figure 4.1.7 Bender elements on cap and pedestal and their scales

4.1.2.5 Falling head permeability test

Figure 4.1.8 and Photograph 4.1.4 show the schematic diagram and view of the falling head permeability test apparatus used for this study. This apparatus was developed so that the falling head permeability test can be conducted under a desired isotropic consolidation stress in the triaxial cell (Yokohama et al. 2012). The apparatus has two double-tube burettes, which can apply a desired water head between the top and bottom ends of the specimen. The detailed methodology of the percolating procedure will be explained later. The applicable specimen size is 100 mm in diameter, and the areas of 91 % in the cap and pedestal are composed by a plate of porous stone to percolate de-aired water.

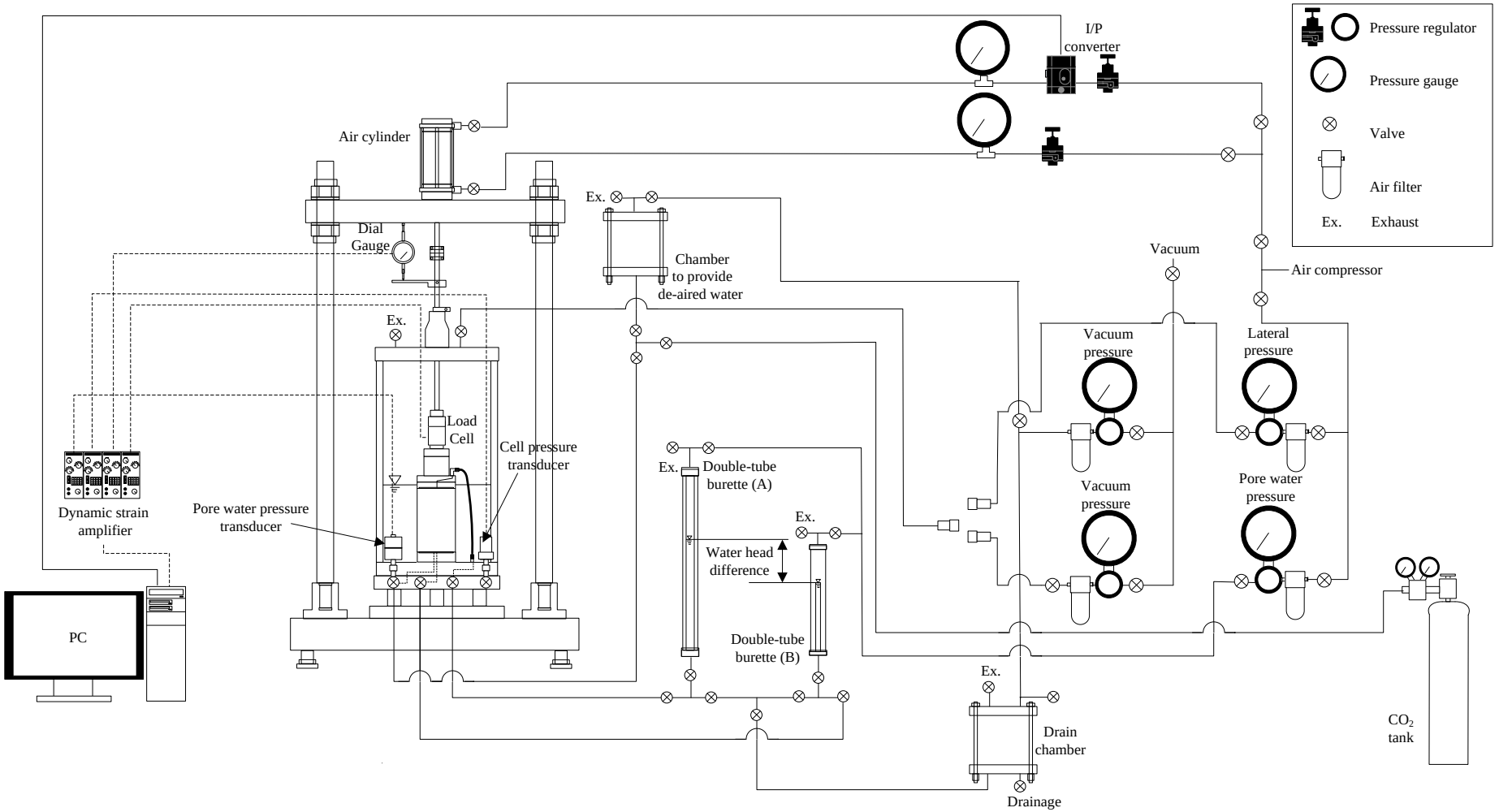

Figure 4.1.8 Permeability test apparatus

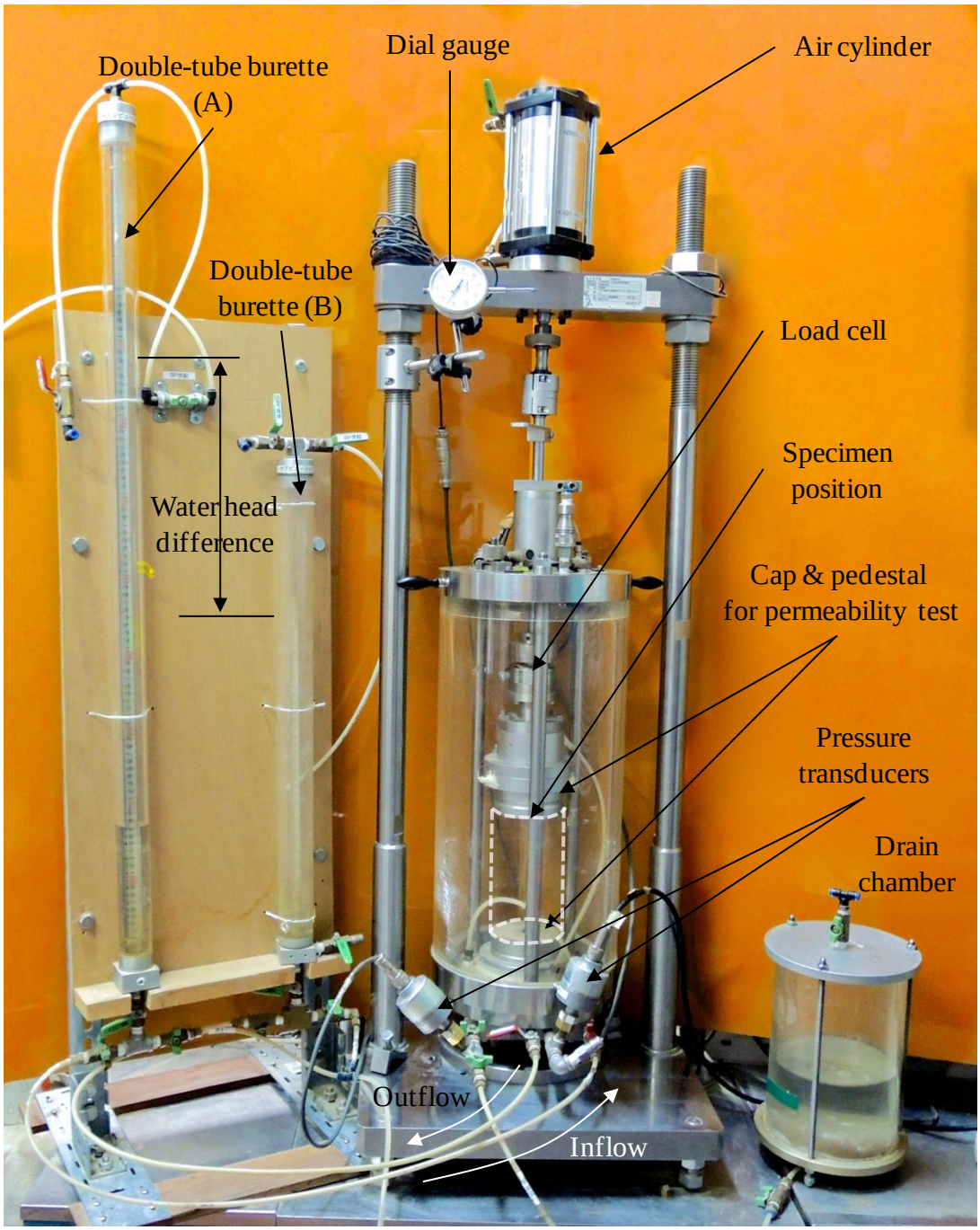

Photograph 4.1.4 Permeability test apparatus

4.1.3 Specimen preparation

In this study, the attempt is basically to examine the mechanical properties of embankment under various environments such as compaction condition, freeze-thawing and particle crushability of constitutive particles. Therefore, the soils were compacted under desired compaction conditions in preparing specimens. First, the soils were moisture-controlled at given water contents w_i (%) prior to compaction. The w_i values vary depending on the testing conditions summarized in Table 4.1.1, while all of the specimens to testify the freeze-thaw effect were compacted at the optimum water content of K soil. After controlling the water content at compaction, compaction was conducted with the 24.5 N rammer in the compaction mold of (b) or (c) shown in Figure 3.2.3 (a). Then, the number of blows was controlled in order to obtain a desired dry density. The compaction mold was chosen appropriately to the type of soil and applicable specimen diameter, D_s (mm) as mentioned in Table 4.1.1. Because I soil can be smoothly trimmed after taken out from the mold without disturbing the specimens, all of them were compacted at D_s = 100 mm with the compaction mold (b) prior to forming. On the other hand, Komaoka volcanic soil sufficiently contains coarse-grained particles, which makes it difficult to trim and form after compaction. Therefore, in any tests using the soil, the specimen was compacted with the compaction mold which has the same diameter to that required for each triaxial test. The specimen preparation methods with regard to each compaction mold are as follows.

First, Figure 4.1.9 shows the procedure of compacting the soil with the compaction mold (c) (*see* Figure 3.2.3 (a)) that has 70 mm in diameter, D_m. In the figure, the rammer (ii) has the frame covering the weight smaller than 70 mm in diameter (*see* Figure 3.2.3 (b)). Moisture-controlled soil was compacted in certain numbers of layers, N_l. After compaction, the top end of the compacted specimen was flattened at the specimen height H_s of 140 mm. Afterwards, the compaction mold was carefully removed with splitting longitudinally, and the specimen was taken out to be placed in the

triaxial cell. This procedure of specimen preparation was followed for the cyclic triaxial tests (I) and (II) using Komaoka volcanic soil as shown in Table 4.1.1. Then, the N_l values required for each test are shown in Table 4.1.5. In the table, the N_l values for the compression test, the bender element test and the permeability test are indicated as well.

Subsequently, the specimen preparation method for the bender element test with the compaction mold (c) using K soil is represented in Figure 4.1.10. In the test, it can be problematic to install the bender elements into the specimen, especially containing coarse-grained particles. In order to solve the difficulty, a plate with a replacement bender element shown in Figure 4.1.11 and Photograph 4.1.5 was separately manufactured. In the center of the plate, the replacement bender element to imitate the ones on the cap and pedestal in the triaxial cell was attached. The plate has a little smaller diameter than 70 mm of the specimen, and can be placed into the compaction mold (c), which corresponds to the preparation process 1) in Figure 4.1.10. Compaction was performed in the given numbers of compaction layers, N_l in Table 4.1.5 with the replacement bender element remaining at the bottom of the mold. After compaction at the last layer, the top end of the specimen was flattened as well as mentioned in Figure 4.1.9. Finally, the flattened top end of the specimen was applied one more blow using the 24.5 N rammer with the plate placed between in the collar, as shown by 5) in Figure 4.1.10. Then, a longitudinal direction of the upper replacement bender element must be the same as that of the lower one. On the other hand, the replacement bender element is applicable for the specimen with D_s = 100 mm using the extra hollow plate shown in Figure 4.1.12 and Photograph 4.1.6. The hollow plate can be attached to the prior plate with 70 mm in diameter, and those plates play the same role in the 100-mm-mold as in the 70-mm-mold.

Figure 4.1.13 indicates the specimen preparation procedure with the compaction mold (b) that has 100 mm in diameter, D_m (*see* Figure 3.2.3 (a)). The compaction process is basically the same to the above. A soil was compacted with the 24.5 N rammer in given N_l. After that, in the case of the

specimen diameter D_s = 100 mm, the top end was flattened in the mold. On the other hand, when the specimens with D_s = 70 mm were required based on Table 4.1.5, those were trimmed to be D_s of 70 mm on a trimmer, after the mold was removed. Finally, the top and bottom ends of the trimmed specimen were flattened at the specimen height H_s = 140 mm using the compaction mold (c).

Thus, each specimen was prepared in each different way due to the limitations of the specimen sizes and the soil materials. Photographs 4.1.7 and 4.1.8 show images of the compacted specimens of I soil and K soil with D_s = 70 and 100 mm, respectively. In order to apply the above specimen preparation method, the specimens must be self-standing without deforming even after the compaction molds are removed as can be seen in the photographs. In this study, all the specimens were prepared under acceptable compaction conditions in terms of the molding water content w_i and the compactive effort so that those could keep self-standing before applying a certain confining pressure in the triaxial cells.

In this study, as explained in *4.2 Testing on full-scale embankment*, thin-wall sampling was conducted during construction of the full-scale embankment for the liquefaction test. The thin-wall samplers have approximately 70 mm in diameter, which is the size applicable for the cyclic triaxial test apparatus introduced in Figure 4.1.4, and 240 mm in height. After carefully inserting and digging out the samplers with Komaoka volcanic soil in-situ compacted, the samples had been totally covered by membranes to avoid drying until those were taken out for the above purpose. Photograph 4.1.9 shows the specimen taken out from the thin-wall sampler, formed at 140 mm in height and placed on the apparatus. As could be recognized in the photograph, the specimen compacted at the optimum condition can keep self-standing enough as well as the compacted ones in the mold as shown in Photograph 4.1.7. In this study, therefore, the specimens sampled from the embankment were used for the liquefaction test without freezing beforehand to avoid any disturbance. On the other hand, the surface of in-situ specimen seems rougher for the liquefaction test to some

extent than the specimens compacted in the mold shown in Photograph 4.1.7, which may possibly cause a problem in system compliance, i.e., membrane penetration during cyclic loading. The effect, in general, can act on increasing liquefaction strength (Miura et al. 1990). In addition, the roughness on the specimen surface certainly triggers inaccurate measurement of the specimen volume more or less. Although there is no correction for the liquefaction test results shown later in this study, keeping in mind the above, those will be explained. The fundamental test data of the specimens sampled are represented in APPENDIX.

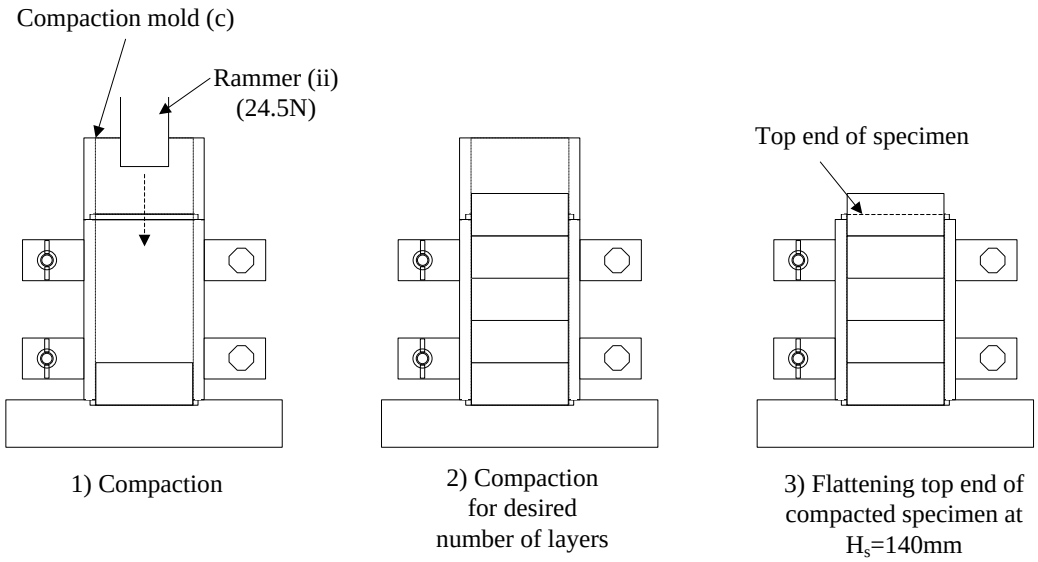

Figure 4.1.9 Specimen preparation using compaction mold (c)

Table 4.1.5 Number of compaction layers

Testing type		Soil material	Compaction mold	$D_s \times H_s$ (mm)	Number of compaction layers, N_l
Cyclic triaxial test	(I) f=0.005Hz	K soil	(c)	70×140	4 ~ 5
	(II) f=0.1Hz	I soil	(b)	70×140	4
		K soil, $K_{1.9}$, $K_{17.4}$, $K_{48.2}$	(c)	70×140	3
Compression triaxial test		I soil, K soil	(b)	100×150	4
Bender element test		I soil	(b)	70×140	4
		K soil	(c)	70×130~	4 ~ 5
Permeability test		I soil, K soil	(b)	100×150~	4

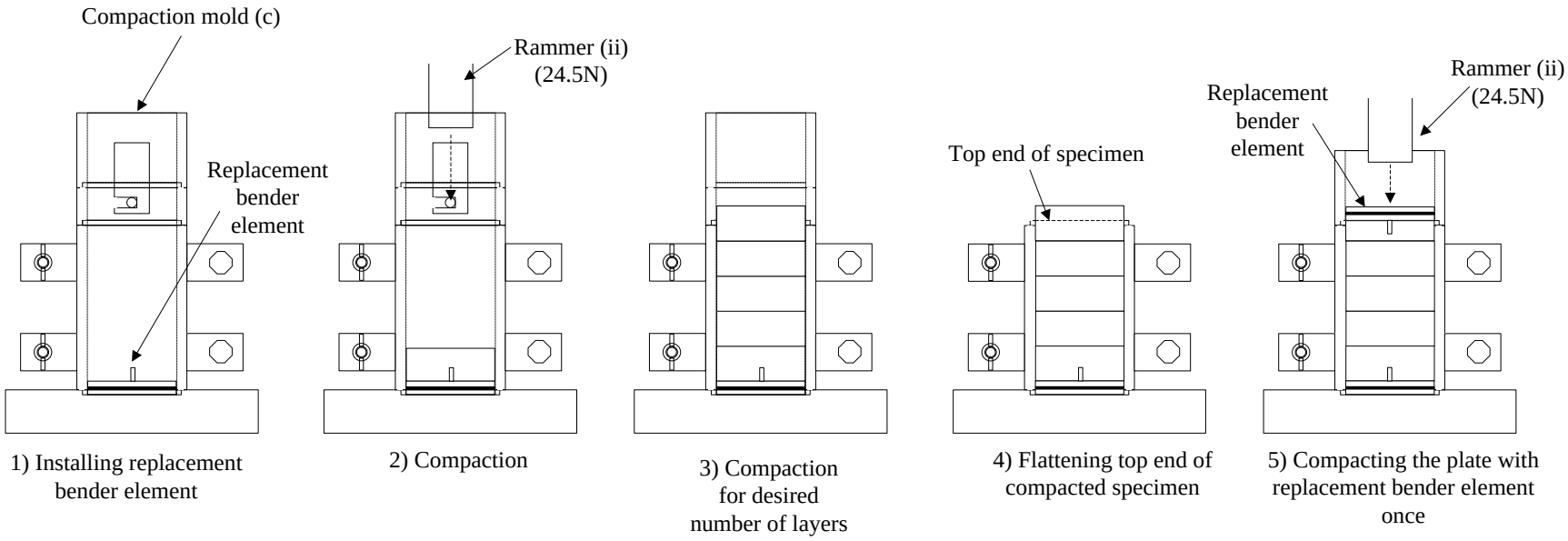

Figure 4.1.10 Specimen preparation using compaction mold (c) for bender element test

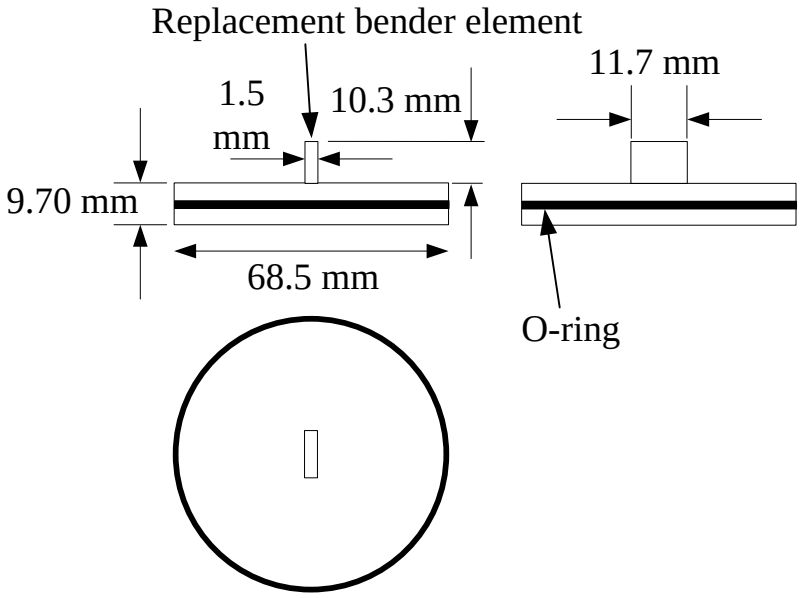

Figure 4.1.11 Replacement bender element for ϕ = 70 mm specimen

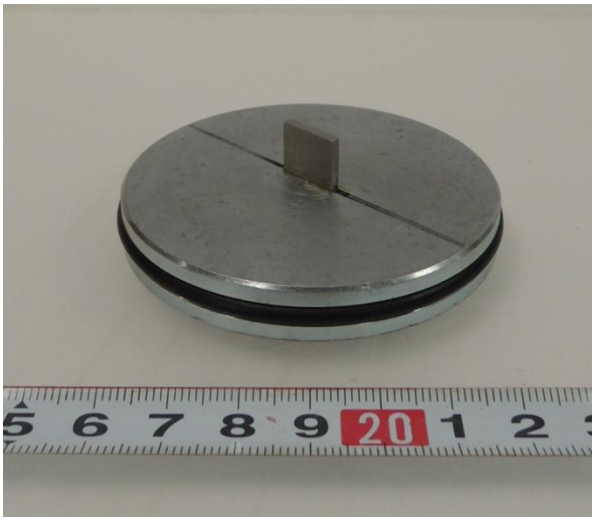

Photograph 4.1.5 Replacement bender element for ϕ = 70 mm specimen

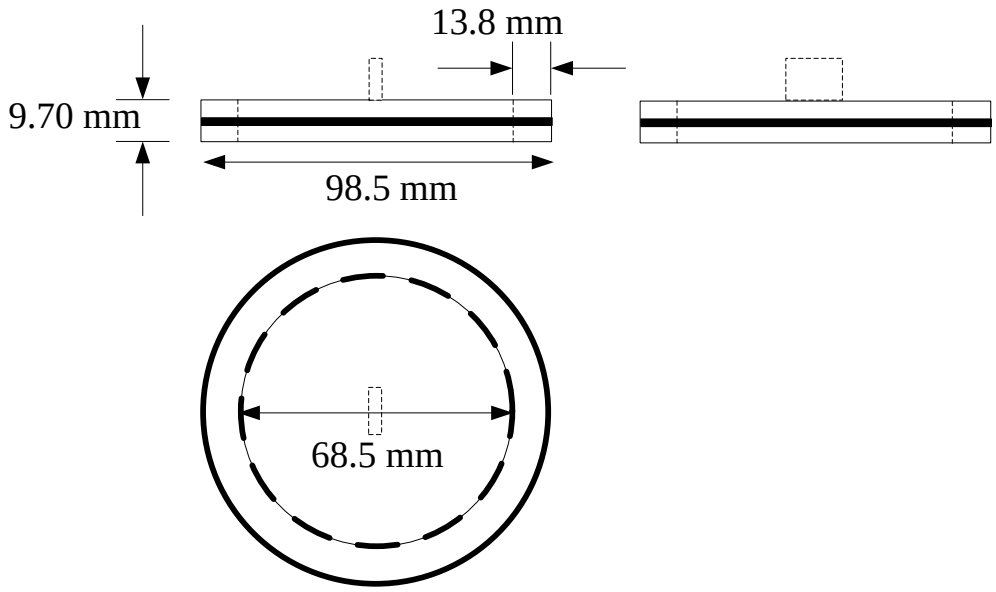

Figure 4.1.12 Replacement bender element for ϕ = 100 mm specimen

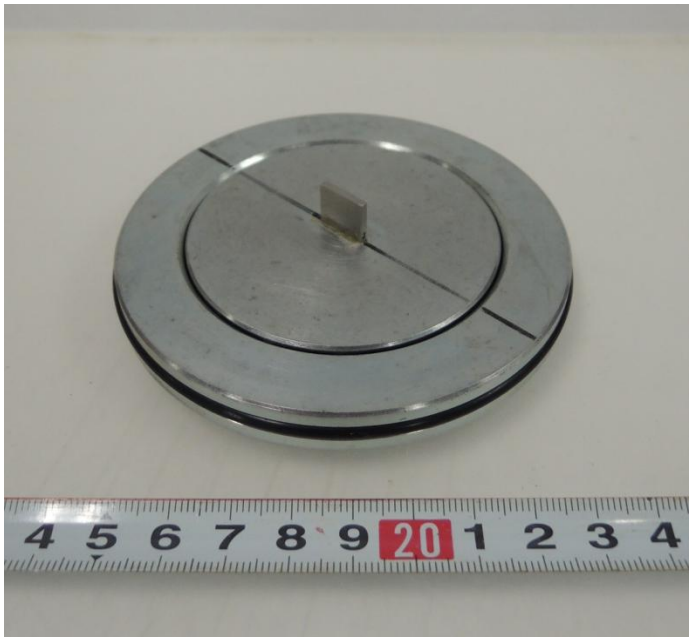

Photograph 4.1.6 Replacement bender element for ϕ = 100 mm specimen

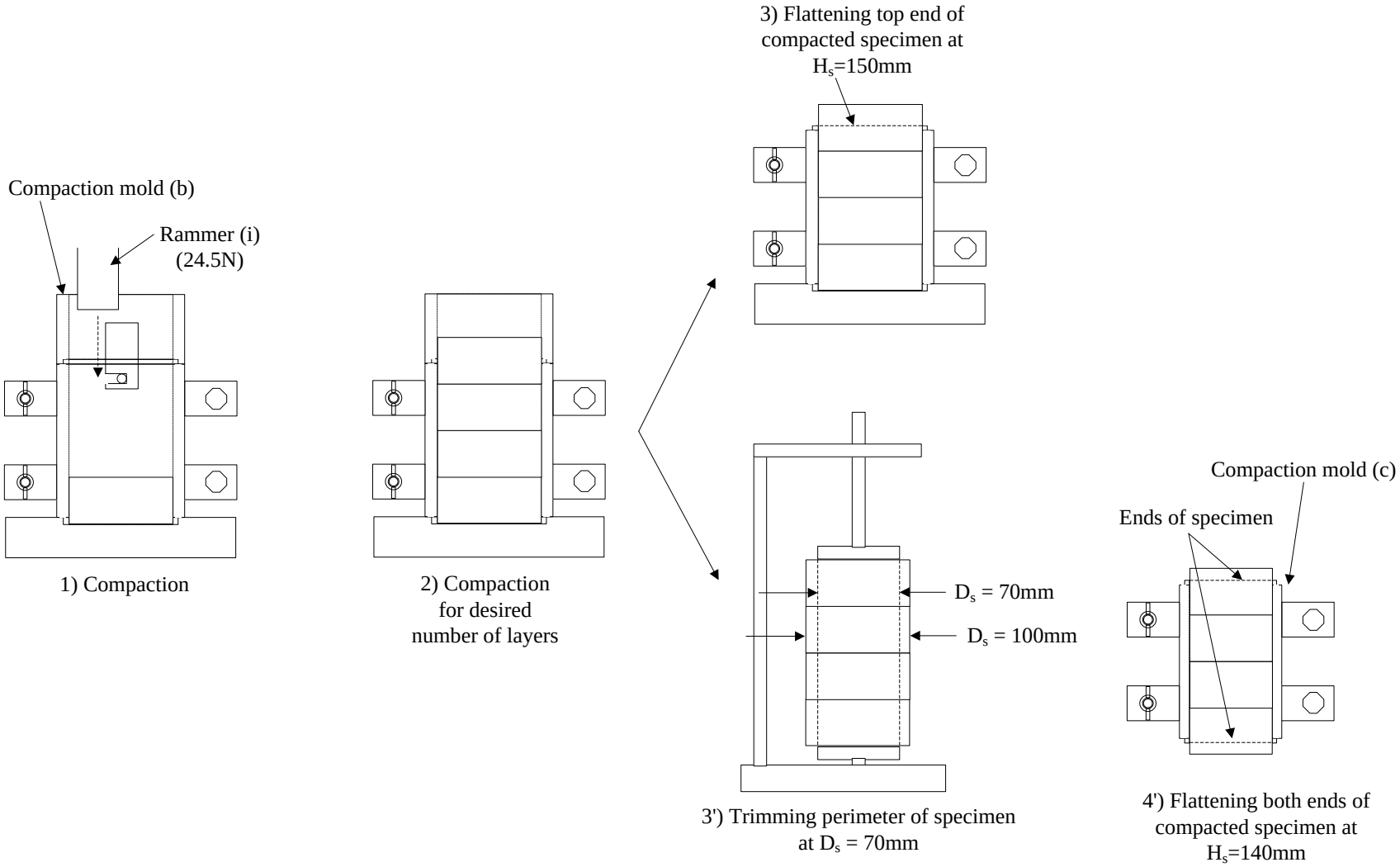

Figure 4.1.13 Specimen preparation using compaction mold (b)

(a) I soil, D_s = 70 mm, Optimum water content condition, 25 blows per a layer

(b) I soil, D_s = 100 mm, Optimum water content condition, 25 blows per a layer

Photographs 4.1.7 Specimen images for I soil

(a) K soil, D_s = 70 mm, Optimum water content condition, 11 blows per a layer

(b) K soil, D_s = 100 mm, Optimum water content condition, 25 blows per a layer

Photographs 4.1.8 Specimen images for K soil

Photograph 4.1.9 $K_{original}$ specimen for liquefaction test sampled by thin-wall sampling from FE-2012; w_i = 42.2%, D_{ci} = 91.0%
(*see 4.2 Testing on full-scale embankment*)

4.1.4 Testing processes and stress-strain states

4.1.4.1 Saturation and consolidation processes

After a compacted specimen was installed into a desired triaxial cell, the apparatus was set up with the specimen covered by a 0.3-mm-thick membrane. The specimen was saturated and consolidated prior to shearing or percolating as follows.

First, pore air inside the specimen was replaced with carbon dioxide to percolate, and afterwards de-aired water was applied to the specimen under the confining pressure σ_c' of 20 kPa. Then, for the wetting specimens densely compacted, however, it can be often very difficult to percolate the carbon dioxide and the de-aired water enough to saturate them. Therefore, the vacuum procedure (Rad and Clough 1984) was additionally applied to every specimen for saturating. Figure 4.1.14 shows the stress state inside the triaxial cell and the specimen during the vacuum procedure. As mentioned above, the specimen is confined at the effective stress, σ_c' = 20 kPa with providing cell pressure prior to the procedure. At the beginning of the procedure, the cell pressure is turned down to 0 kPa while the vacuum pressure is increased to 20 kPa through the pore pressure path connected to the top of the specimen. Then, it is considered that the σ_c' value can be kept 20 kPa, throughout. Afterwards, with keeping σ_c' 20 kPa, the pore pressure and the cell pressure are decreased up to -90 and -70 kPa, respectively. Under the stress state, the pore air can be forcibly eliminated from inside the specimen. In addition, it is possible to simultaneously provide the de-aired water into the specimen from the bottom end with applying the same vacuum pressure to the upper chamber connected to the bottom side of specimen. After no air can be found, each pressure is controlled in the opposite procedure to restitute the specimen under the initial condition.

Back pressure was applied with σ_c' kept 20 kPa to fully saturate the specimen through the burette

after the vacuum procedure. In this study, it is considered fully-saturated condition that the pore pressure coefficient B of the specimen achieves 0.95 or more. Then, if the B value was less than 0.95, the above saturating procedure was repeated. The available specimens, which are nevertheless not saturated enough in terms of the B value, were judged for the saturation condition by the degree of saturation S_r more than 85 %. After fully saturated, each specimen was isotropically consolidated at a desired effective consolidation stress σ_c' shown in Table 4.1.6. In the cyclic triaxial test, the bender element test and the permeability test, σ_c' of 50kPa was applied. On the other hand, the specimen for the compression triaxial test was consolidated under σ_c' of 50, 100 or 150 kPa.

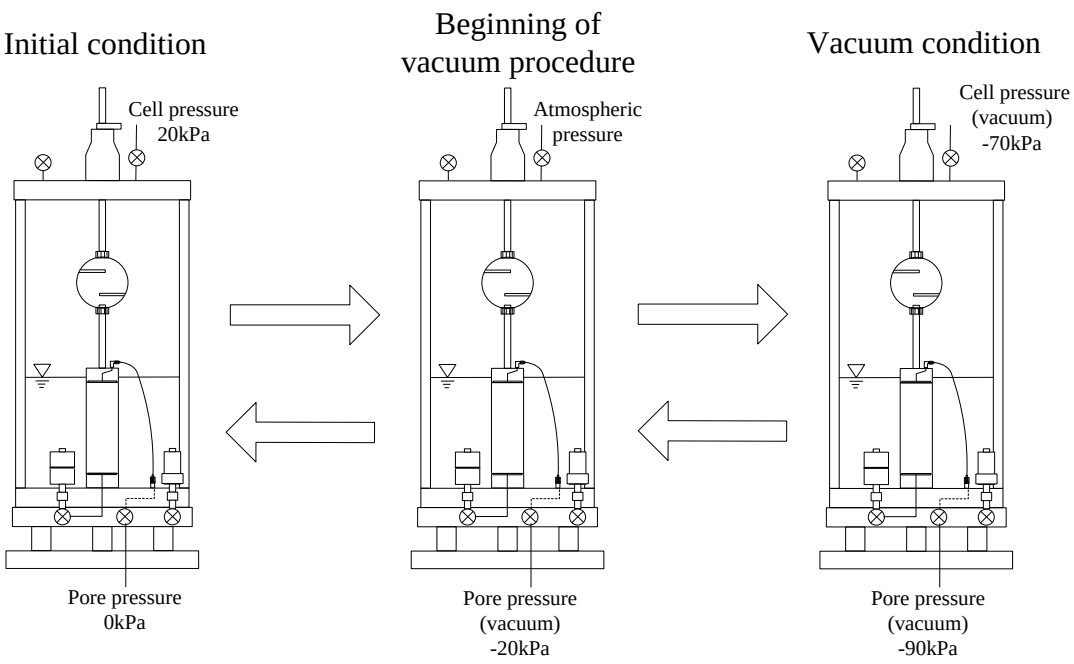

Figure 4.1.14 Pressure states in triaxial cell during vacuum procedure

Table 4.1.6 Consolidation stresses for triaxial tests

Testing type		Soil material	Effective consolidation stress (kPa)
Cyclic triaxial test	(I) f=0.005Hz	K soil	50
	(II) f=0.1Hz	I soil	50
		K soil, $K_{1.9}$, $K_{17.4}$, $K_{48.2}$	50
Compression triaxial test		I soil, K soil	50, 100, 150
Bender element test		I soil	50
		K soil	50
Permeability test		I soil, K soil	50

4.1.4.2 Shearing and percolating processes

After ensuring the drainage due to consolidation stopping, each specimen was sheared or percolated in the following way.

First, in the cyclic triaxial tests (I) and (II) (*see* Table 4.1.1), the stress-controlled cyclic loads were applied with the frequency f of approximately 0.005 and 0.1 Hz, respectively, under undrained condition and the constant total stress state. The cyclic loading processes of the tests (I) and (II) were continued until double amplitude axial strain *DA* reached 5 and 10 %, respectively. Then, the *DA* value is equal to the sum of compression, $\varepsilon_{\text{a comp.}}$ and extension strains $\varepsilon_{\text{a ext.}}$.

The compression triaxial test was conducted at the loading rate $\dot{\varepsilon}_{\text{a}}$ of 0.1%/min under undrained condition, which corresponds to CU test. The monotonic load was continued up to the axial strain ε_{a} of 15 %. The effective consolidation stresses are 50, 100 and 150 kPa as mentioned above.

In the bender element test, a rectangular wave was induced by the function generator through the bender element in the cap. The shear wave propagated inside the specimen was received as an electric oscillation by the oscilloscope connected with the other bender element in the pedestal. Figure 4.1.15 shows the diagram of the input and output signals. In this study, the travelling time of shear wave, Δt_{BE} is identified by the time from point S to point C in the figure, which is so-called "start-to-start" (Kawaguchi et al. 2001). Then, the first half-wave including points A and B should be considered "near-field-effect". The calculation method of the shear wave velocity and shear modulus is as mentioned in Equations (4.1) and (4.2) using the measured Δt_{BE} value, respectively.

The falling head permeability test was conducted using the two double-tube burettes connected with the top and bottom ends of the specimen, respectively, shown in Figure 4.1.8. The de-aired water percolates from the top end to bottom end of the specimen throughout the testing. The amount of inflowing water and the elapsed time required to percolate the water, Δt_{P} were measured. In this study, because the relation between hydraulic gradient i and permeability coefficient k becomes

constant within the range of *i* less than 3.0 from a preliminary test, the after-mentioned discussion will be focusing on the results with *i* of around 2.0. Then, the *k* value is the permeability coefficient at the temperature of 15 °C, which can be calculated from Equations (4.3) and (4.4);

$$k = k_T \cdot \frac{\eta_T}{\eta_{15}} \tag{4.3}$$

$$k_T = \frac{a_b \cdot H_c}{A_c \cdot (\Delta t_P)} \cdot \ln \frac{\Delta L_1}{\Delta L_2} \tag{4.4}$$

where, η_T and η_{15} are the viscosity coefficients of water at the temperatures of given T and 15 °C, respectively. Furthermore, a_b and A_c are the areas of the double-tube burette (A) (*see* Figure 4.1.8) and the specimen after consolidation, respectively. The H_c value is the specimen height after consolidation. In addition, ΔL_1 and ΔL_2 are the water head differences of two burettes before and after percolation, respectively.

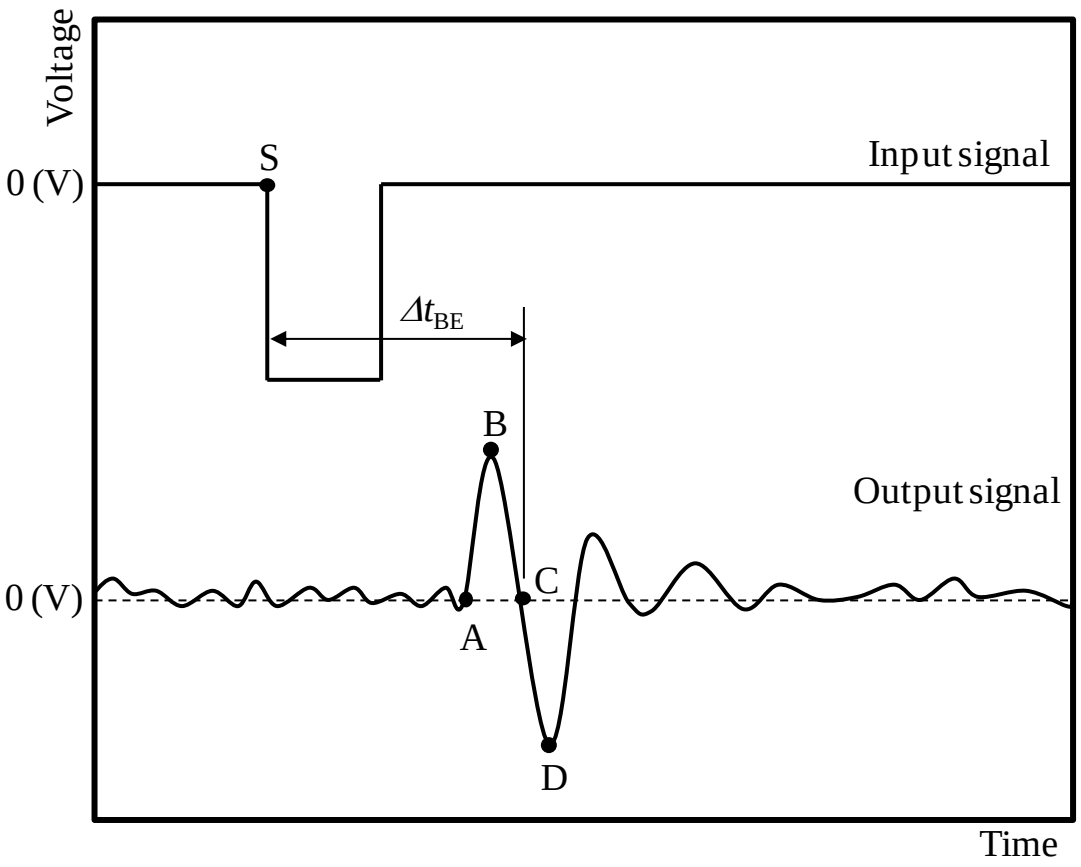

Figure 4.1.15 Identification of traveling time of shear wave

4.1.4.3 Freeze-thaw process

In order to simulate one-dimensional freeze-thaw sequence, the compacted specimen was covered with the frost heave cell in the triaxial cell before saturated. Then, non-frozen fluid was filled in the triaxial cell as cell water to cool the specimen instead of tap water. After setting up, the afore-mentioned vacuum procedure was followed to saturate the specimen. In order to evaluate freeze-thaw effect in more susceptible condition, the target degree of saturation S_r was higher than 80 %. After saturation, the cell water replaced with the non-frozen fluid had circulated with cooled by T-C bath (A) (*see* Figure 4.1.1(b)) until each temperature of the top and bottom ends of specimen maintained around 0 to 1 °C. On the other hand, the effective axial stress σ_a' was kept constant at 20 kPa throughout freezing and thawing. In order to avoid supercooling, the thermal shock was applied at the bottom end of specimen prior to freezing. Subsequently, a freezing front rose from the bottom end up through the pedestal at a certain cooling velocity by T-C bath (B) (*see* Figure 4.1.1(b)). Then, de-aired water was allowed to supply and drain from the top end of specimen through the double-tube burette which measured the amount of drainage during freezing and thawing. The freezing velocities V_f (mm/hr), which are calculated in Equation (4.5), are within the range of 0.45 to 1.26 mm/hr for all of the frozen specimens;

$$V_f = \Delta H_f / \Delta t_f \tag{4.5}$$

where, ΔH_f (mm) and Δt_f (hr) are the maximum amount of axial displacement induced by freezing and the required time to cause the corresponding ΔH_f value, respectively. After ensuring that the axial displacement due to freezing became constant, both of the T-C baths were turned off to thaw the specimens. After thawed at the temperature of around 20 °C, the frost heave cell was immediately taken out under the effective confining stress σ_c' of 20 kPa by providing the vacuum pressure through the pore water path to the specimen. Finally, the specimens that experienced the freeze-thawing

sequence, were fully saturated and consolidated prior to cyclic loading as well as the non-frozen ones in the afore-mentioned way.

4.1.4.4 Stress and strain states of triaxial tests

Figure 4.1.16 shows boundary conditions of specimen in each testing process in terms of stress and strain. In addition, Figures 4.1.17 (a) and (b) indicate the total stress and pore pressure varying in the processes under the saturated condition and in the freeze-thawing one, respectively. In this study, saturation and consolidation are carried out under an isotropic stress state, where the effective mean principal stress p' is equal to the effective confining stress σ_c'. Then, the σ_c' value was always kept less than $\sigma_c' = 50$ kPa at shearing or permeability tests until those processes as shown in Figures 4.1.17. On the other hand, the radial displacement is confined by the frost heave cell at the freeze-thawing process, which means that no radial strain ε_r can be caused. Therefore, if K_0 denotes a coefficient of earth pressure at rest, the effective mean principal stress p' during freeze-thawing should be represented as $p' = (1+2K_0)\sigma_a'/3$ as expressed in Figure 4.1.16 (II). After freezing and thawing, in the case that B value cannot reach 0.95 even under the back pressure, a series of saturating procedure was repeated before shearing. Shearing and percolation processes (III) ~ (VI) in Figure 4.1.16 were all conducted under the isotropic and normal consolidation condition. Because the permeability test (V) and the bender element test (VI) in the figure are non-destructive tests, the stress-strain states during testing must be corresponding to the isotropic consolidation state (I). On the other hand, because the pore water pressure was measured during cyclic and monotonic shearing (III) and (IV), the testing results will be discussed based on the effective stress as defined in the figure.

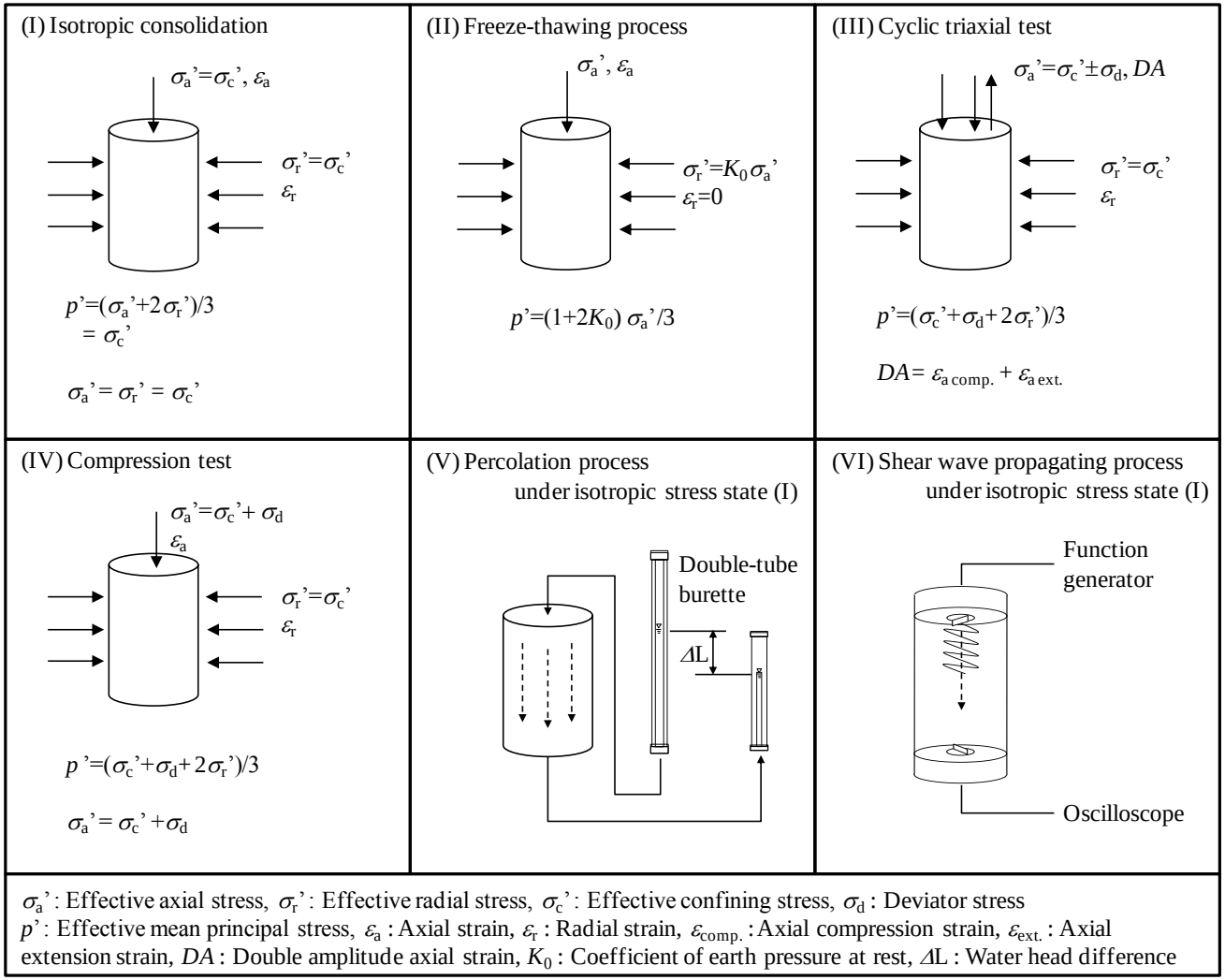

Figure 4.1.16 Stress and strain states during each testing process

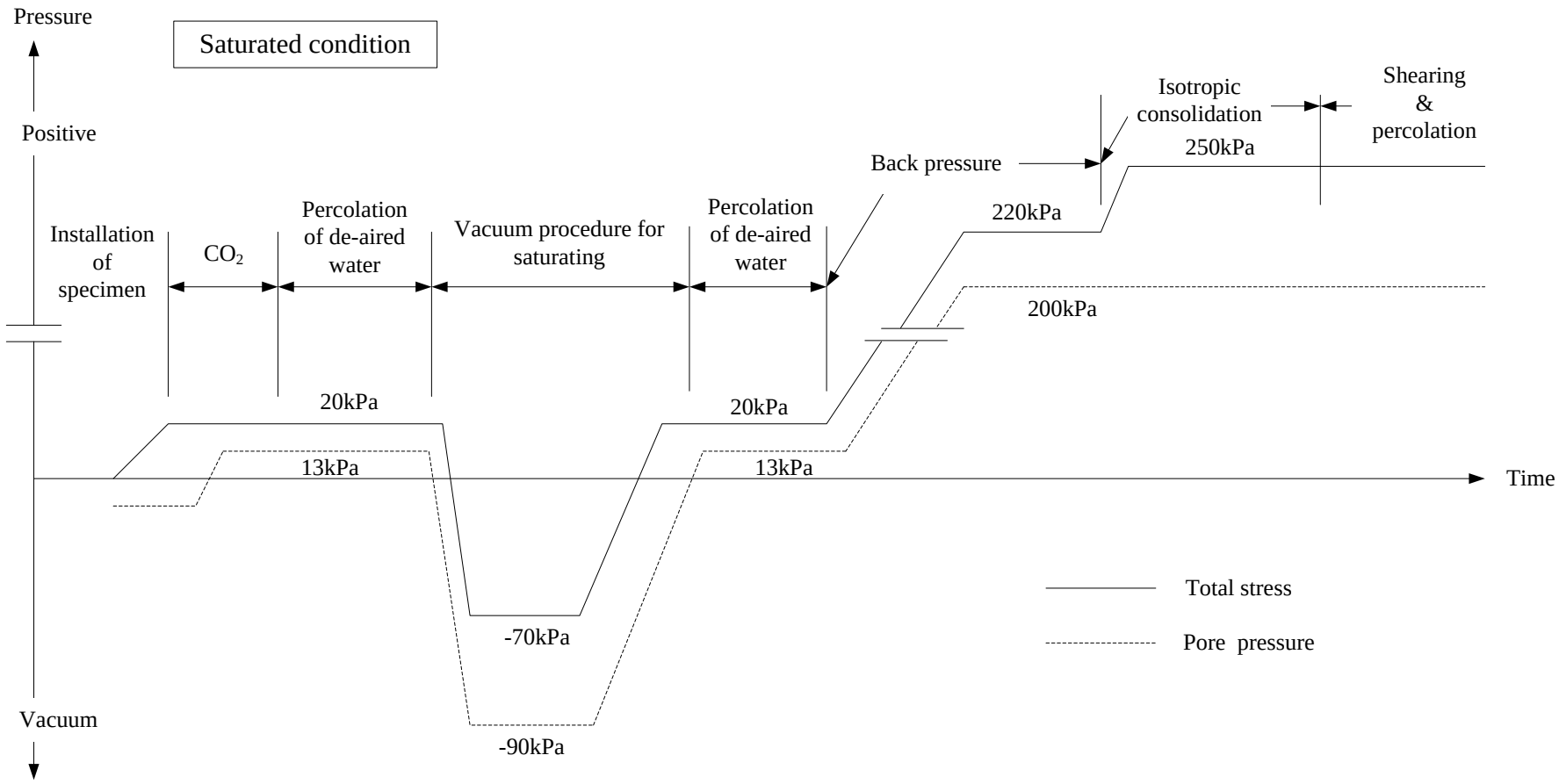

Figures 4.1.17 Testing process and stress states of specimen (a) Saturated condition

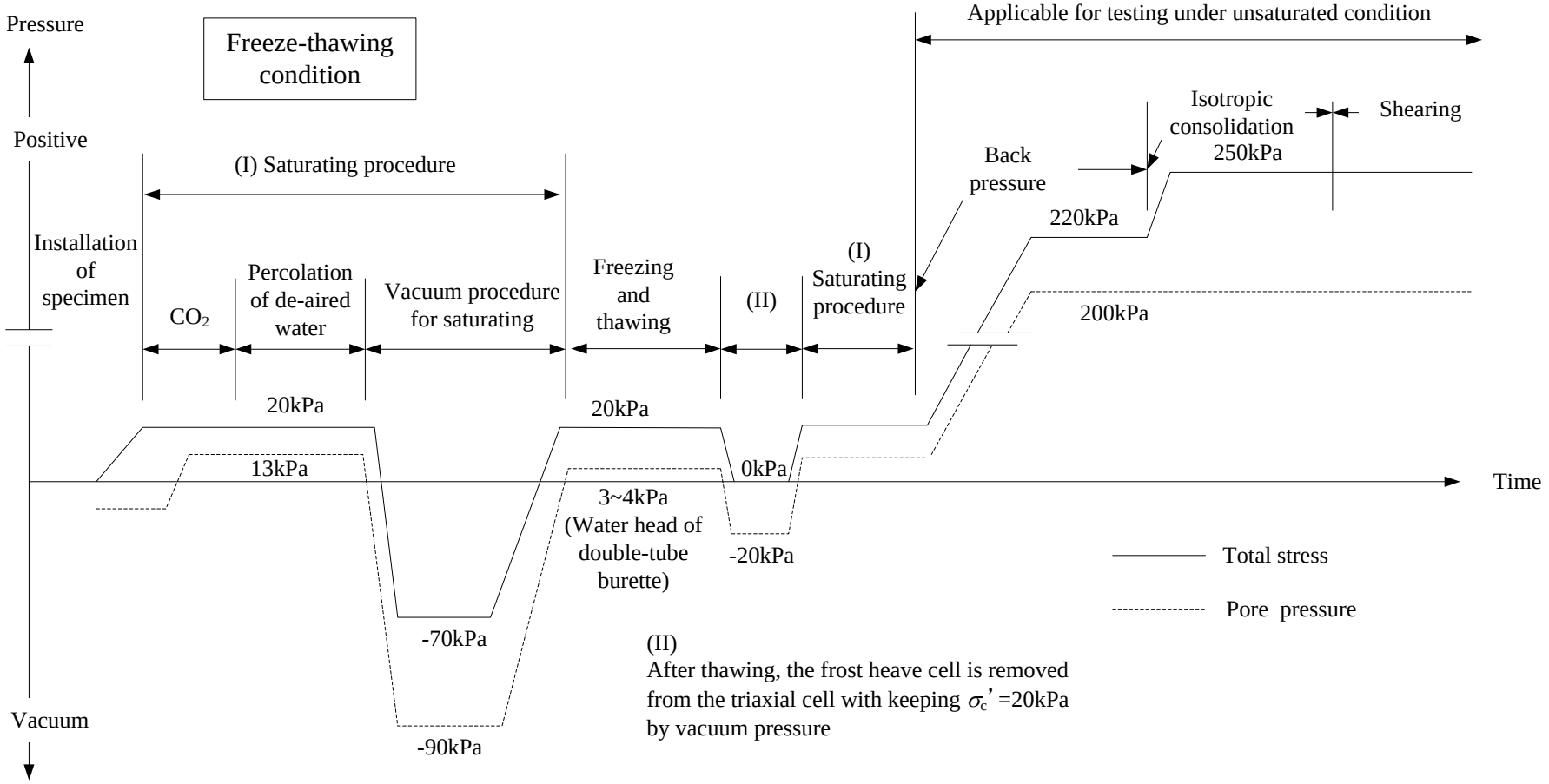

Figures 4.1.17 Testing process and stress states of specimen (b) Freeze-thawing condition

4.1.4.5 Testing process under unsaturated condition

In general, embankment is considered to be under unsaturated condition, and on the other hand, mechanical properties of soil can be significantly affected by degree of saturation. Therefore, the freeze-thawing triaxial apparatus shown in Figures 4.1.1 was newly developed so that the degree of saturation of specimens could be arbitrarily controlled. In this section, the testing procedure under unsaturated condition will be introduced.

Figure 4.1.18 shows the total stress, pore water and pore air pressures varying at the unsaturated test condition. In this test, the pedestal installing a ceramic disk and the cap with a porous metal were used as the pore water and pore air paths, respectively. Note that the porous metal in the cap was covered by a glass micro fiber filter beforehand. The specifications of the ceramic disk and the filter are indicated in Table 4.1.7.

After setting up the triaxial cell with a compacted specimen put on the pedestal with the ceramic disk saturated, pore air inside the specimen is eliminated by the vacuum procedure, the de-aired water is provided as well as under the saturated condition in Figure 4.1.17 (a). However, it can be very difficult to percolate the de-aired water through the ceramic disk to the compacted specimen because of their lower permeability, especially in the case that the specimen is more densely-compacted. Therefore, it is better to compact a soil at wetter water content beforehand, or to prepare another pore water path to saturate on the pedestal, but those would be a future work. After the attempt of saturation, the specimen is applied back pressure in stages with keeping net stress σ_{net} 20 kPa as shown in Figure 4.1.18. The net stress is expressed as follows (Fredlund 1993);

$$\sigma_{net} = \sigma - u_a \tag{4.6}$$

where, σ represents total stress. Ensuring sufficient water inflow by the back pressure, the specimen is isotropically consolidated at σ_{net} = 50 kPa. After the drainage stops, certain suction, which means matric suction in this thesis, can be applied to control degree of saturation of the

specimen with decreasing the pore water pressure. In this thesis, although no result of shear behavior under the unsaturated condition is shown, the water retentivity test shown in Figure 3.2.8 followed the above-mentioned procedure.

Table 4.1.7 Specifications of ceramic disc and glass microfiber filter

	Brand	Diameter	Air entry value	Particle retention in liquid
		mm	kPa	μm
Ceramic disk	-	64.5	100	-
Glass microfiber filter	Whatman	70	-	1.6*

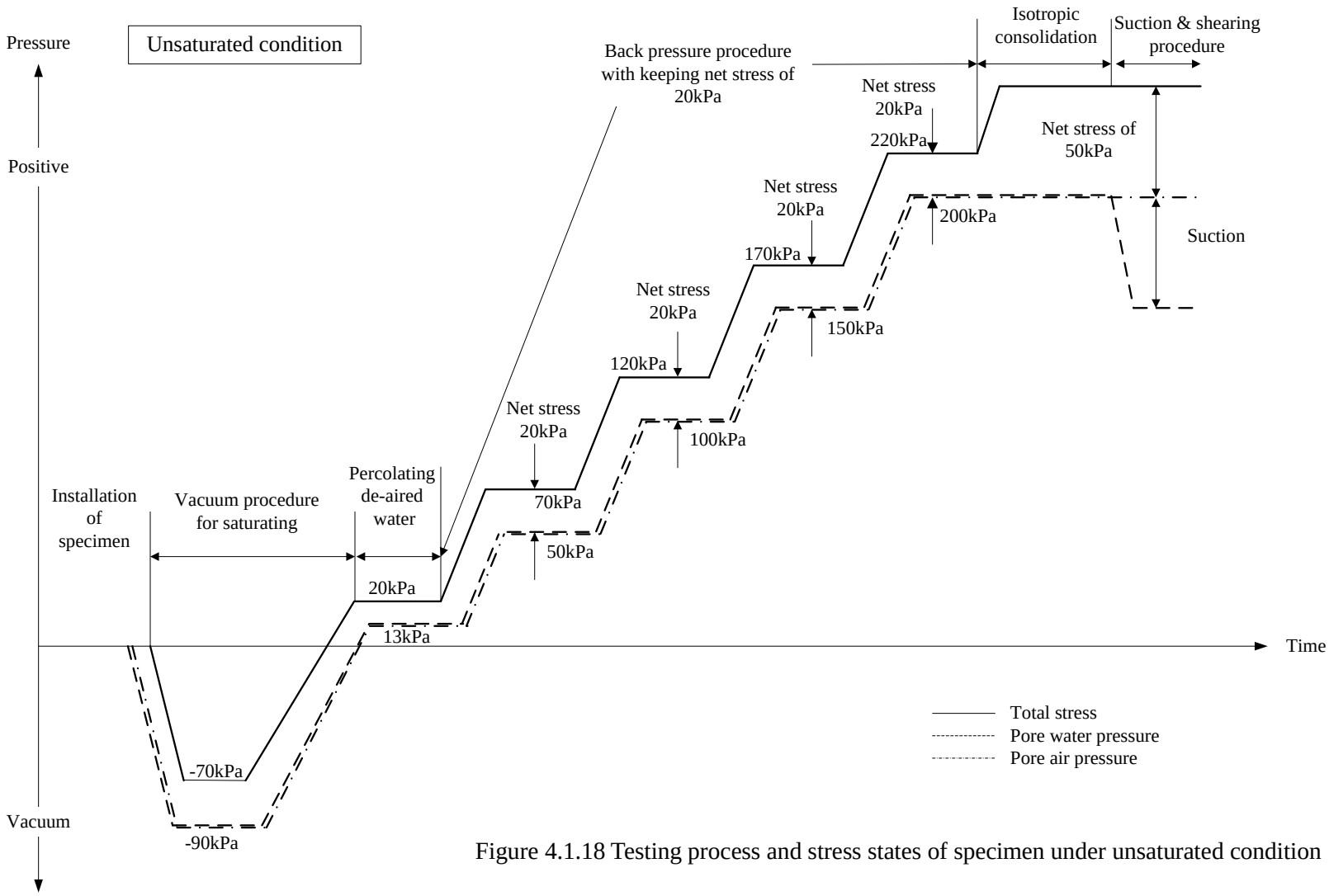

Figure 4.1.18 Testing process and stress states of specimen under unsaturated condition

4.2 Testing on full-scale embankment

4.2.1 Introduction

The aim of in-situ testing is to clarify slope failure mechanism of embankment constructed by a crushable volcanic soil in a cold region such as Hokkaido, based on the measurements of moisture movement (moisture distribution), change in pore pressure and acceleration inside the embankment. In this study, full-scale embankments and a cut slope were constructed at a testing site in Sapporo city. Photograph 4.2.1 shows a whole view of the testing site. The site is located at latitude 42°57′13″ north and longitude 141°21′46″ east, which is equal to the sampling site of Komaoka volcanic soil. As mentioned in *CHAPTER 3*, Shikotsu pumice flow deposit, Spfl, widely and thickly covers the site. The embankments and the cut slope were constructed using Komaoka volcanic soil.

Figure 4.2.1 indicates the overall condition of the in-situ testing. First, the site reconnaissance was conducted to determine the accurate location, scale and specifications of the embankment and the cut slope on April in 2011. Afterwards, a trial construction was carried out using Komaoka volcanic soil on June in 2011 so as to figure out in-situ compaction properties. Based on above works, the full-scale embankment and the cut slope (referred to as FE-2011 and CS, respectively in the thesis) were constructed on September in 2011 for the purpose of in-situ measurement. The results and discussion of monitoring and the rainfall-induced slope failure phenomenon that actually occurred on FE-2011 have been revealed (Kudo et al. 2012, Kawamura and Miura 2013b and Kawamura et al. 2013). Thus, because the FE-2011 embankment led to some slope failures, a new embankment was constructed using the same soil material next to FE-2011 on October in 2012, which is introduced as FE-2012 in the figure. In this study, some equipment for water supply was prepared to simulate inflow of water into earth structures due to snow melting in cold regions. Certain periods when the

water was forcibly provided into the embankments are shown in Figure 4.2.1. On the other hand, in the term, auger drilling with a post-hole auger was performed to calibrate water contents measured by soil moisture meters. In the figure, moreover, three kinds of soil materials, $K_{original}$, Soil 1 and Soil 2, sampled in the site are shown with the sampling dates. Although $K_{original}$ shown in Photographs 3.1.3 mainly occupies the site as a soil material, Soil 1 and Soil 2 were locally detected especially inside the cut slope CS, which are considered different in the degree of weathering from $K_{original}$. Photographs 4.2.2 (a) and (b), Table 4.2.1 and Figure 4.2.2 indicate Soil 1 and Soil 2, those physical properties and grain size distributions with those of $K_{original}$, respectively. Those soils contain similar or larger amount of finer fractions, and the natural water contents w_n (%) are basically higher than that of $K_{original}$. In the table, the in-situ dry densities investigated by the thin-wall sampling method will be required to analyze soil moisture monitoring results on CS as explained after.

FE-2012 was constructed under comparatively-idealized and detailed conditions in terms of boundary condition, compaction control and arrangement of measurement instruments, compared with FE-2011. That is, FE-2012 can interrupt water moving in and out between the embankment and natural ground with some impermeable sheets and panels arranged at the boundary. In addition, the compaction control by means of the sand replacement method was densely performed in constructing FE-2012. After construction, eight soil moisture meters (56 points), four tensiometers, and two accelerometers monitor the mechanical behavior of FE-2012. Therefore, in this thesis, a series of the in-situ testing results will be discussed focusing on FE-2012 with comparing those of the cut slope, CS.

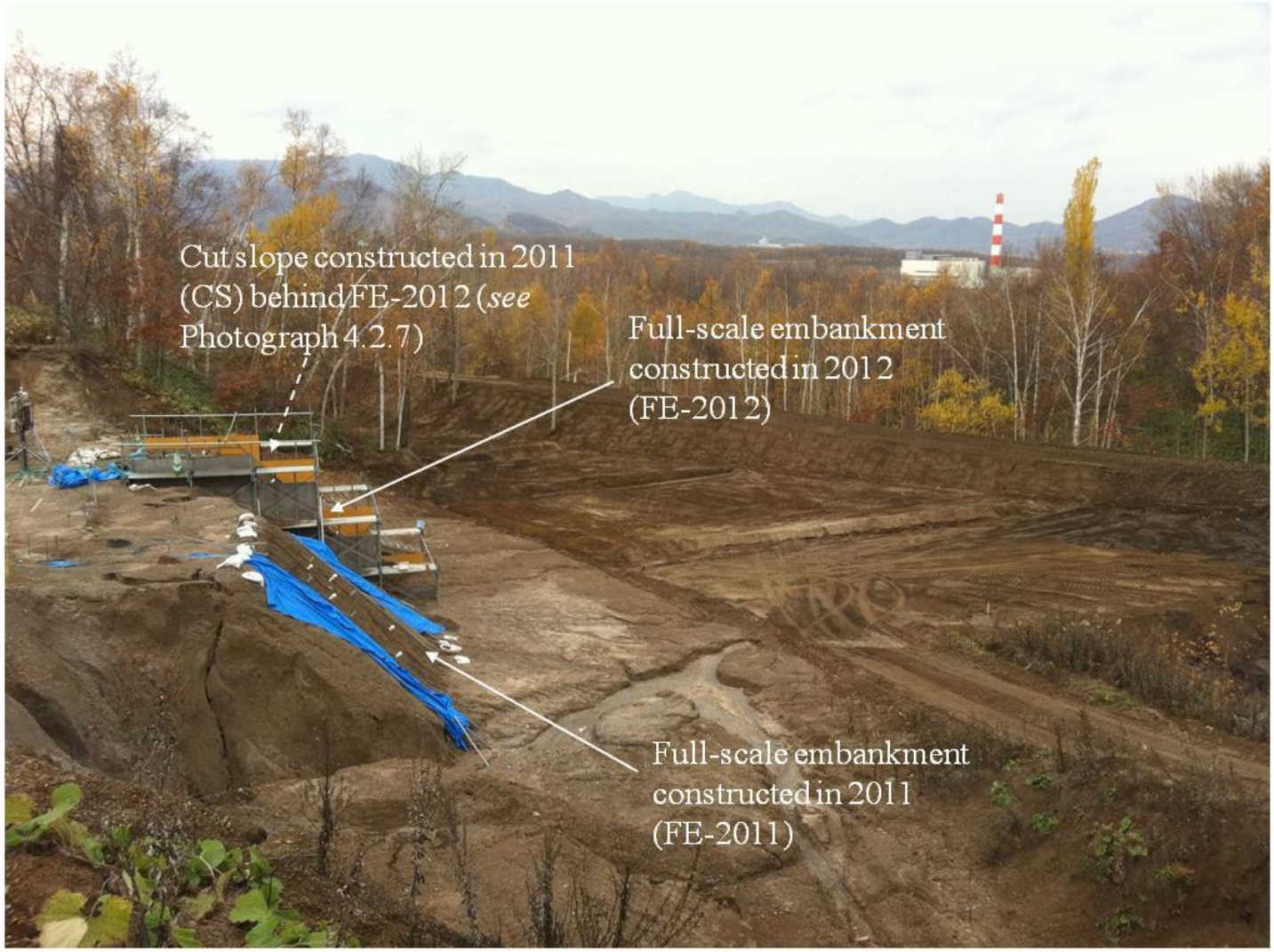

Photograph 4.2.1 Whole view of embankment site

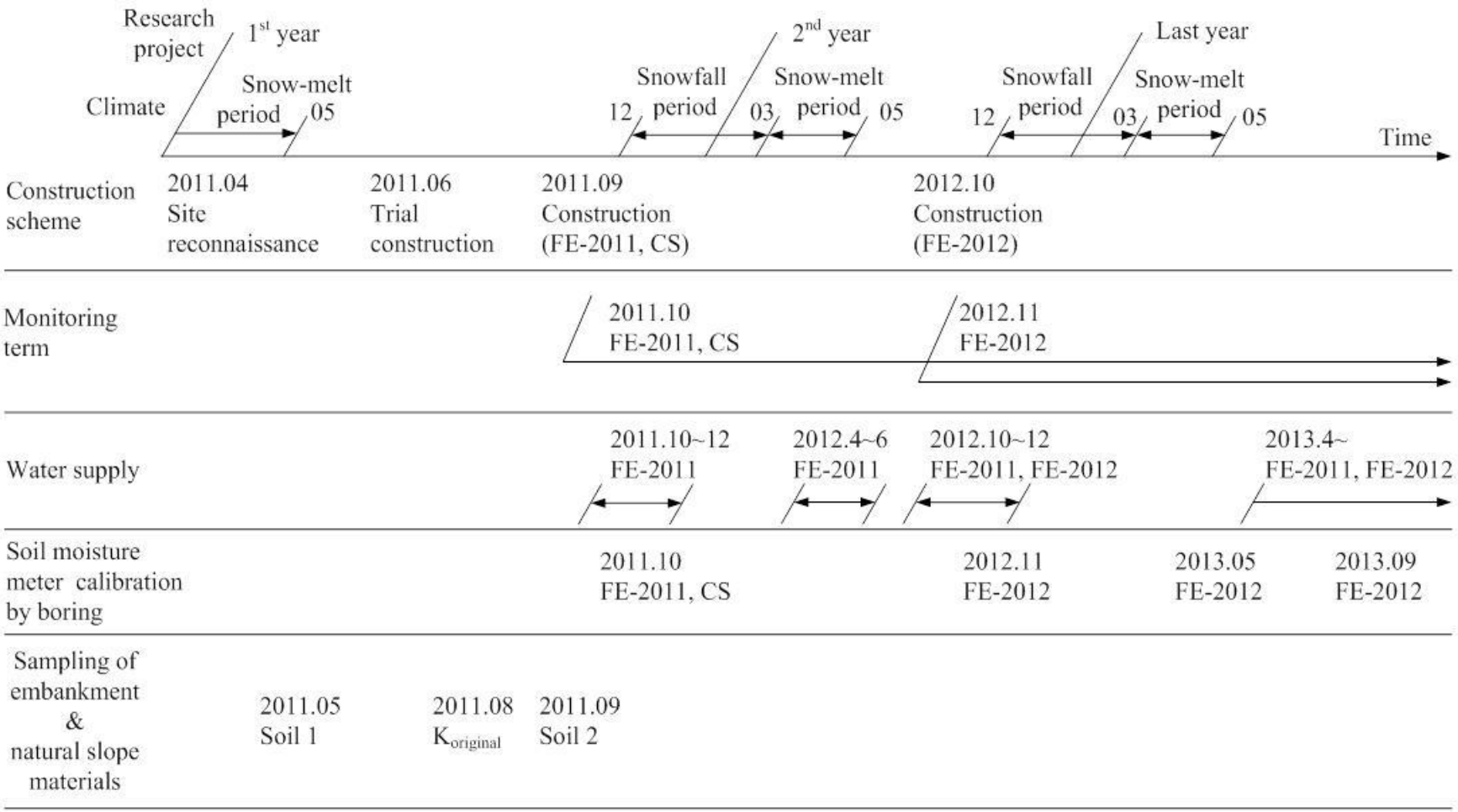

Figure 4.2.1 Whole picture of in-situ testing on full-scale embankment

(a) Soil 1 (w = 55.5%)

(b) Soil 2 (w = 90.2%)

Photographs 4.2.2 Sampled soil materials in cut slope, CS

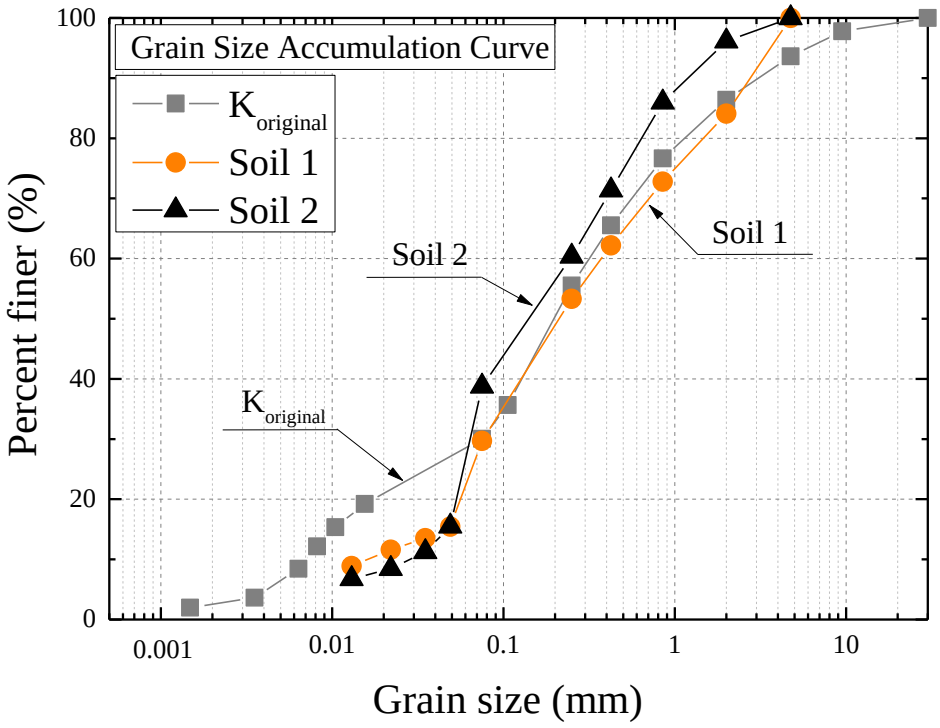

Figure 4.2.2 Grain size distributions of Soil1, Soil2 and $K_{original}$

Table 4.2.1 Physical properties of Soil1, Soil2 and $K_{original}$

Sample Name	Gravel	Sand	Silt	Clay	F_c	D_{max}	D_{50}	U_c
	%	%	%	%	%	mm	mm	-
Soil 1	3.9	57.4	-	-	29.7	4.75	0.208	23
Soil 2	15.9	54.4	-	-	38.8	4.75	0.142	8
$K_{original}$	13.6	56.3	23.6	6.4	30.0	>9.5	0.197	45

Sample Name	In-situ thin-wall sampling		ρ_s	w_L	w_P	I_p	Compaction A-c		Compaction A-b	
	w_n	ρ_d					w_{opt}	ρ_{dmax}	w_{opt}	ρ_{dmax}
	%	g/cm^3	g/cm^3	%	%	%	%	g/cm^3	%	g/cm^3
Soil 1	55.9	0.749	2.572	32.8	23.2	9.6	-	-	29.0	1.229
Soil 2	65.1	0.584	2.471	70.1	Unavailable	NP	-	-	-	-
$K_{original}$	35.0	0.840	2.512	46.7	Unavailable	NP	40.5*	1.059*	34.2*	1.090*

4.2.2 Full-scale embankment slope constructed in 2012

4.2.2.1 Scheme and preliminary study

The full-scale embankments, FE-2011 and -2012, were designed and constructed based on the site reconnaissance and the trial construction conducted beforehand as explained above. In the trial construction, the in-situ roller compaction was carried out to figure out the in-situ compaction properties. In constructing the embankment, the hand-guided compaction roller was employed for compaction, whose typical specifications are shown in Table 4.2.2. The weight and compacting width are 6.1 kN and 650 mm, respectively. Photograph 4.2.3 demonstrates the trial construction operating the compaction roller, which was conducted using $K_{original}$ at the embankment site. The compacting height per a layer was 0.3 m on the plane of 2 m in depth and 3 m in length as shown in the photograph.

Figure 4.2.3 indicates the results of the sand replacement method on the compaction plane to investigate degree of compaction. In the figure, the compaction curve using K soil from the laboratory compaction test is drawn as well. From the figure, it is recognized that the water contents at compaction w_i tend to be lower than the optimum water content w_{opt} of 40.5 %, and the degree of compaction varies from 75 % to 92.5 % of the maximum dry density ρ_{dmax} of 1.059 g/cm^3 (1.059 Mg/m^3), which is denoted as D_c. Furthermore, Figure 4.2.4 represents the relation between the dry density and the number of roller compactions on the basis of the trial construction. According to the figure, Komaoka volcanic soil seems not to become dense even though the number of roller compactions increases up to 10 times.

Figure 4.2.5 shows the results of compaction control by means of the sand replacement method and the thin-wall sampling on the full-scale embankment constructed in 2011, FE-2011. The

density investigation with the sand replacement method was conducted at seven points on each layer of the embankment heights of 1.0, 2.6 and 5.0 m, which corresponds to the compacted soil volumes of about 78, 178 and 270 m^3 at each height. Then, the same hand-guided compaction roller as that of the trial construction operated. Note that the roller compactions were conducted 4 times per a layer of 0.25 m in height until the embankment height reached 5 m. Because of the embankment construction after rain-fall, the soil materials were compacted at wet condition of w_{opt}. Accordingly, the degree of compaction became higher than that of the trial construction. Finally, FE-2011 was built with the scale of 5 m in height, 12 m in width and 7 m in depth, and was formed at 45 degrees for the slope angle, which were discussed in detail by Kawamura et al. (2012) and Kawamura and Miura (2013b).

Keeping in view the above, the full-scale embankment constructed in 2012, FE-2012 was designed as illustrated in Figure 4.2.6. The embankment slope shape of FE-2012 is basically similar to that of FE-2011; i.e., the height of 5 m and angle of 45 degrees were adopted. However, the width of 4 m was selected. In addition, in order to avoid water moving in and out between the embankment and the natural ground, the back and base of the embankment were covered with impermeable sheets, and some water-repellent panels were structured at the lateral faces with supported by some braces. Each section at 1-meter intervals, where the after-mentioned measurement instruments are installed, are referred to as L-, C- and R-sections from the left at the embankment as shown in the figure, respectively. On the other hand, three roller compactions per a layer of 0.25 m were determined so that the mean degree of compaction D_c could reach 85 %. Figure 4.2.7 indicates the compacting paths that the hand-guided compaction roller should trace. After every three compactions, the compaction roller was moved into the next path to continue. The lateral and back ends, where it is difficult to operate the compaction roller, were carefully compacted by a plate compactor.

Table 4.2.2 Typical specifications of hand-guided compaction rollers used for construction

Type of compaction roller	Dimensions					Drum size		Vibrating power			Traveling speed
	Operating weight (kN)	Overall width (mm)	Overall length (mm)	Overall height (mm)	Wheel base (mm)	Diameter (mm)	Width (mm)	Centrifugal force (kg)	Frequency (vpm)	Gradability (°)	Forward (km/h)
Hand-guided compaction roller	6.1	692	2620	1130	520	355	650	1100	3300	20	0~3

Photograph 4.2.3 Trial construction on 2011.06

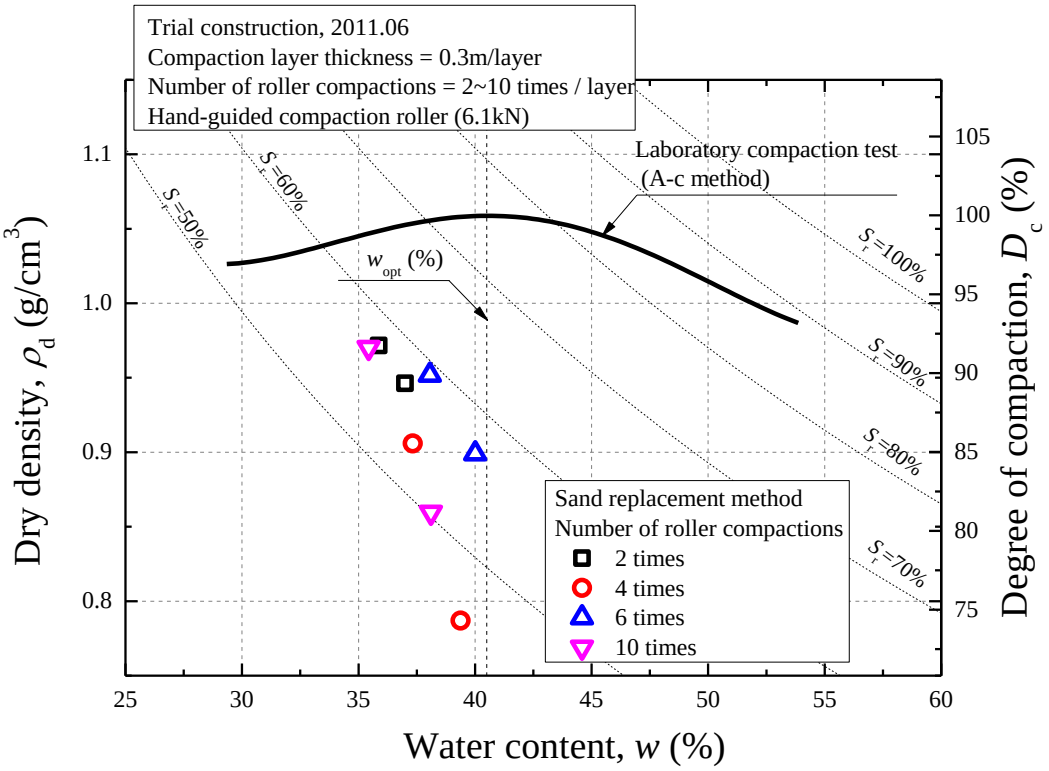

Figure 4.2.3 Result of sand replacement method on trial construction

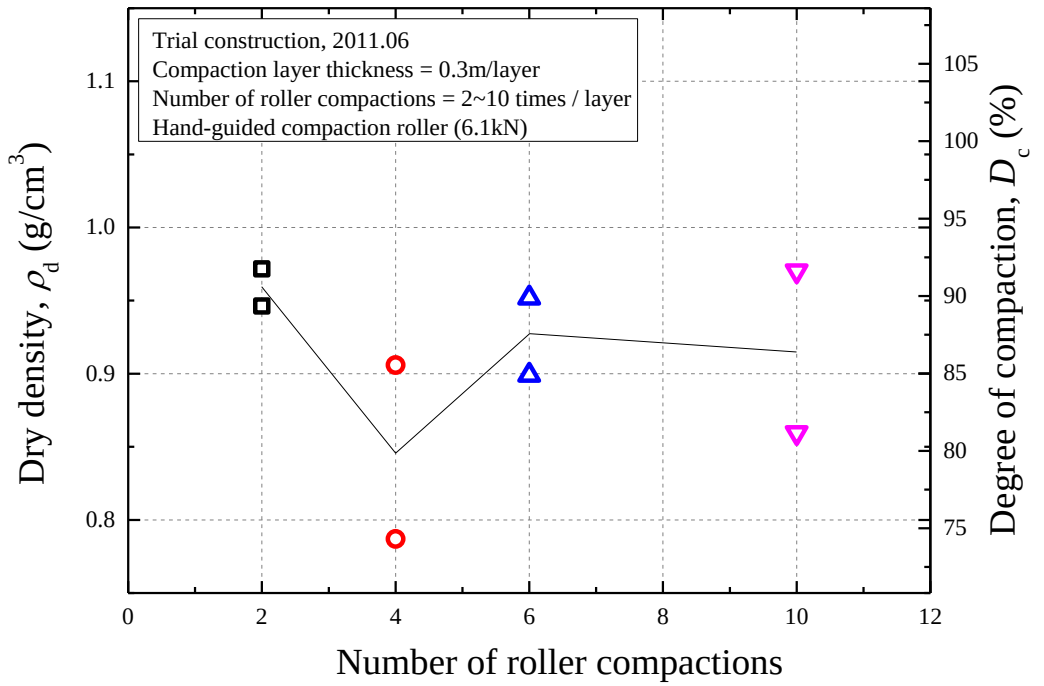

Figure 4.2.4 Relation between dry density and number of roller compactions on trial construction

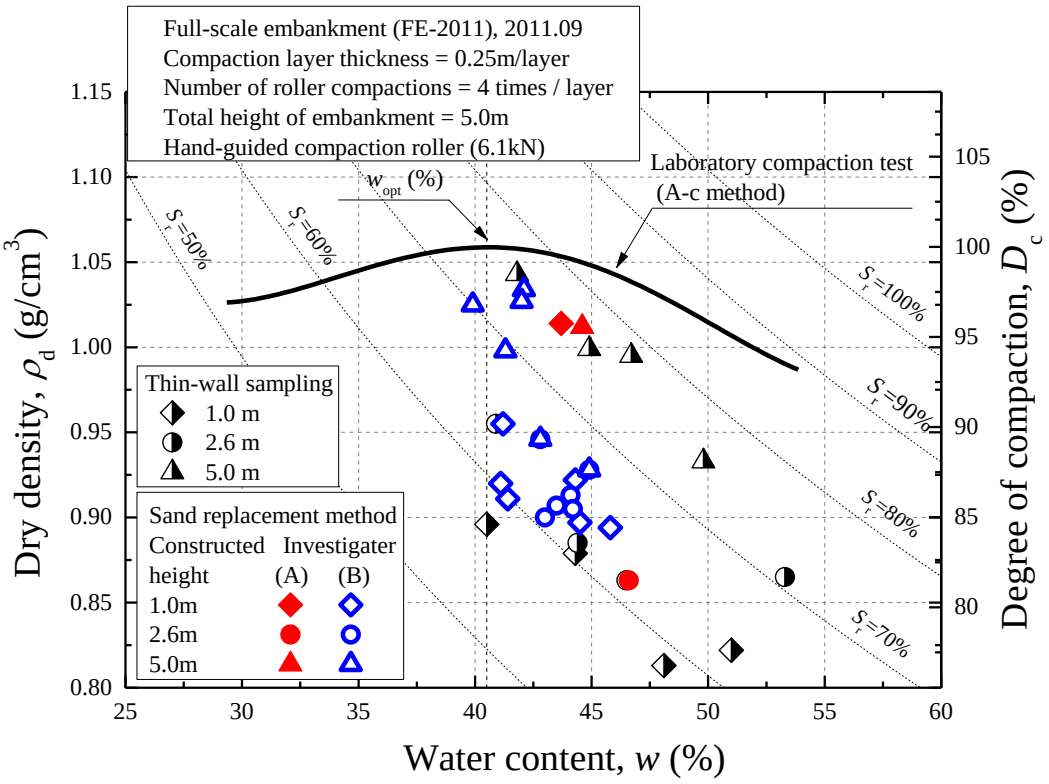

Figure 4.2.5 Compaction control of full-scale embankment constructed in 2011, FE-2011

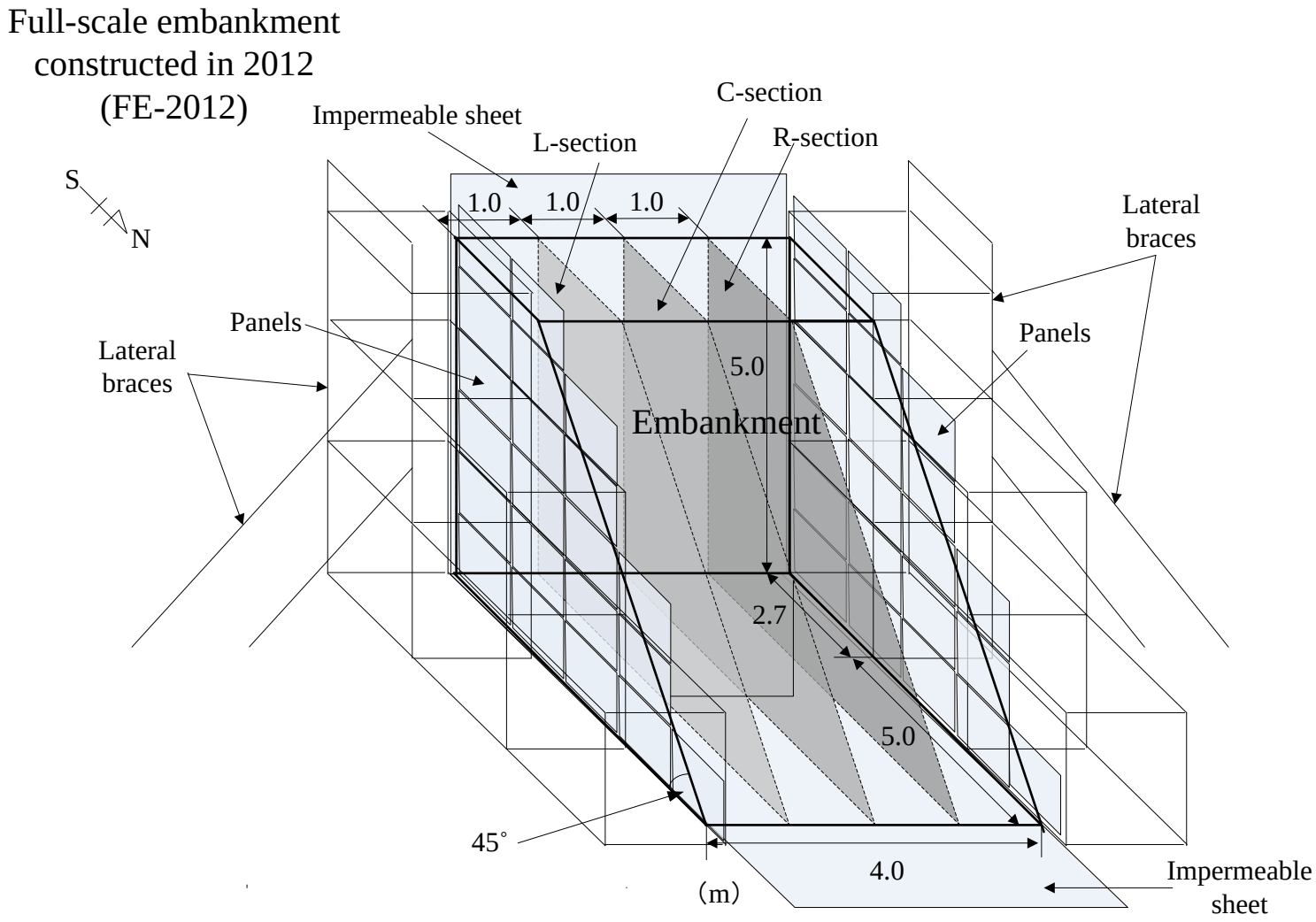

Figure 4.2.6 Schematic diagram of full-scale embankment constructed in 2012, FE-2012

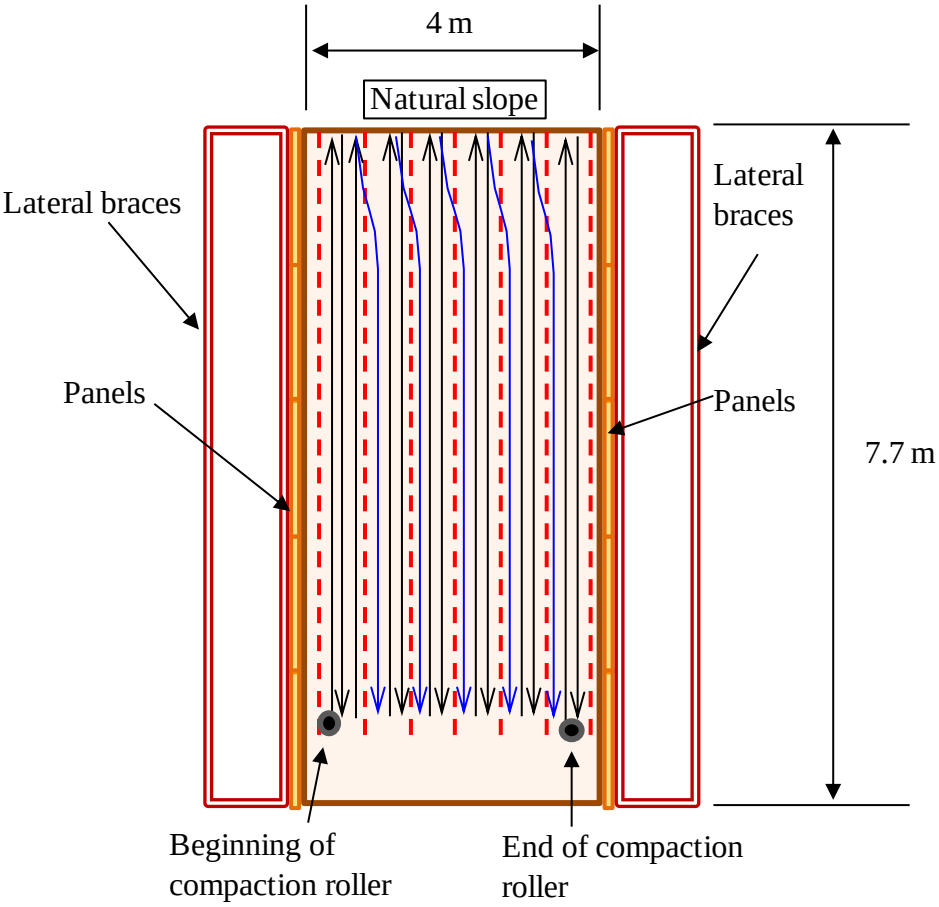

Figure 4.2.7 Roller compaction condition on a compaction layer

4.2.2.2 Construction

The construction of FE-2012 was conducted on October in 2012. Photographs 4.2.4 (a) ~ (h) show a sequence of the constructing procedures. Before compacting the soil, the impermeable sheets and the panels supported by lateral braces were structured at each face as presented in Photographs 4.2.4 (a) ~ (c). Afterwards, the soil, $K_{original}$ (*see CHAPTER 3*), was spread and compacted on each layer of 0.25 m, which is shown in Photograph 4.2.4 (d). The detailed procedure to compact is as explained in the previous section. When the height of embankment during construction achieved 1, 2, 3 and 4 meters, the sand replacement method was conducted at 4 points a layer for compaction control as shown in Photographs 4.2.4 (e) and (f). Photograph 4.2.4 (g) demonstrates the embankment completed with forming the slope at 45 degrees after the embankment height of 5 m was accomplished. In addition, Photograph (h) shows the water supply pipes installed from on the embankment crest after construction, which will be mentioned later.

Figure 4.2.8 illustrates the points where the densities were investigated with the sand replacement method. Those were chosen at 1 and 3 meters in depth from the back face and the intervals of 1 m in height on L- and R-sections. In addition, in the figure, the locations of thin-wall sampling for the liquefaction test on C-section are shown, in which four specimens were sampled; i.e., No.1 ~ No.4. The sampling was carried out at 1, 3 and 4 meters in height.

Figure 4.2.9 shows the w-ρ_d relation on the compaction plane obtained from the sand replacement method. From the figure, it could be understood that the soils were compacted at slightly wetter water contents of w_{opt}, within 41.2 ~ 43.5 %. The observed dry densities were 0.980 ~ 1.060 g/cm^3 (0.98 ~ 1.06 Mg/m^3), which corresponds to the range of 92.5 ~ 100.1 % in the degree of compaction D_c. As a result, the average ρ_d and D_c are 1.020 g/cm^3 (1.020 Mg/m^3) and 95.9 %, respectively, which will be required to calculate the water content from the soil moisture observation. On the other hand, in the figure, the w-ρ_d relation of the specimens sampled by thin-wall sampling is also

exhibited. From the figure, the specimens are considered looser a little compared with the results of sand replacement results, while the water contents are within the similar range.

Figures 4.2.10 (a) ~ (c) demonstrate the arrangement of water supply pipes installed into the embankment. In particular, in Figures 4.2.10 (b) and (c), those are separated to show on the embankment crest and on the slope for the help of understanding, respectively. The water are reserved in three tanks, and provided through each hose pipe into the embankment as shown in Figure 4.2.10 (a). The tanks are located 3 m higher than the embankment crest, and the amount of water inflow can be controlled by each valve equipped with the tanks. The volume of water possible to reserve in the tank is around 1 m^3. The water supply pipes illustrated in the figures have some holes to drain at certain locations and intervals as shown in Figure 4.2.11. In the figure, L_a and L_b indicate the length of sections with water supply holes, which have the diameter of 5 mm, and with no hole in a pipe, respectively. On the other hand, L_c is the diameter of the pipe. Table 4.2.3 summarizes the specifications of each water supply pipe with the period of use. That the periods using each pipe vary is because the water supply can easily cause piping phenomena inside the embankment. That is, every time the piping occurred, other pipes were newly prepared and installed, and the water supply has been attempted repeatedly. From the investigation for piping, it was confirmed that such phenomena basically tended to be caused along the embankment boundary.

(a) Structuring lateral braces

(b) Laying impermeable sheets

Photographs 4.2.4 Construction procedures of FE-2012

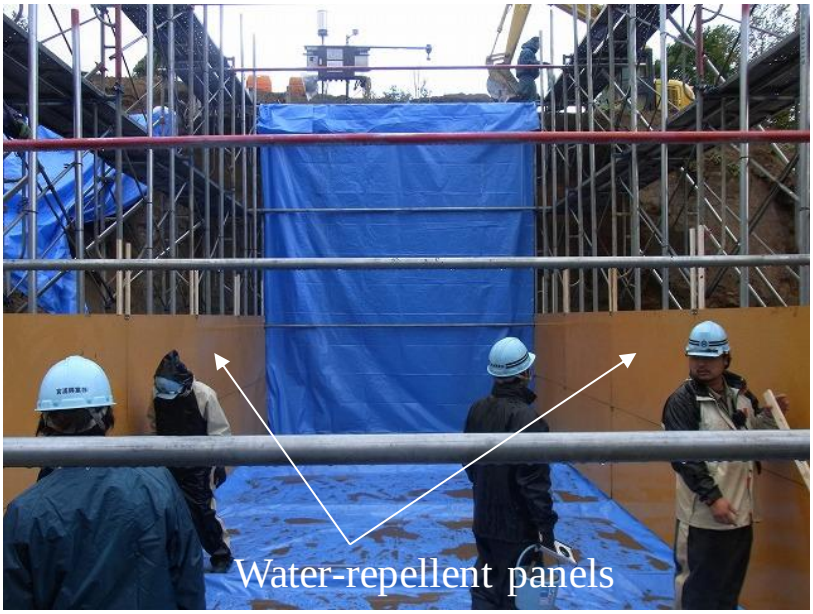

(c) Building water-repellent panels

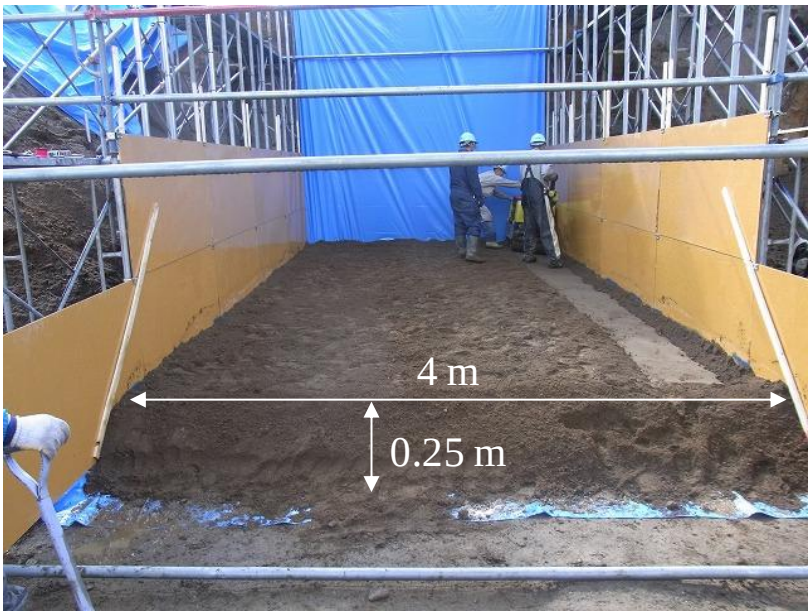

(d) Compacting Komaoka volcanic soil of 0.25 m per a compaction layer

Photographs 4.2.4 Construction procedures of FE-2012

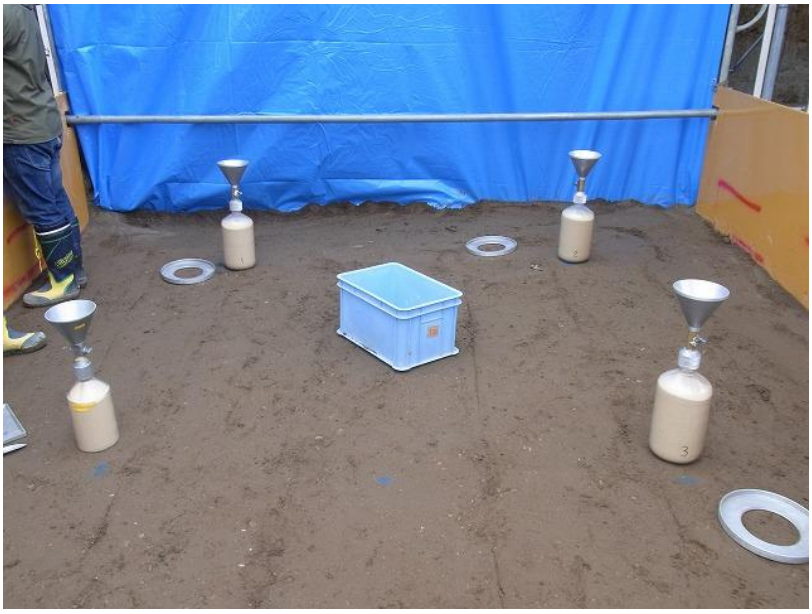

(e) Arrangement of locations for sand replacement method

(f) Conducting sand replacement method

Photographs 4.2.4 Construction procedures of FE-2012

(g) FE-2012 completely constructed

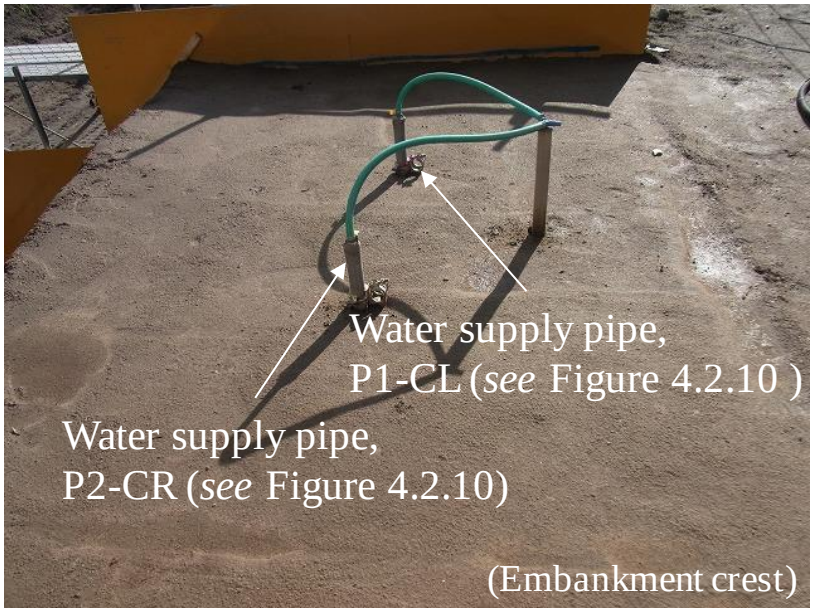

(h) Water supply pipes

Photographs 4.2.4 Construction procedures of FE-2012

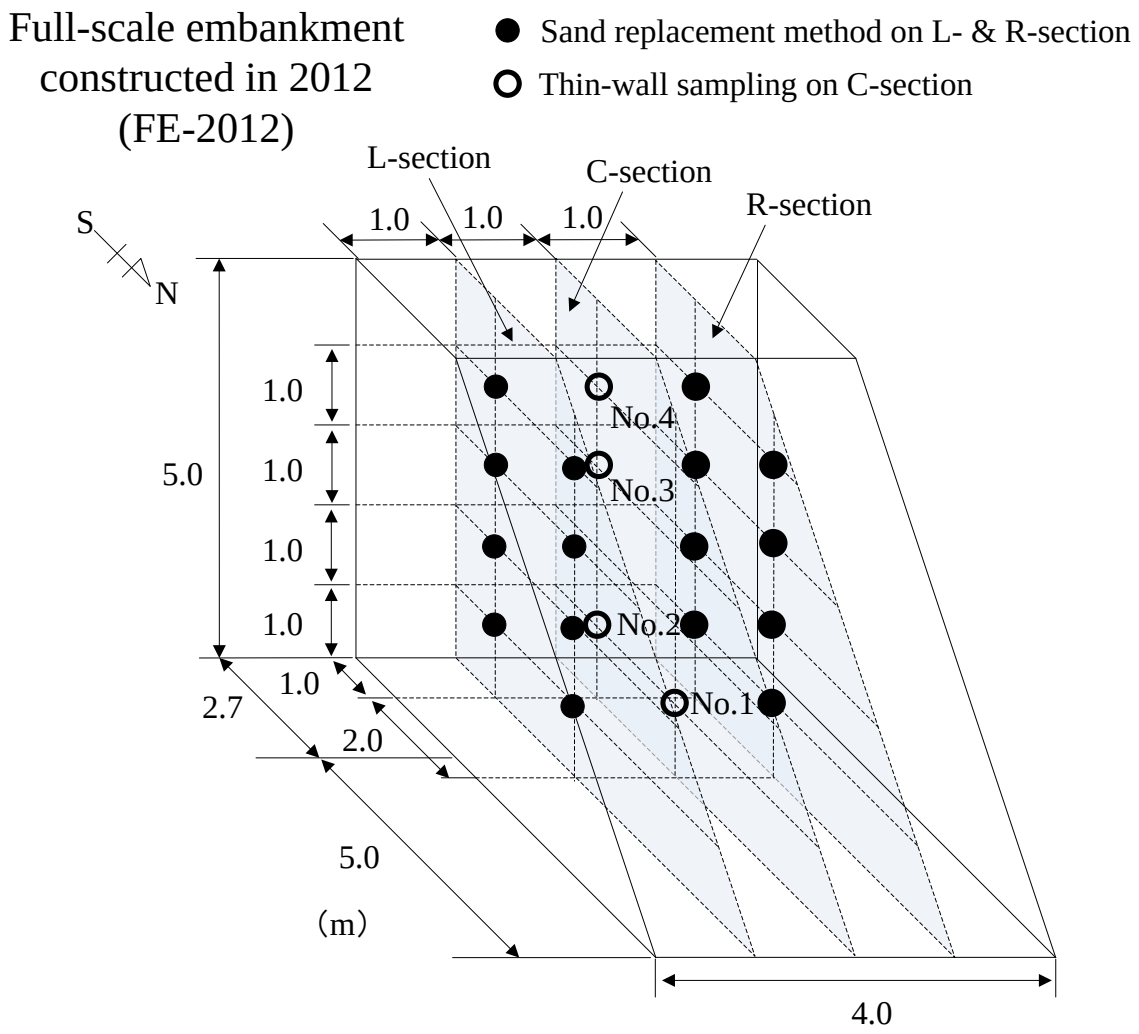

Figure 4.2.8 Arrangement of compaction control for FE-2012 by means of sand replacement method and thin-wall sampling

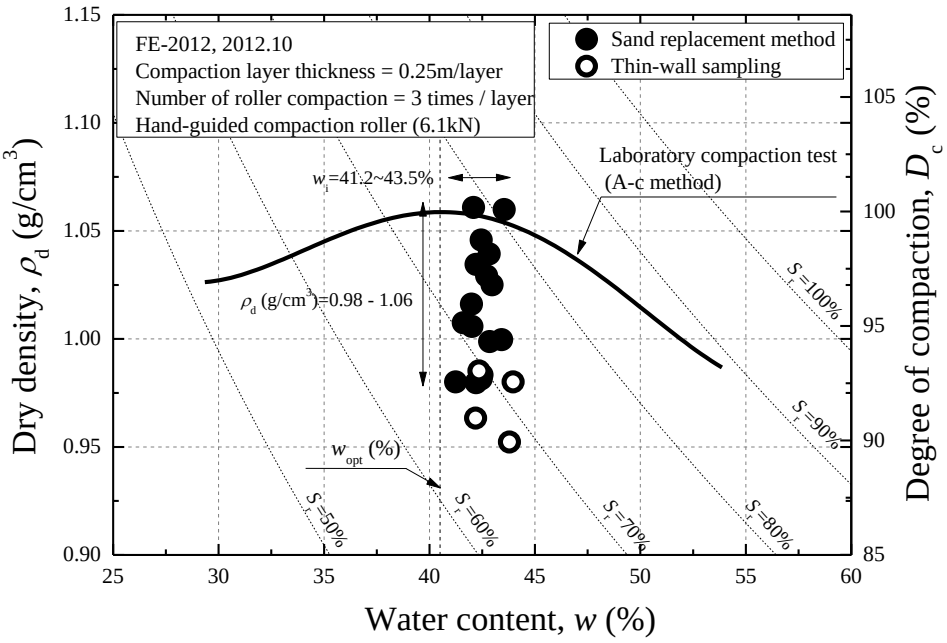

Figure 4.2.9 Result of compaction control for FE-2012 by means of sand replacement method and specimens by thin-wall sampling

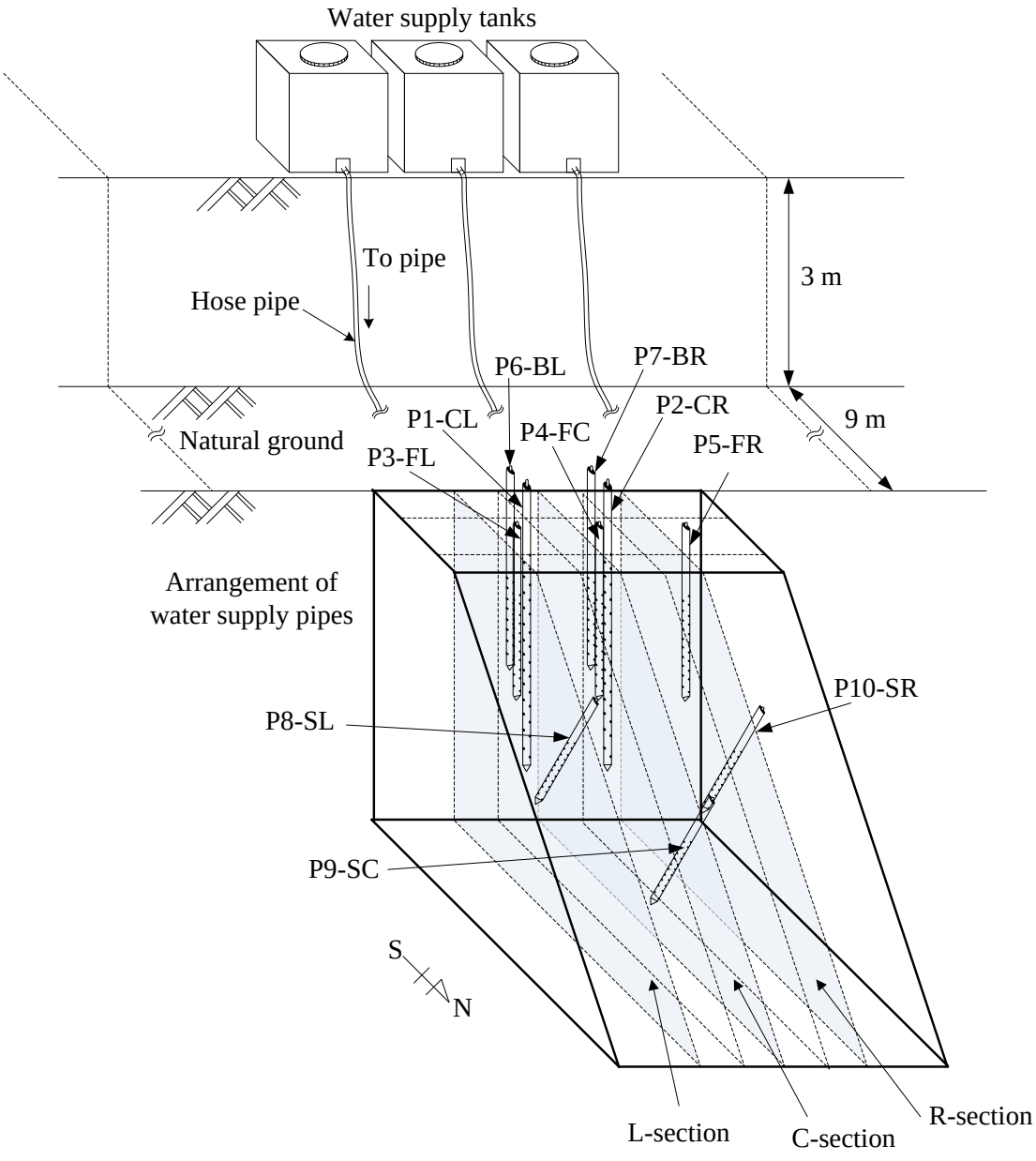

Figures 4.2.10 Arrangements of water supply pipes and tanks (a) Whole arrangement

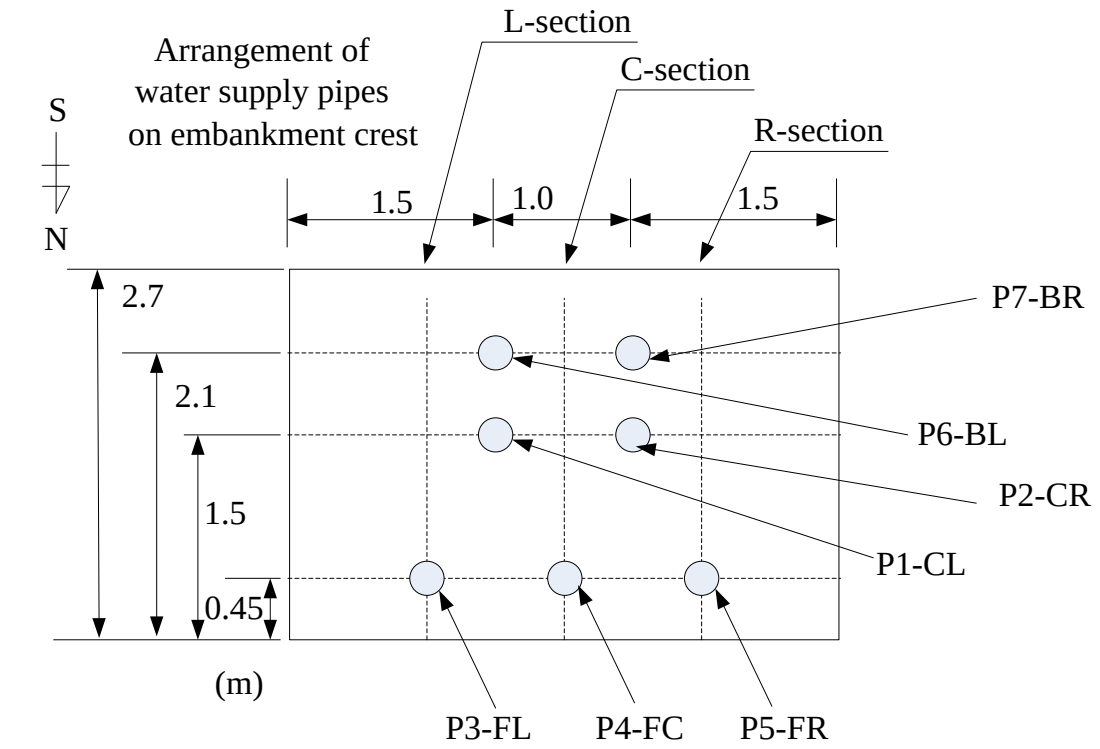

(b) Water supply pipes on embankment crest

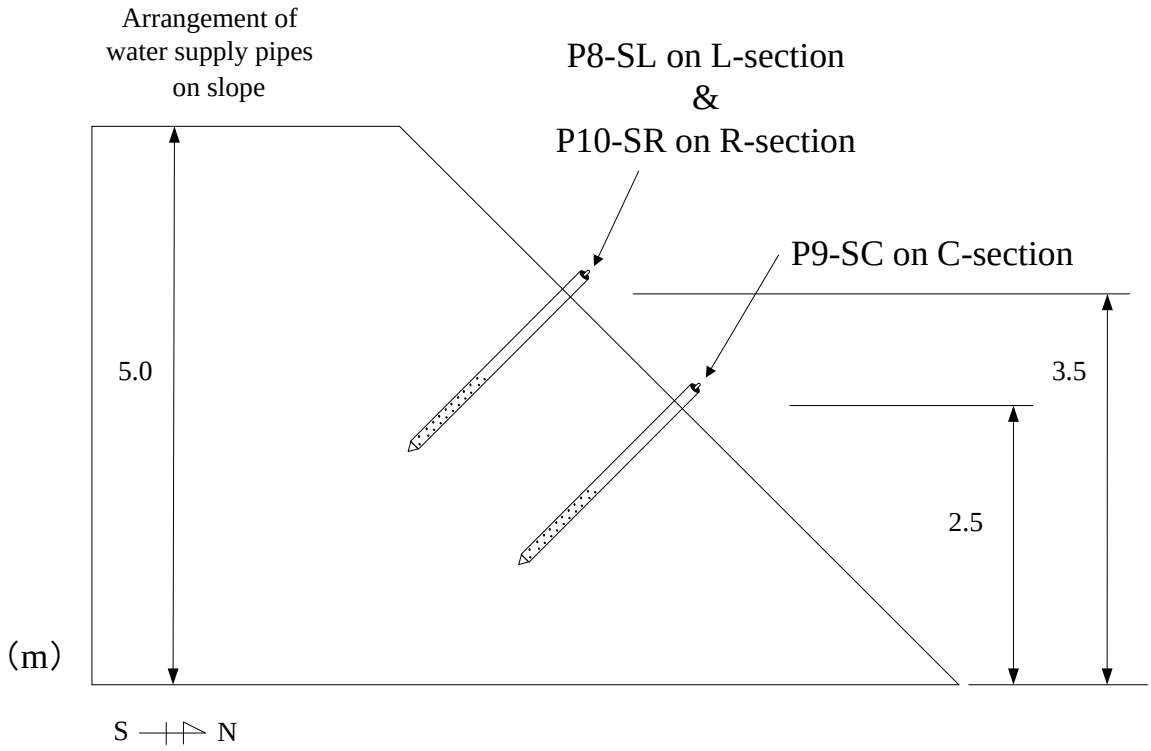

(c) Water supply pipes in embankment slope

Figures 4.2.10 Arrangements of water supply pipes and tanks

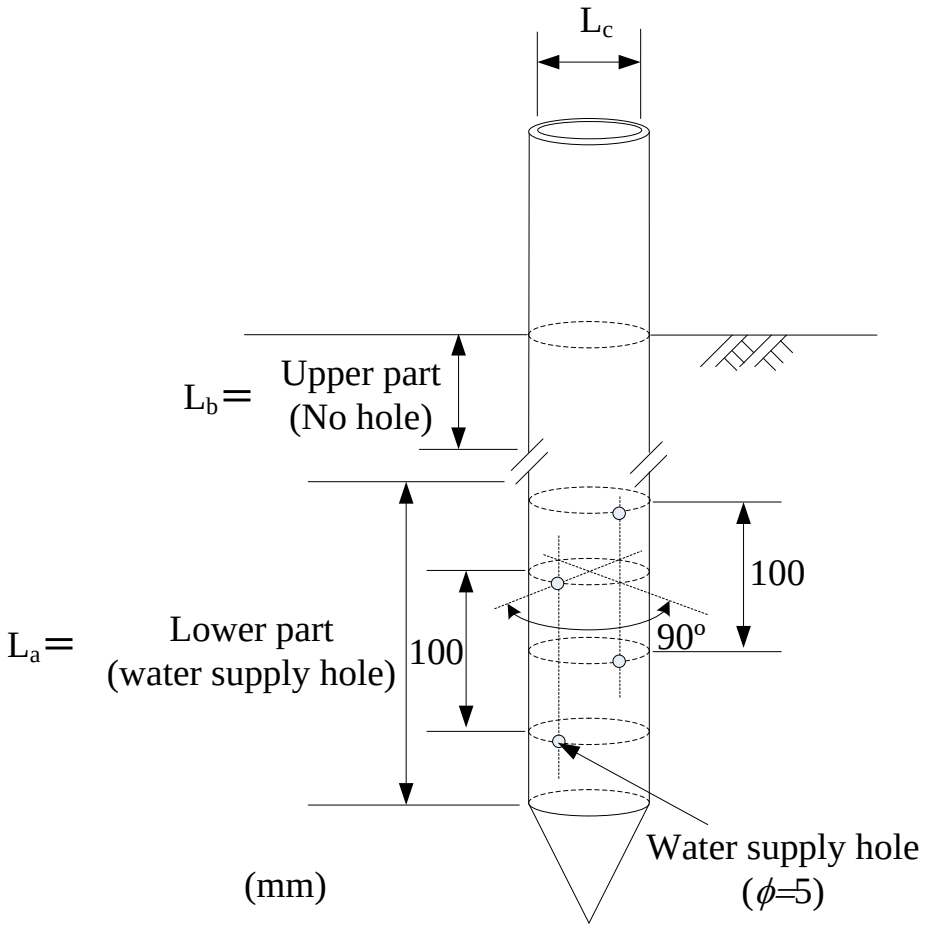

Figure 4.2.11 Water supply pipe and its specifications

Table 4.2.3 Specifications of water supply pipes

Name	L_a	L_b	L_c	Material	Period of use
	mm	mm	mm		
P1-CL	3500	500	45	Iron tube	2012.11.20 ~ 2012.11.30
P2-CR	3500	500	45		2013.5.8 ~ 2013.7.08
P3-FL	1600	100	45		2013.07.27 ~ 2013.08.06
P4-FC	1600	100	45		
P5-FR	1600	100	45		
P6-BL	1500	1000	45		2013.09.13 ~ 2013.10.04
P7-BR	1500	1000	45		
P8-SL	1000	1000	30	Flexible rubber tube	2013.10.11 ~ 2013.10.18
P9-SC	1000	1000	30		
P10-SR	1000	1000	30		

4.2.2.3 Measurement instruments and their arrangement

Figure 4.2.12 illustrates the whole arrangement of measurement instruments on the full-scale embankment FE-2012 and the cut slope CS. In this study, the monitoring targets are volumetric moisture content, pore pressure, acceleration and temperature inside the embankment. At the same time, the climatic information such as outside air-temperature and the amount of rainfall and snow accumulation in winter was observed. The data measured by each instrument were automatically accumulated once every ten minutes in the data logger shown in the figure. Photographs 4.2.5 (a) and (b) show the view of data accumulation system including the data logger. The power required to operate a series of measuring system is being provided by the solar panel and the storage battery indicated in Photograph 4.2.5 (a). In reading and saving the data, a notebook can communicate directly with the data logger as demonstrated in Photograph 4.2.5 (b).

Figures 4.2.13 (a) and (b) represent the accurate locations of the measurement instruments inside the embankment slope on L- and R-sections and C-section, respectively. In addition, Photographs 4.2.6 (a) ~ (g) and Table 4.2.4 show the measurement instruments and those specifications. The fundamental features are as follows;

(a) Soil moisture meter

Four sets of soil moisture meters were installed in the same arrangement on L- and R-sections, respectively, as shown in Figure 4.2.13 (a). One was buried at 1 m from the top of slope on the crest on each section, which are denoted as SM_{L0} and SM_{R0}, respectively. The others were located at the heights of 4, 3 and 2 meters perpendicularly on the slope, which are shown as $SM_{L1\sim3}$, $SM_{R1\sim3}$. Each set is composed of 7 soil moisture meters as indicated in Photograph 4.2.6 (a), which measure the volumetric moisture contents at 0.2, 0.4, 0.6, 0.8, 1.0, 1.2 and 1.5 meters in depth from the surface. Therefore, the total monitoring points for soil moisture reach 56 in the embankment, FE-2012. Each soil moisture meter has the size of 70 mm in length and 50 mm in diameter, and it is applicable

for measurement under any conditions of oven dry to saturation. The area of measuring the soil moisture with single soil moisture meter is within the radius of 100 mm around. After installing the set of soil moisture meters into a bore hole at the desired location, the hollow between the soil and the instrument was stopped with kaolin-cement mixture. The measurement value observed by the soil moisture meter is the volumetric moisture content θ_w (%). In analyzing the data, the θ_w value is transformed to the water content *w* (%) based on Equation (4.7) as follows;

$$w = \frac{\rho_w}{\rho_d} \cdot \theta_w \tag{4.7}$$

where ρ_w and ρ_d (g/cm^3) is the densities of water and soil mass, respectively. Then, the ρ_d value for FE-2012 is 1.020 g/cm^3.

(b) Tensiometer

Four tensiometers were buried at 0.6 m in depth from the surface on C-section as shown in Figure 4.2.13 (b), which are referred to as $T_{C0\sim3}$. The reading range of the tensiometer is around from 10 ~ -70 kPa. After ensuring the porous cup indicated in Photograph 4.2.6 (b) touched the bottom of bore hole, the soil, Komaoka volcanic soil, was filled up into the hole.

(c) Accelerometer

Two accelerometers were horizontally installed at the heights of 2.5 and 0.5 m on C-section, which are denoted as A_{C1} and A_{C2}, respectively in Figure 4.2.13 (b). The maximum acceleration to measure is ±4g. In burying the instruments, the direction at which those are put should be paid attention on based on the three-dimensional direction shown in Photograph 4.2.6 (c). After installing into the bore hole, Komaoka volcanic soil was filled up as well as in the case of tensiometers.

(d) Thermometer for soil temperature

A set of thermometers measures the temperatures inside the embankment slope at the depths of 0, 0.1, 0.2, 0.4, 0.6, 0.8, and 1.0 m on C- section as shown in Figure 4.2.13 (b). The instrument was

installed into a bore hole with the hollow stopped with clean sand and finally covered with Komaoka volcanic soils in order to avoid the inflow of water.

(e) Snow gauge, (f) Rainfall gauge and (g) Thermometer for air temperature

The snow gauge, the rainfall gauge and the thermometer of air temperature shown in Photographs 4.2.6 (e) ~ (g) were placed so as to obtain the climatic information at the embankment site. They were assembled with the data accumulation system as indicated in Photograph 4.2.5 (a).

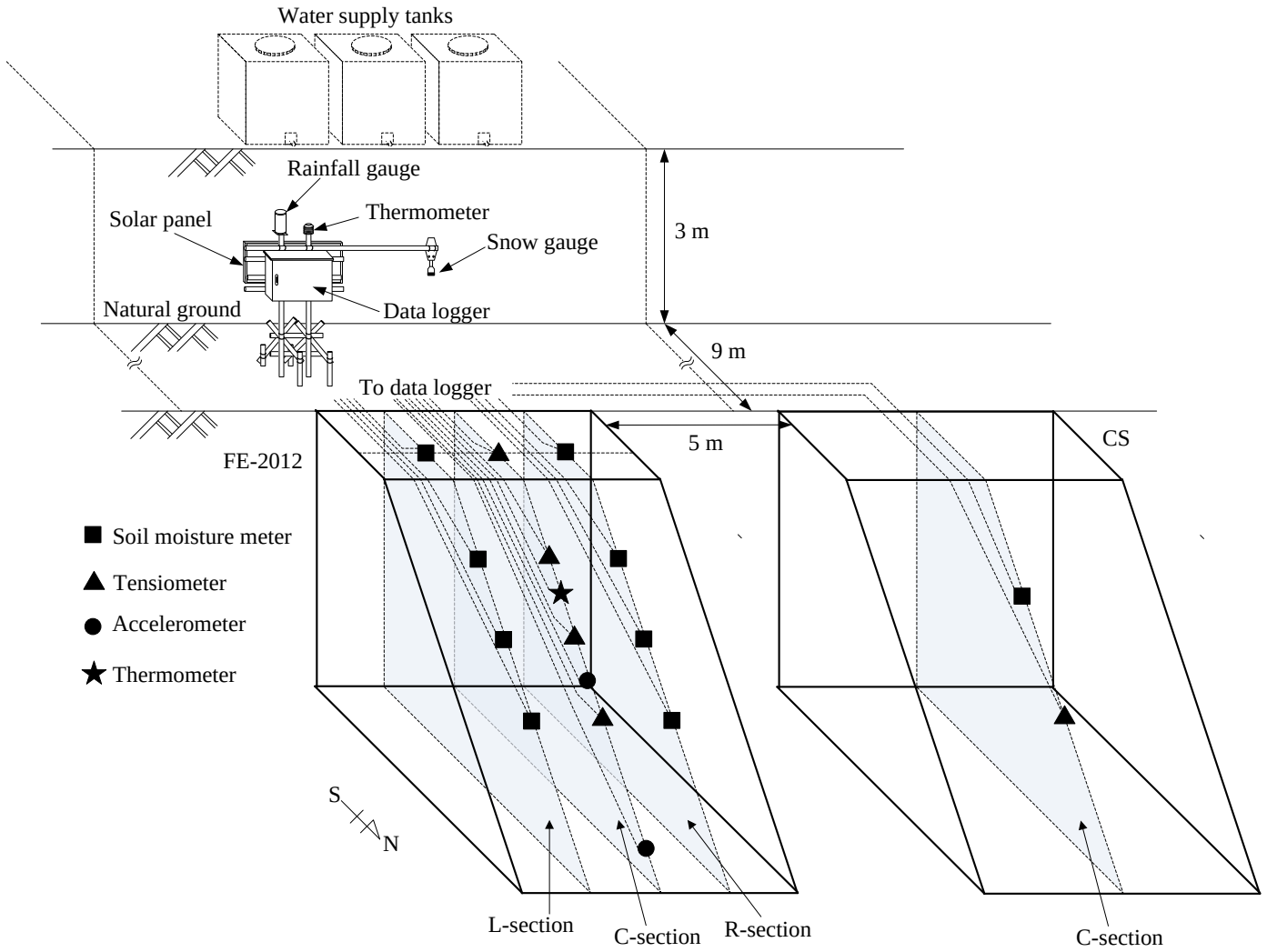

Figure 4.2.12 Arrangement of measurement instruments for FE-2012 and CS

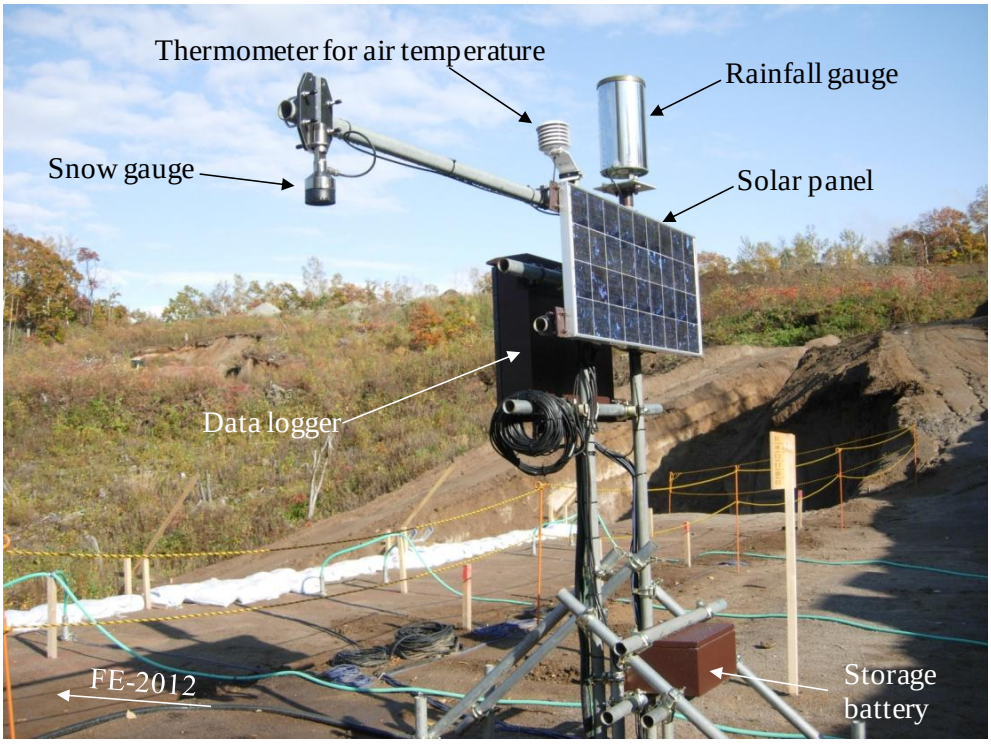

(a) Assembled measurement instruments and data accumulation system

(b) Reading monitoring data

Photographs 4.2.5 Data accumulation system

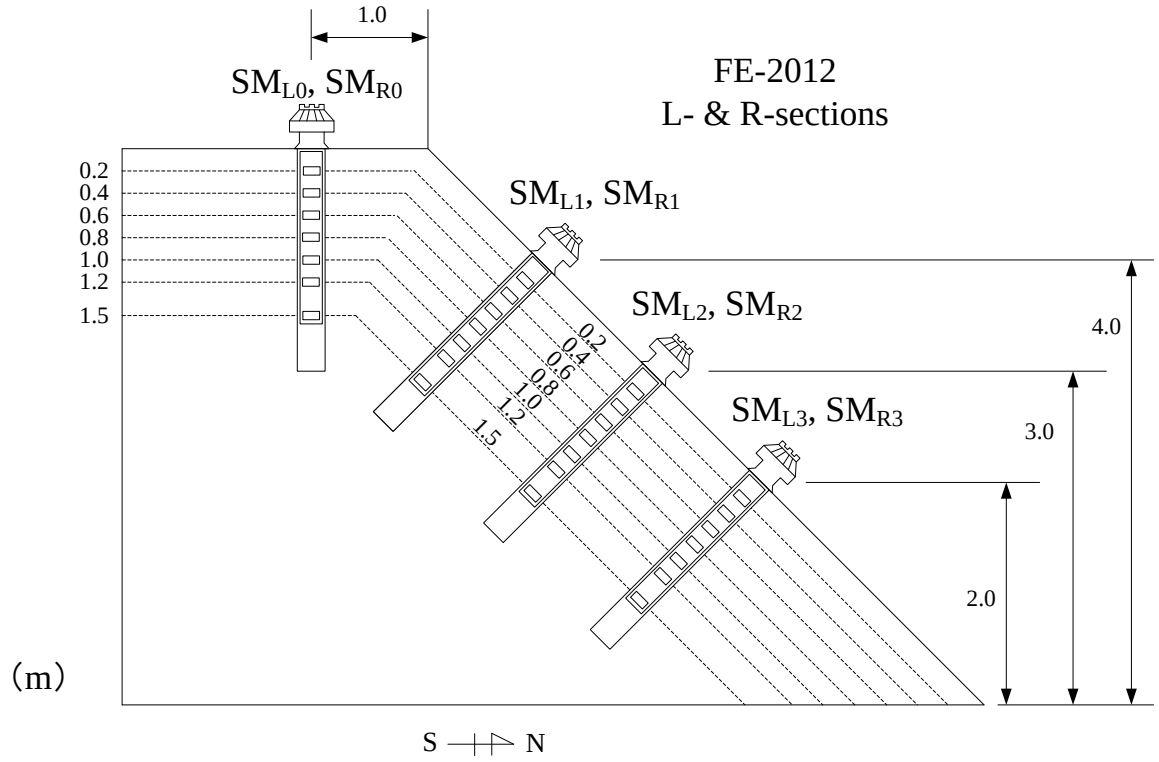

(a) L- & R-sections

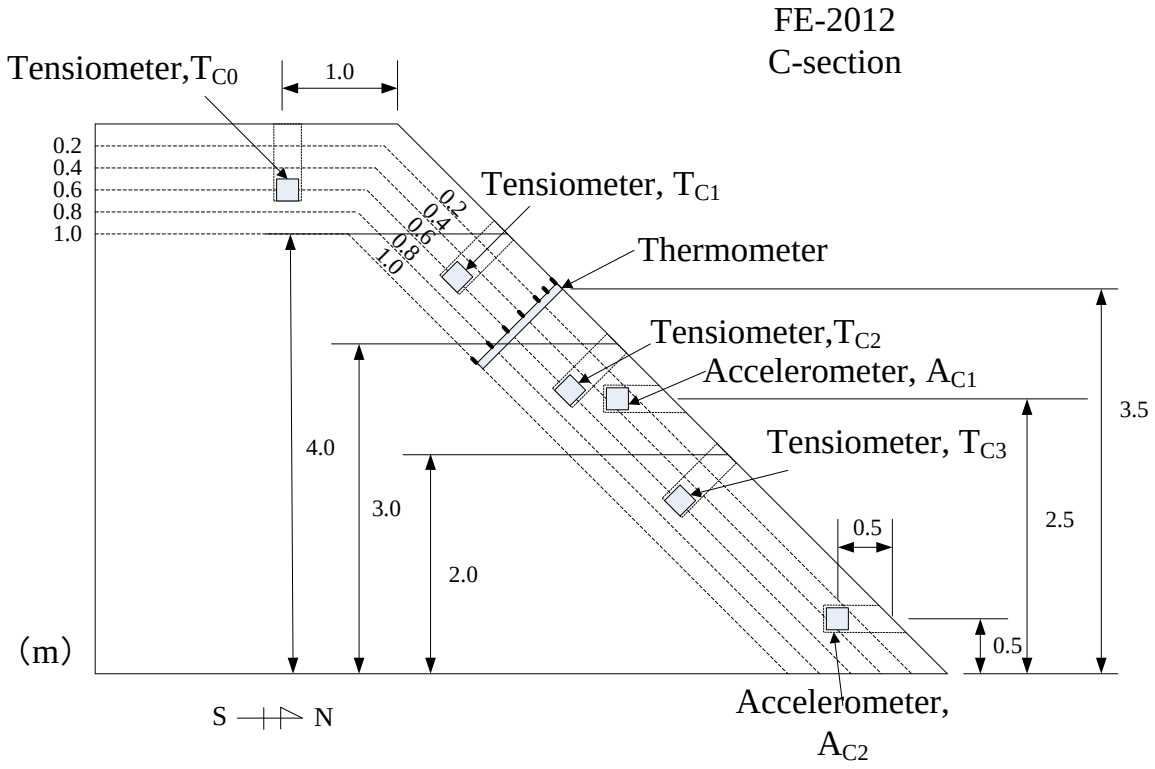

(b) C-section

Figures 4.2.13 Arrangement of measurement instruments for FE-2012

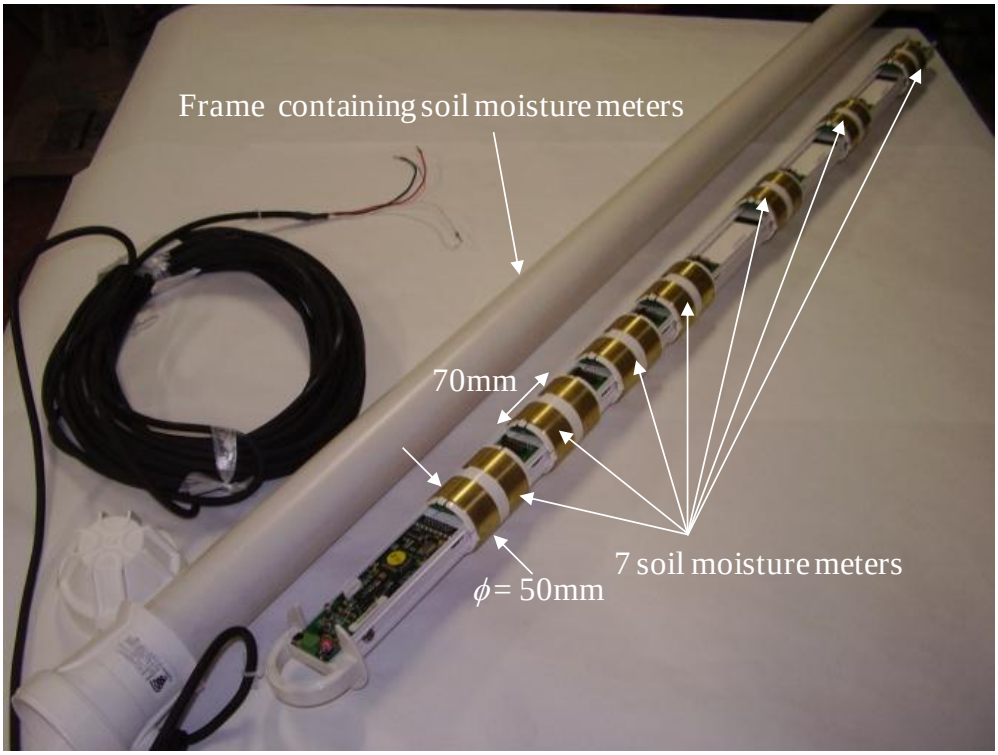

(a) Soil moisture meters

(b) Tensiometer

Photographs 4.2.6 Measurement instruments

(c) Accelerometers

(d) Thermometers for soil temperature

Photographs 4.2.6 Measurement instruments

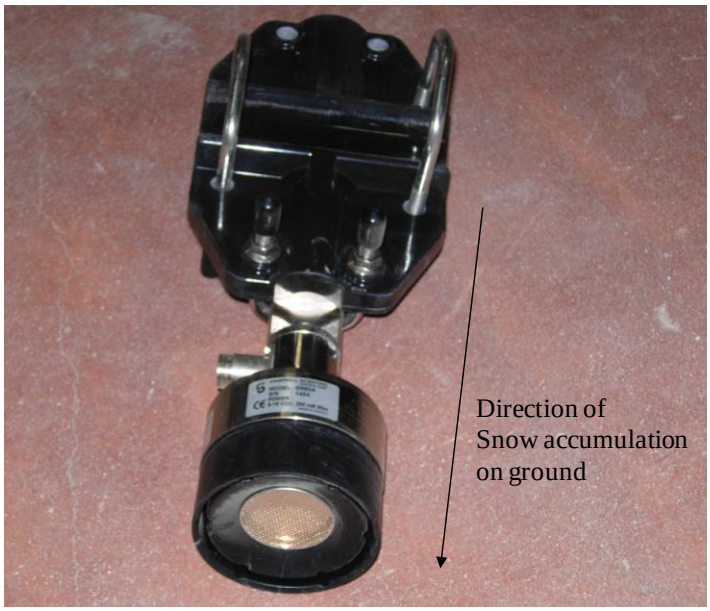

(e) Snow gauge

(f) Rainfall gauge

Photographs 4.2.6 Measurement instruments

(g) Thermometer for air temperature

Photographs 4.2.6 Measurement instruments

Table 4.2.4 Specifications of monitoring instruments

Monitoring instruments		Specifications	Brands	Models
(a)	Soil moisture meter	Precision: +/-0.003% vol., Reading range: Oven dry to saturation	Climatec, Inc.	CST-SM-Sensor-Pset-1.5
(b)	Tensiometer	Precision: +/-0.5%, Reading range: 100cmH_2O~-700cmH_2O	Climatec, Inc.	UNSUC CSK-5500AEL
(c)	Accelerometer	+/-4g, Precision: 500+/-10% (mV/G)	Microstone Co., Ltd.	MA3-04AD
(d)	Thermometer for soil temperature	Class A, +/-(0.15+0.002t)°C	Climatec, Inc.	7 depths-20
(e)	Snow gauge	Precision: +/-10mm or 0.4% FS, Reading range: 0.5 to 10m	Climatec, Inc.	C-SR50A
(f)	Rainfall gauge	Precision: +/-0.5mm, Reading range: 20mm	Climatec, Inc.	CTK-15PC
(g)	Thermometer for air temperature	Class A, +/-(0.15+0.002t)°C, radiation shield type	Climatec, Inc.	-

4.2.3 Cut slope and its monitoring

Photographs 4.2.7 (a) and (b) show the cut slope CS and its positional relation with FE-2012. The slope was cut at 45 degrees with the height controlled at 5 m as well as FE-2012. In the cut slope, the soil moisture and pore pressure were measured at the points indicated in Figure 4.2.14. The set of soil moisture meters and the tensiometer were installed at 2 and 4 meters in slope length from the top of slope, respectively, along the center section, C-section shown in the figure. They are denoted as SM-CS and T-CS, respectively. In the CS slope, as mentioned above, Soil 1 and Soil 2 shown in Photographs 4.2.2 were locally detected within the depths of 0.4 m and from 0.4 to 0.6 m, respectively, while the CS slope are mainly composed of $K_{original}$ (*see* Photographs 3.1.3). Therefore, it is considered that the physical properties of soil materials are different from that of $K_{original}$ at such depths. Accordingly, the in-situ dry densities at the depths of 0 ~ 0.4, 0.4 ~ 0.6 m and more than 0.6 m were adopted as 0.749, 0.584 and 0.840 g/cm^3 (0.749, 0.584 and 0.840 Mg/m^3) from Table 4.2.1 to calculate the water content based on Equation (4.7) from the soil moisture measurement.

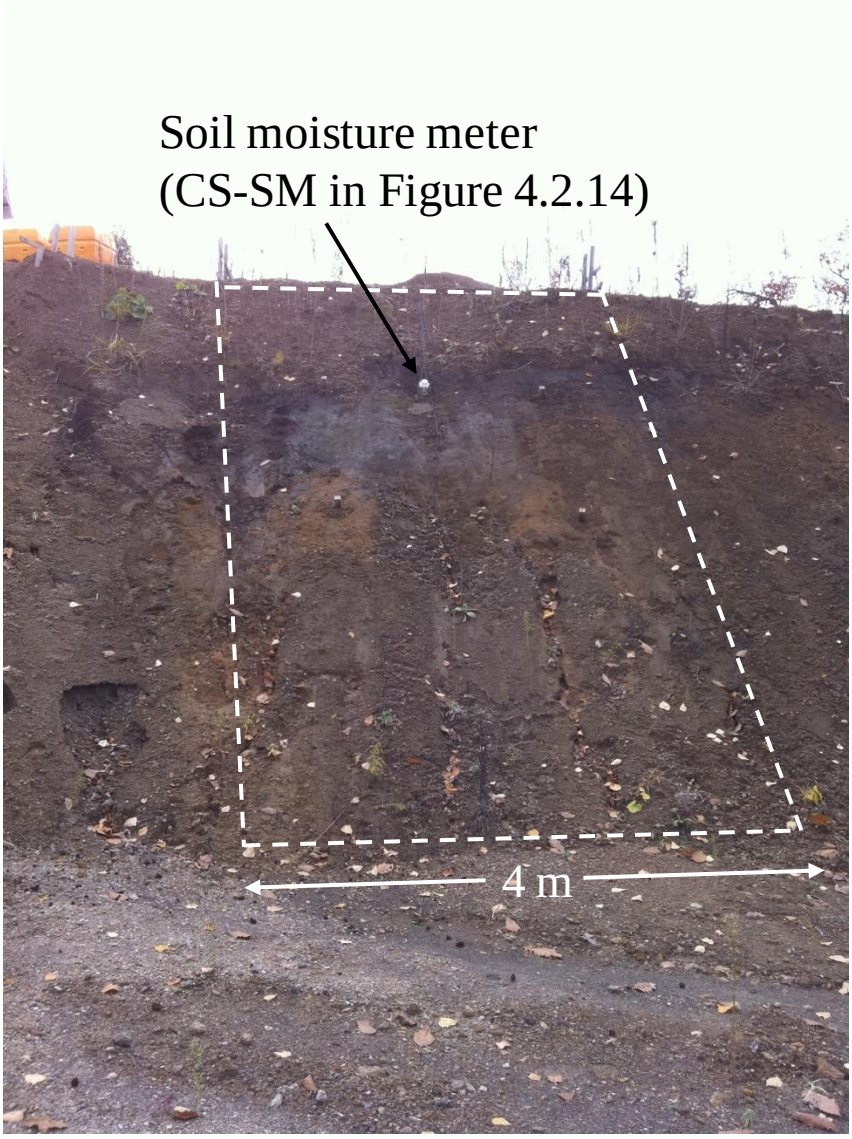

(a) Whole view

Photographs 4.2.7 Cut slope constructed in 2011, CS

(b) Positional relation of CS with FE-2012 (On 2013.11.06)

Photographs 4.2.7 Cut slope constructed in 2011, CS

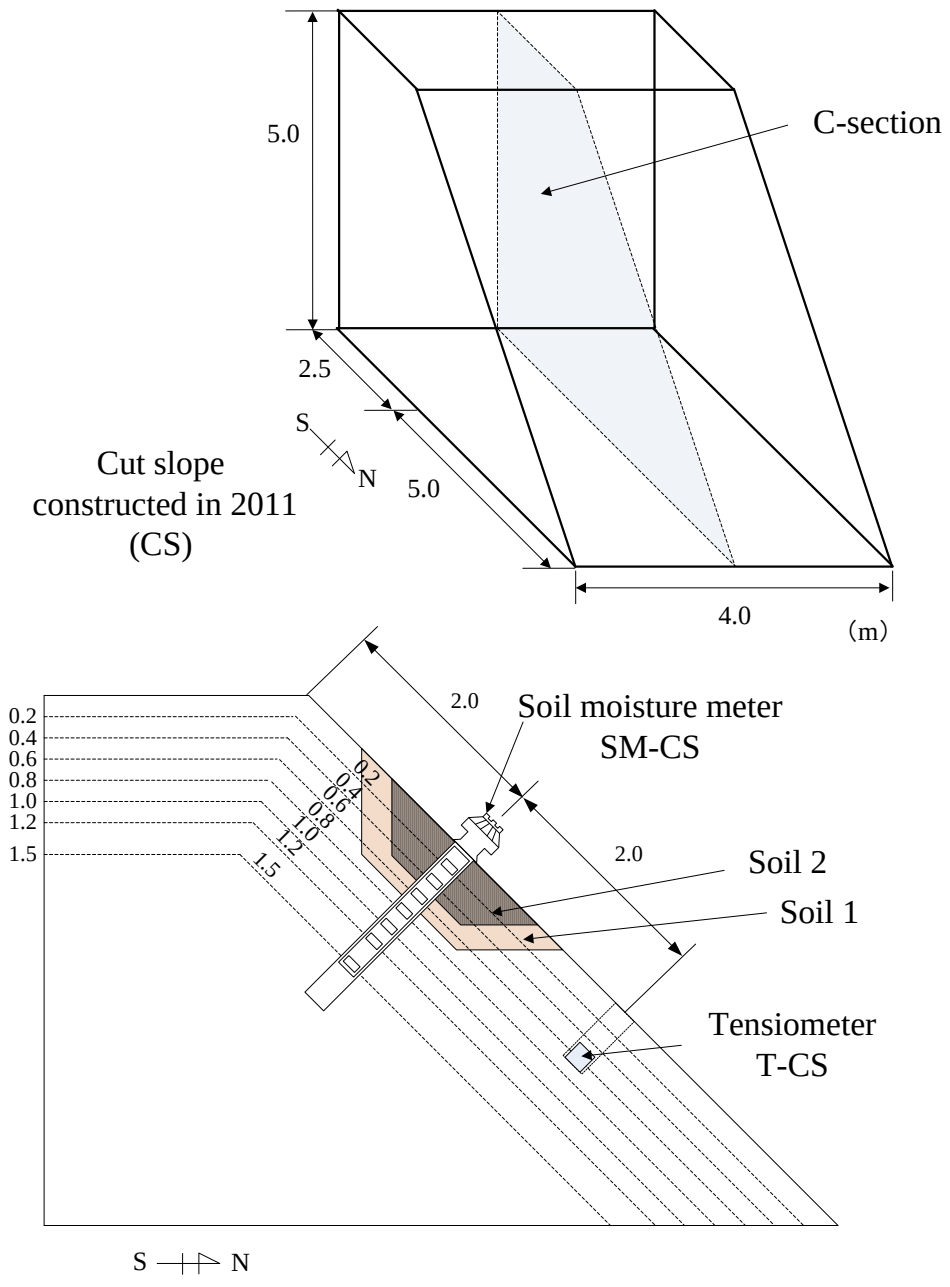

Figure 4.2.14 Arrangement of measurement instruments, and Soil 1 and Soil 2 deposited in cut slope

CHAPTER 5 TEST RESULTS AND DISCUSSIONS

5.1 Change in mechanical properties due to compaction conditions

5.1.1 Introduction

Mechanical properties of Ikeda sandy silt (I soil) and Komaoka volcanic soil (K soil) compacted under various compaction conditions will be shown in terms of cyclic shear behavior, monotonic compression shear behavior, shear modulus at small strain and hydraulic conductivity. Then, the compaction conditions were controlled based on the afore-mentioned compaction test results as indicated in Figure 5.1.1. The optimum water content w_{opt} and maximum dry density ρ_{dmax} are 25.0 % and 1.446 g/cm^3 (1.446 Mg/m^3) for I soil, and 40.5 % and 1.059 g/cm^3 (1.059 Mg/m^3) for K soil, respectively. Furthermore, in order to distinguish the compaction conditions of triaxial specimens in the same manner for both materials, the compaction plane are expressed as the relation of the water content at compaction w_i and initial dry density normalized by each w_{opt} and ρ_{dmax} as shown in Figure 5.1.2, which are denoted as w_i/w_{opt} and D_{ci}. Therefore, w_i/w_{opt} of 1.0 and D_{ci} of 100 % correspond to the optimum water content and the maximum dry density. In this study, the w_i/w_{opt} range from 0.9 to 1.1 was determined as optimum condition, while drier and wetter condition were defined by the range of w_i/w_{opt} lower than 0.9 and higher than 1.1, respectively. The classification on the basis of the water content at compaction is represented in Table 5.1.1. Figures 5.1.3 (a) ~ (d) demonstrate the compaction conditions of triaxial specimens for I soil and K soil with

regard to each laboratory element test.

In addition, Figure 5.1.4 shows the relation of dry densities between before and after saturation and consolidation for all the triaxial specimens, although the compaction condition is not classified based on w_i/w_{opt}. From the figure, the change in degree of compaction D_c (%) due to saturation and consolidation reaches 2.5 % in the shrinking side and 1.3 % in the swelling one, respectively. However, no obvious tendency can be found depending on the difference in initial degree of compaction D_{ci}. The fact is considered that change in mechanical properties due to compaction conditions discussed below should result from not saturation and consolidation procedures, but various compacted soil structures. The additional discussion will be done in *5.3 Change in mechanical properties due to finer fraction*.

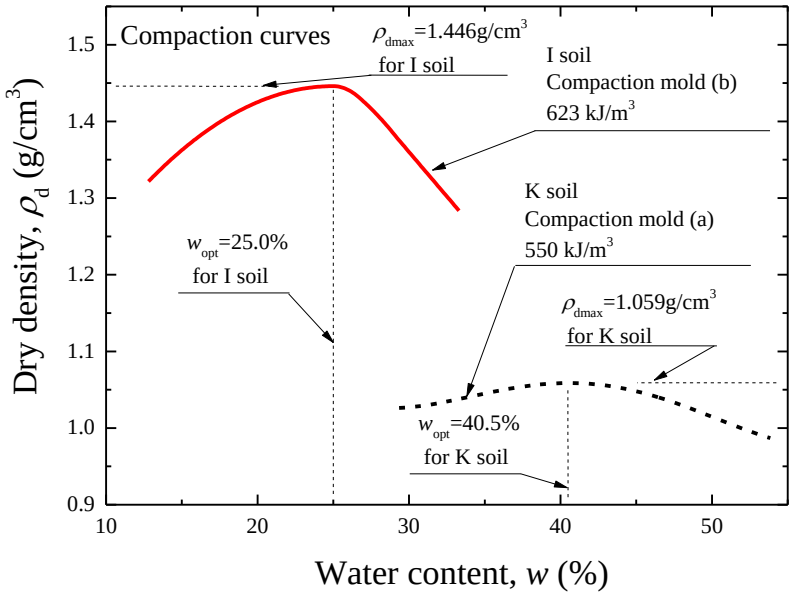

Figure 5.1.1 Compaction curves of I soil and K soil

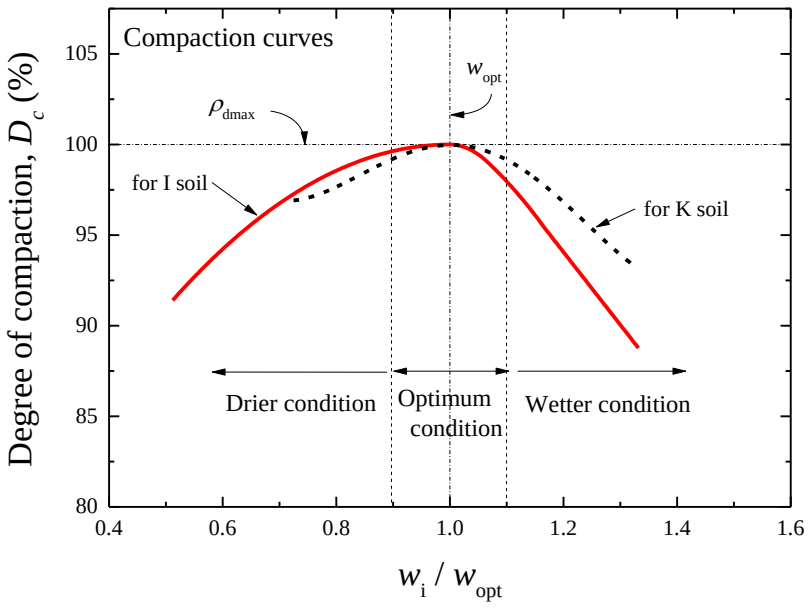

Figure 5.1.2 Compaction curves of I soil and K soil normalized by optimum conditions

Table 5.1.1 Classification of compaction condition in terms of water content at compaction

Compaction conditions	Water content at compaction
Optimum condition	$0.9 \leq w_i/w_{opt} \leq 1.1$
Drier condition	$w_i/w_{opt} < 0.9$
Wetter condition	$1.1 < w_i/w_{opt}$

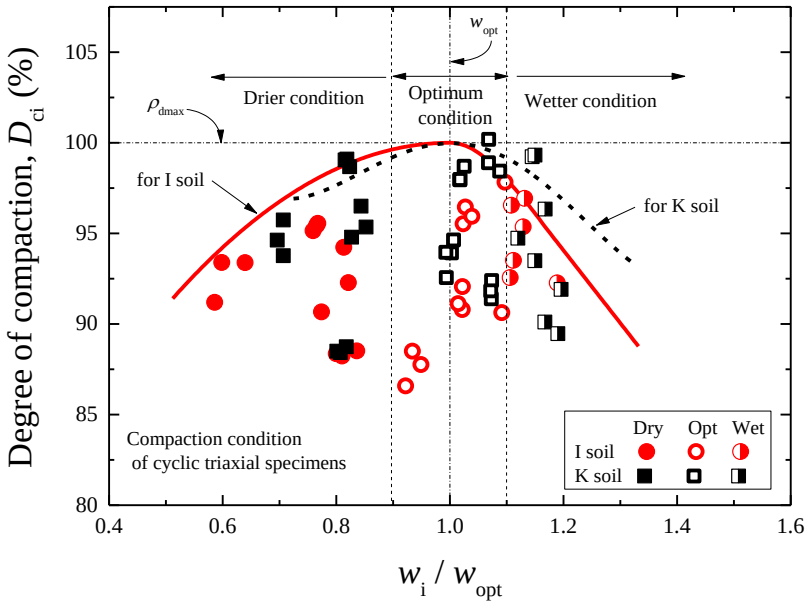

(a) Cyclic triaxial test

Figures 5.1.3 Compaction conditions of triaxial specimens for I soil and K soil

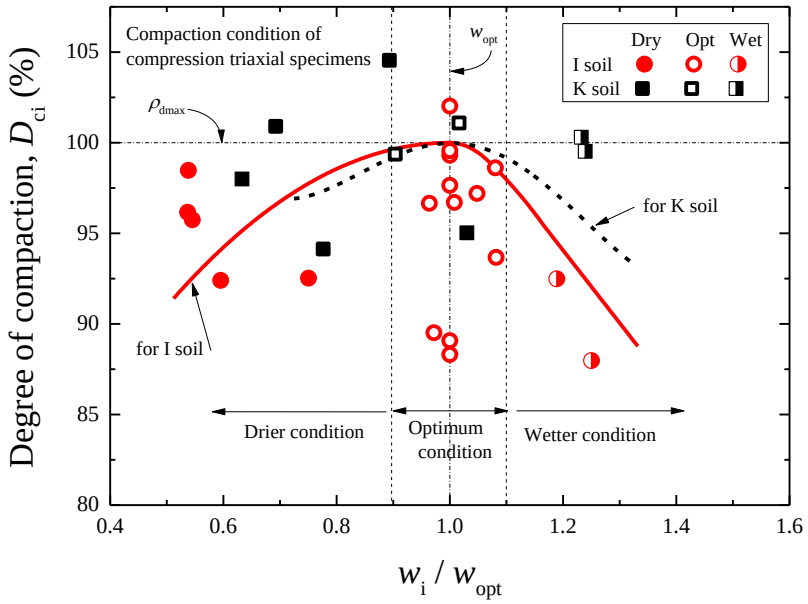

(b) Triaxial compression test

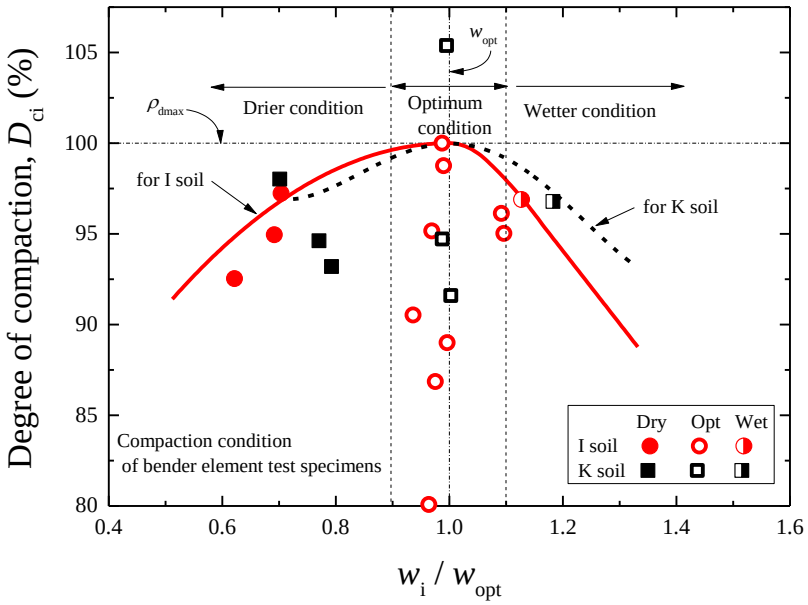

(c) Bender element test

Figures 5.1.3 Compaction conditions of triaxial specimens for I soil and K soil

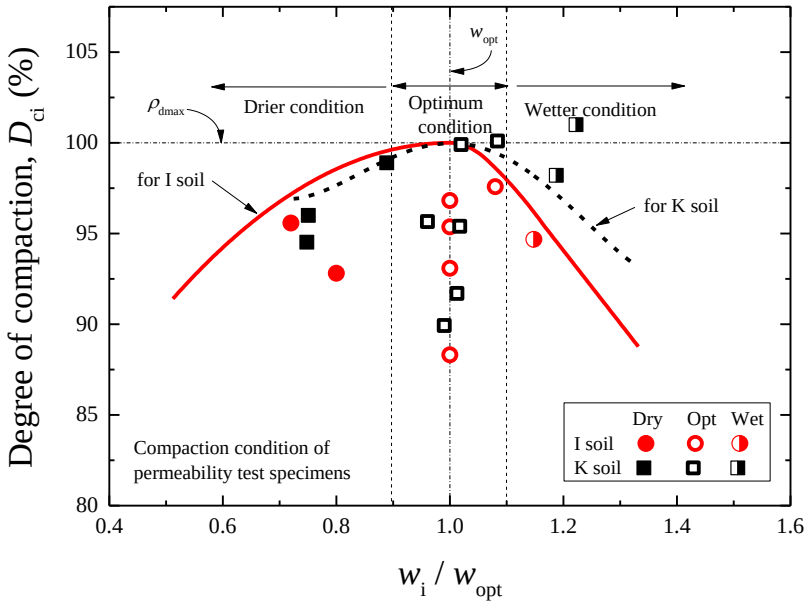

(d) Permeability test

Figures 5.1.3 Compaction conditions of triaxial specimens for I soil and K soil

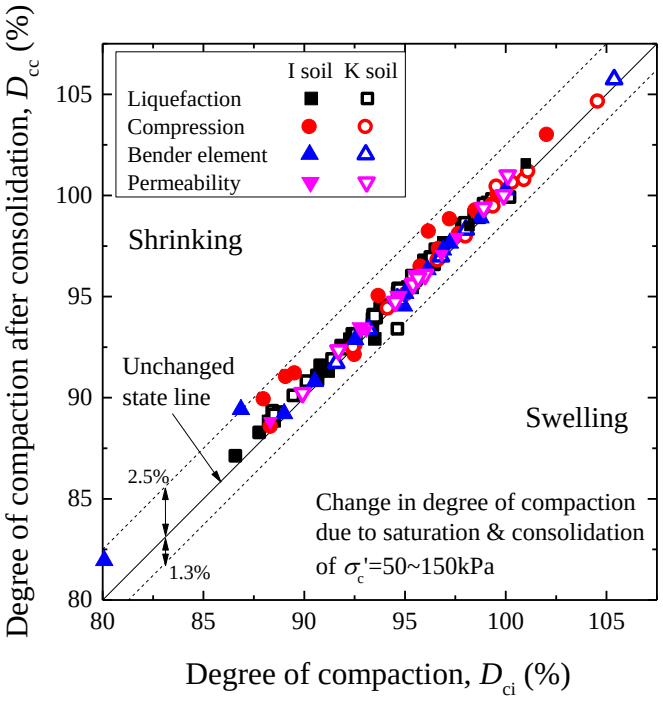

Figure 5.1.4 Change in degree of compaction (dry density) due to saturation and consolidation of triaxial specimens for I soil and K soil

5.1.2 Cyclic strength-deformation properties

Figures 5.1.5 (a) and (b) show the time histories of axial strain ε_a (%) and excess pore water pressure Δu normalized by the effective consolidation stress σ_c' during cyclic loading for I soil, respectively. The specimens were compacted at different water contents w_i/w_{opt} of 0.82 to 1.19, and applied cyclic loads with cyclic stress ratios *SR* of 0.31 to 0.32 at degrees of compaction after consolidation D_{cc} of 91.4 to 92.9 %, respectively. Then, the cyclic stress ratio *SR* is calculated by $\sigma_d/2\sigma_c$'. The cyclic loading continued until double amplitude axial strain *DA* achieved 10 %, which is equal to the summation of both compression and extension strains. From the figures, it is obvious that the molding water content w_i/w_{opt} can significantly affect the cyclic strength, and the cyclic deformation tends to rapidly evolve with w_i/w_{opt} higher even under the similar D_{cc} and *SR* conditions. On the other hand, in terms of the excess pore water pressure (Δu) behavior, the specimen compacted wet of the optimum raises Δu at a higher rate, and leads to liquefaction. Such behavior reduces with w_i/w_{opt} lower, and the excess pore water pressure can very gently rise in the specimen compacted dry of the optimum compared with the above.

The above behavior of I soil is basically consistent with the testing results of K soil as shown in Figures 5.1.6 (a) and (b). The K soil specimens compacted at D_{cc} of about 99 % were also cyclically sheared with the similar *SR* of 0.32. Focusing on the number of loading cycles N_c before *DA* = 5 % as illustrated in Figure 5.1.6 (a), it can be recognized that the increase in molding water content triggers the cyclic strength deterioration. However, the wetter condition does not necessarily cause cyclic strength of K soil to decrease when permitting the larger strain of 10 % in *DA*. The fact is considered to result from the cyclic mobility phenomenon that tends to occur in a dense sand, and change in deformation behavior depending on the molding water content, which will be discussed below again. From Figure 5.1.6 (b), the excess pore water pressure Δu seems to come close to the effective confining stress σ_c' at N_c of about 10 under the wetter condition. On the other

hand, the same behavior as Δu reaches σ_c' appears over 20 to 30 cycles of loads in the specimens compacted at the lower water content. Thus, the soil compacted at higher molding water content is prone to stronger negative dilatancy due to cyclic shearing, and accordingly the cyclic strength can reduce to a significant extent.

In order to examine the difference in cyclic deformation as mentioned above, Figures 5.1.7 and 5.1.8 indicate the N_c-DA relations for I soil and K soil, respectively. Note that the number of loading cycles N_c and double amplitude axial strain DA are divided by each value at DA = 10 %. The specimens shown in the figures are the same as the ones in Figures 5.1.5 and 5.1.6, except the specimen at w_i/w_{opt} of 0.64 additionally included in Figure 5.1.7. According to both figures, a similar trend could be found; i.e., the cyclic deformation behavior varies related to the molding water content in the same manner. The drier condition shows that little strain occurs at the beginning of loading, but then the cyclic deformation rapidly develops to failure at a specific inflection point. In contrast, the specimen tends to evolve the cyclic deformation at a relatively-constant rate under the wetter condition. The fact seems to reflect the difference of dilatancy behavior, and the specimen compacted at higher molding water content can remarkably develop the cyclic deformation from the beginning of loading with the excess pore water pressure increasing at a higher rate.

Figures 5.1.9 and 5.1.10 demonstrate the relationships between the cyclic stress ratio SR and number of loading cycles N_c to cause the double amplitude axial strain DA of 5 % for I soil and K soil, respectively. Each average of water content at compaction w_i and degree of compaction after consolidation D_{cc} shown in the figures were calculated from the w_i and D_{cc} values of three or four specimens to draw a liquefaction curve. The cyclic shear strength SR_{20} discussed below are examined on the basis of the SR values to achieve DA = 5 % at N_c of 20 obtained from the liquefaction curves in Figures 5.1.9 and 5.1.10.

Figure 5.1.11 represents the D_{cc}-SR_{20} relations of I soil and K soil with regard to the compaction

conditions for molding water content. First, from the results of I soil, it is clear that the cyclic strength SR_{20} significantly increases with the degree of compaction higher. Furthermore, such behavior becomes remarkable under the drier condition, while little strength increase can be observed under the wetter condition. In addition, the critical influence of the molding water content on the cyclic strength could be definitely recognized even though the compacted specimens have the same dry density after consolidation. That is, the highest cyclic strength appears in the drier compaction condition, and the cyclic strength tends to reduce with the specimens compacted at higher water content. On the other hand, the cyclic strength behavior of I soil fundamentally agrees well with that of K soil. In the case of K soil, the molding water content effect seems to become obvious over the degree of compaction of 95 %. Thus, it could be understood that the cyclic strength SR_{20} of compacted soils is susceptible not only to the density index but also to the water content at compaction, in particular with the soil compacted more densely.

For the purpose to evaluate the cyclic strength increase behavior related to the compaction conditions, Figure 5.1.12 demonstrates each SR_{20} value divided by SR_{20} at D_{cc} = 90 % and the optimum condition. According to the left figure to show the relation with the degree of compaction after consolidation D_{cc}, the SR_{20} value at D_{cc} of 100 % increases double as higher as that at D_{cc} of 90 % under the optimum condition. Moreover, the trend is almost the same for both I soil and K soil as shown in the figure. However, it is also clear that the strength increase due to the increment of D_{cc} can be affected by the water content at compaction. Then, from the relations with the molding water content, little increase in the cyclic strength due to D_{cc} is found at the w_i/w_{opt} value of 1.2 equal to the wetter condition, while the D_{cc} effect on the cyclic strength becomes remarkable at the drier condition. On the basis of the above results of the cyclic triaxial tests for both I soil and K soil, it could be concluded that the peak cyclic strength appears at the drier water content of w_{opt}, and the cyclic strength tends to reduce and converge to a similar strength value at w_i/w_{opt} of around 1.2

regardless of dense or loose soils.

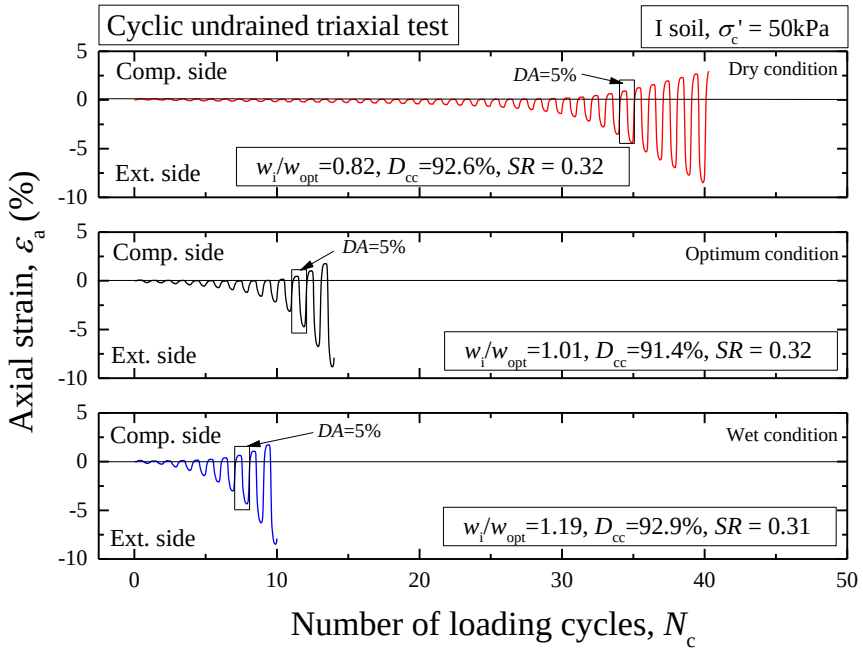

Figure 5.1.5 (a) Time histories of axial strain on cyclic triaxial test under various molding water content conditions for I soil

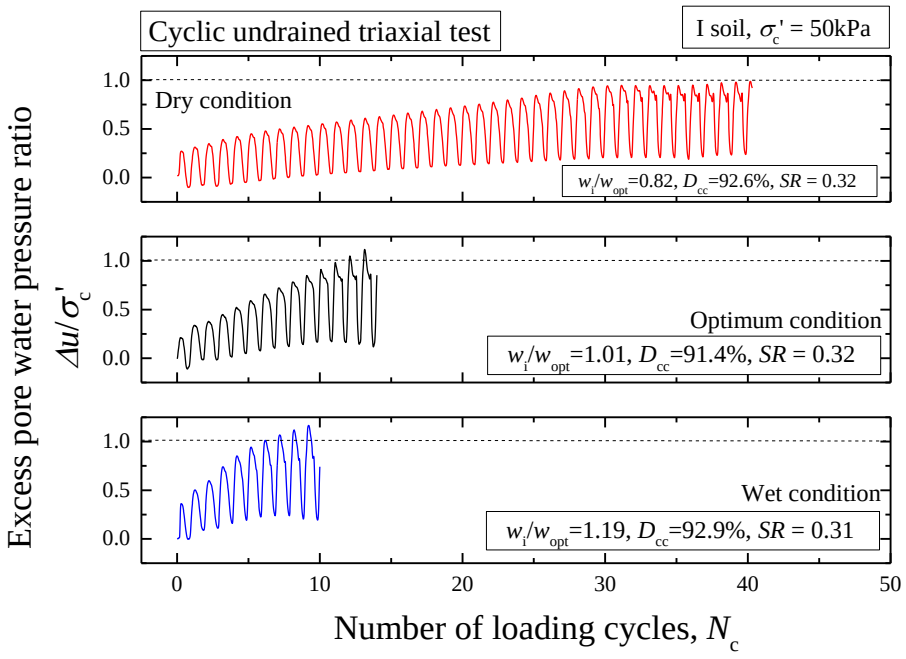

Figure 5.1.5 (b) Time histories of excess pore water pressure on cyclic triaxial test under various molding water content conditions for I soil

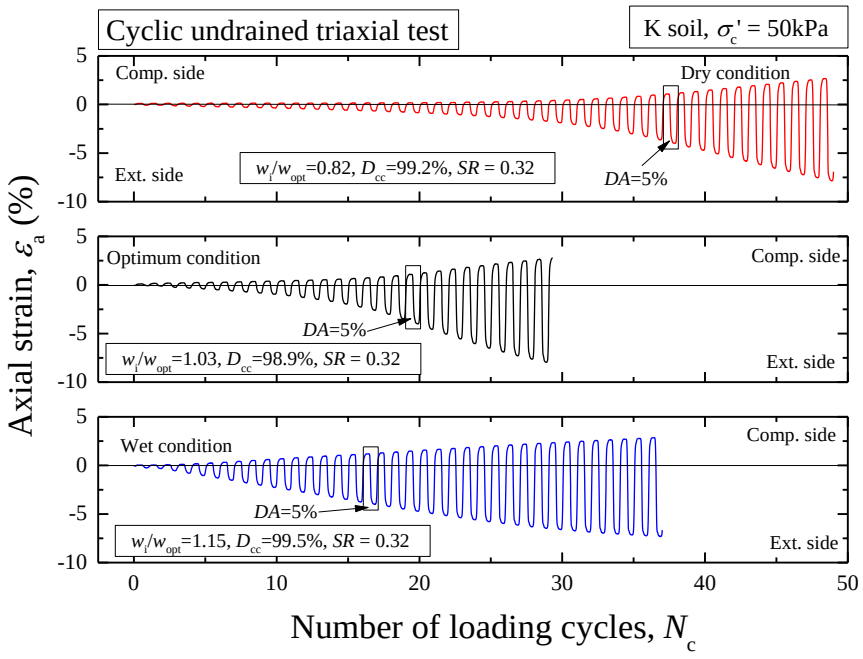

Figure 5.1.6 (a) Time histories of axial strain on cyclic triaxial test under various molding water content conditions for K soil

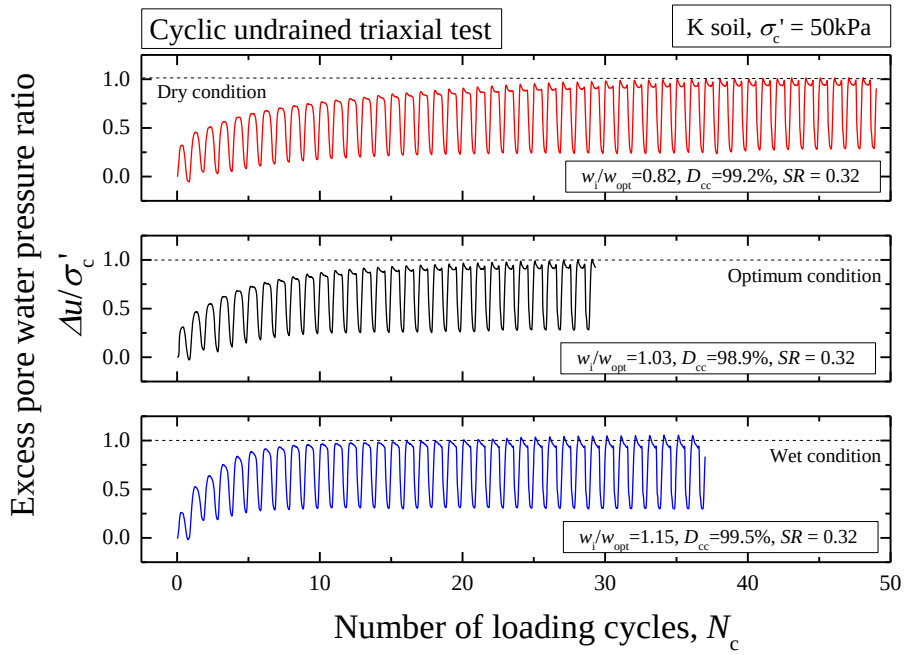

Figure 5.1.6 (b) Time histories of excess pore water pressure on cyclic triaxial test under various molding water content conditions for K soil

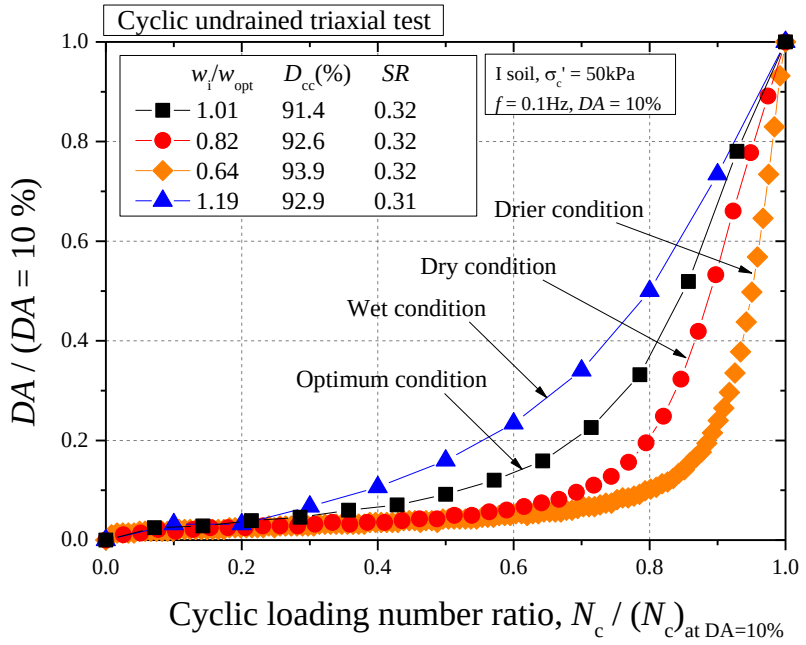

Figure 5.1.7 N_c-*DA* relation under various molding water content conditions for I soil

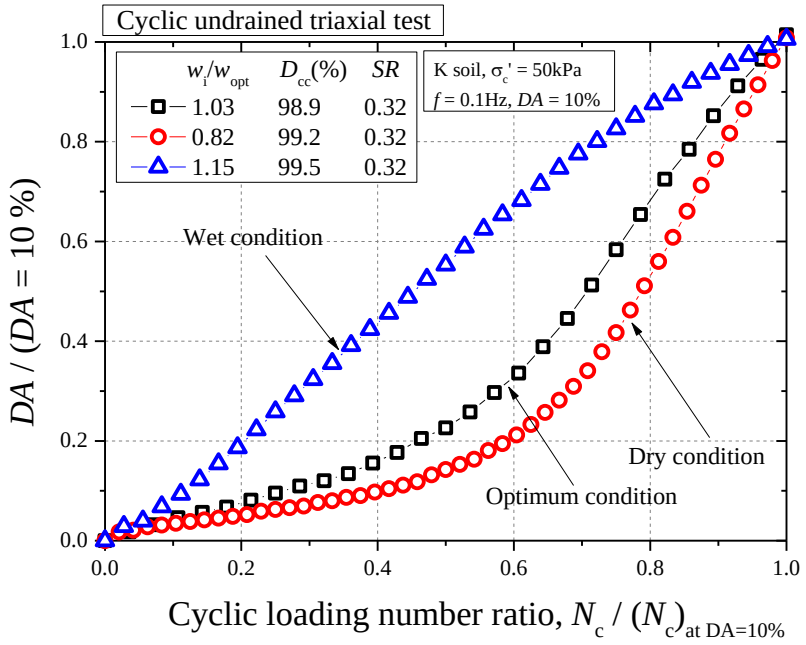

Figure 5.1.8 N_c-*DA* relation under various molding water content conditions for K soil

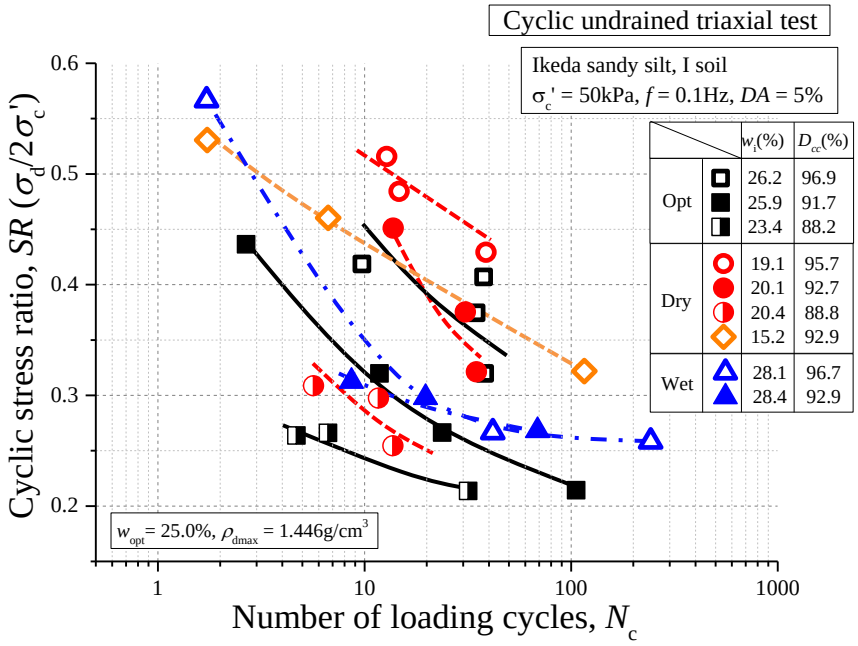

Figure 5.1.9 Liquefaction curves under various compaction conditions: N_c-DA relation to cause DA = 5% for I soil

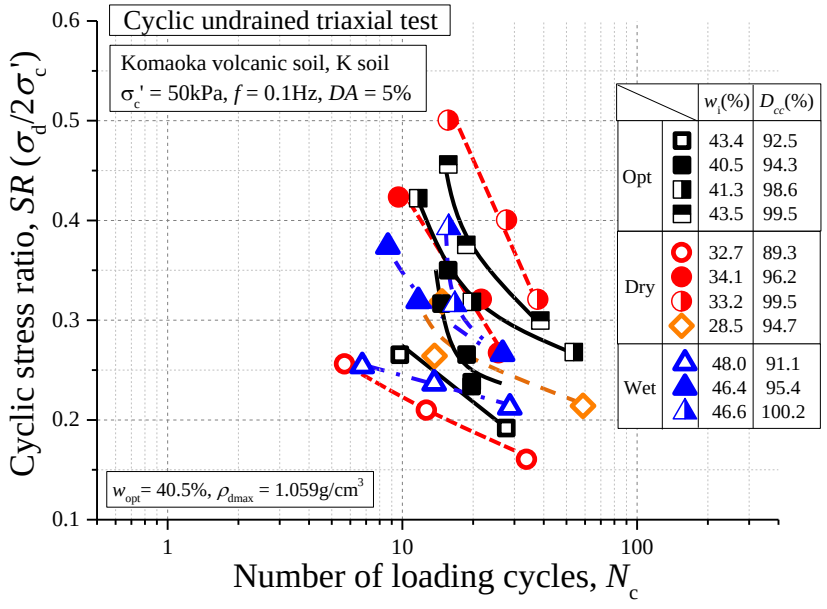

Figure 5.1.10 Liquefaction curves under various compaction conditions: N_c-DA relation to cause DA = 5% for K soil

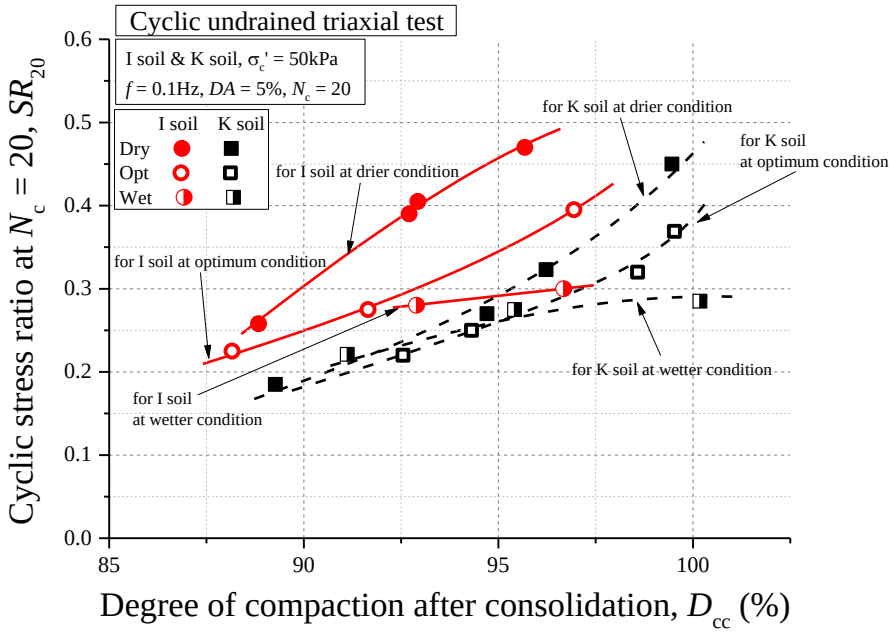

Figure 5.1.11 D_{cc} - SR_{20} relations for I soil and K soil

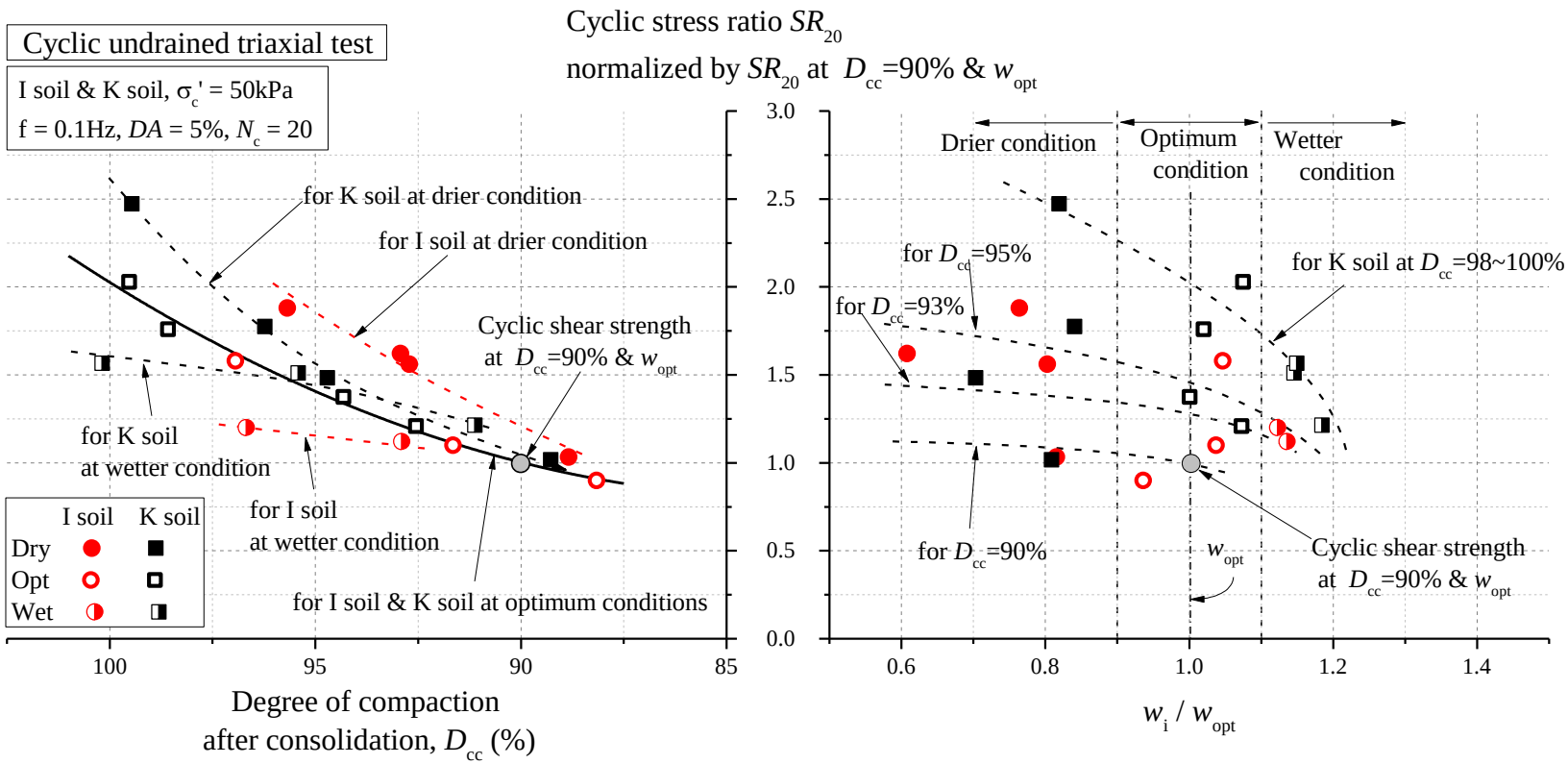

Figure 5.1.12 Relations of D_{cc} and w_i/w_{opt} with SR_{20} normalized by SR_{20} at D_{cc} = 90% and optimum conditions for I soil and K soil

5.1.3 Triaxial compression properties

In this section, the influences of the molding water content, degree of compaction and effective consolidation stress on the monotonic compression behavior of I soil and K soil will be elaborated. The compression tests were conducted under the undrained condition, which corresponded to CU test. First, Figures 5.1.13 (a) and (b) show the relations of axial stress and excess pore water pressure with axial strain and the effective stress paths for I soil to observe the effect of the molding water content. The specimens were compacted at similar D_{cc} within 88.6 to 92.4 %, and consolidated under σ_c' of 50 kPa. From the stress-strain relations, it is obvious that the specimens with the various water contents at compaction behave in different ways. Especially, the specimens of the drier and optimum conditions show the strain softening behavior, while that of the wetter condition represents the increase in the shear strength until the end of testing, i.e., the strain hardening behavior. Furthermore, within the axial strain less than 5 %, the excess pore water pressure tends to increase more significantly at higher molding water content condition. Accordingly, in Figure 5.1.13 (b), the specimen of the wetter condition shows the drastic decrease in the effective mean principal stress p', compared with those of the optimum and the drier conditions. Afterwards, however, the specimen compacted wet of the optimum exerts the higher shear strength with the strong swelling behavior to reach failure. On the other hand, both of optimum and drier conditions turn the shrinking effective stress paths. Such differences in the dilatancy behavior attributed to the effect of molding water content can be also confirmed in the results of K soil in Figures 5.1.14 (a) and (b). In the figures, those specimens were compacted at the comparatively-high degree of compaction of 96.8 to 100.8 % and consolidated at 50 kPa. From the figures, the specimen of the wetter condition causes the higher negative dilatancy at the beginning of loading, but shifts to the strongest swelling behavior with the strain hardening. In contrast, the specimens of the optimum and drier conditions tend to reach

the peak shear strength at the comparatively-small strain level with the negative excess pore water pressure behavior. The difference of dilatancy behavior at the smaller strain level is likely to be closely related with the results of the cyclic shear behavior discussed in *5.1.2*. That is, it could be understood that the specimen compacted wet of the optimum that represents the strong negative dilatancy at the beginning of monotonic compression, has the lower strength in the liquefaction procedure where the positive excess pore water pressure accumulates. Furthermore, because the positive dilatancy behavior conversely becomes remarkable with the axial strain ε_a largely developing, the specimen of the wetter condition is considered to exert the stronger cyclic shear resistance at *DA* of 5 to 10 % than those of the drier and optimum conditions as shown in Figure 5.1.6 (a).

Next, Figures 5.1.15 (a) and (b) illustrate the stress-strain curves and excess pore water pressure behavior, and the effective stress paths for I soil to discuss the effect of degree of compaction at the similar molding water content and effective consolidation stress. According to the stress-strain relation, it is seen that the increase in the degree of compaction D_{cc} leads to the critical strength increment, and then the peak shear strength can be exerted five times with D_{cc} increased from 88.6 to 99.6 %. Moreover, the excess pore water pressures Δu of the specimens with D_{cc} of 96.9 and 99.6 % shift to the negative values with the axial strain developing, while the specimens loosely compacted at D_{cc} of 88.6 % keeps the positive Δu value. The difference of Δu tendency is definitely realized on each effective stress path as shown in Figure 5.1.15 (b). That is, the densely-compacted specimens indicate the strong dilative behavior in contrast to the shrinking loose soil.

The influence of effective consolidation stress σ_c' on the shear behavior of I soil is shown in Figures 5.1.16 (a) and (b). The specimens compacted at the relatively-higher or lower degree compaction and the similar optimum water content condition were consolidated with σ_c' of 50, 100 or 150 kPa. From Figure 5.1.16 (a), it could be recognized that the shear strength of compacted I soil increases with the increment of σ_c' when comparing in each set of similar degree of compaction. On

the other hand, the excess pore water pressure (Δu) behavior during shearing tends to vary depending on the degree of compaction D_{cc}. In the set of the specimens densely compacted, it can be seen that the positive Δu behavior turns negative with the strong dilative behavior regardless of σ_c'. However, the three specimens loosely compacted indicate the similar Δu tendency in terms of that the Δu behavior is kept positive, throughout. Such difference in the Δu behavior resulting from the degree of compaction appears in Figure 5.1.16 (b) as well. In the figure, the compacted I soil specimens with lower D_{cc} show the shrinking behavior regardless of σ_c', while the ones with higher D_{cc} are prone to the dilative behavior in each case. According to those results, it is understood that the degree of compaction can be the critical influential factor on the shear behavior of the compacted I soil, compared with the effective consolidation stress σ_c', within σ_c' less than 150 kPa.

Figures 5.1.17 and 5.1.18 demonstrate the relation of the peak shear strength q_{max} with the degree of compaction D_{cc} and molding water content w_i/w_{opt} of I soil and K soil, respectively. Then, the q_{max} value is defined as the maximum of deviator stress appearing at the axial strain ε_a less than 15 %. From the results of I soil, it is apparent that the increase in D_{cc} can lead to the drastic increase of q_{max} under the optimum condition. Furthermore, although the testing results of K soil are more limited, the q_{max} values are considered to increase with D_{cc} higher as shown in Figure 5.1.18. According to some codes to specify the compaction control (e.g., Japan Road Association 2010), in general, the shear strength increase expected by compacting more densely over 90 % in degree of compaction tends to be not taken into account for the embankment stability. However, in the present study, the increase of the shear strength becomes remarkable with D_{cc} higher than 90 %. On the other hand, in terms of the molding water content, the q_{max} values tend to increase with the specimens compacted at wetter water content from each right side of the figures. The tendency on the effect of water content at compaction on the monotonic shear strength has the inverse relation with that on the cyclic strength shown in Figure 5.1.12. The fact is supposed to result from the difference of dilatancy behavior in

each test as mentioned above. That is, unlike the liquefaction phenomenon where the specimen causes the failure due to the accumulation of the positive excess pore water pressure Δu, the monotonic shear strength can be increased by the negative Δu, which corresponds to the positive dilatancy, during the undrained compression shearing. Because, in particular, the positive dilatancy became remarkable at ε_a less than 15 % under the wetter condition of compaction as discussed in Figures 5.1.13 and 5.1.14, it could be interpreted that the higher molding water content led to higher q_{max} by 15 % in ε_a.

Figure 5.1.19 indicates the relations of D_{cc} and w_i/w_{opt} with the axial strain at failure where the peak shear strength q_{max} appears, which is referred to as ε_{af} (%), for I soil and K soil. From the figure, it is seen that the ε_{af} value significantly increases with D_{cc} higher under the optimum condition. This is attributed to the stronger swelling behavior caused with the specimen compacted more densely as shown in Figures 5.1.15. In addition, the difference of ε_{af} depending on the molding water content appears, and it can be recognized that the specimens represent the higher ε_{af} values with w_i/w_{opt} increasing. Thus, because the axial strain to exert the peak shear strength can remarkably vary in each compaction condition, the shear strength of compacted soils must be determined based on the relation between an acceptable strain for every embankments and the compaction conditions.

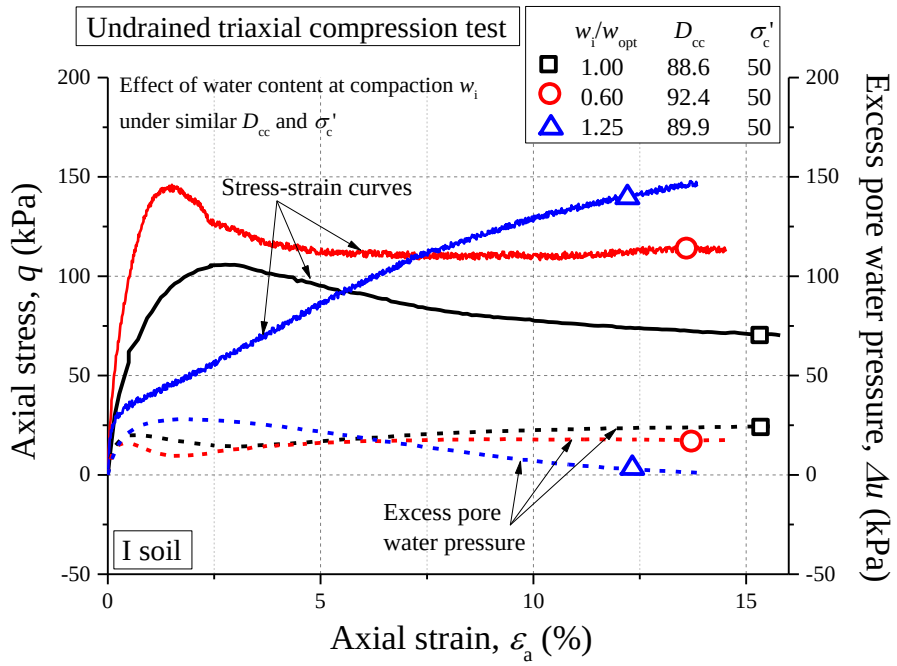

(a) Stress-strain and Δu-strain relations

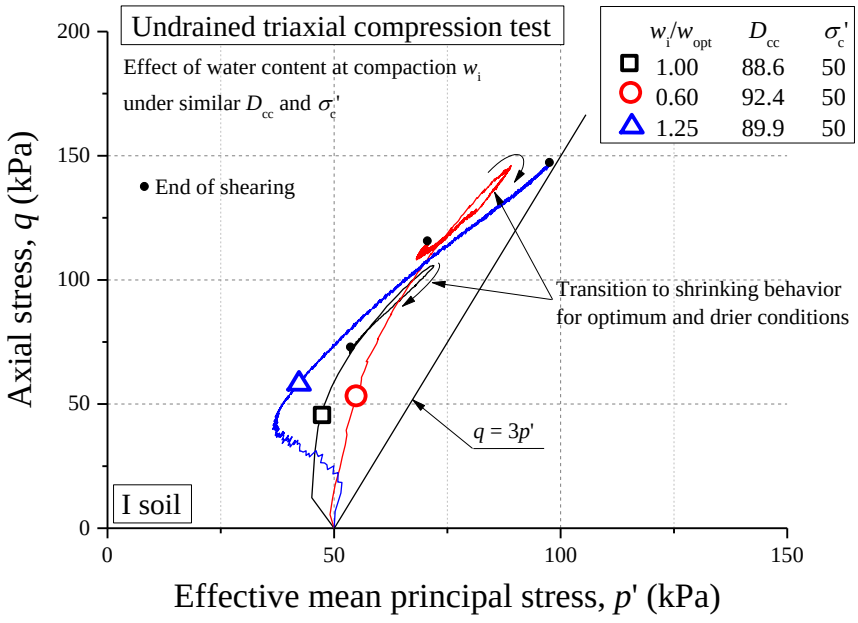

(b) Effective stress paths

Figures 5.1.13 Triaxial compression test results at different w_i/w_{opt} under similar D_{cc} and σ_c' conditions for I soil

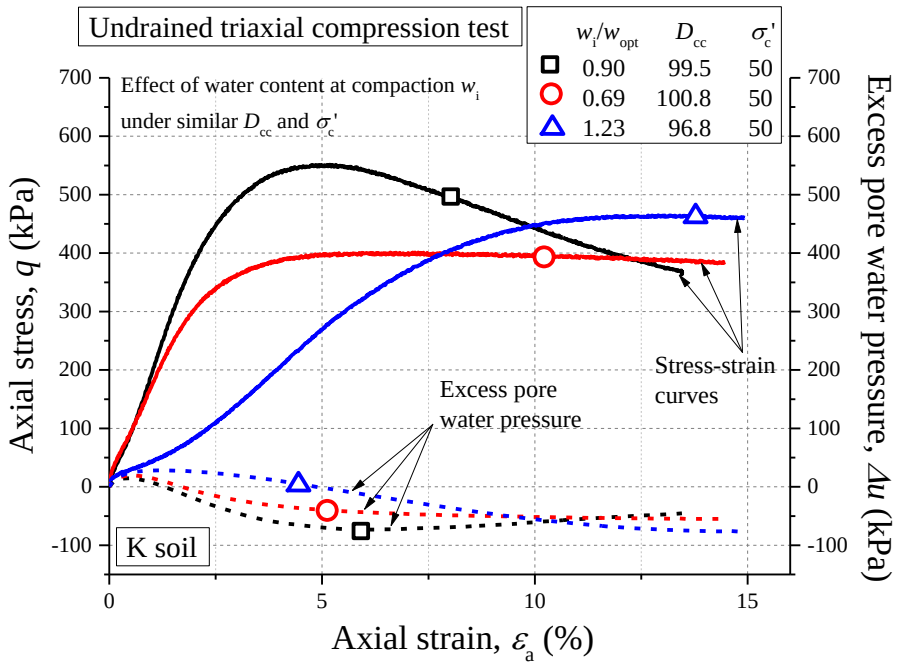

(a) Stress-strain and Δu-strain relations

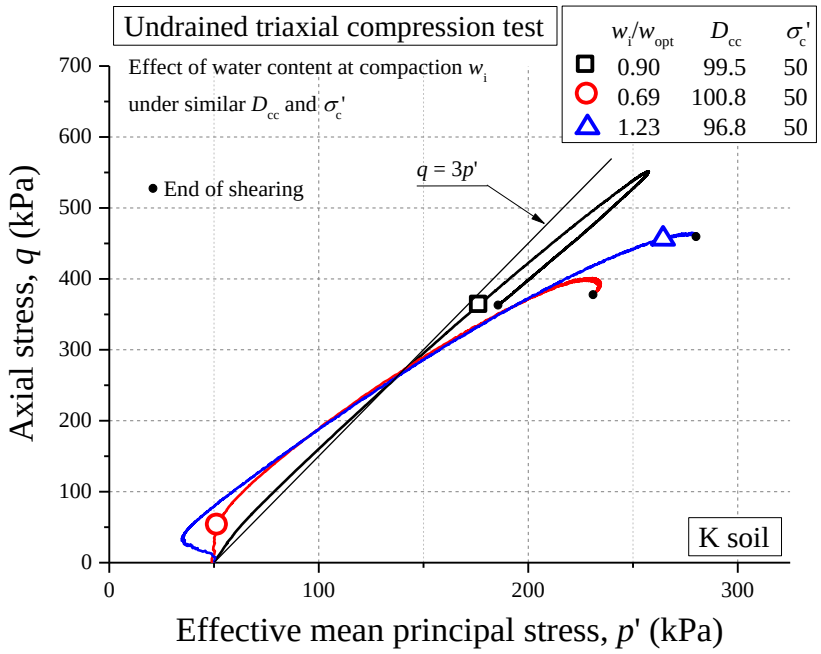

(b) Effective stress paths

Figures 5.1.14 Triaxial compression test results at different w_i/w_{opt} under similar D_{cc} and σ_c' conditions on for K soil

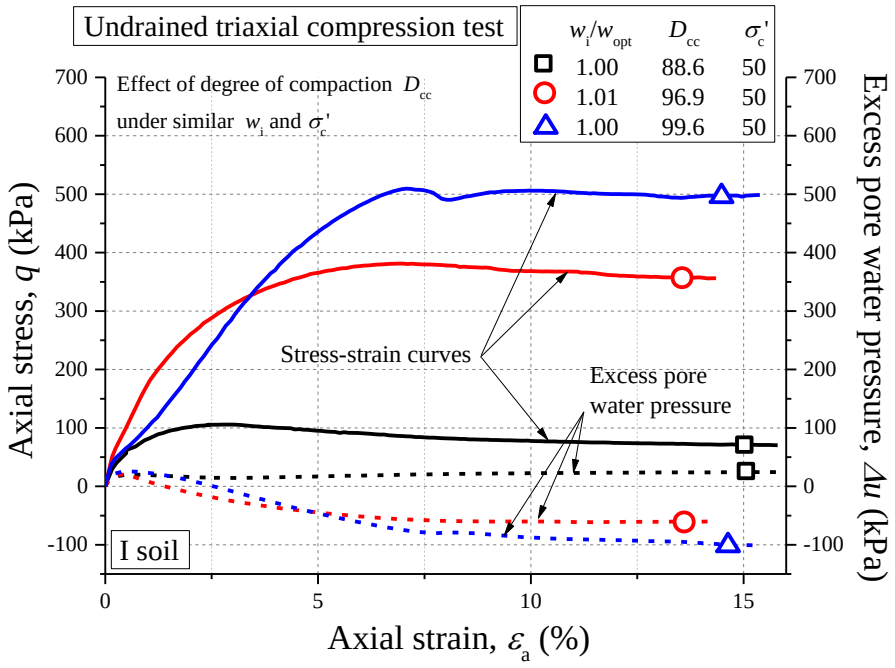

(a) Stress-strain and Δu-strain relations

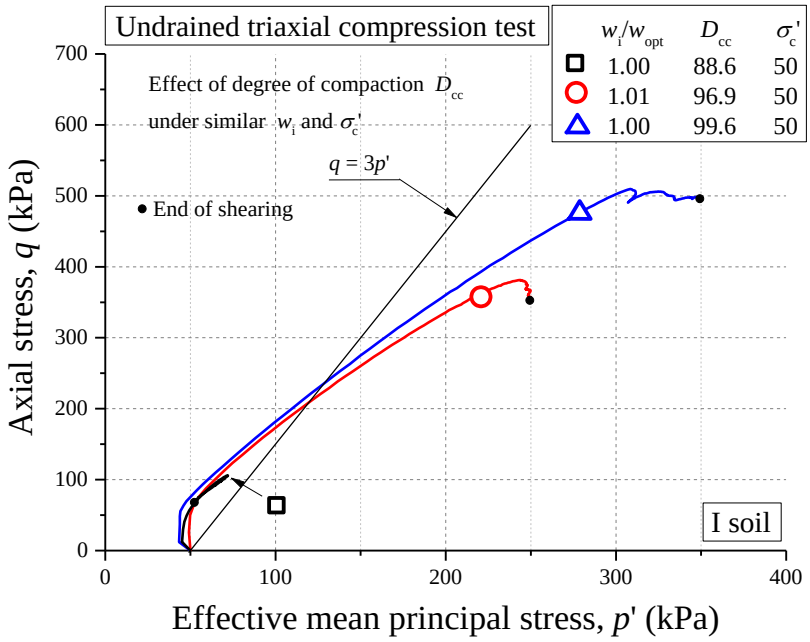

(b) Effective stress paths

Figures 5.1.15 Triaxial compression test results at different D_{cc} under similar w_i/w_{opt} and σ_c' conditions for I soil

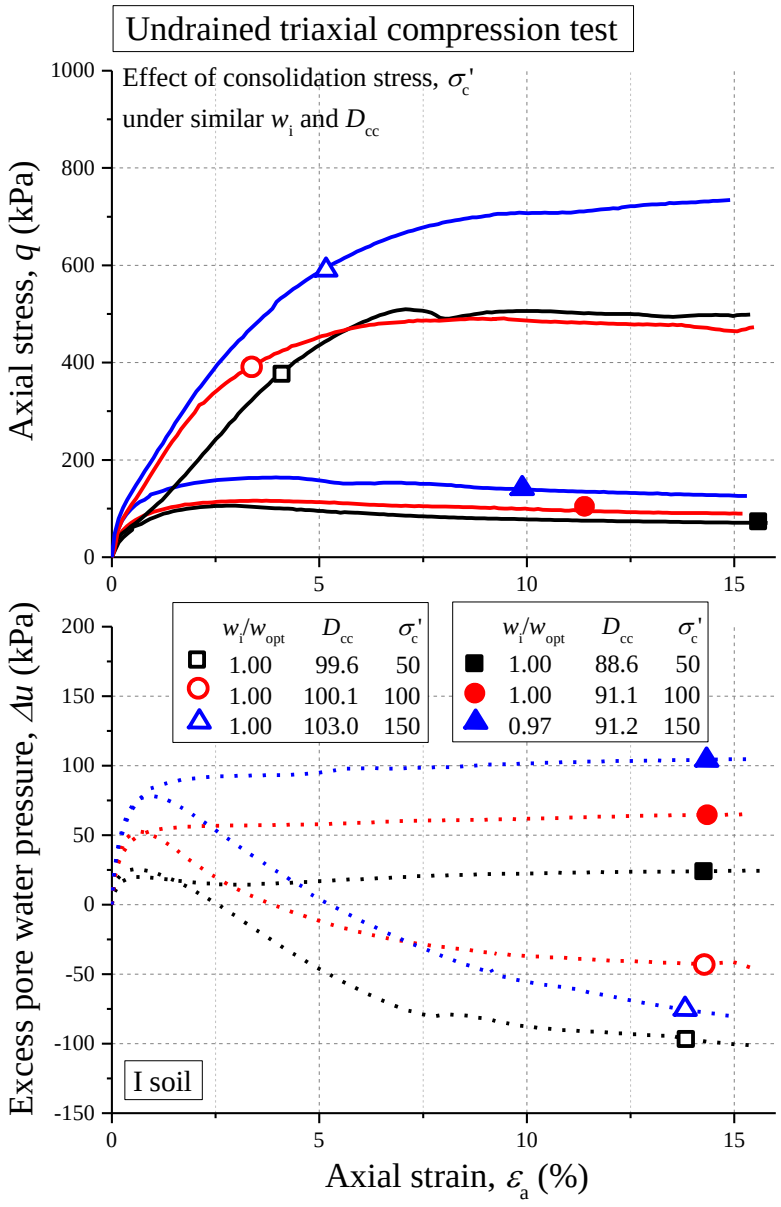

(a) Stress-strain and Δu-strain relations

Figures 5.1.16 Triaxial compression test results at different σ_c' under similar w_i/w_{opt} and D_{cc} conditions for I soil

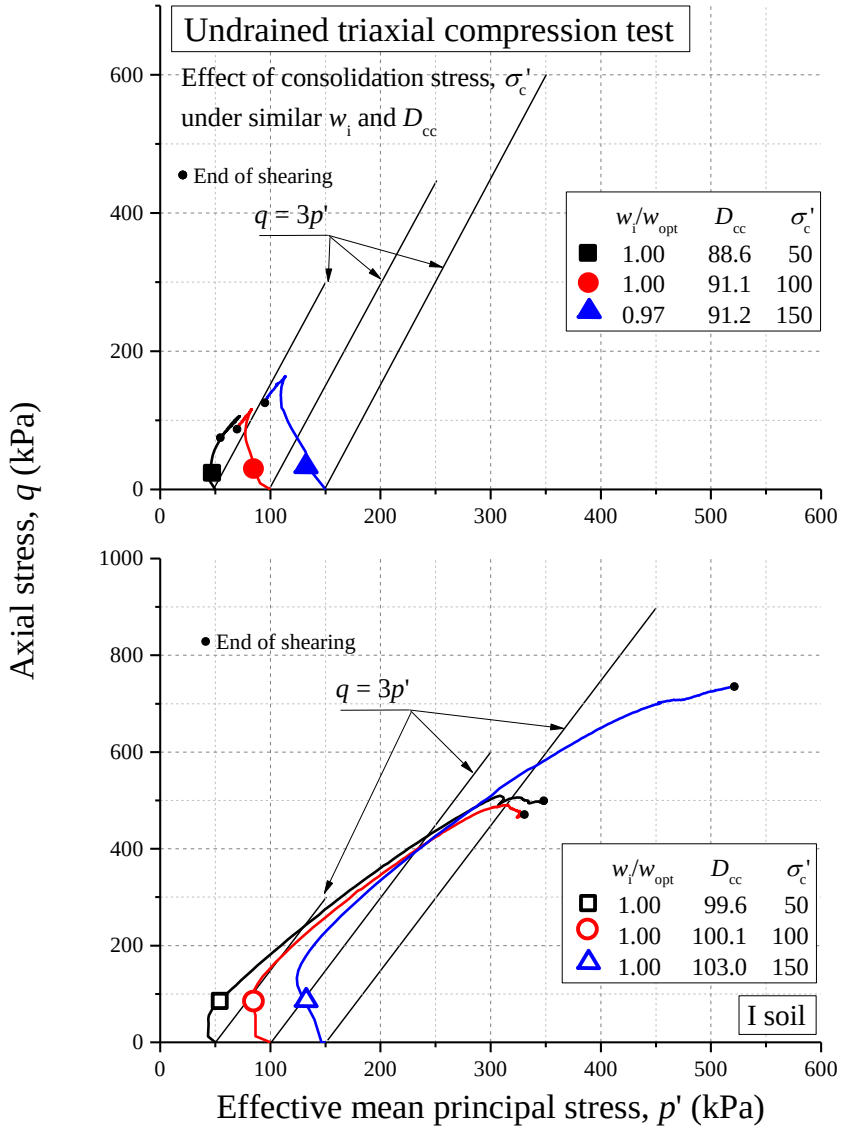

(b) Effective stress paths

Figures 5.1.16 Triaxial compression test results at different σ_c' under similar w_i/w_{opt} and D_{cc} conditions for I soil

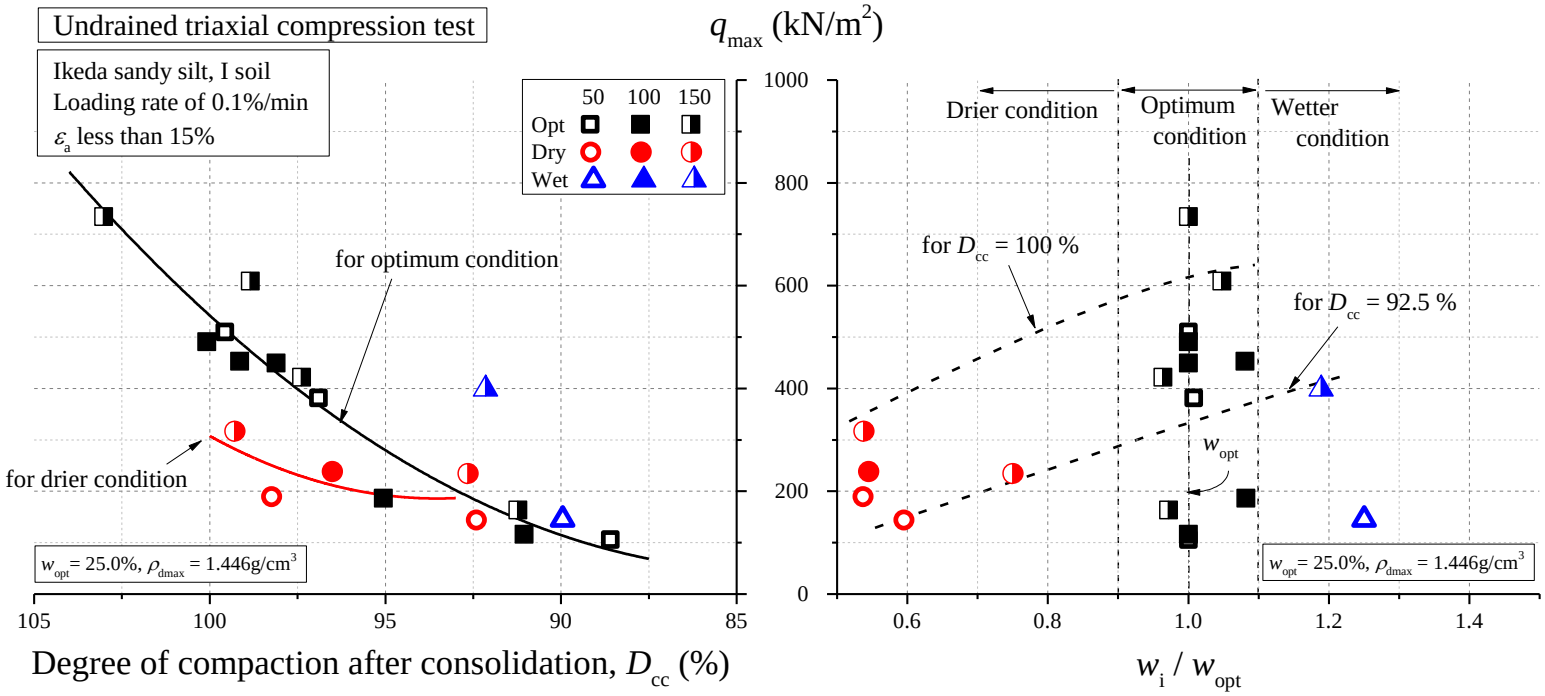

Figure 5.1.17 q_{max}-D_{cc} and -w_i /w_{opt} relations under various compaction and consolidation conditions for I soil

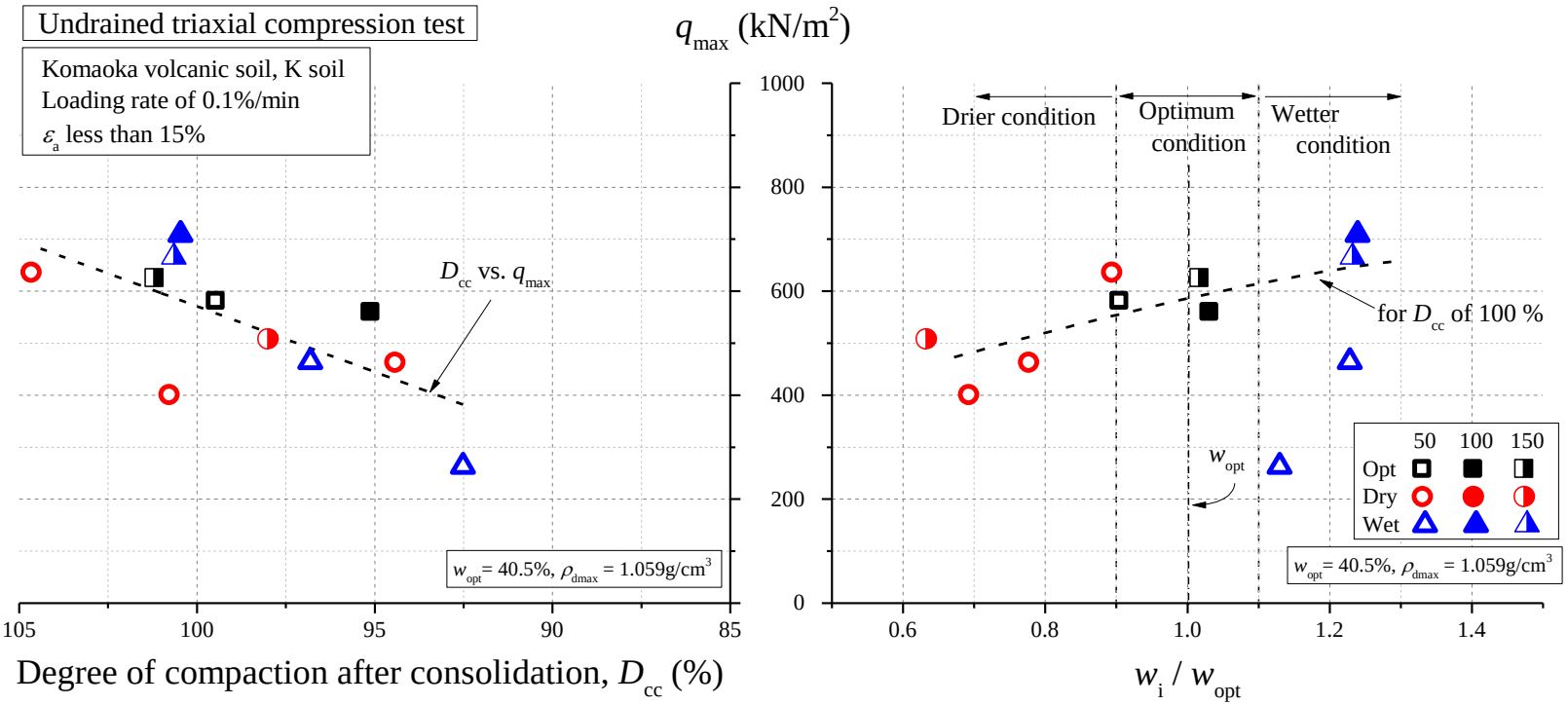

Figure 5.1.18 q_{max}-D_{cc} and -w_i/w_{opt} relations under various compaction and consolidation conditions for K soil

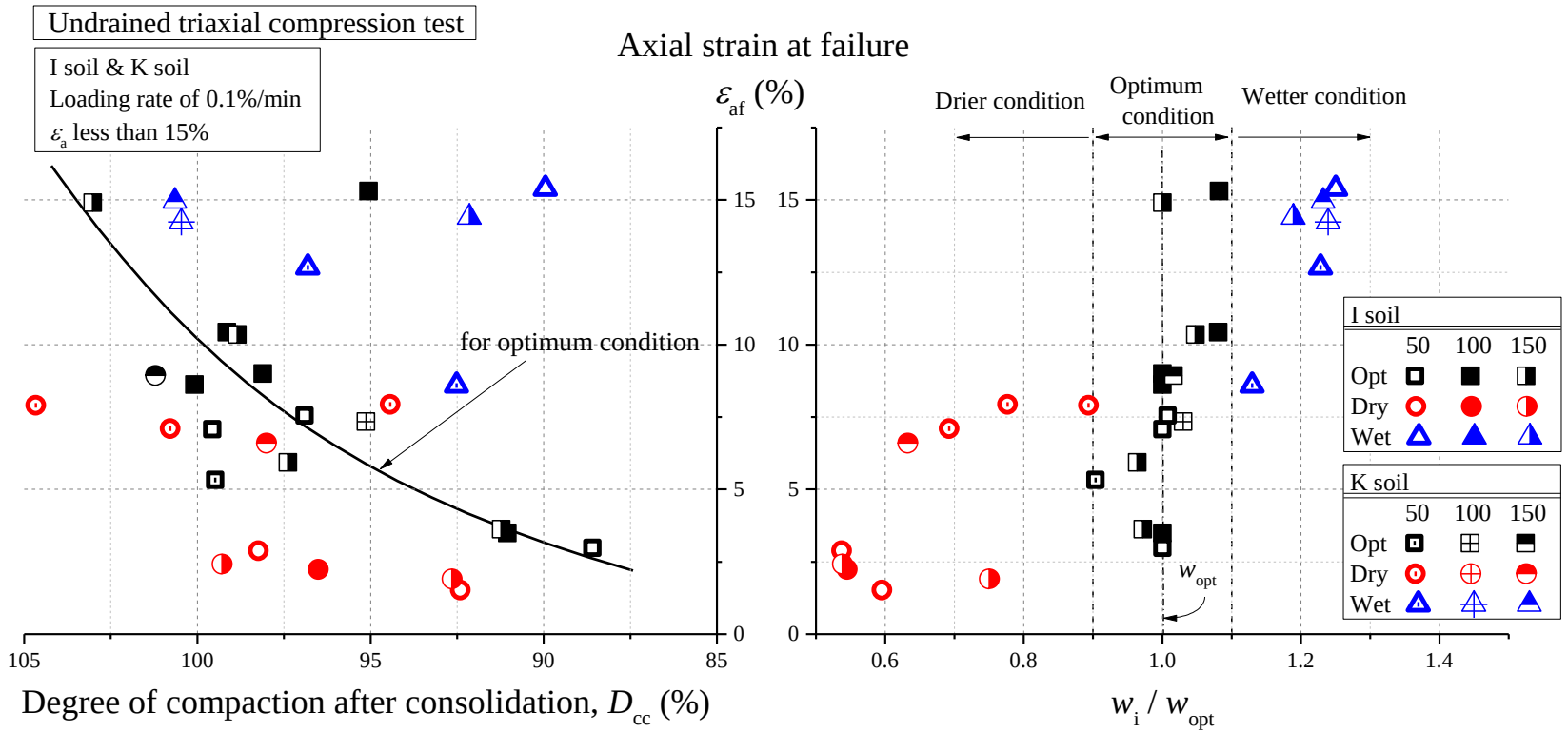

Figure 5.1.19 Axial strain at failure ε_{af} -D_{cc} and -w_i /w_{opt} relations under various compaction and consolidation conditions for I soil and K soil

5.1.4 Shear stiffness at small strain

Figure 5.1.20 plots the shear moduli G_{BE} (MPa) of I soil and K soil on the bender element test related with the degree of compaction D_{cc} and the molding water content w_i/w_{opt}. From the G_{BE}-D_{cc} relations, it is seen that the G_{BE} values increase and the specimens become stiffer with compacted more densely for both soil materials. In particular, the stiffness increase of I soil at D_{cc} = 100 % reached about 1.5 times as higher as at D_{cc} = 90 %. Regarding the effect of molding water content, furthermore, the peak values of G_{BE} tend to appear at the optimum or a little wetter conditions. Therefore, at the range of w_i/w_{opt} less than 0.8, the significant stiffness reduction can be found. Thus, based on the above results, the stiffness behavior at the small strain level is not always consistent with the cyclic shear behavior at the large strain level as shown in *5.1.2*, *CHAPTER 5*. Instead, both are prone to the converse behavior in the effect of molding water content on each cyclic shear behavior. The fact may be attributed to the excess pore water pressure developing during the seismic action at the large strain level and the microscopic soil fabric that can vary depending on the compaction conditions etc., which will be a future's work for a better understanding.

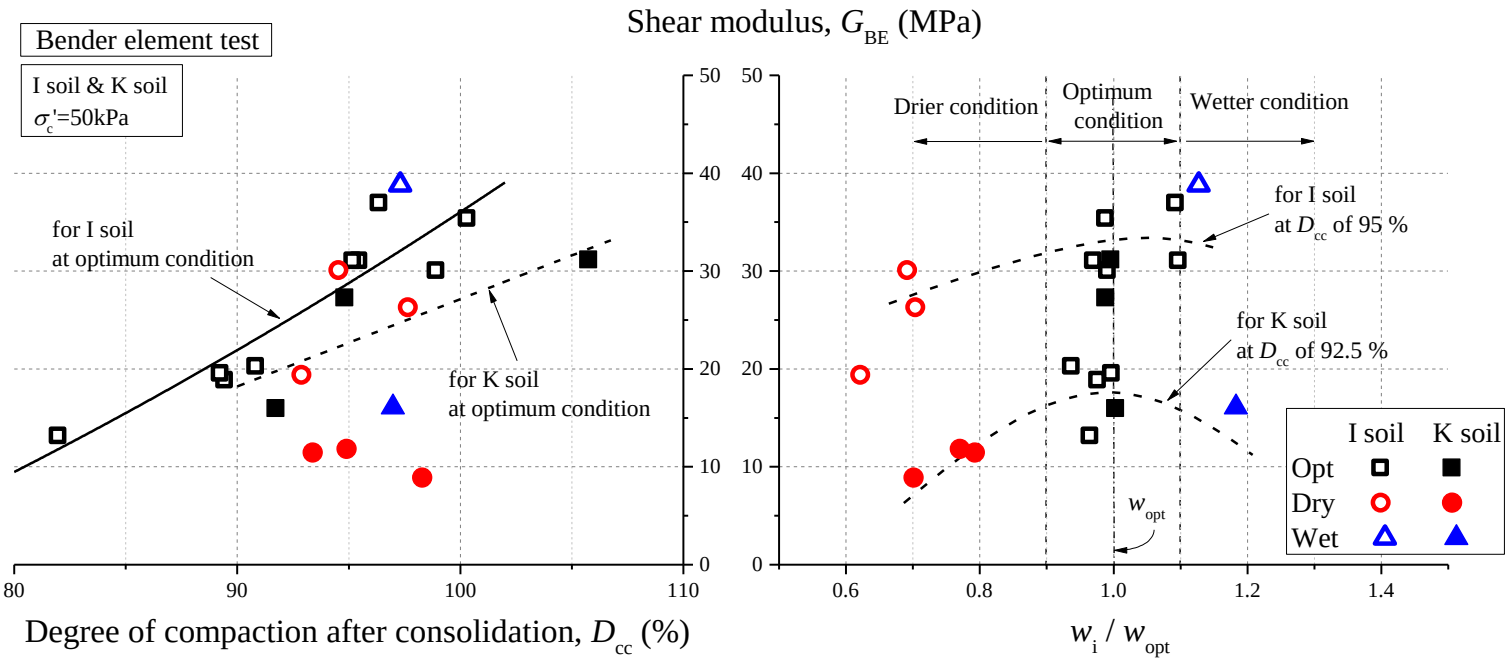

Figure 5.1.20 G_{BE}-D_{cc} and -w_i /w_{opt} relations on bender element test under various compaction conditions for I soil and K soil

5.1.5 Permeability

Figure 5.1.21 indicates the relations of the permeability coefficient k (m/s) of I soil and K soil with the degree of compaction D_{cc} and the molding water content w_i/w_{opt}. The effects of D_{cc} and w_i/w_{opt} are considered to appear in the figure; i.e., the k values significantly decrease with D_{cc} higher for both I soil and K soil, which achieves 10 % or less at D_{cc} = 100 % compared with those at D_{cc} = 90 %. In addition, from the right figure, the higher the molding water content becomes, the lower the permeability is even at the same degree of compaction. Such tendency is consistent with the previous results (e.g., Lambe 1958b), and it is clear that the permeability of I soil and K soil can be affected by the compaction conditions such as the degree compaction and water content at compaction.

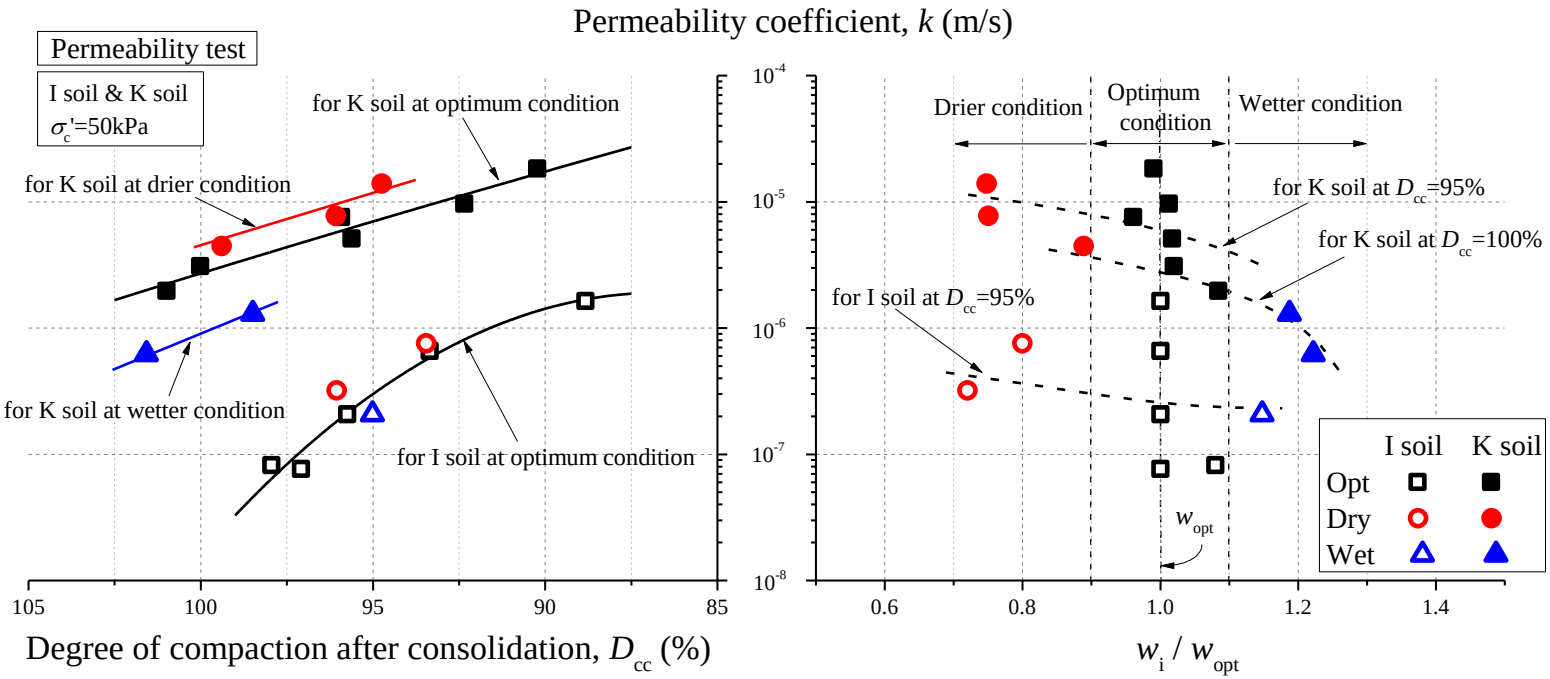

Figure 5.1.21 k-D_{cc} and -w_i /w_{opt} relations on permeability test under various compaction conditions for I soil and K soil

5.2 Change in mechanical properties due to freeze-thaw sequence

5.2.1 Introduction

In order to clarify the effect of freeze-thaw sequence on the cyclic shear behavior, a series of cyclic triaxial tests was conducted using the K soil specimens either with or without freeze-thawing, which are expressed as frozen specimens and non-frozen specimens, respectively. It should be noted that the frozen specimen never indicates frozen soil but frozen and thawed soil. The specimens were compacted 55 times with the 24.5 N rammer in five layers at the optimum condition, based on the classification of compaction condition defined in Figure 5.1.2. The mass of wet soil required per a layer at compaction was fixed at 0.2 kg. The initial dry density ρ_{di} (g/cm^3) and initial degree of compaction D_{ci} (%) are 1.027 g/cm^3 (1.027 Mg/m^3) and 97.0 % in average (variation in ±3 %), respectively. In addition, to evaluate the effect of difference in dry density on the experimental results, the cyclic triaxial tests were performed with the K soil specimens which were compacted 16 and 32 times in four layers, respectively. The dry densities of the specimens are 0.940 and 0.988 g/cm^3 (0.940 and 0.988 Mg/m^3) in average, and corresponding to 88.8 % and 93.3 % for D_{ci}. Figure 5.2.1 shows the compaction conditions of the specimens. Using those specimens, a series of freeze-thawing and cyclic shearing tests were conducted based on the test procedures of *CHAPTER 4*. After freeze-thawing, saturation and consolidation under the effective stress σ_c' of 50 kPa, the cyclic loads were applied with the frequency *f* of 0.005 Hz under the undrained condition.

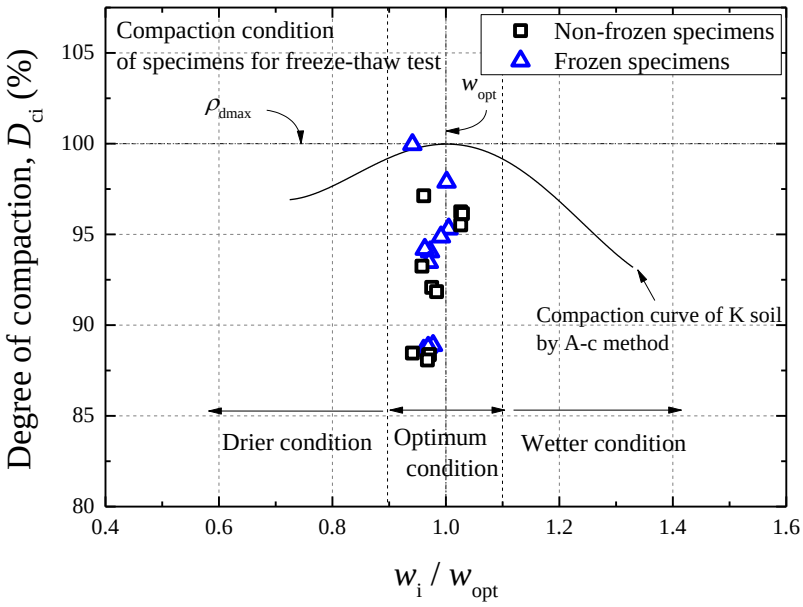

Figure 5.2.1 Compaction conditions of specimens for freeze-thaw test

5.2.2 Volume change and moisture movement of soil subjected to freezing and thawing

Figures 5.2.2 (a) ~ (c) show the time histories of axial strain ε_a (%), drainage ΔV (ml) and each temperature (°C) during freeze-thawing with the specimens compacted at the initial degrees of compaction D_{ci} of 97.0, 88.8 and 93.3 %, respectively. It is noted that the positive values in the axial strain ε_a and drainage ΔV mean the compression strain and to drain, respectively. From the behavior of the specimen compacted densely shown in Figure 5.2.2 (a), it is seen that the specimen continues significant dilation, and causes the freezing expansion rate ε_f (%) of 4.9 % as the temperature of pedestal drops, and is being kept constant. The ε_f value is calculated by Equation (5.1),

$$\varepsilon_f = \Delta H_f / H_i \tag{5.1}$$

where, ΔH_f and H_i are the maximum axial displacement induced by freezing and the specimen height before freezing, respectively. Such dilation is advanced with the specimen absorbing water. After showing subtle discharge at the beginning of freezing, the water tends to be continually provided into the specimen up to 10 ml. As a result, a certain quantity of the axial strain ε_a of the specimen remains with the water absorbed even after completely thawed. Meanwhile, the specimen which is loosely-compacted seems different in the freeze-thaw behavior (*see* Figure 5.2.2 (b)). Namely, the specimen rapidly effuses the water with swelling due to freezing for the first about 50 hours, and then shifts to drainage behavior. The freezing expansion rate ε_f reaches 2.6 %. In addition, from Figure 5.2.2 (c), the specimen of D_{ci} = 93.3 % indicates the intermediate behavior in terms of swelling (ε_f) and drainage. In particular, although the pore water is drained at the beginning of freezing, afterwards the specimen is freezing with absorbing the water compared with the initial state.

Thus, as the initial degree of compaction increases, the freezing expansion rate ε_f tends to be higher, and the relation is illustrated in Figure 5.2.3. From the figure, it is understood that the ε_f

values of denser specimens become approximately twice as much as those of looser specimens. This fact implies that freezing of soil leads to more significant change in soil fabric to the specimen compacted at the higher degree of compaction. The above-mentioned tendency on volume change and moisture movement behavior during freeze-thawing agrees qualitatively with those of the other frozen specimens, although the drawings are omitted.

As shown in Figures 5.2.2, the axial strain ε_a cannot return to the initial state of ε_a=0 even after the specimens are completely thawed. This fact indicates that the specimens remain in soil fabric changed by freezing after thawed. In order to identify volume change due to freeze-thawing and consolidation, Figure 5.2.4 shows the relations between the initial degree of compaction D_{ci} and degree of compaction after consolidation D_{cc} under the effective stress σ_c' of 50 kPa. From the figure, it is obvious that the freeze-thaw effect on the volume change behavior appears. At the range over 90 % in D_{ci}, the volume change occurs in the swelling side after thawing and consolidation, and the corresponding decrement of degree of compaction becomes more significant as D_{ci} increases. However, at lower than 90 % in D_{ci}, conversely, the volume of the specimen changes toward the shrinking side to a lesser extent regardless of whether the specimen is freeze-thawed. Those facts have a good agreement with some previous findings (Viklander 1998 and Nakamura et al. 2011); that is, the void ratios are prone to converge at a certain unique void ratio between the initial ones whether an initial soil structure is loose or dense, as freeze-thaw cycles increase. In addition, they reported that the variation in volume becomes the most remarkable at the first cycle of freeze-thaw sequence. Thus, the experimental results indicated that the volume change due to freeze-thaw sequence evolves in either side of swelling or shrinking depending on the initial degree of compaction.

Furthermore, based on the standpoint that the crushability of constitutive particles contributes to mechanical deterioration (Miura et al. 2003), the increment of finer content through a sequence

of testing processes such as freeze-thawing, consolidation and cyclic loading was examined as shown in Figure 5.2.5. Although there is variation in experimental data, it appears that the specimens show higher crushability under the freeze-thawed condition, as those are more densely compacted. That seems to reflect the swelling behavior during freezing; i.e., freezing denser specimens can stimulate more change in the soil fabric compared with looser specimens. Accordingly, it could be understood that the increment of finer particle due to freeze-thaw sequence has the positive correlations with the initial degree of compaction and the freezing expansion rate. This study, however, is still not applicable to identify the individual effect of the increment of finer particle induced by freeze-thawing on cyclic deformation-strength characteristics discussed below.

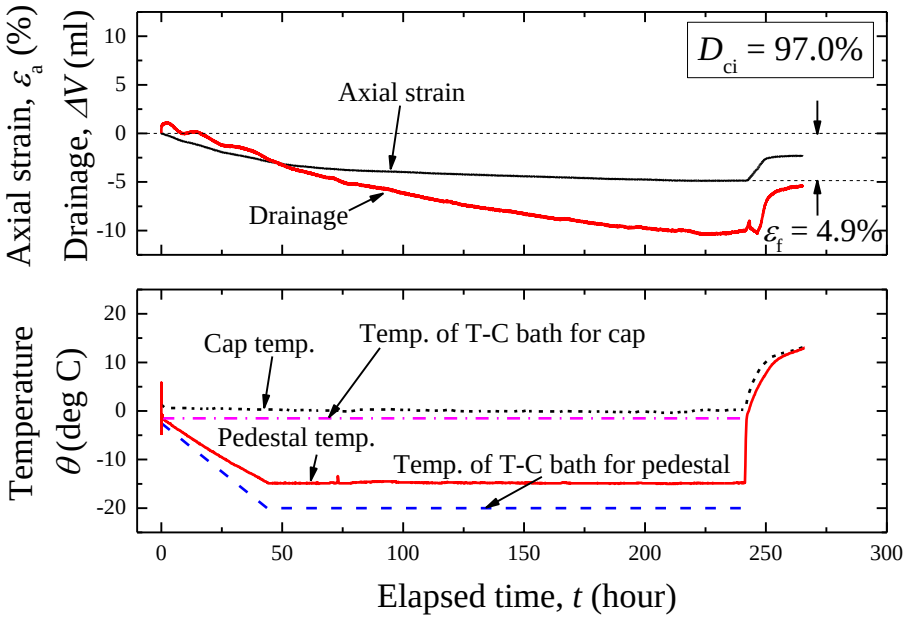

(a) D_{ci} = 97.0%

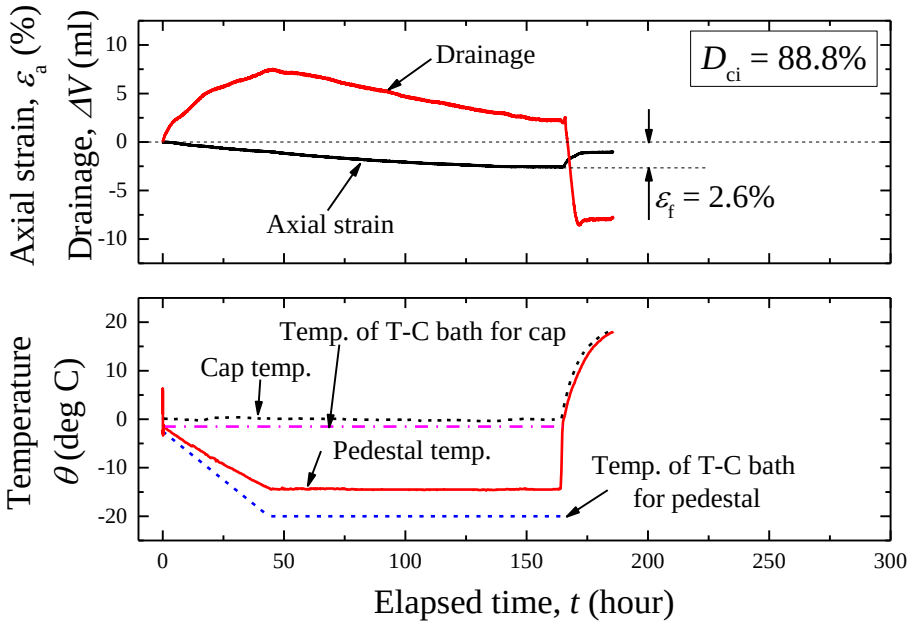

(b) D_{ci} = 88.8%

Figures 5.2.2 Freeze-thaw behavior of compacted specimens at different D_{ci}

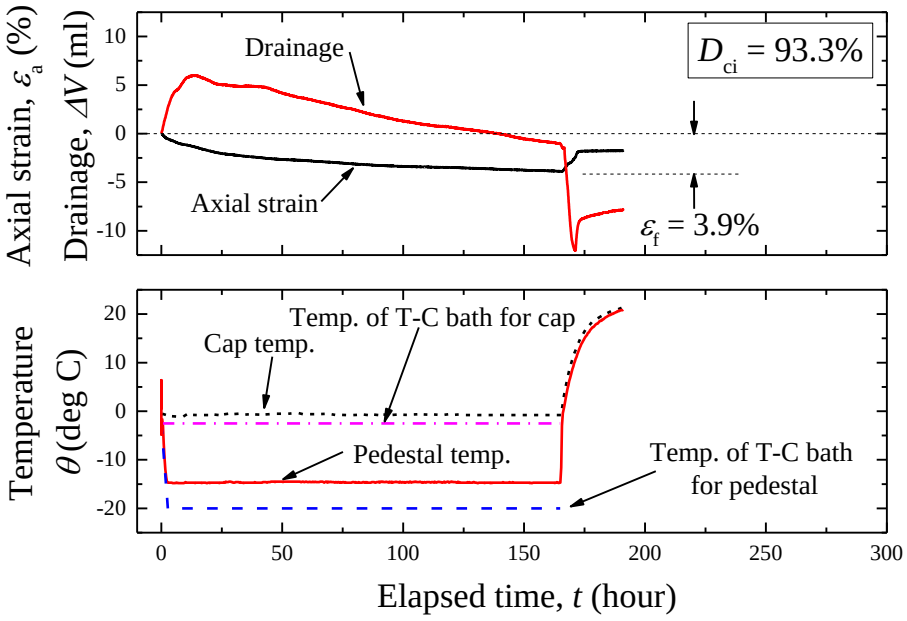

(c) D_{ci} = 93.3%

Figures 5.2.2 Freeze-thaw behavior of compacted specimens at different D_{ci}

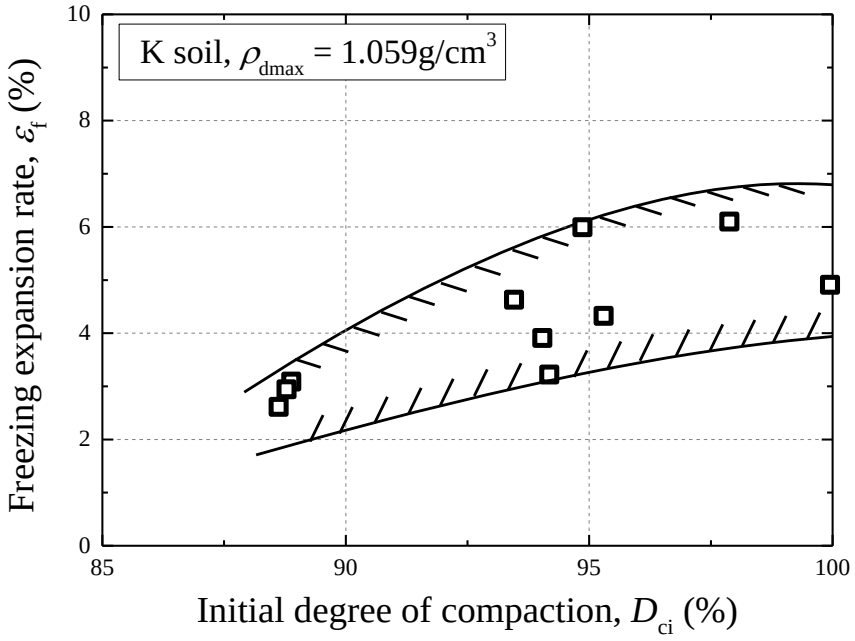

Figure 5.2.3 Freezing expansion rate ε_f vs. D_{ci}

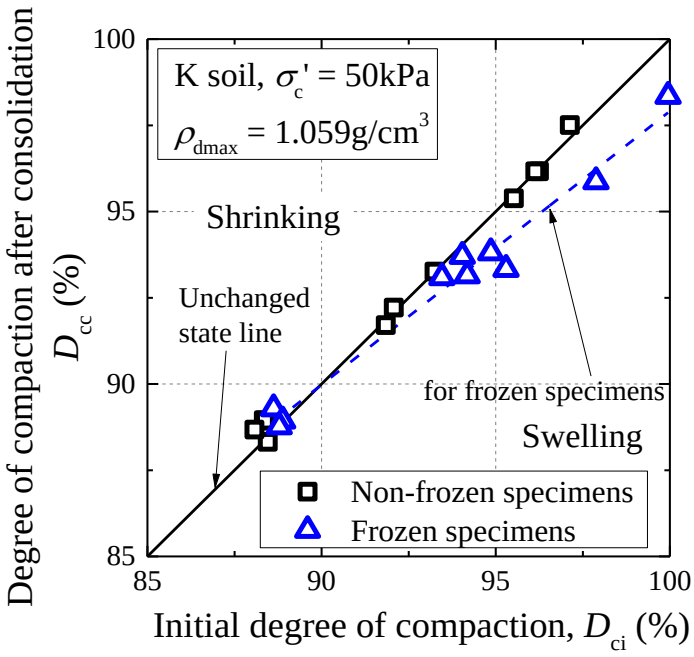

Figure 5.2.4 Change in degree of compaction (dry density) due to freeze-thaw sequence

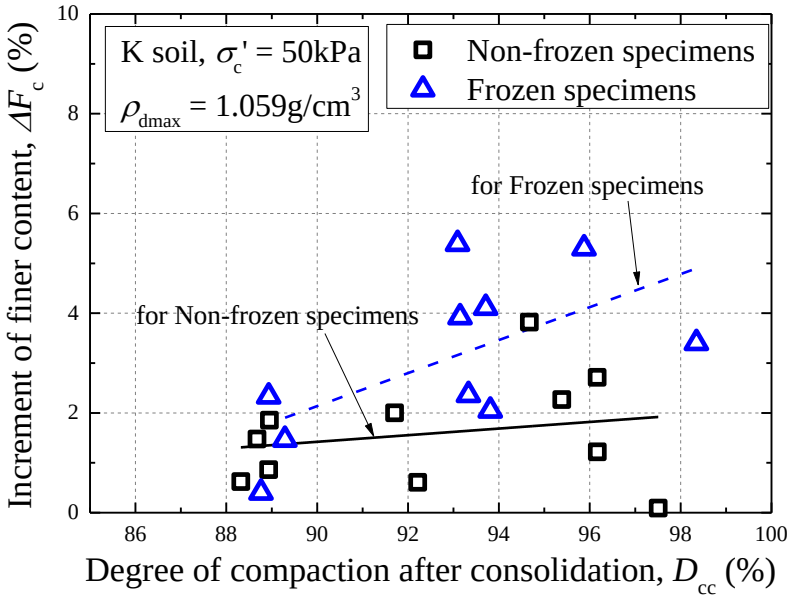

Figure 5.2.5 Particle breakage due to freeze-thawing related to degree of compaction

5.2.3 Cyclic strength-deformation properties

5.2.3.1 Effect of freeze-thaw sequence on cyclic shear characteristics

Figures 5.2.6 (a) and (b) show the time histories of deviator stress σ_d and axial strain ε_a up to 5 % in the double amplitude axial strain *DA* with regard to each cyclic stress ratio *SR*, with the frozen specimens and the non-frozen ones, respectively. The specimens were densely compacted at the initial degree of compaction D_{ci} of 97.0 %. In comparison with the number of loading cycles N_c to cause the *DA* value of 5 %, it is clear that the specimen reached *DA* = 5 % with very few cycles of loading under the freeze-thawed condition regardless of the magnitude of *SR*. In other words, freeze-thawing leads to considerable deterioration on liquefaction resistance for K soil densely-compacted. Furthermore, when focusing on directions of progressing the deformation during cyclic loading, the non-frozen specimens tend to generate the extension strain dominantly as the N_c value increases. In contrast, in the case of the frozen specimens, the axial strains seem to develop not only the extension side but also in the compression one. Such a tendency may be attributed to anisotropic behavior of the K soil specimens resulting from change in soil fabric induced by freeze-thawing as discussed later.

Figures 5.2.7 and 5.2.8 illustrate the time histories of excess pore water pressure Δu and effective mean principal stress *p*' during cyclic loading, which are normalized by the effective confining pressure σ_c' of 50 kPa, respectively. Those specimens correspond with each one shown in Figures 5.2.6. In terms of the $\Delta u/\sigma_c$'-N_c relations, those show that the excess pore water pressure rapidly increases from the beginning of loading after freeze-thawing. As a result, the frozen specimens immediately cause initial liquefaction that Δu reaches 95 % of σ_c'. The trend on Δu, on the other hand, is consistent with the behavior of the effective mean principal stress *p*' during cyclic loading. That is, the specimens exposed to freeze-thaw sequence show *p*'

decreasing at a higher rate, and lead to liquefaction as the loading cycle increases, in comparison of the non-frozen specimens.

Such differences in the behavior of Δu and p' resulting from freeze-thawing could be understood on each effective stress path for the frozen specimens and the non-frozen ones as shown in Figures 5.2.9 (a) ~ (d). The testing results are represented with regard to each *SR*, which equal to those in Figures 5.2.6. Those figures indicate that the frozen specimens tend to reach liquefaction rapidly with drastic decrease of the effective stress. That is similar to the typical case of loose clean sands in liquefying. On the other hand, the non-frozen specimens are gradually liquefied with moderate decrease of the effective stress as well as dense clean sands. According to the figures, the differences in the decreasing effective stress become very conspicuous at the first cycles of loading. Thus, it is obvious that freeze-thawing causes the stronger negative dilatancy under seismic action, and it contributes to the cyclic strength degradation as elaborated in Figures 5.2.6.

In order to discuss the variation in liquefaction strength due to freeze-thaw sequence, Figure 5.2.10 represents each relationship between the cyclic stress ratio *SR* and number of loading cycles N_c to cause *DA* reaching 1 % and 5 %, Δu increasing to 95 % of σ_c' and p' decreasing to 5 % of σ_c', respectively. From the figure, it is definitely found out that the freeze-thaw sequence can remarkably degrade the liquefaction strength of K soil regardless of failure definitions of *DA*, Δu and p' in evaluating the liquefaction strength. In accordance with the liquefaction strength curves in Figure 5.2.10, Figure 5.2.11 presents the cyclic stress ratio at N_c of 10 and 20 in each liquefaction strength line, which are denoted as SR_{10} and SR_{20}, respectively. When focusing on SR_{20}, the liquefaction strength can decrease up to around 70 % under the freeze-thawed condition for any cases related to *DA*, Δu and p'. In addition, it is also realized that the cyclic stress ratio *SR* to reach *DA* = 1 % with 20 cycles is approximately corresponding with those to attain $\Delta u/\sigma_c$' =

0.95 and p'/σ_c' = 0.05. On the other hand, regarding the SR_{10} value, the difference between the frozen specimens and the non-frozen ones becomes more significant compared with SR_{20}. The SR_{10} value at *DA* = 5 % of frozen specimens, for example, reaches 63 % to that of non-frozen specimens. That means the freeze-thawed specimens have lower liquefaction resistance than the non-frozen specimens under higher cyclic stress.

The relationship between the maximum of $\Delta u/\sigma_c'$ at each cycle where the *DA* value reaches 1 and 5 % and each cyclic stress ratio *SR* is presented in Figure 5.2.12. It clearly shows some difference at *DA* = 1 % depending on whether the specimen underwent freeze-thaw sequence. The frozen specimens tend to reach *DA* of 1 % with lower excess pore water pressures, and this tendency becomes remarkable as the value of *SR* is higher. Furthermore, while the *DA* value develops up to 5 %, the excess pore water pressure completely reaches the confining pressure with any *SR* in both the frozen and the non-frozen specimens because the $\Delta u/\sigma_c'$ values are over 1.0 as shown in Figure 5.2.12. Thus, freeze-thaw sequence may induce larger strain with lower excess pore water pressure due to cyclic loading before the initial liquefaction.

In order to obtain a better understanding on cyclic deformation progresses in a different way as shown in Figure 5.2.6 (b), Figure 5.2.13 reveals the N_c-*DA* relation with each cyclic stress. Note that the values in both axes are divided by each N_c and *DA* at *DA* = 5 %. From the figure, the corresponding tendencies depending on freeze-thaw sequence can be found out; i.e., the axial strain of the frozen specimens increases proportionately to some extent under any cyclic stress ratio conditions, as the loading cycle increases. In contrast, the specimens that have not undergone freeze-thaw sequence are likely to exponentially increase *DA* from a certain N_c. Considering the points where the initial liquefaction, $\Delta u/\sigma_c'$ = 0.95, occurs as described in Figure 5.2.13, those for the non-frozen specimens seem to be located in which the cyclic deformation rapidly glows. Such a tendency is, however, not consistent with the frozen specimens, and the

cyclic deformation for them develops at a relatively-constant rate on the relation of N_c vs. *DA*. Therefore, it can be said that the K soil specimens tend to deform more remarkably by cyclic action from the beginning of loading due to freeze-thaw sequence.

Furthermore, Figure 5.2.14 represents the ratio of extension axial strain $\varepsilon_{a\ ext.}$ to *DA* = 1 % and 5 % with each cyclic stress, respectively, to discuss change in anisotropic behavior induced by freeze-thawing. With respect to the non-frozen specimens, the axial strain keeps around 80 to 90 % of *DA* in the extension side at any *DA* and *SR*, which means that the cyclic deformation develops dominantly toward the extension side. However, in any results of frozen specimens, the extension axial strain fluctuates less than 80 % of *DA*, and it does not always advance prior to the compression axial strain $\varepsilon_{a\ comp}$. Such a trend particularly becomes significant at the smaller strain level and under the lower cyclic stress. Thus, it is clear that freeze-thaw sequence has the influence on not only the liquefaction strength but also cyclic deformation behavior.

The aforementioned tendency seems similar to the typical liquefaction behavior of clean sands that have anisotropic mechanical properties on the conventional liquefaction test. In other words, the change in cyclic deformation behavior due to freeze-thawing shown in this study may be related with structural anisotropy of the soil particles induced by a peculiarity of the conventional liquefaction test. Then, the anisotropic behavior is associated to a configuration or an orientation of the constitutive particles that are non-spherical under the gravity action, and the experimental peculiarity indicates that the effective mean principal stress *p*' is not kept constant during cyclic loading. According to Oda (1972) and Miura and Toki (1984), it was verified that if a longitudinal axis of each particle dominantly deposited in a certain direction, is inclined at δ degrees to the maximum principal stress direction as shown by δ-specimen in Figure 5.2.15, the anisotropic mechanical behavior varies depending on the δ value. In the case of δ = 90°, which is equal to 90°-specimen in the figure, for example, the axial strain in the extension

side where p' decreases tends to increase dominantly on the cyclic triaxial test. Based on 0°-specimen with δ = 0° on the other hand, the compression axial strain develops significantly due to cyclic loading. In addition, a specimen with a certain δ within 0° to 90° shows intermediate behavior on monotonic and cyclic deformation behavior. These are closely similar to the difference in cyclic deformation behavior of K soil compacted with or without freeze-thaw sequence. On the basis of the prior discussion about cyclic deformation behavior, it can be said that K soil densely compacted, which is similar to 90°-specimen on the deposited direction, changes in the soil fabric toward the δ value less than 90° due to freeze-thawing in Figure 5.2.15. Thus, because the compacted K soil specimens are prone to the strong anisotropy in liquefying, and the cyclic deformation behavior can be definitely affected by freeze-thaw sequence, it is important to examine the relationship between anisotropic fabrics of compacted soils and each stress direction such as freeze-thaw sequence and cyclic loading.

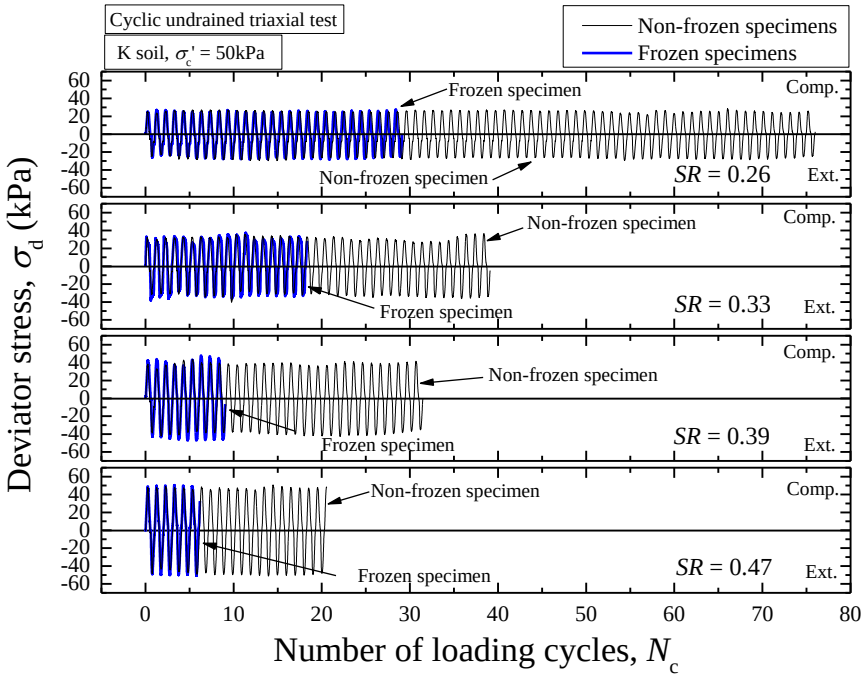

(a) Cyclic deviator stress

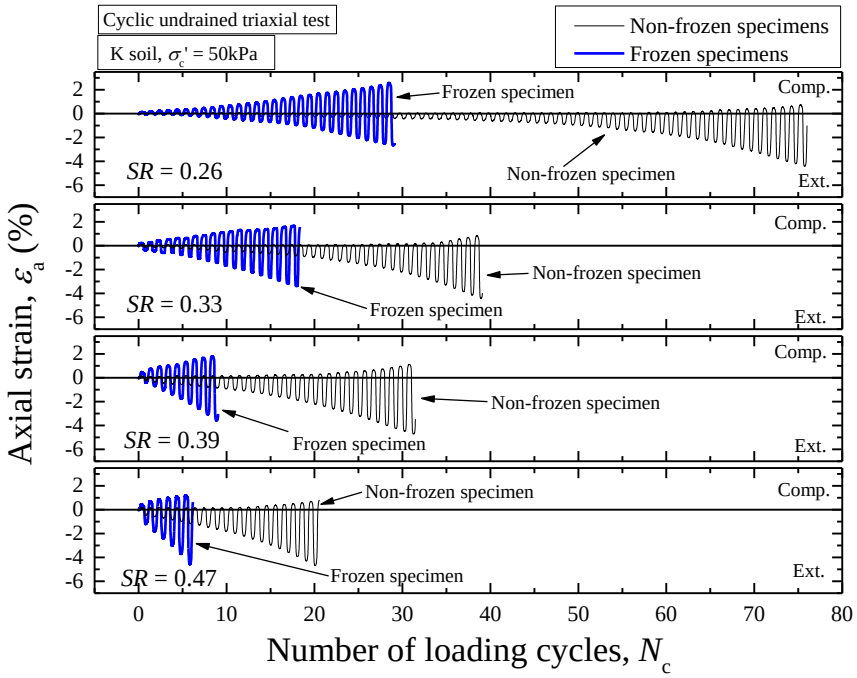

(b) Axial strain

Figures 5.2.6 Time histories on cyclic triaxial tests for frozen and non-frozen specimens

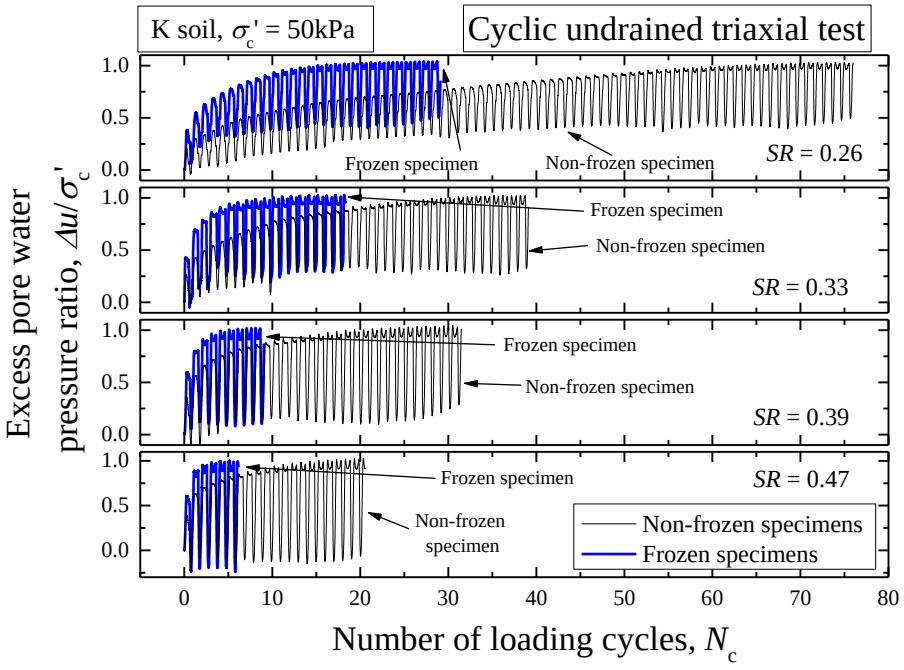

Figures 5.2.7 Time histories of excess pore water pressure on cyclic triaxial tests for frozen and non-frozen specimens

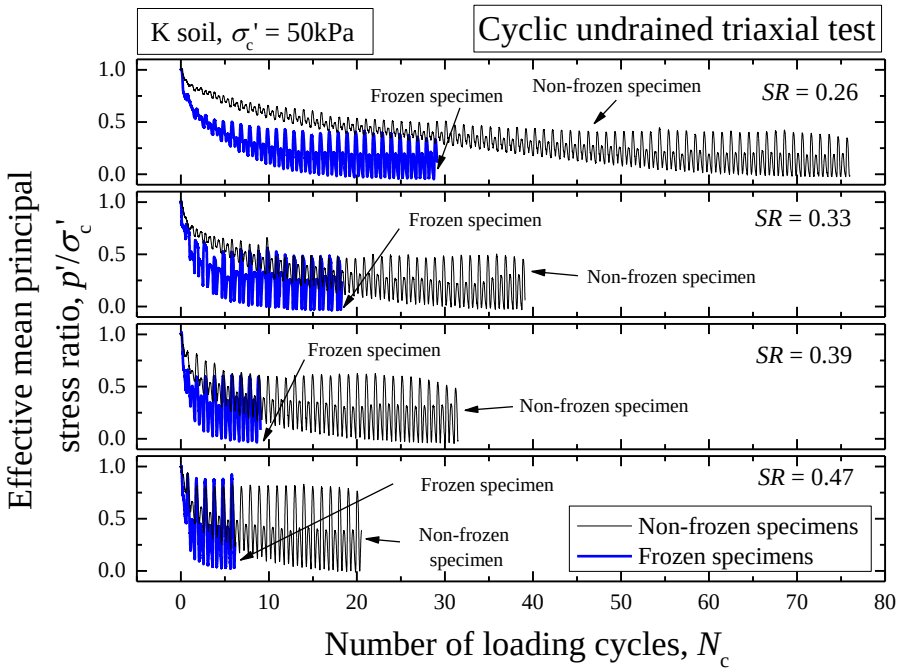

Figures 5.2.8 Time histories of effective mean principal stress on cyclic triaxial tests for frozen and non-frozen specimens

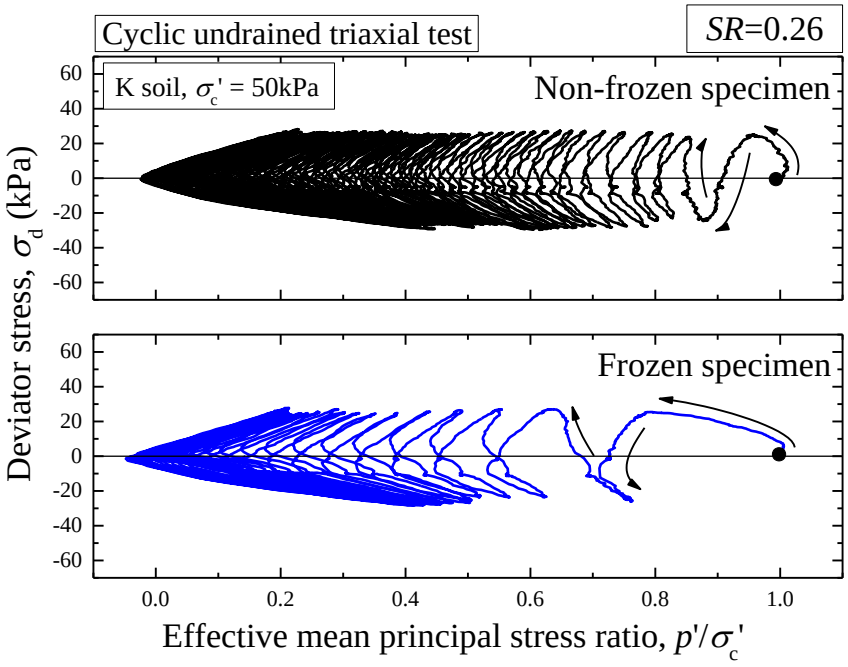

(a) *SR* = 0.26

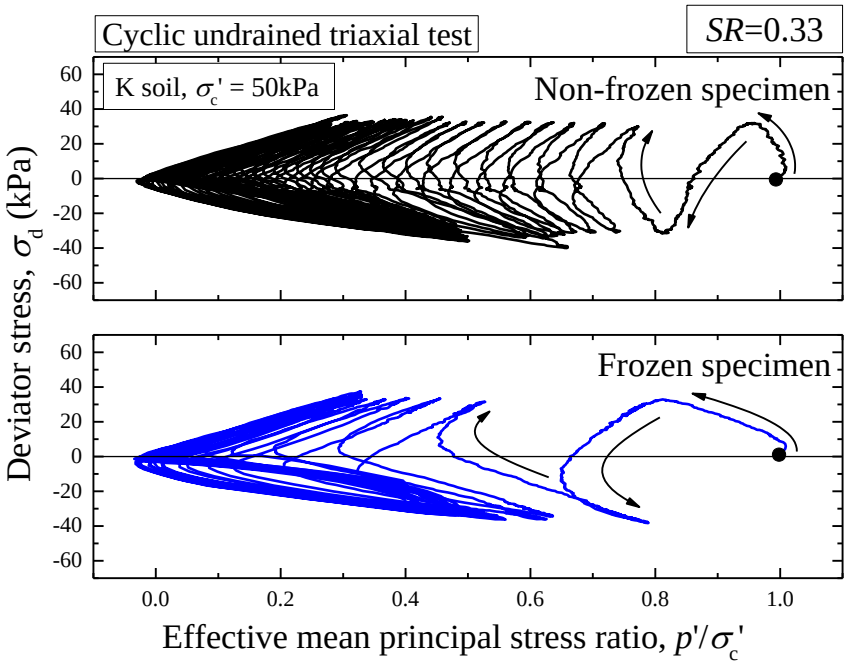

(b) *SR* = 0.33

Figures 5.2.9 Effective stress paths during cyclic loading
with regard to each cyclic stress ratio

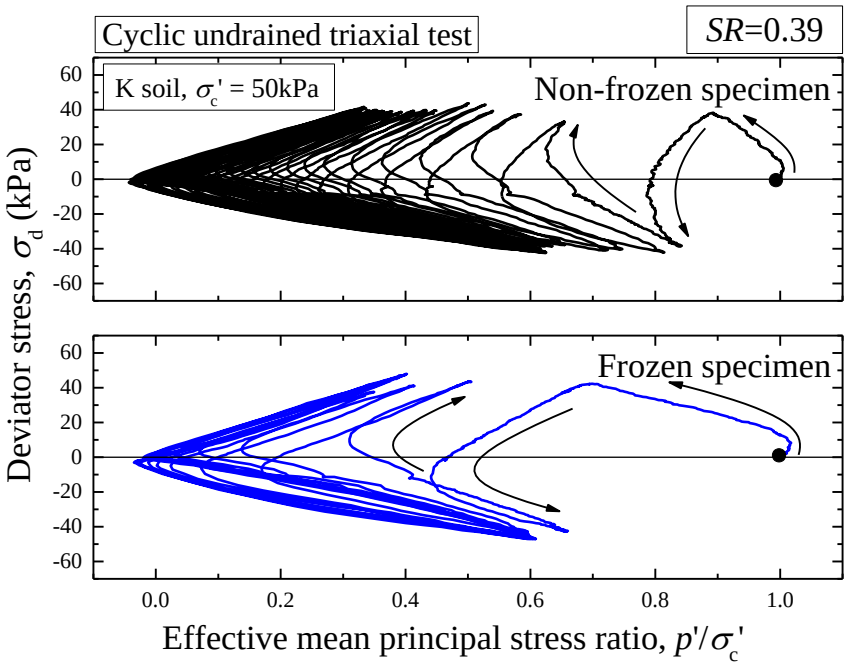

(c) *SR* = 0.39

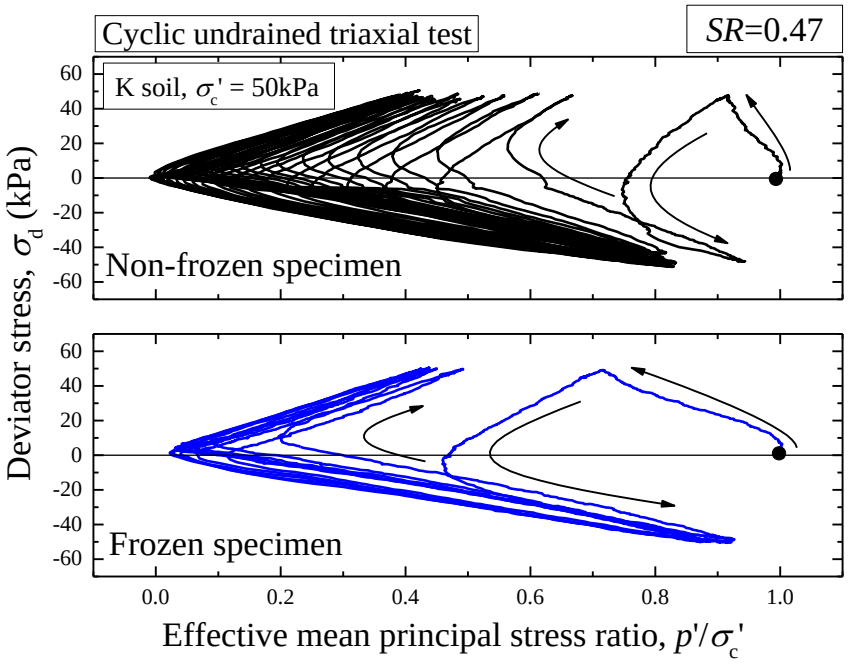

(d) *SR* = 0.47

Figures 5.2.9 Effective stress paths during cyclic loading
with regard to each cyclic stress ratio

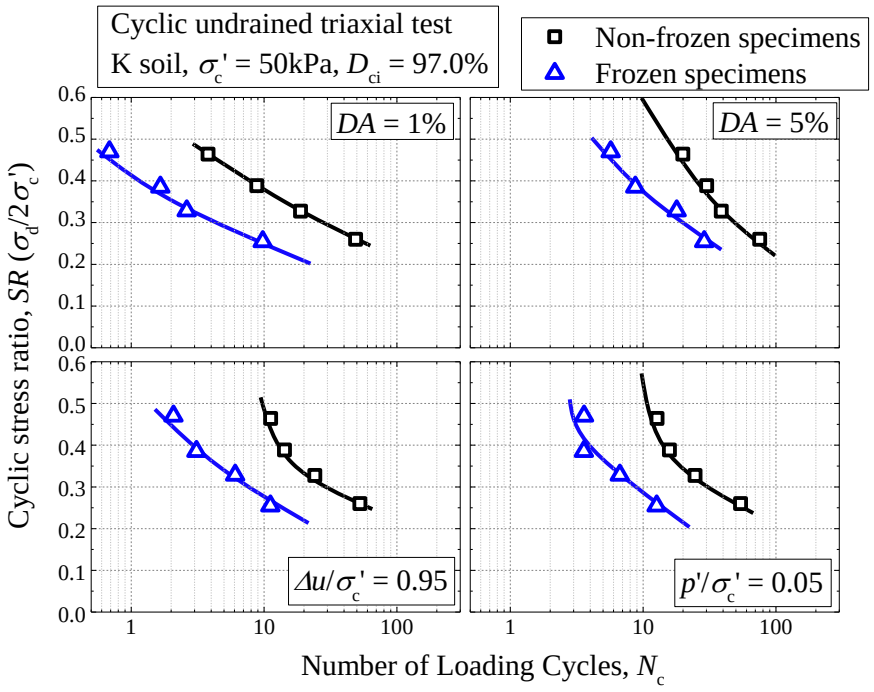

Figure 5.2.10 Liquefaction strength to attain *DA* of 1 and 5 %, Δu increasing 95 % of σ_c' and p' decreasing 5 % of σ_c' at D_{ci}=97.0%

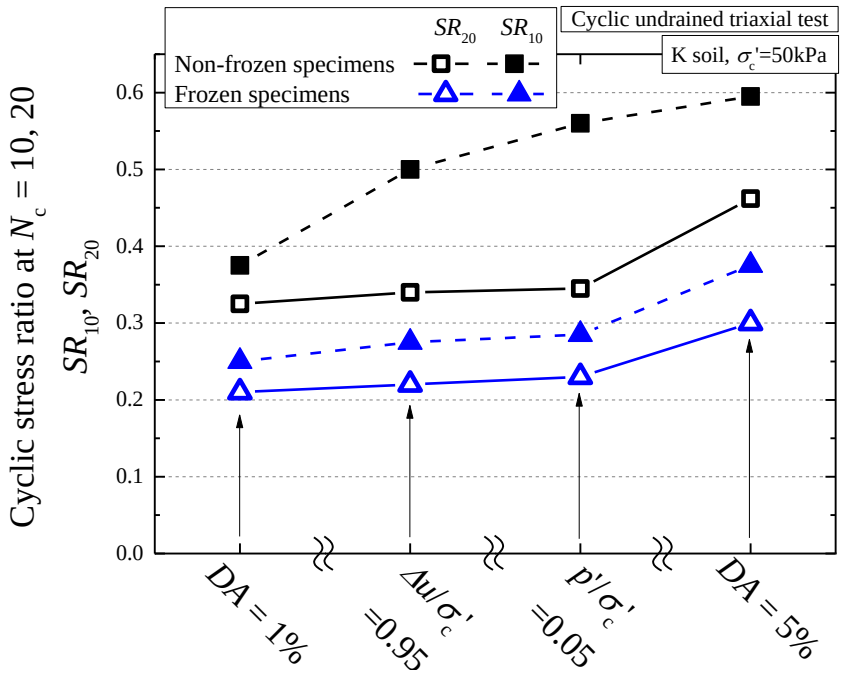

Figure 5.2.11 Cyclic strength values to attain *DA* of 1 and 5 %, $\Delta u/\sigma_c$'=0.95 and p'/σ_c'=0.05 at N_c of 10 and 20, SR_{10} and SR_{20}

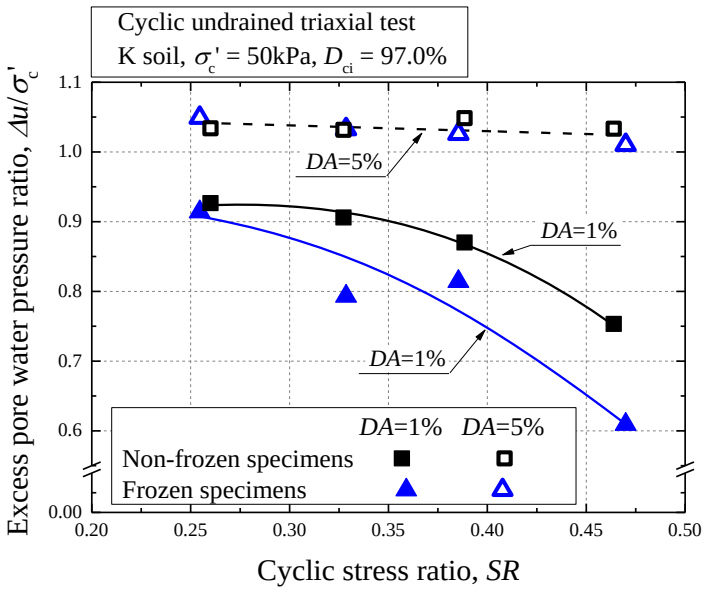

Figure 5.2.12 Excess pore water pressure ratio at *DA* = 1 and 5 %

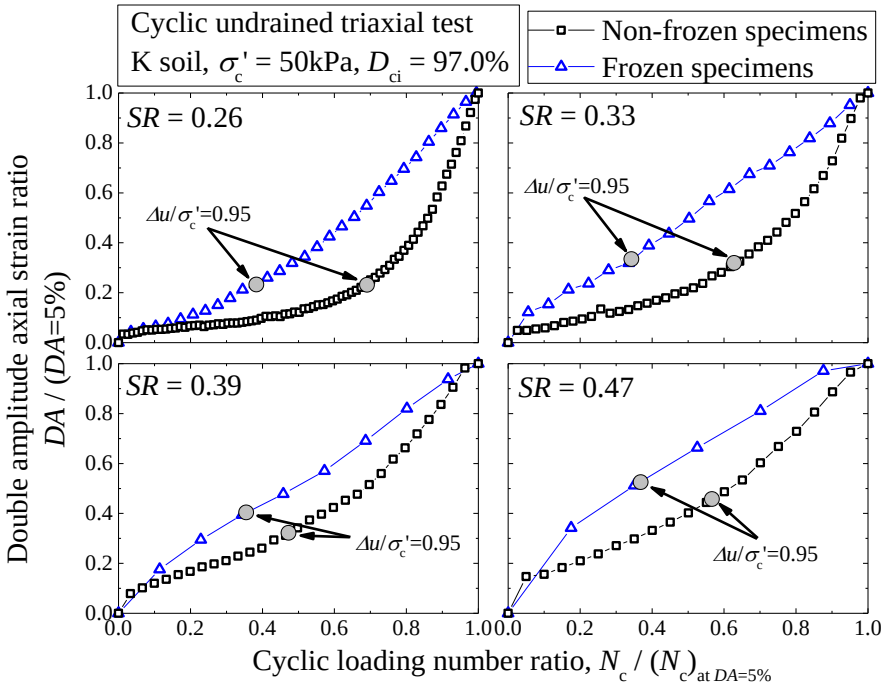

Figure 5.2.13 Cyclic deformation behavior: relation of *DA*/(*DA*=5%) vs. $N_c/N_{c\ \text{at}\ DA=5\%}$

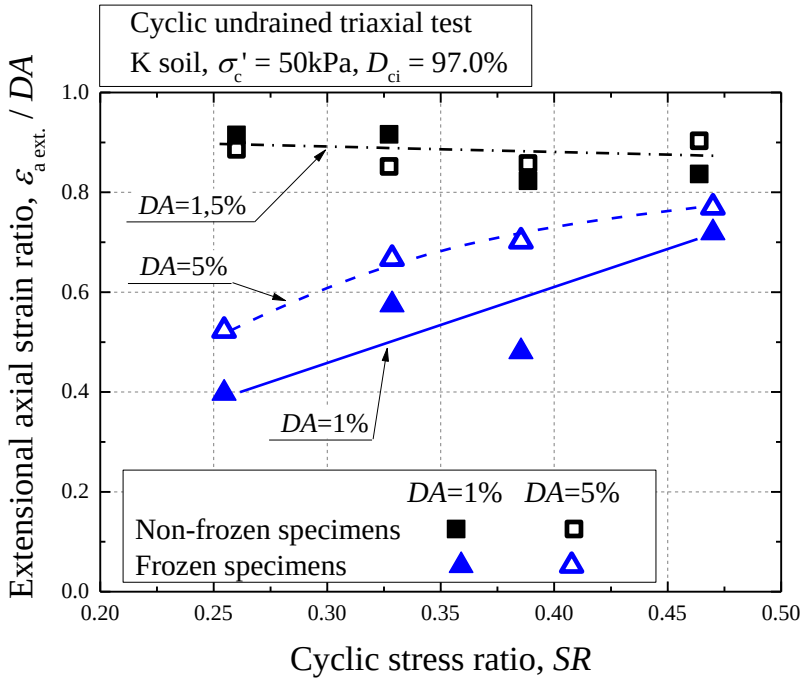

Figure 5.2.14 Anisotropic behavior during cyclic loading: extensional axial strain ratio at *DA* = 1 and 5 %

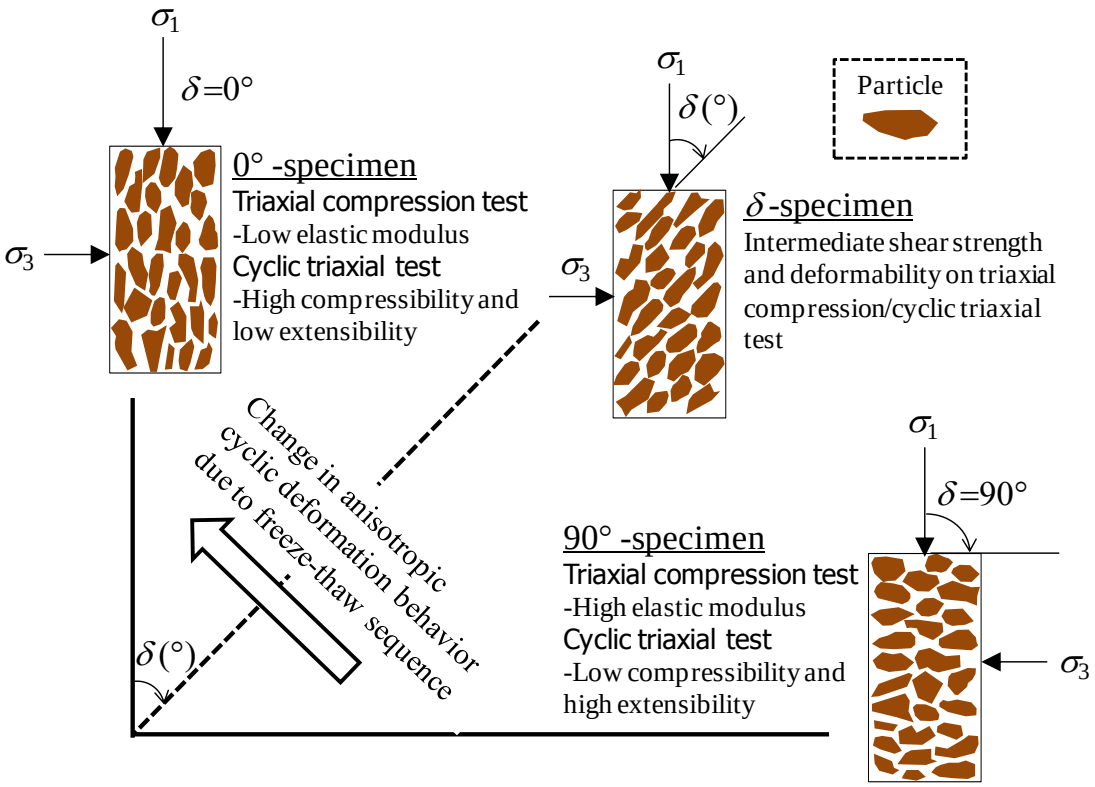

Figure 5.2.15 Soils with fabric anisotropy and their mechanical properties

5.2.3.2 Effect of degree of compaction on cyclic shear behavior of freeze-thawed specimen

In the previous section, the remarkable change in cyclic strength-deformation behavior due to freeze-thaw sequence was elucidated. However, according to the volume change and moisture movement behavior occurring in freezing and thawing, those can be strongly influenced by the initial degree of compaction. Figures 5.2.16 (a) and (b) indicate the effect of initial degree of compaction D_{ci} on the time histories of axial strain ε_a and excess pore water pressure ratio $\Delta u/\sigma_c'$ up to 5 % in *DA*, respectively. Both the frozen and the non-frozen specimens compacted at each D_{ci} of 97.0, 93.3 and 88.8 % were applied cyclic loading within the *SR* range of 0.23 to 0.27. From Figure 5.2.16 (a), it is seen that freeze-thawing causes the drastic decrease in N_c to reach *DA* = 5 % for the specimens with D_{ci} of 97.0 % as explained in Figures 5.2.6. The trend of cyclic strength deterioration is likely to be consistent with the result of D_{ci} = 93.3 %, and the change in the anisotropic behavior resulting from freeze-thaw sequence can be recognized as well. However, according to the results of the specimens loosely compacted at D_{ci} = 88.8 %, it shows little difference in cyclic strength behavior despite freeze-thawing. In these cases, furthermore, the specimens indicate the comparatively-similar tendency in cyclic deforming regardless of freeze-thawing unlike the above two cases different in D_{ci}. The aforementioned relation of freeze-thaw effect with the initial degree of compaction agrees well to that in excess pore water pressure behavior during cyclic loading as described in Figure 5.2.16 (b). Therefore, the densely-compacted specimens which cause the cyclic strength deterioration due to freeze-thawing show that the excess pore water pressure increases at higher rates than those of the non-frozen specimens. In contrast, when compacted at D_{ci} of 88.8 %, the specimens with or without freeze-thaw sequence basically correspond to each other on the excess pore water pressure behavior.

Figures 5.2.17 (a) ~ (c) demonstrate the effective stress paths of the specimens shown in Figures 5.2.16 with regard to each initial degree of compaction D_{ci}. From the figures, it could be understood that the decreases of effective stress due to freeze-thawing become remarkable for the two specimens densely compacted, while the loose specimen of D_{ci} = 88.8 % represents the similar stress paths regardless of the freeze-thaw sequence.

Figure 5.2.18 shows the N_c-DA relation as well as Figure 5.2.13 with respect to each freeze-thaw sequence and degree of compaction. The non-frozen specimens tend to follow a unique path on N_c vs. DA similar to one another, even though compacted at the different degrees of compaction. In addition, those results indicate the typical behavior that the cyclic deformation abruptly develops after the excess pore water pressure reaches 95 % of the effective confining stress as explained with Figure 5.2.13. On the other hand, for the frozen specimens, the effect of freeze-thawing on the cyclic deformation behavior obviously appears while becoming lesser in the case of D_{ci} = 88.8 %. It shows that although the K soil specimens can be definitely influenced by freeze-thawing, the cyclic strength might be more susceptible to dry density (degree of compaction) than freeze-thaw sequence in the loosely-compacted condition.

Figures 5.2.19 (a) and (b) represent each liquefaction strength curve to attain DA = 1 % and 5 %, $\Delta u/\sigma_c'$ = 0.95 and p'/σ_c' = 0.05 with the specimens compacted at 93.3 and 88.8 % in D_{ci}, respectively. From Figure 5.2.19 (a), although the freeze-thawing effect on cyclic strength becomes smaller than that of D_{ci} = 97.0 %, freeze-thaw sequence triggers the cyclic strength degradation for the K soil specimens. However, if the specimens are compacted more loosely to become D_{ci} of 88.8 %, little influence of freeze-thawing on the liquefaction strength can be recognized as shown in Figure 5.2.19 (b).

Based on the liquefaction strength curves shown in Figures 5.2.10 and 5.2.19, Figure 5.2.20 describes the relations between the degree of compaction after consolidation D_{cc} and each SR_{20} to

reach the *DA* values of 1 % and 5 %. It is clear to indicate some differences in cyclic strength behavior caused by freeze-thawing; i.e., 1) freeze-thawing disturbs the increase in cyclic strength accompanied with the increase in degree of compaction, 2) the SR_{20} value for *DA* = 1 % can hardly increase under the freeze-thawed condition while compacted more densely, unlike the non-frozen specimens. According to this study, it is emphasized that the cyclic strength characteristics of K soil can remarkably deteriorate with exposed to freeze-thaw sequence. At the same time, however, such effects of freeze-thawing ought to be incorporated into the relation with the initial degree of compaction prior to freezing.

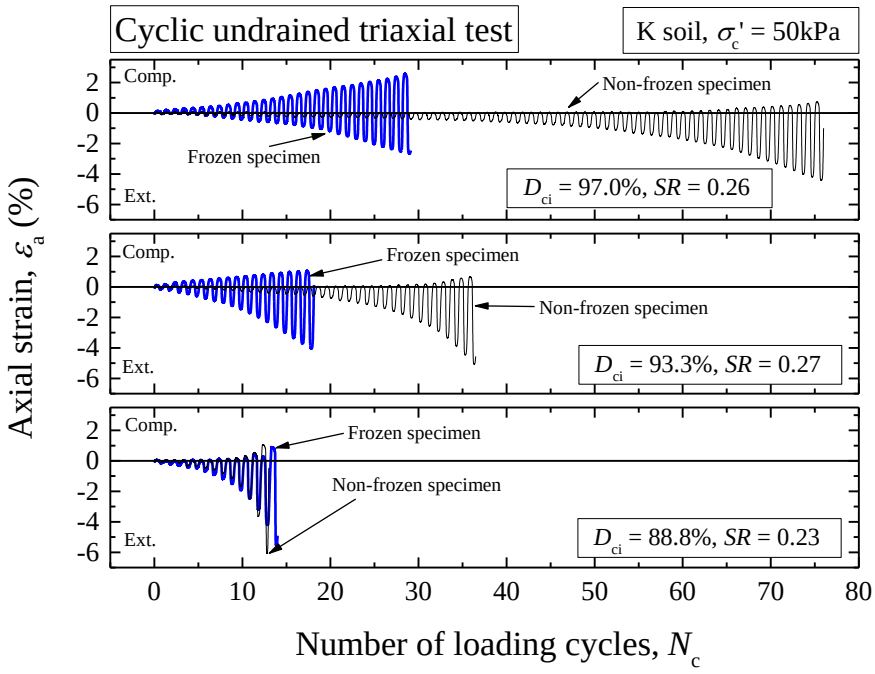

(a) Axial strain

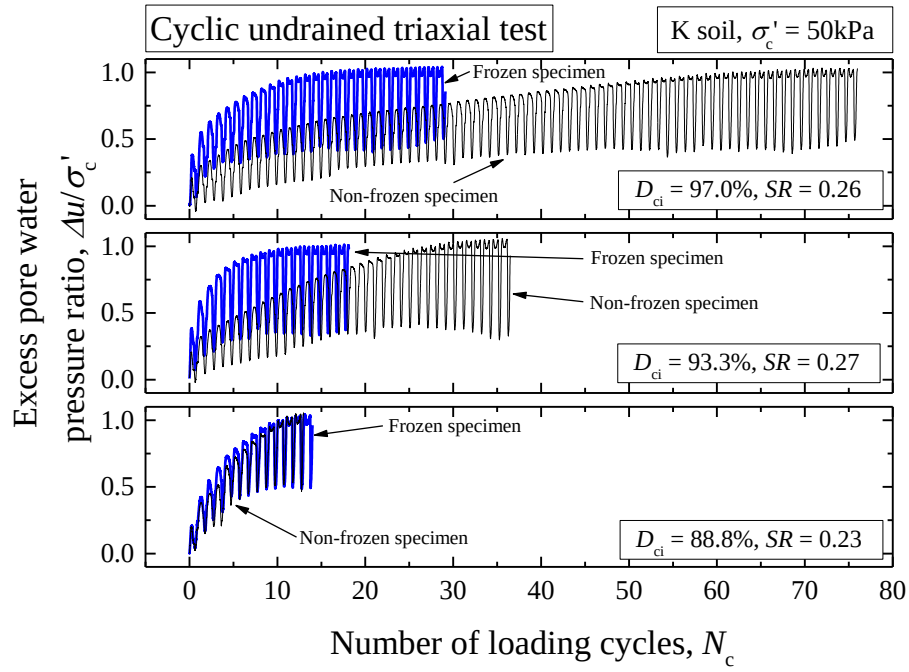

(b) Excess pore water pressure

Figures 5.2.16 Time histories on cyclic triaxial tests for frozen and non-frozen specimens compacted at different degrees of compaction

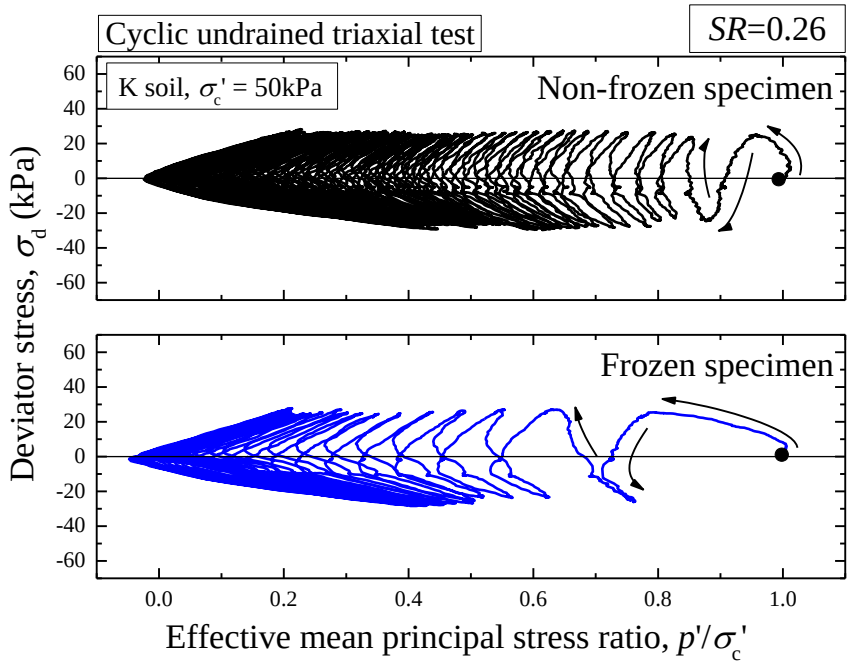

(a) D_{ci} = 97.0%

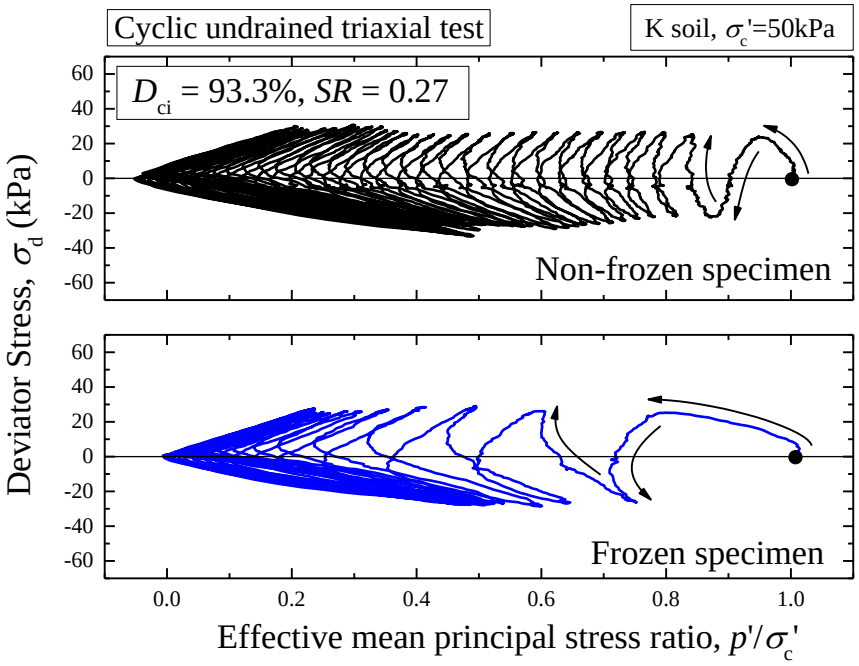

(b) D_{ci} = 93.3%

Figures 5.2.17 Effective stress paths during cyclic loading with regard to each degree of compaction

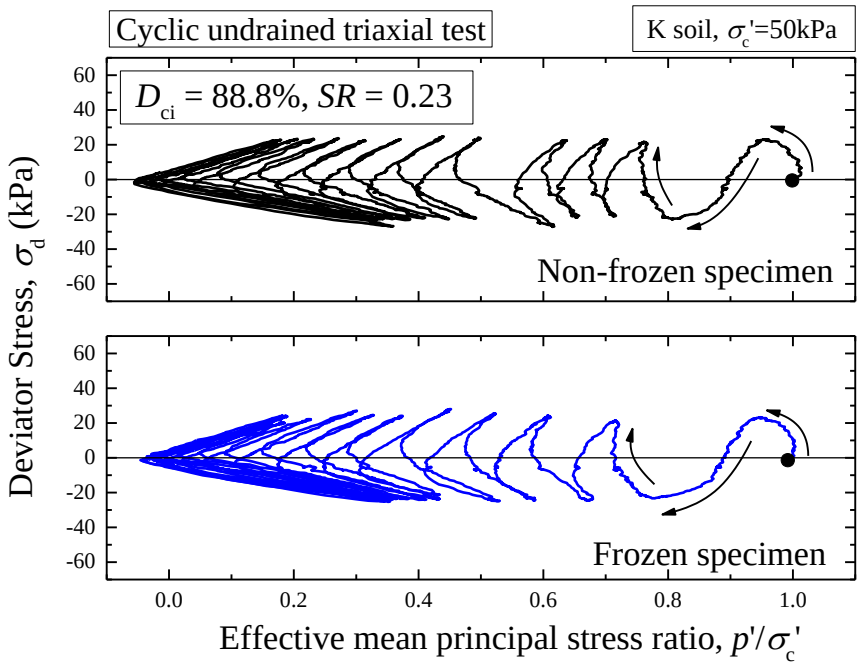

(c) D_{ci} = 88.8%

Figures 5.2.17 Effective stress paths during cyclic loading with regard to each degree of compaction

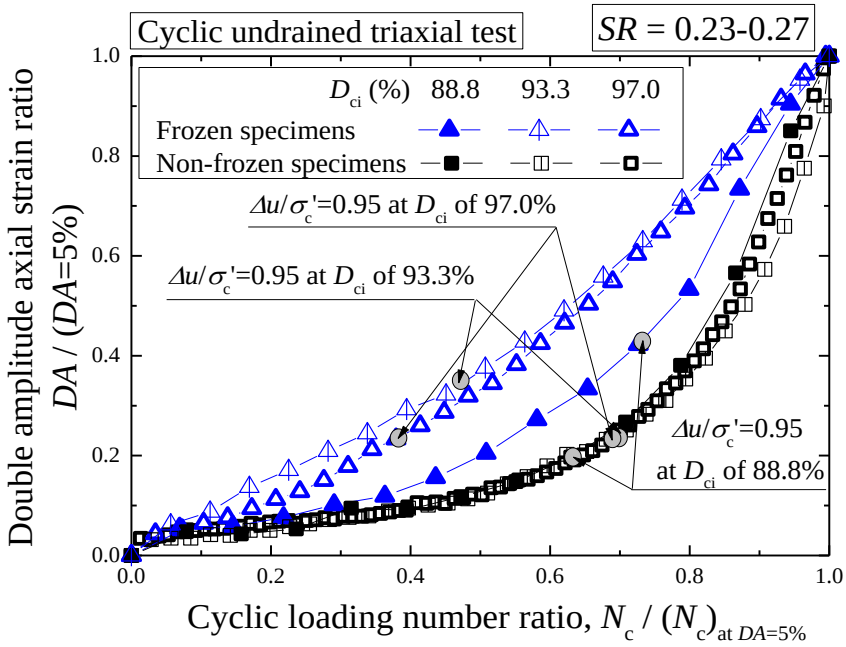

Figure 5.2.18 Cyclic deformation behavior for specimens different in degree of compaction: relation of $DA/(DA=5\%)$ vs. $N_c/N_{c\ at\ DA=5\%}$

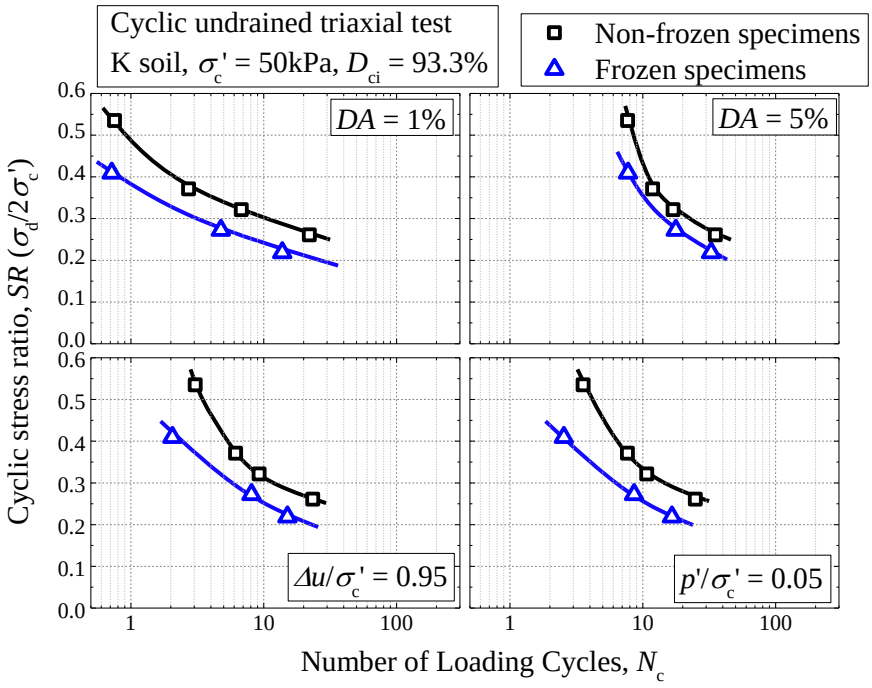

(a) D_{ci} = 93.3%

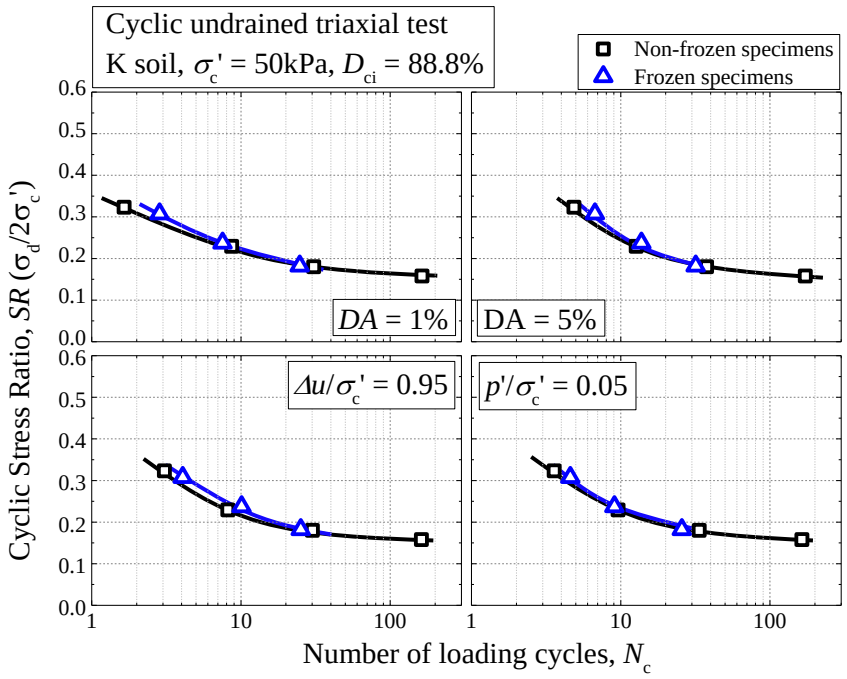

(b) D_{ci} = 88.8%

Figures 5.2.19 Liquefaction strength to attain *DA* of 1 and 5 %, *Δu* increasing 95 % of σ_c' and *p*' decreasing 5 % of σ_c'

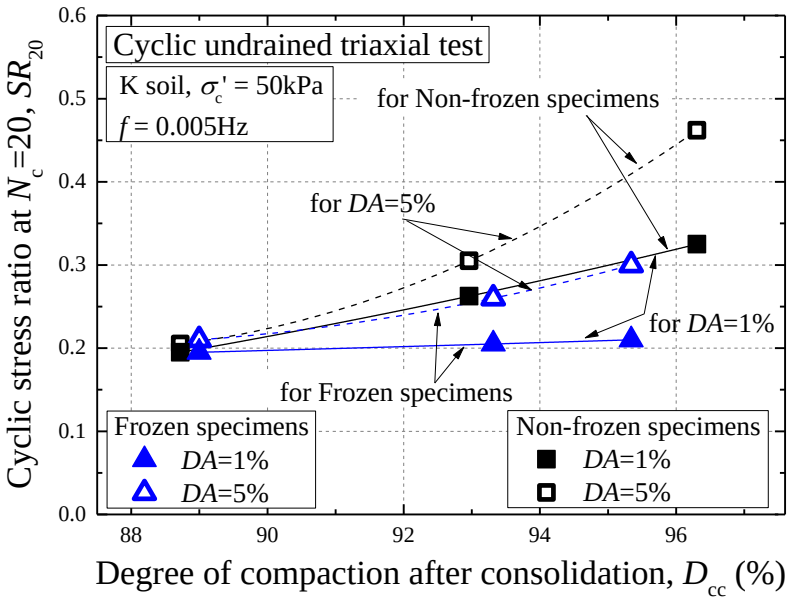

Figure 5.2.20 Relations between D_{cc} and SR_{20} at DA=1 and 5% for frozen and non-frozen specimens

5.3 Change in mechanical properties due to finer fraction

5.3.1 Introduction

Embankments constructed in Hokkaido using coarse-grained volcanic soils are considered to be exposed to the various factors to crush the constitutive particles, such as compaction, consolidation, earthquakes and freeze-thawing (Miura et al. 2003 and Ishikawa and Miura 2011). In this study, change in cyclic mechanical properties of compacted volcanic soils due to finer fraction was examined focusing on the difference of finer content F_c (%).

A series of liquefaction tests was conducted using the cyclic triaxial apparatus shown in Figure 4.1.4. The used materials are K soil, $K_{1.9}$, $K_{17.4}$ and $K_{48.2}$ introduced in *CHAPTER 3*. Those specimens were compacted under various compaction conditions based on the molding water content w_i (%) and initial degree of compaction D_{ci} (%). Afterwards, the saturation and consolidation procedures mentioned in *CHAPTER 4* were followed prior to cyclic shearing. The cyclic loads were applied with the frequency f of 0.1 Hz under the undrained condition until the double amplitude axial strain reached 10 %.

In the thesis, the cyclic shear strength properties will be discussed on the basis of the relation between the cyclic stress ratio SR and number of cyclic loads N_c to cause the double amplitude axial strain DA of 5 %. Figures 5.3.1 (a) ~ (d) show the SR-N_c relations of $K_{1.9}$, $K_{17.4}$, K soil and $K_{48.2}$, respectively. The results of K soil in Figure 5.3.1 (c) are exactly the same to those in Figure 5.1.10. The averages of molding water contents w_i (%) and dry densities after consolidation ρ_{dc} (g/cm^3) for each liquefaction curve are shown in the figures, which include the variations in ±2 % and ±0.018 g/cm^3, respectively. The following discussion is focused on the SR values to cause DA of 5 % with N_c of 20, namely SR_{20}, obtained from each liquefaction curve in Figures 5.3.1. Then, in understanding change in cyclic

shear strength properties of compacted soils due to finer fractions, two concepts will be employed;

1) Effect of finer content at compaction on the cyclic strength behavior, simulating some embankments compacted using some volcanic soils different in grain size distribution,

2) Effect of increment of finer content due to particle breakage on the cyclic shear strength behavior, simulating an embankment compacted using a crushable volcanic soil, and it is exposed to the various factors to cause particle crushing.

Regarding the above second discussion, this study concentrates on only the difference of finer content using four materials degradation-controlled beforehand, and therefore, it cannot identify how and how much the particle breakage occurs due to the various factors mentioned above. In the thesis, accordingly, it is presumed that the change in the cyclic strength resulting from the difference of finer content simulate the influence of increment of finer content due to the particle crushing.

On the other hand, embankments ordinarily exist under unsaturated condition with cohered by suction. Therefore, it has been concerned that the inflow of water through rainfall, ground water and snowmelt etc. may have the potential to diminish the suction effect, and as a result to trigger significant subsidence of the compacted embankments. Considering that the compacted specimens are fully saturated prior to the examination of cyclic shearing characteristics in the present study, the discussion of the saturation effect on volume change of the specimens will be required. Figures 5.3.2 (a) ~ (d) show the changes in dry density and water content between before and after the saturation and consolidation procedures of $K_{1.9}$, $K_{17.4}$, K soil and $K_{48.2}$, respectively. In the figures, the rates of dry density after consolidation to that at compaction are shown in brackets, and then the positive values correspond to shrinking behavior. In addition, the relations between the initial degree of compaction D_{ci} and that after consolidation D_{cc} are represented in Figure 5.3.3 with regard to each soil material and compaction condition defined in Figure 5.1.2. From Figures 5.3.2 (a) ~ (d), the specimens loosely compacted are basically prone to the stronger shrinkage, but the rates of dry

density reach 1.0 % or less, which are considered insignificant. Furthermore, no tendency of the volume change depending on the molding water content can be found. Such trends are consistent with those in the degrees of compaction in Figure 5.3.3; i.e., it is obvious that the volume change behavior due to the saturation and consolidation procedures conducted in the study cannot be significantly affected by the compaction conditions.

Then, that the effective consolidation stress σ_c' of 50 kPa is sufficiently-small in comparison of the compactive stress seems to be a main reason to explain the above behavior. Iseda and Mizuno (1971) testified that the shrinking behavior of compacted soil caused by consolidation became remarkable with the σ_c' value increasing over the compactive stress. According to Ohta et al. (1991), the compactive stresses by means of the 24.5 N rammer are equivalent to 200 kPa or more. Furthermore, it is pointed out that the volume change behavior due to saturation can be susceptible to the molding water content under the consolidation stresses enough to cause the significant subsidence (Takada et al. 1986). Based on the above, the specimens compacted with Komaoka volcanic soils are considered to retain the soil structure at compaction to some extent even after the saturation and consolidation with σ_c' = 50 kPa, because of little change in volume and no tendency depending on the compaction conditions. The fact implies that the influence of difference in soil structures built by compaction predominates as the cause of the following results, compared with that of the volume change and the corresponding soil structure change due to saturation and consolidation after compaction.

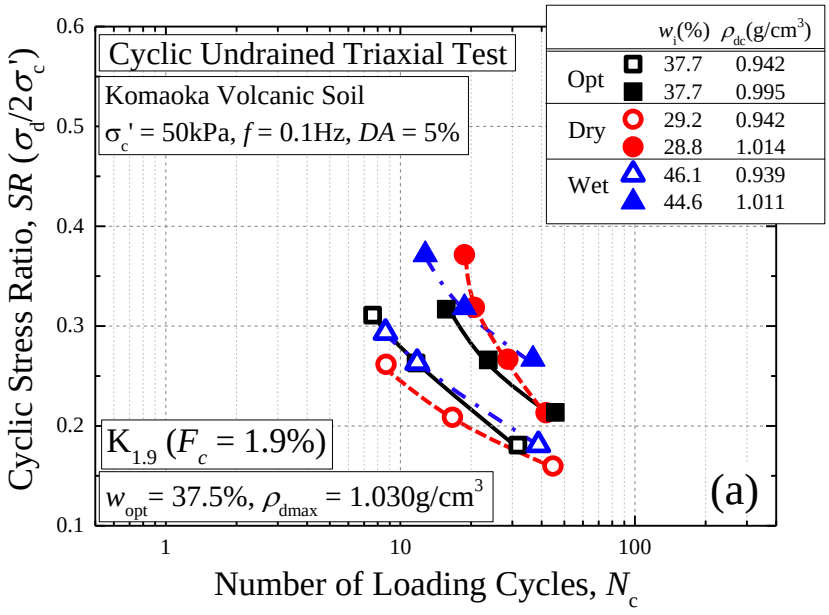

(a) $K_{1.9}$

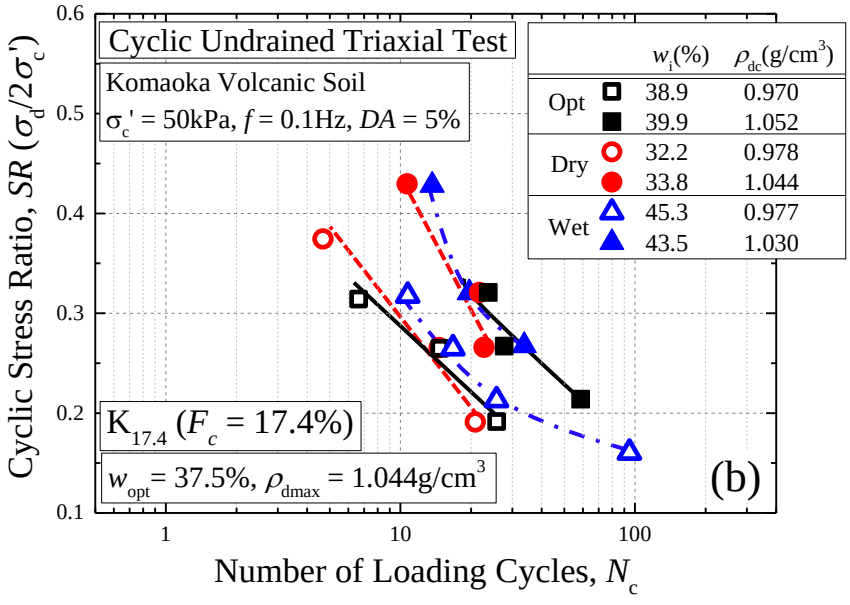

(b) $K_{17.4}$

Figures 5.3.1 Liquefaction curves to cause *DA* = 5%

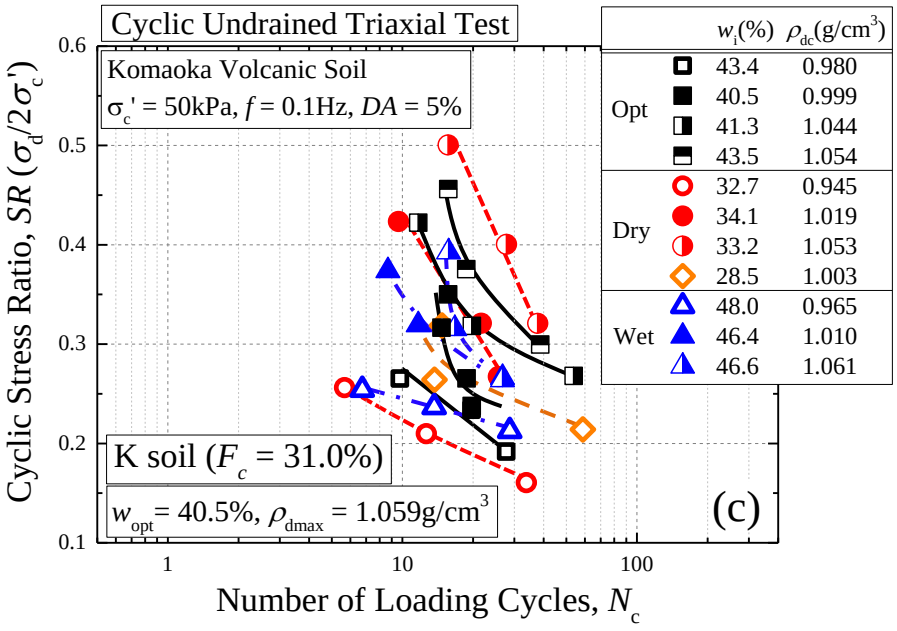

(c) K soil

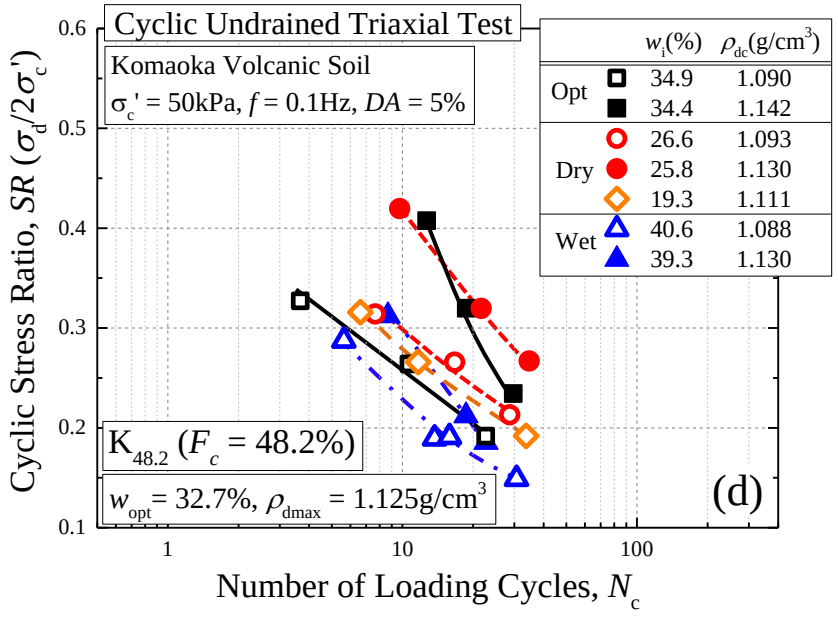

(d) $K_{48.2}$

Figures 5.3.1 Liquefaction curves to cause *DA* = 5%

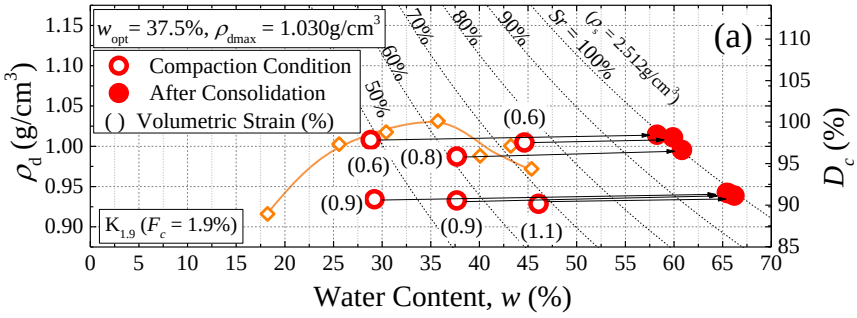

(a) $K_{1.9}$

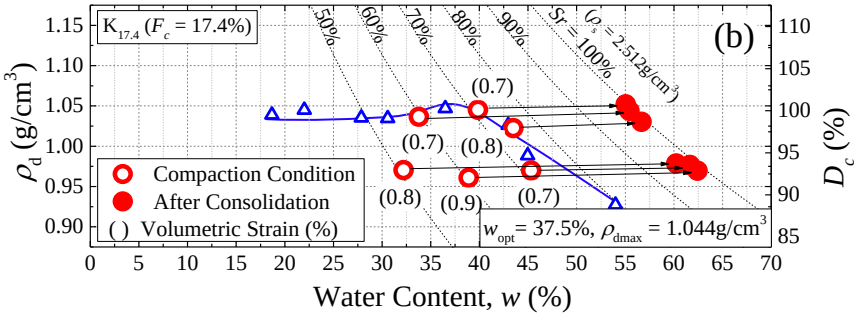

(b) $K_{17.4}$

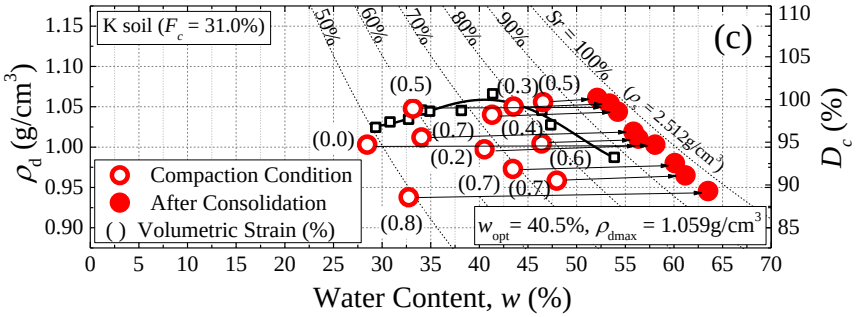

(c) K soil

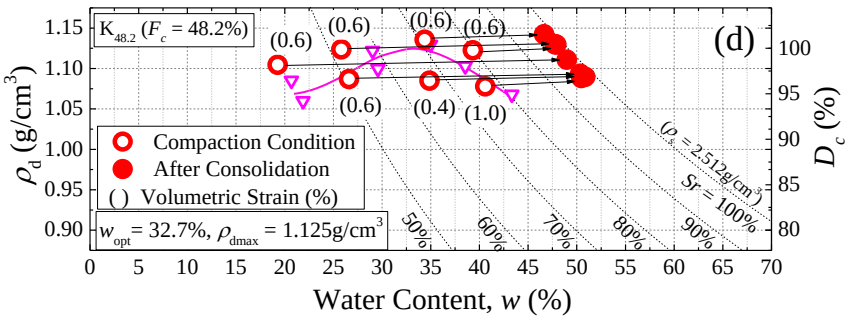

(d) $K_{48.2}$

Figures 5.3.2 Volume change behavior due to saturation and consolidation

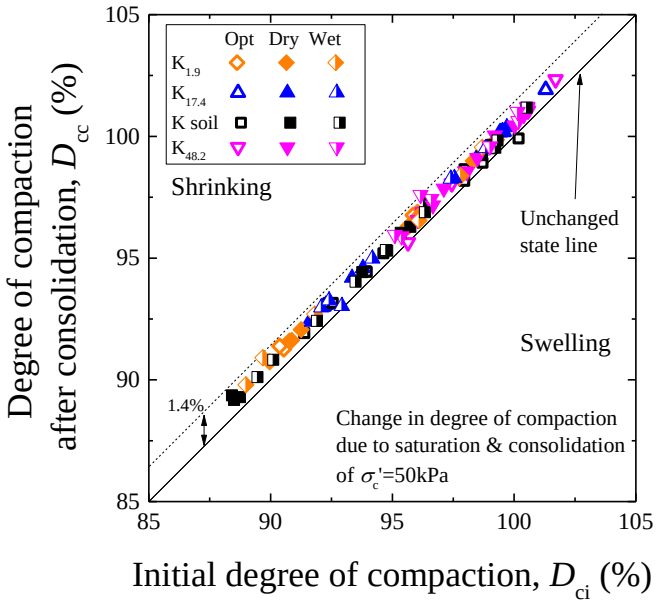

Figure 5.3.3 Change in degree of compaction (dry density) due to saturation and consolidation for $K_{1.9}$, $K_{17.4}$, K soil and $K_{48.2}$

5.3.2 Effect of finer content at compaction on cyclic strength behavior

In this section, the effect of finer content F_c (%) at compaction on the cyclic strength behavior under various compaction conditions will be discussed, simulating some embankments compacted using some volcanic soils different in grain size distribution. Then, because the compaction properties vary depending on the F_c value as mentioned in *CHAPTER 3*, the compaction conditions are classified based on each optimum water content w_{opt} (%) and maximum dry density ρ_{dmax} (g/cm^3) (*see* in Table 3.2.1 (b)) in the same manner to Figure 5.1.2. Figure 5.3.4 shows the compaction conditions of the cyclic triaxial specimens using $K_{1.9}$, $K_{17.4}$, K soil and $K_{48.2}$. Note that each condition is plotted with the averages of molding water content w_i/w_{opt} and initial degree of compaction D_{ci} (%) of the specimens belonging to the same group to obtain a liquefaction curve indicated in Figures 5.3.1. Additionally, those of I soil specimens are illustrated as well by way of comparison.

In order to examine the cyclic strength behavior that varies depending on the compaction conditions and the finer content F_c of compacted soils, the cyclic strength values SR_{20} are plotted on each compaction plane with the isolines of SR_{20} for $K_{1.9}$, $K_{17.4}$, K soil and $K_{48.2}$ in Figures 5.3.5 (a) ~ (d), respectively. In addition, Figure 5.3.6 indicates the result of I soil coordinated in the same manner on the basis of Figure 5.1.9. Note that both axes in the compaction planes are normalized by each w_{opt} and ρ_{dmax}, and the degree of compaction is the value after consolidation, D_{cc} (%). First, regarding the effect of degree of compaction, it is clear that its increase can lead to the increase in the cyclic strength for any soil materials shown in the figures to a certain degree. On the other hand, mentioning the influence of the molding water content, an obvious difference can be recognized between the soil materials. That is, from Figures 5.3.5 (a) and (b), because the specimens have the similar SR_{20} values comparing the results on the same degree of compaction, the cyclic strength tends to be uniquely determined by the degree of compaction regardless of the molding water content w_i/w_{opt} for $K_{1.9}$ and $K_{17.4}$, which have the comparatively-low finer contents. In contrast, for K soil and $K_{48.2}$

that contain the finer fractions over 30 % in F_c, it is obvious that the effect of w_i/w_{opt} on the cyclic strength appears as shown in Figures 5.3.5 (c) and (d). The SR_{20} values increase with the w_i/w_{opt} value lower, and therefore the peak cyclic strength can be found in the drier sides. Furthermore, under the optimum condition and the wetter one where the w_i/w_{opt} values become 0.9 to 1.1 and over 1.1, respectively, the cyclic strength is prone to the drastic decrease with w_i/w_{opt} higher even though the specimens are cyclically sheared at the same dry density. Then, within w_i/w_{opt} of 0.8 to 1.2 and D_{cc} more than 98 %, the SR_{20} values at the wetter condition are reduced to about 60 % of those at the drier condition for K soil and $K_{48.2}$. Such cyclic strength behavior depending on the molding water content could be confirmed in the result of I soil as well, as shown in Figure 5.3.6. Thus, although the property of the finer fractions such as the plasticity differs between Komaoka volcanic soil and Ikeda sandy silt, from the viewpoint of finer content F_c, the significant effect of the molding water content on the cyclic strength seems to emerge at F_c increasing over 30 % within the target water content range.

Figure 5.3.7 demonstrates the relations of the cyclic strength SR_{20} with the degree of compaction D_{cc} and compaction energy ratio E, which is equal to the number of blows in compacting specimens normalized by 75 times. First, from the SR_{20}-D_{cc} relations, as mentioned above, the $K_{1.9}$ and $K_{17.4}$ specimens show those unique relations to a certain degree regardless of the water content at compaction, and the SR_{20} values become almost similar between $K_{1.9}$ and $K_{17.4}$. In contrast, it could be understood that the cyclic strengths are exerted in different ways depending on the molding water content even though the specimens were compacted at the same density, in both cases of K soil and $K_{48.2}$. Furthermore, focusing on $K_{48.2}$, the cyclic strengths are likely to be totally lower compared with those of the other materials. The fact is considered to result from the difference of soil structures as a possible reason as explained later. On the other hand, in the relations between SR_{20} and E, it is obviously seen that the increases in the compaction energy contribute to the cyclic strength

increase, and it seems to be similar tendency among $K_{1.9}$, $K_{17.4}$, K soil and $K_{48.2}$. Furthermore, little influence of the molding water content w_i can be found even for K soil and $K_{48.2}$, and the relations between SR_{20} and E become comparatively-unique regardless of w_i, in contrast to the above relations with the degree of compaction.

In order to reveal the effect of particle breakage on the above testing results, Figure 5.3.8 plots the increment of finer content ΔF_c (%) throughout a series of the cyclic triaxial tests with regard to each soil material. From the figure, it is seen that the particle breakage becomes remarkable with the initial finer content lower and the specimen denser, although there is variation in the experimental data. Accordingly, the $K_{1.9}$ specimens, which contain the finer content F_c of 1.9 % prior to compaction, indicate the highest crushability of the constitutive particles, and their ΔF_c values achieve almost more than 5 %. In contrast, in the case of $K_{48.2}$ that has F_c of 48.2 %, very little increment of finer fractions can be detected. Therefore, it could be understood that the $K_{48.2}$ specimens did not cause the particle crushing under the compaction, consolidation and cyclic shearing conditions adopted in the study. The fact implies that the effect of the compaction conditions on the cyclic strength behavior of $K_{48.2}$ mentioned above does not result from particle crushing and the corresponding rearrangement of soil structure, but the finer fractions contained beforehand in compacting. Furthermore, for K soil that has F_c of 31.0 %, a little particle breakage can be confirmed with the specimens compacted more densely. That means the above strength behavior of K soil is possibly affected by both effects of the finer fractions at compaction and its increment throughout the testing.

In the previous researches, it has been pointed out that the quantitative and qualitative characteristics of finer fractions such as the finer content F_c (%) and the plasticity index *IP* have a significant influence on strength-deformation behavior in liquefying (Kuwano et al. 1993, Hwang et al. 1993, Yajima et al. 1999, Sato et al. 1997 and Liu and Mitchell 2006). Furthermore, such effect has been often discussed based on change in soil fabric with F_c increasing. Therefore, the soil fabrics of

compacted soil using $K_{1.9}$, $K_{17.4}$, K soil and $K_{48.2}$ at cyclic shearing were briefly observed as follows. Prior to the discussion, Equations (5.2) and (5.3) represent the definitions of void ratio and granular void ratio, which are referred to as e and e_g (Thevanayagam et al. 2002).

$$e = \frac{V_v}{V_{sc} + V_{sf}} \tag{5.2}$$

$$e_g = \frac{V_v + V_{sf}}{V_{sc}} \tag{5.3}$$

where, V_v, V_{sf} and V_{sc} are the volumes of void, finer fractions and coarse fractions, respectively. Hence, the granular void ratio corresponds to the volume ratio of the void including the finer fractions to the coarse fractions, regarding the finer fractions as the void, unlike the void ratio generally used. Figure 5.3.9 shows the e and e_g values after consolidation for each specimen of $K_{1.9}$, $K_{17.4}$, K soil and $K_{48.2}$, related with the finer content after shearing F_c' (%). To be exact, it is not possible to identify the soil fabric during shearing, which can vary depending on grain size distribution, because the sieving analysis for the F_c' value was conducted after shearing. However, it is presumed that the particle breakage during cyclic shearing procedure, where the effective stress decreases, could not be significant, based on the previous researches (Miura and Yagi 1997). Accordingly, the F_c' value can be regarded as the finer content during cyclic shearing in this study. In the figure, additionally, the maximum and minimum void ratios (JGS 0161-2009), e_{max} and e_{min} of $K_{1.9}$ are shown as the broken lines to help understanding of each soil fabric. From Figure 5.3.9, it could be understood that the void ratio e of $K_{1.9}$ comes close to its granular void ratio e_g, and the e value tends to decrease with F_c' higher while the e_g value increases. The fact is attributed to the decrement of coarse fractions with the finer fractions increasing. Furthermore, from the solid line to approximate the change in the granular void ratio e_g, the e_g value achieves e_{max} = 2.734 of $K_{1.9}$ at F_c' of 34.2 %. Then, $K_{1.9}$ with e_{max}, whose finer fractions were almost eliminated, is considered corresponding to the loosest soil

structure that the coarse fractions can build. That means the transition of soil structures at F_c' of 34.2 %; i.e., the coarse fractions to play a main role to build the soil fabric at F_c' less than 34.2 % tend to be involved inside the finer fraction fabric at F_c' of 34.2 % or more. Accordingly, the soil fabrics of $K_{1.9}$ and $K_{17.4}$ are likely to be supported by the coarse fractions, while that of $K_{48.2}$ are probably sustained by the finer fractions. Moreover, the K soil specimens seem under the transitional situation of soil fabric changing due to the finer content. Keeping in mind the above, it could be concluded that the afore-mentioned effect of the molding water content on the cyclic strength behavior tends to be remarkable on the K soil and $K_{48.2}$ specimens, whose soil fabrics begin to be mainly built by the finer fractions. On the other hand, the cyclic strength properties of $K_{1.9}$ and $K_{17.4}$ which are fundamentally structured by the coarse fractions, are considered insusceptible to the water content at compaction. However, because the above discussion can indirectly associate the cyclic strength behavior that varies depending on the finer content with the soil structures, an advanced study will be required.

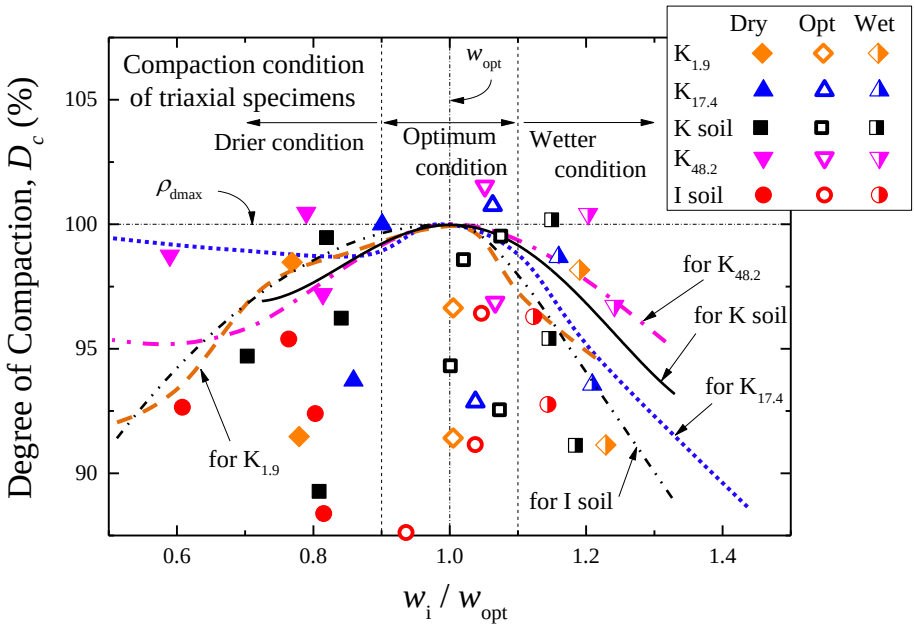

Figure 5.3.4 Compaction conditions of specimens on cyclic triaxial test based on each optimum condition for $K_{1.9}$, $K_{17.4}$, K soil, $K_{48.2}$ and I soil

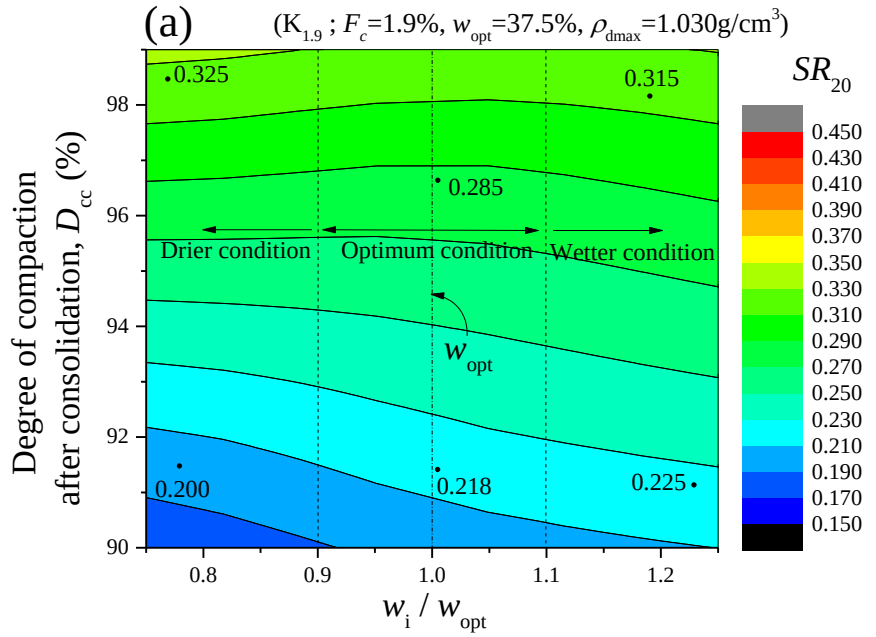

(a) $K_{1.9}$

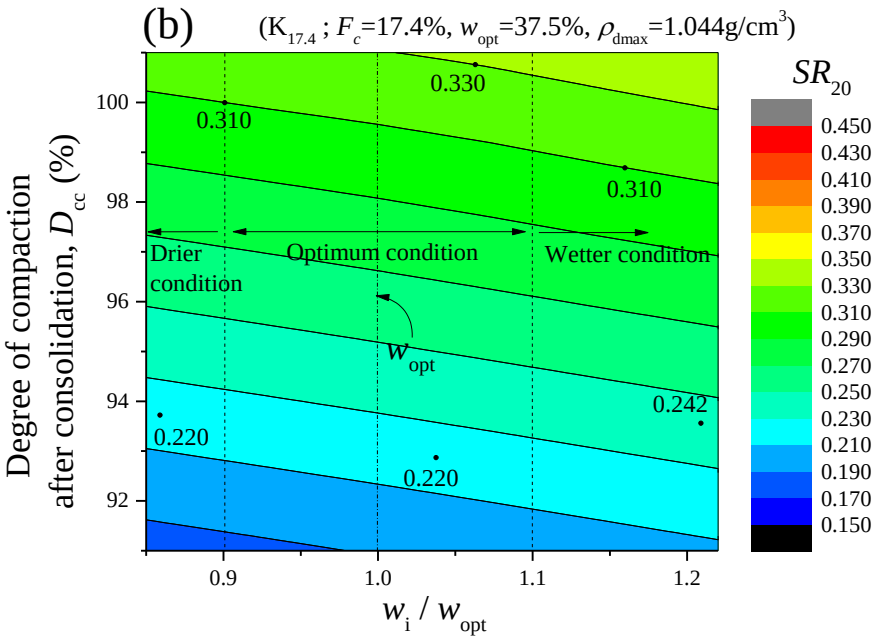

(b) $K_{17.4}$

Figures 5.3.5 Cyclic strength behavior on each compaction plane

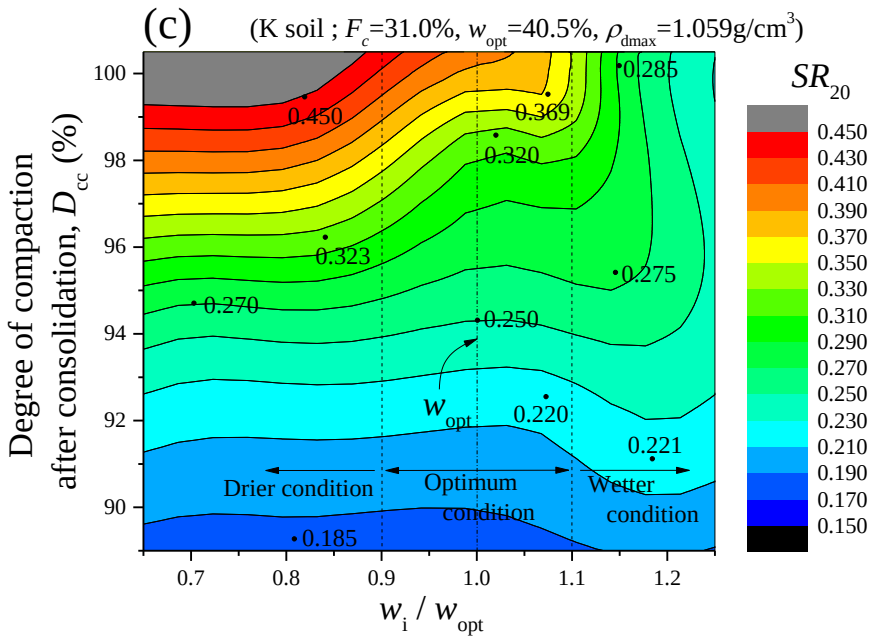

(c) K soil

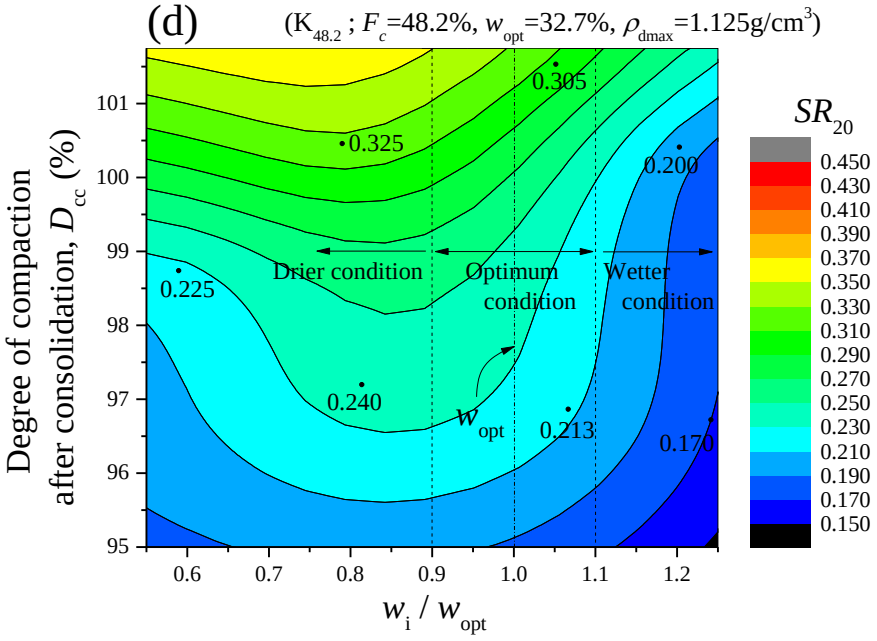

(d) $K_{48.2}$

Figures 5.3.5 Cyclic strength behavior on each compaction plane

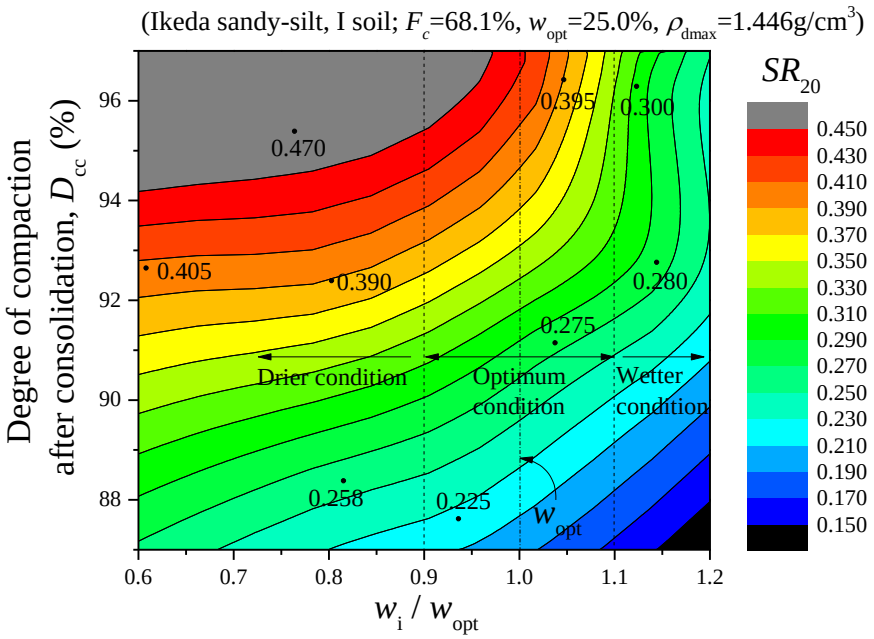

Figure 5.3.6 Cyclic strength behavior on compaction plane for I soil

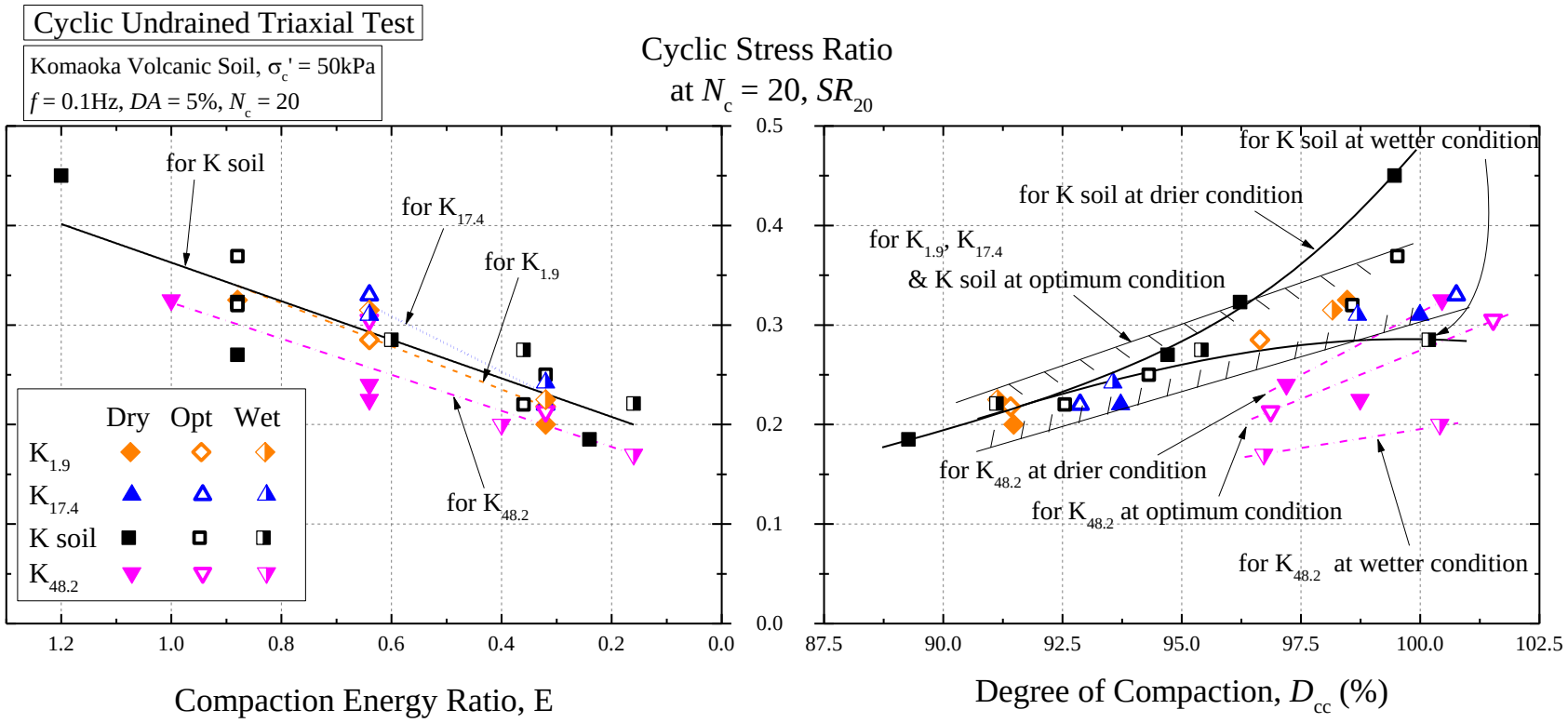

Figure 5.3.7 SR_{20}-E and -D_{cc} relations under various compaction and finer content conditions

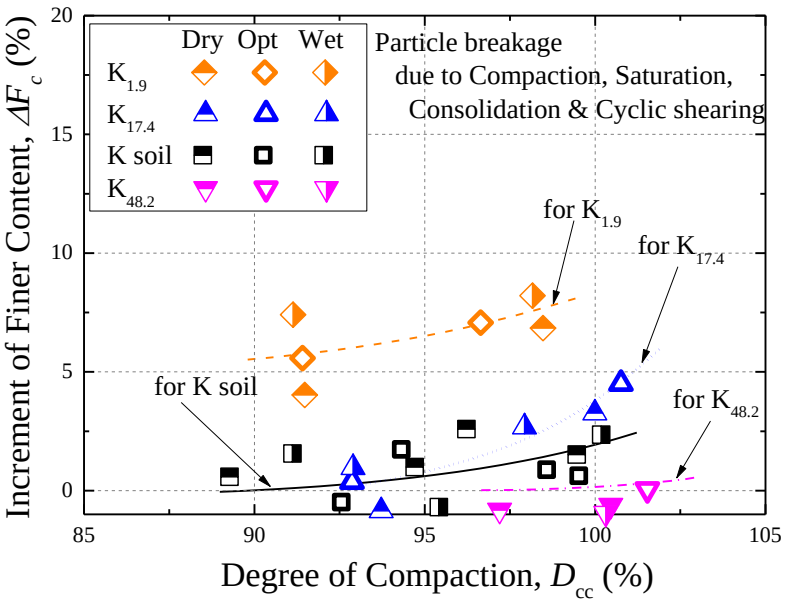

Figure 5.3.8 Particle breakage due to compaction, saturation, consolidation and cyclic shearing under various compaction and finer content conditions

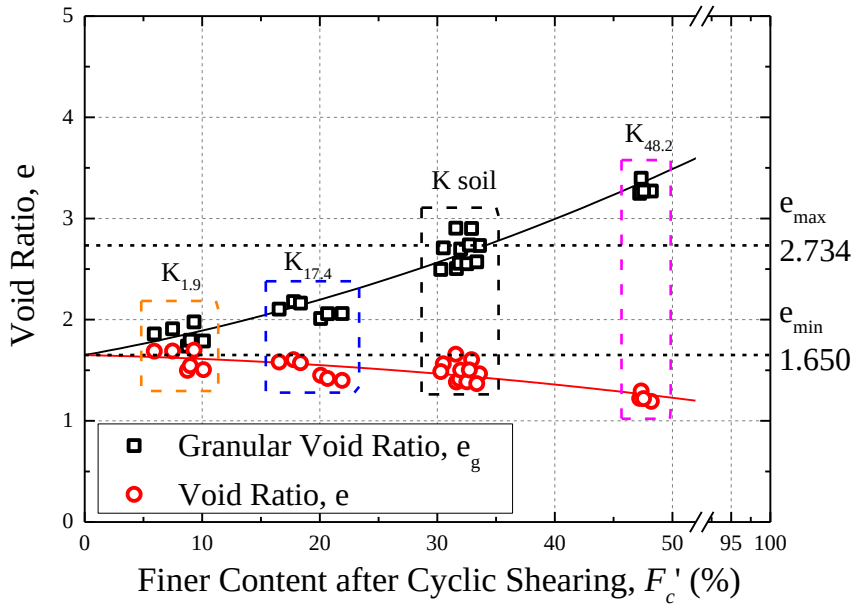

Figure 5.3.9 Changes in void ratio and granular void ratio related to finer content

5.3.3 Effect of increment of finer content due to particle breakage on cyclic shear behavior

In this section, the effect of increment of finer content due to particle breakage on the cyclic shear strength behavior will be discussed, simulating an embankment compacted using a crushable volcanic soil, and it is exposed to the various factors to cause particle crushing. As mentioned above, although the specimens, whose constitutive particles are crushed under desired stress conditions, cannot be simulated, the above discussion is proceeded based on a series of testing results using four soil materials different in the finer content beforehand. To achieve the above aim, the compaction conditions of the specimens shown in Figure 5.3.4 were anew classified in a different way as indicated in Figure 5.3.10. That is, the specimens were categorized according to the water content at compaction w_i (%), to discuss the particle breakage effect developing under a fixed water content condition or changing water content condition. The categorized water content w_i ranges of (I) to (IV) are (I) 37.7 ~ 41.3 %, (II) 32.2 ~ 34.9 %, (III) 25.8 ~ 29.2 % and (IV) 43.4 ~ 48.0 %, respectively.

First, Figure 5.3.11 plots the relations between the cyclic strength SR_{20} and dry density after consolidation ρ_{dc} (g/cm^3) of $K_{1.9}$, $K_{17.4}$, K soil and $K_{48.2}$ classified based on the above. From the figure, the $K_{48.2}$ specimens reach the highest dry densities, but it is not likely to contribute to the strength increase in any compaction conditions. On the other hand, $K_{1.9}$, $K_{17.4}$ and K soil in the w_i range (I) tend to have a unique positive correlation of SR_{20} with ρ_{dc}. In the following discussions, the cyclic strength changing with the finer content increased will be mainly explained on the basis of Figure 5.3.11, simulating the specimens densified due to particle crushing. That is because Komaoka volcanic soil is compacted more densely with the finer content higher even under the same compactive effort, according to the compaction test shown in Figures 3.2.5 and 3.2.7, *CHAPTER 3*.

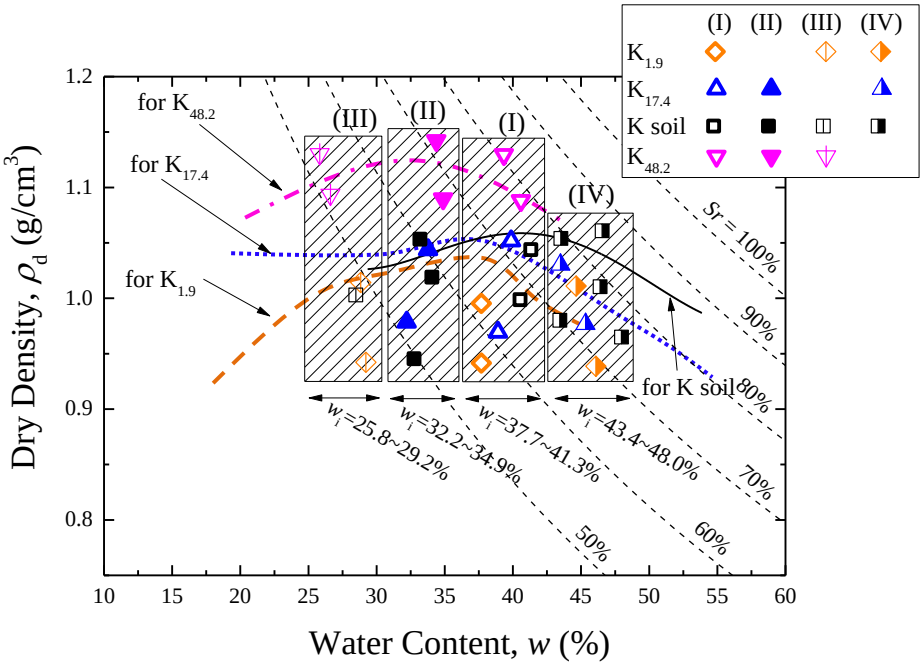

Figure 5.3.10 Classification of compaction conditions based on molding water content w_i for $K_{1.9}$, $K_{17.4}$, K soil and $K_{48.2}$

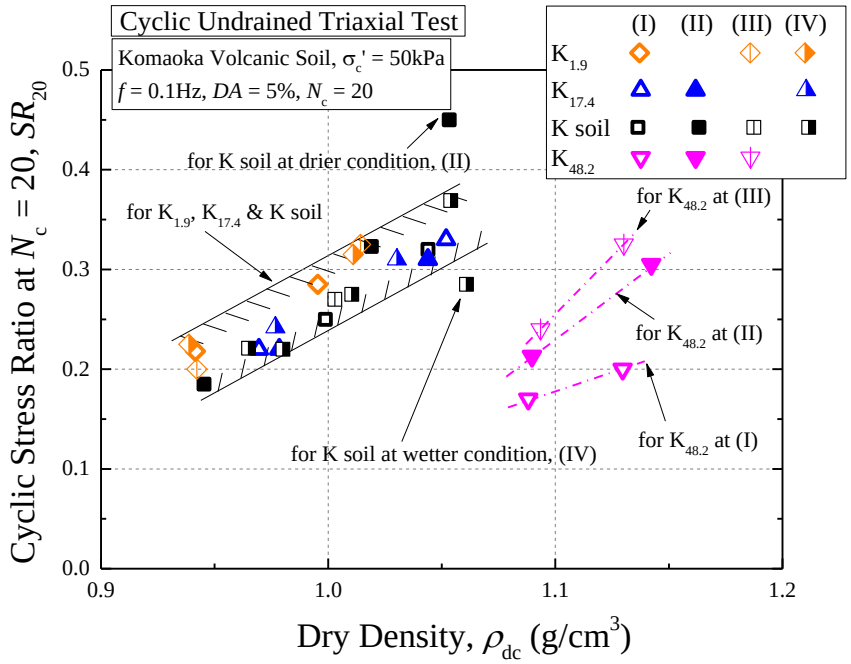

Figure 5.3.11 SR_{20}-ρ_{dc} relations for $K_{1.9}$, $K_{17.4}$, K soil and $K_{48.2}$

5.3.3.1 Change in cyclic shear strength due to particle breakage with water content constant

In this section, change in the cyclic strength of compacted volcanic soils due to particle breakage that occurs under a constant water content will be clarified. Figures 5.3.12 (a) and (b) indicate the relations of the finer content after cyclic shearing F_c' (%) with the cyclic strength SR_{20} and dry density after consolidation ρ_{dc} (g/cm^3) in the cases of (I), (IV) and (II), (III), respectively. Note that the shaded area represents the degree of compaction D_c of 90 to 100 % changing with the finer content F_c (*see* Figure 3.2.7 (b)), and the following discussion will be proceeded related to this D_c range. First, from the path belonging at the water content (I) in Figure 5.3.12 (a), it is seen that the cyclic strength basically increases with the finer content F_c' higher and the corresponding dry density (ρ_{dc}) increasing, at the range of F_c' < 32.7 %. Once the F_c' value exceeds 32.7 %, however, the cyclic strength shifts to decreasing regardless of keeping the ρ_{dc} value increasing. The fact indicates that the change behavior of the cyclic strength due to the particle crushing and the corresponding densification may vary at a specific F_c' value higher than 32.7 %. In addition, the above trend agrees well to the cyclic strength change represented by (IV)-a in Figure 5.3.12 (a), and therefore the strength increase appears accompanied with ρ_{dc} increasing. On the other hand, it is recognized that the cyclic strength change (IV)-b is prone to the decreasing behavior before the F_c' value reaches 32.6 %. That is considered to result from the higher molding water content w_i of 48.0 %; i.e., the difference in w_i becomes significant enough to affect the cyclic strength even in the same water content range (IV) as pointed out in *5.3.2*. Furthermore, from Figure 5.3.12 (b), it is obvious that the peak of the cyclic strength change in the water content (II) appears at the F_c' value of 32.5 %, while the dry density keeps increasing throughout with F_c' higher. In the case of (III)-a, although the similar tendency can be recognized, the decreasing behavior of cyclic strength seems to be weaker. In addition, the path of (III)-b, where the ρ_{dc} value becomes over the maximum dry density ρ_{dmax} at F_c' value of 47.6 %, shows

that the cyclic strength keeps increasing throughout until the F_c' value achieves 47.6 %. In both figures, the other paths regarding the particle crushing with densification could be chosen except the above, but those were considered qualitatively consistent with the afore-mentioned behavior.

Keeping in mind the above, it may be concluded that the relation between the cyclic strength SR_{20} and dry density ρ_{dc} has a positive correlation until F_c' reaches a specific value, and such a relation shifts to the negative one over the threshold of F_c'. Moreover, the threshold of F_c' to change the cyclic strength behavior is likely to depend on the water content at which the particle crushing develops with densification. That is, based on the above results, the higher water content the specimen is, at the lower finer content the correlation between SR_{20} and ρ_{dc} turns negative. In this study, such a threshold of F_c' is considered to appear at around 30 %.

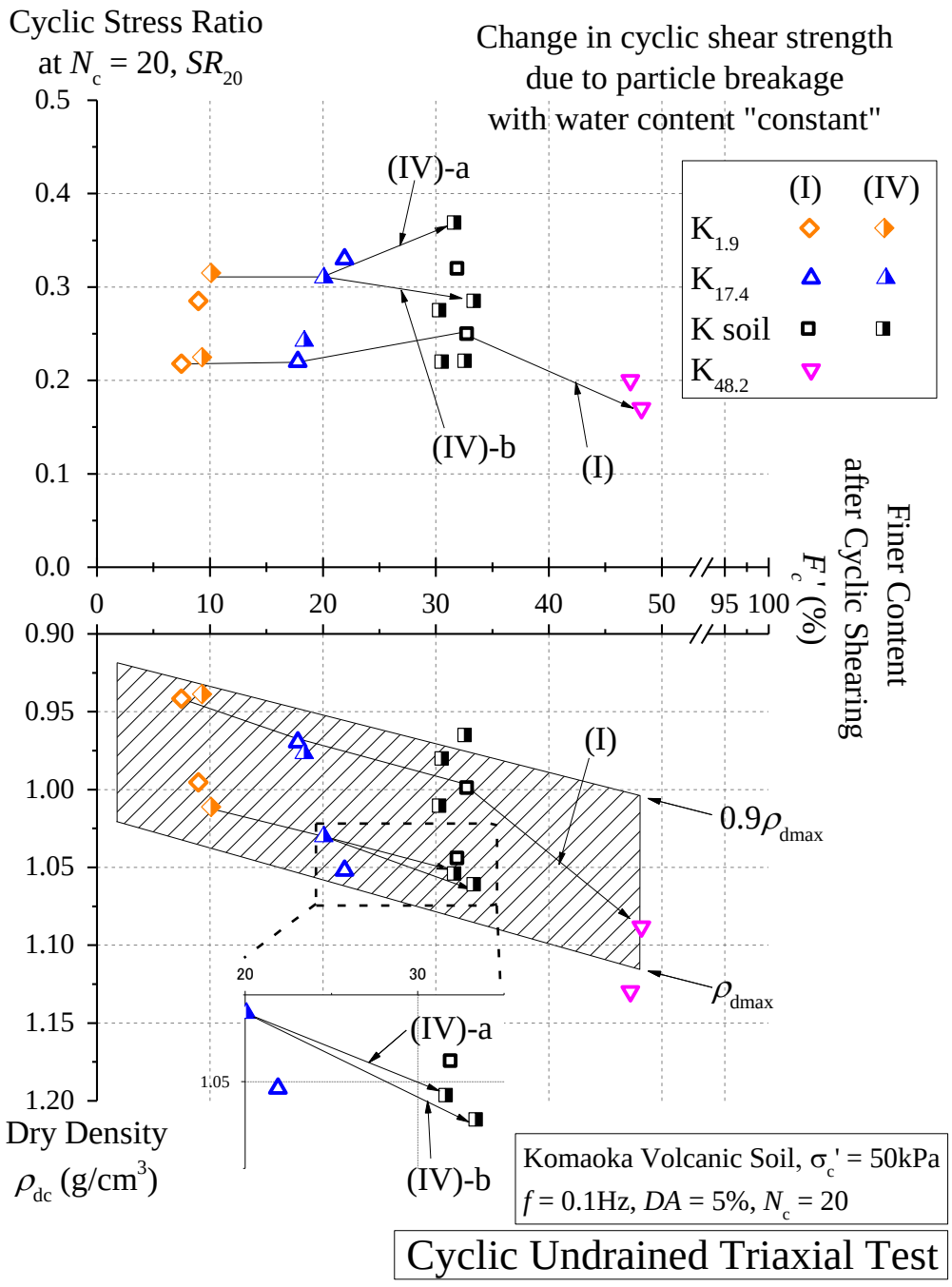

(a) Water content ranges (I) and (IV)

Figures 5.3.12 Change in cyclic shear strength due to particle breakage with water content constant

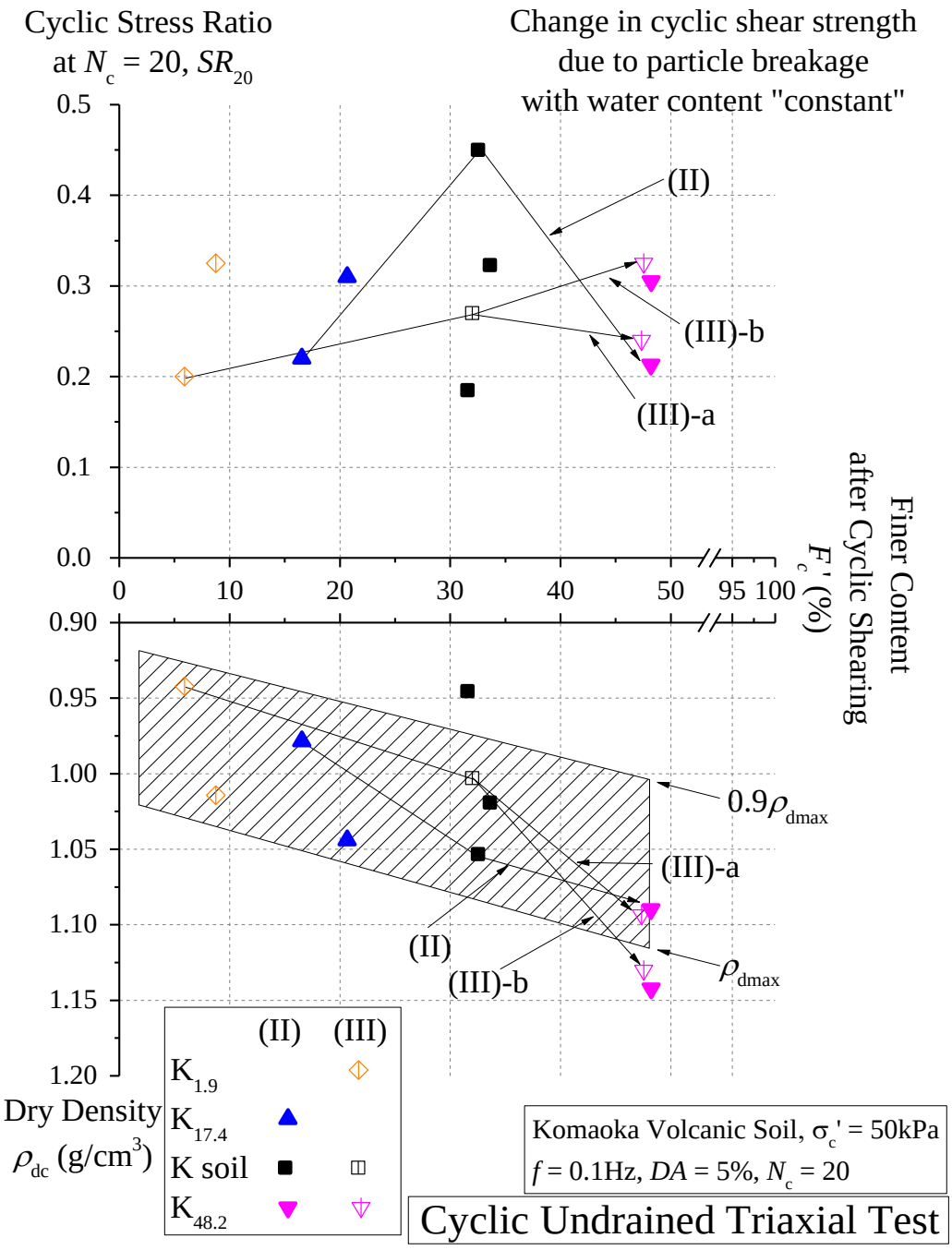

(b) Water content ranges (II) and (III)

Figures 5.3.12 Change in cyclic shear strength due to particle breakage with water content constant

5.3.3.2 Change in cyclic shear strength due to particle breakage with water content changing

In this section, change in the cyclic strength of compacted volcanic soils due to particle breakage that occurs under the changing water content will be discussed. Figure 5.3.13 shows the relations of the finer content F_c' (%) with the cyclic strength SR_{20} and dry density ρ_{dc} (g/cm^3) as well as the previous section. In the figure, the solid arrows simulate the paths where the water content changes during particle crushing with densification. Additionally, the condition that the water content keeps constant discussed in the previous section is given by the dotted arrows for comparison. First, let us look at the paths changing the water content from (I) to (IV), which are represented by (I)-to-(IV)-a and -b, comparing with the constant water content paths of (I)-a and -b. At F_c' increasing from 10 to 20 %, the cyclic strengths are prone to increase with densification in the similar manner regardless of whether the water content changes or not. On the other hand, different behavior appears at F_c' over 20 %; that is, the increment of cyclic strength with densification becomes obviously weaker if the water content increases from (I) to (IV), compared with the constant water content (I) condition. Such a tendency can be also recognized in the comparison of (II)-to-(I)-c with (II)-c, and it is clear that the cyclic strength increasing is strongly inhibited due to the water content becoming higher. In addition, at the procedure where the F_c' value achieves 48 % (*see* (II)-to-(I)-d and (II)-d in the figure), both conditions cause the cyclic strength to decrease with densification, but the changing water content path (II)-to-(I)-d indicates the stronger strength decreasing behavior. On the other hand, comparing the results of (III)-to-(II)-e and (III)-e at the similar F_c' range, where the water contents are comparatively-low, although the above strength decreasing behavior emerges with the water content changing, the degree tends to be smaller than the case of higher water content. Based on the above discussion, it may be derived that the cyclic strength affected by the particle crushing with densification explained in the previous section is also susceptible to whether the water content changes

throughout or not. Therefore, the strength increasing with densification can be reduced while the cyclic strength has a positive correlation with the dry density, until the F_c' value achieves around 30 %. Moreover, at F_c' increasing over 30 %, the change in water content tends to stimulate the strength decrease more significantly with the particle breakage.

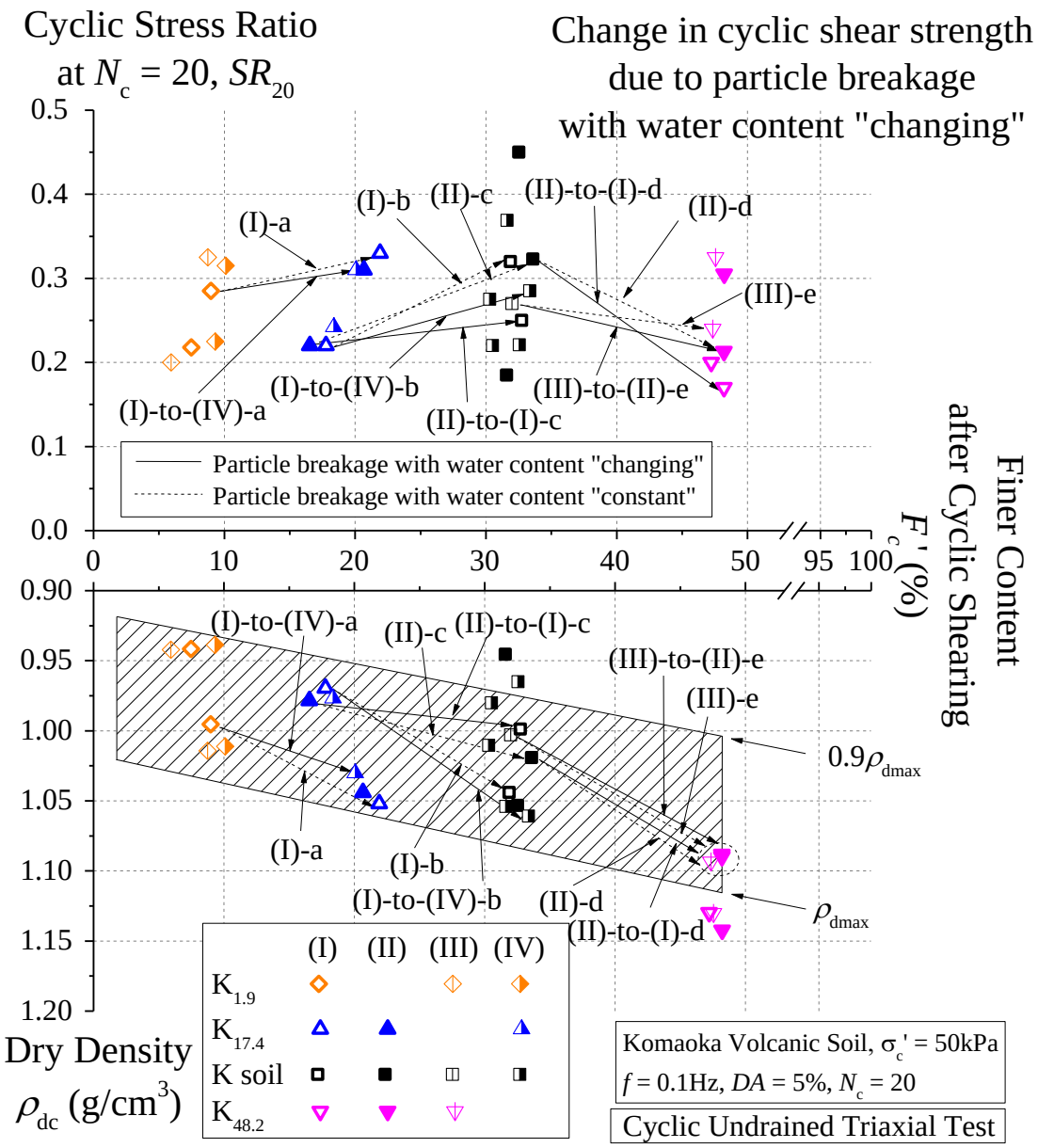

Figure 5.3.13 Change in cyclic shear strength due to particle breakage with water content changing

5.4 Long-term monitoring of full-scale embankment slope and failure test

5.4.1 Introduction

The mechanical properties inside the embankment such as moisture and pore pressure distributions and their changes have been long monitored (2012.11 ~ 2013.11) with the embankment exposed to the natural environmental conditions, e.g., freeze-thawing, inflow of snowmelt, rainfall and earthquake. The attempt had lasted until the embankment led to slope failure at high moisture content condition due to the inflow of water. The results will be in detail analyzed and disclosed in the near future, and therefore, some of them is being briefly discussed in this section.

Figure 5.4.1 shows the climatic condition, air and soil temperatures, rainfall and accumulative snowfall, during whole monitoring term at the embankment site. From their results, at this site, the air temperature dropping below 0 °C was observed for about five months from 2012.11 to 2013.4. Accordingly, the intermissive sub-zero state of soil temperature, when it is regarded as freeze-thaw period in this thesis, can be confirmed inside the embankment within 0.2 m in depth. During the freeze-thaw period the deeper locations inside the embankment keep calm fluctuation of temperature resulting from heat-retention due to accumulated snow. In the snowfall period, a maximum accumulative snowfall of 1750 mm was observed on March, and afterward the rapid snowmelt occurred until the end of April. In the rainfall period, the amount of rainfall reached up to about 20 mm/hr. at a maximum. In the following section, the monitoring results will be introduced with regard to each period and event.

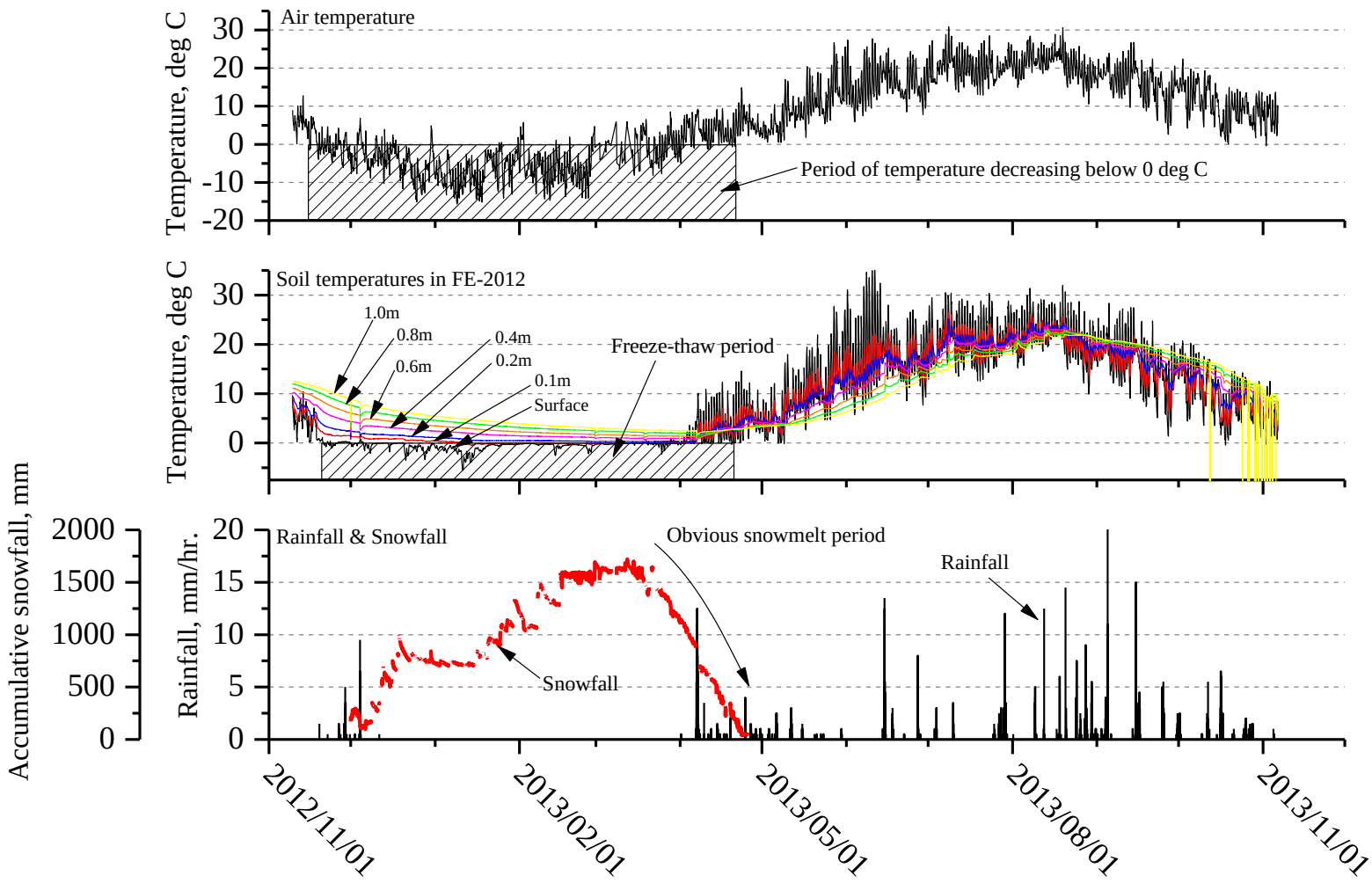

Figure 5.4.1 Climatic condition during whole monitoring term in embankment site

5.4.2 Moisture change and pore pressure properties

5.4.2.1 Freeze-thaw and rainfall periods

Figure 5.4.2 shows change in water content measured by the eight sets of soil moisture meters, $SM_{L0\sim L3,\ R0\sim R3}$ (*see CHAPTER 4*), inside FE-2012 throughout the measurement term. From the figure, it is obvious that the soil moisture behavior at the shallowest layer of 0.2 m in depth from the slope surface indicates sharp fluctuation as well as the trend of soil temperatures. During the freeze-thaw period, as a general trend, the water contents lower at the shallower layer, and drying is pregressing. Afterwards, wetting develops due to rainfall and the compulsory water inflow inside through the water supply pipes; as a result, the water contents achieve approximately 50 %, although the water contents more than 50 % can be also locally confirmed for SM_{R0}.

Figure 5.4.3 illustrates change in pore pressure inside the embankment, FE-2012, and the cut slope, CS. In the figure, the water content fluctuation at 0.6 m in depth, which is corresponding to that of tensiometers, for FE-2012 and CS, rainfall and snowfall are shown as well. The tensiometers, T_{C0} and T_{C3}, had operated to show the similar behavior to the others until February 2012, but were finally stopped due to unexplained error. First, after the embankment was constructed, the pore pressure inside the embankment tends to lower with the water content decreased as mentioned above, as the freeze-thaw period begins and elapses. At the end of the freeze-thaw period, when snowmelt is considered to be remarkably progressing, the drastic increase of pore pressure can be recognized with the water content increased. Such behavior is consistent with the case of the cut slope, and the pore pressure fluctuates linking to the water content at the same depth. Then, that the water content inside the cut slope is relatively higher than those of the embankment, is attributed to the difference in soil materials. As introduced in *CHAPTER 4*, the different soil materials, Soil 1 and Soil 2 which has higher natural water contents, are detected at the depth less than 0.8 m from the slope surface.

Furthermore, at the rainfall event of June shown in the figure, in particular, the pore pressures for FE-2012 rapidly rised close to 0 kPa, and subsequently, it has kept little suction, less than 10 kPa, until the embankment causes slope failure. Then, from the investigation result to identify slip surface, it is estimated at 0.6 ~ 0.8 cm in slope depth, which is equal to that of the tensiometers buried. Meanwhile, the rainfall and water supplying certainly increase the water content inside the embankment, and it is considered to trigger the slope failure. The fact implies that the loss of suction does not always cause collapse of soil, but the slope failure phenomenon needs the increment of water content over certain critical moisture state. Therefore, to evaluate a potential risk of slope failure by water content is considered rational.

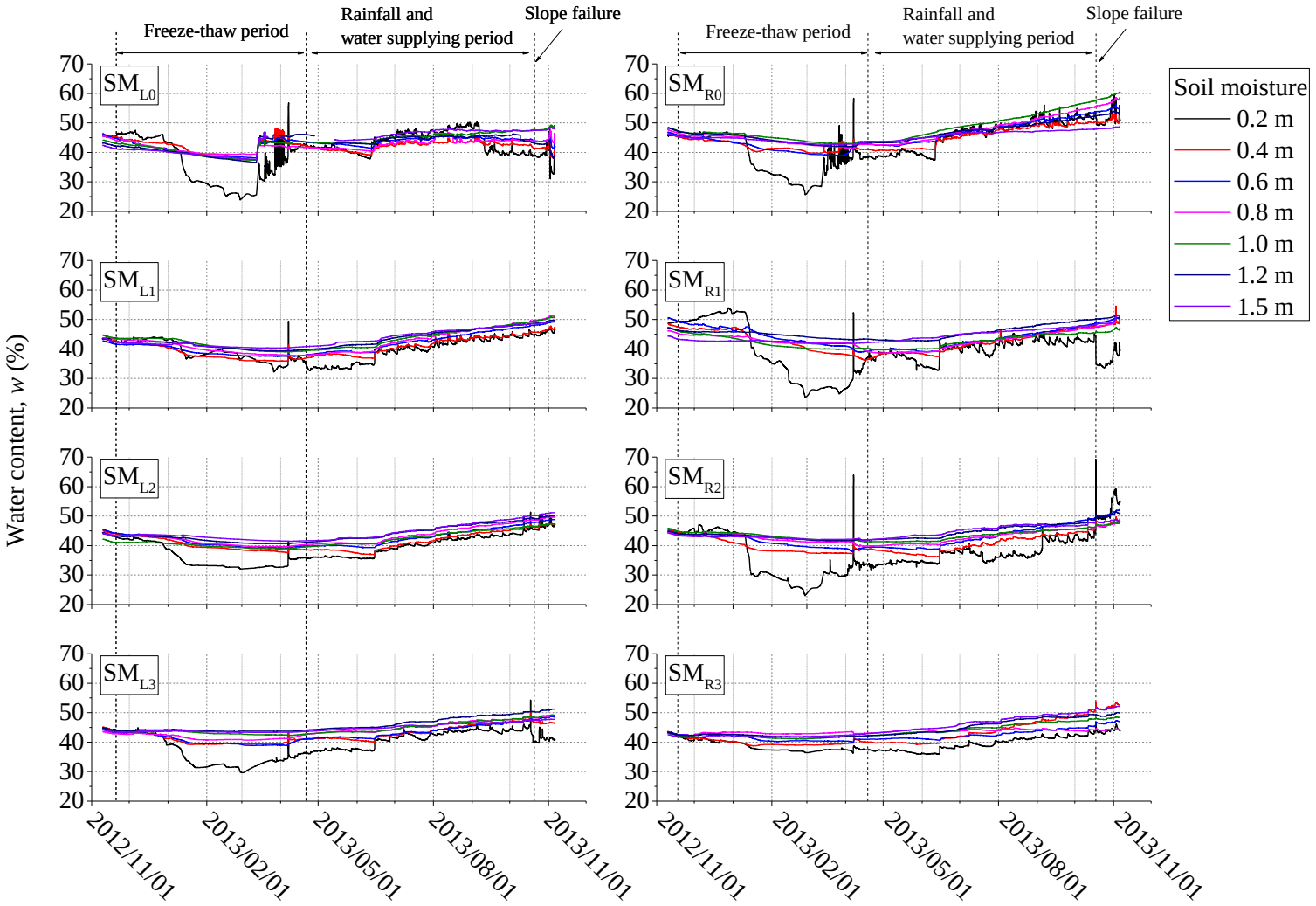

Figure 5.4.2 Moisture changes during whole monitoring term in FE-2012

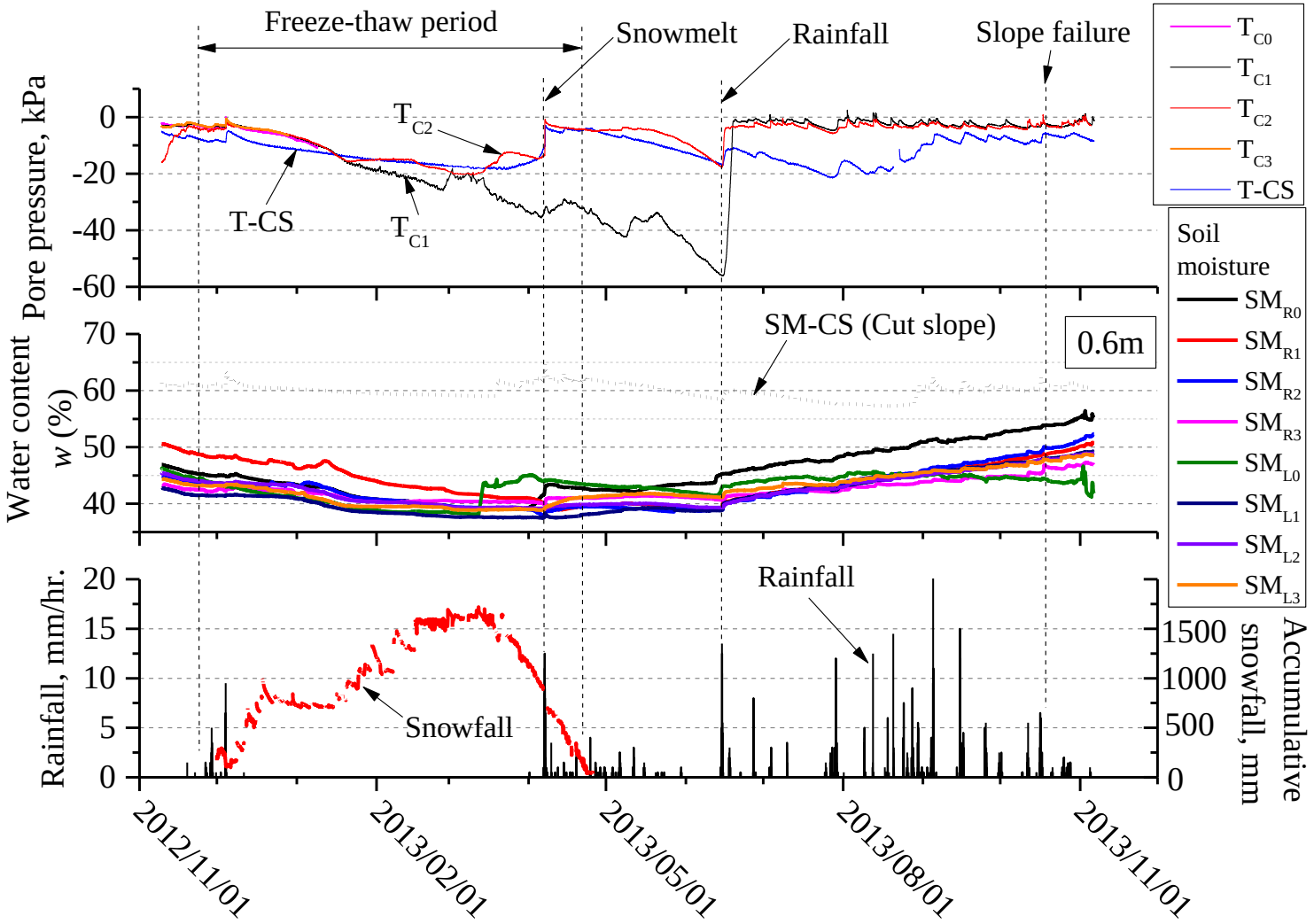

Figure 5.4.3 Pore pressure and moisture change behaviors at 0.6 m in depth in FE-2012 and CS

5.4.2.2 Slope failure

Photographs 5.4.1 (a) and (b) show views of slope failure of the embankment taken on 2013.10.18 and 2013.11.15, respectively. The former was taken immediately after the slope failure, because that the occurrence was at the previous day, 17th, can be estimated from the site investigation and the monitoring results, i.e., discontinuity change of soil moistures. On 2013.11.15, when the latter photograph was taken, the soil involved in the slope failure was eliminated in order to identify the slip surface. Maximum height and depth of slope failure reach approximately 3.0 m and 0.6 to 0.8 m, respectively, at the time of the occurrence. The amount of soil involved in the failure was estimated at about 6 m^3. No rain and no visible change of the embankment could be found on 17th, the previous day. Therefore, it could be presumed that the failure rapidly occurred, but it is attributed not to typical surface failure with shallower layer falling off but to sliding at a weak layer due to water supply. In addition, it is confirmed that the slope failure has been secondarily widened at around the mid slope and top of the embankment as could be seen in Photograph 5.4.1 (b).

Figures 5.4.4 (a) and (b) indicate water content distributions of the L- and R-sections (*see* Figure 4.2.6) on 2013.10.17, when the slope failure just occurred. It is obvious that the water content in the embankment is not homogeneous on each section. In addition, higher moisture state over 55 % in water content can be confirmed at the base, which reaches about 95 % in degree of saturation at average ρ_d = 1.020 g/cm^3 of the embankment as also shown in the figure. Thus, even this embankment, compacted densely at around 95 % in degree of compaction and optimum condition, is considered saturated sufficiently due to the water supply and rainfall. Furthermore, because the soil at such base layer became slurry, it could be understood that the embankment was under very unstable state losing bearing resistance. The slip surface was located at approximately 0.6 to 0.8 m in depth from the slope surface from the site investigation. The water content at the slip surface, therefore, can be estimated mainly at 47 to 51 % from Figures 5.4.4.

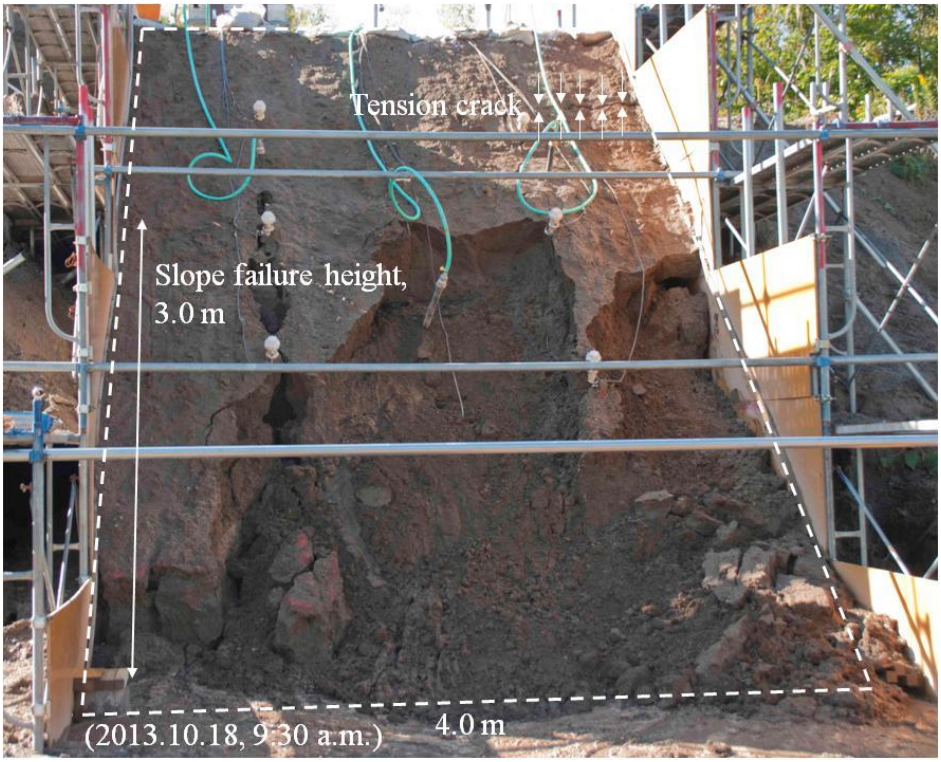

(a) Slope failure of FE-2012 immediately after the occurrence on 2013.10.18

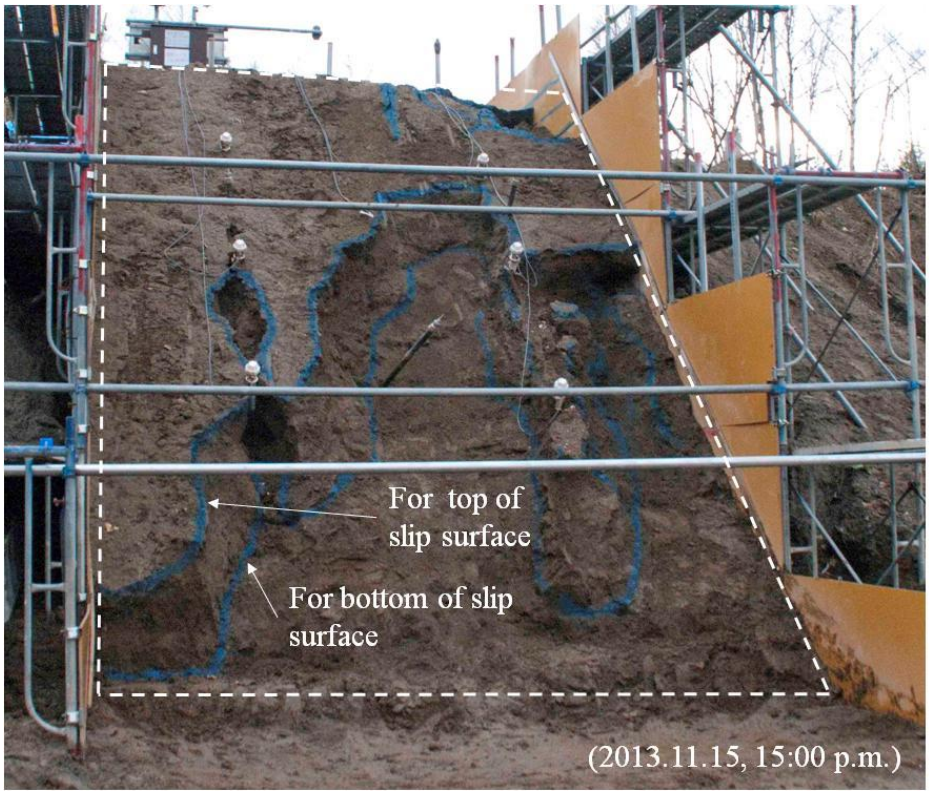

(b) Slip surface identified on 2013.11.15

Photographs 5.4.1 Views of embankment after slope failure

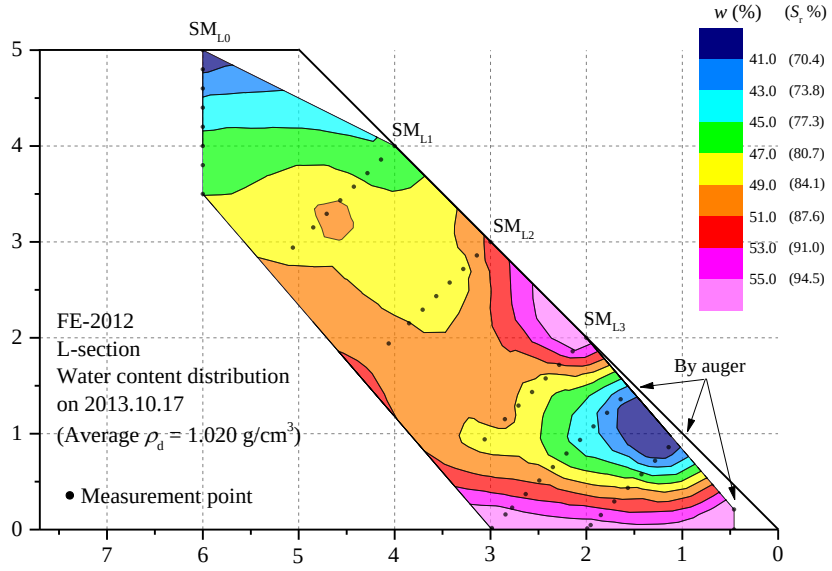

(a) L-section

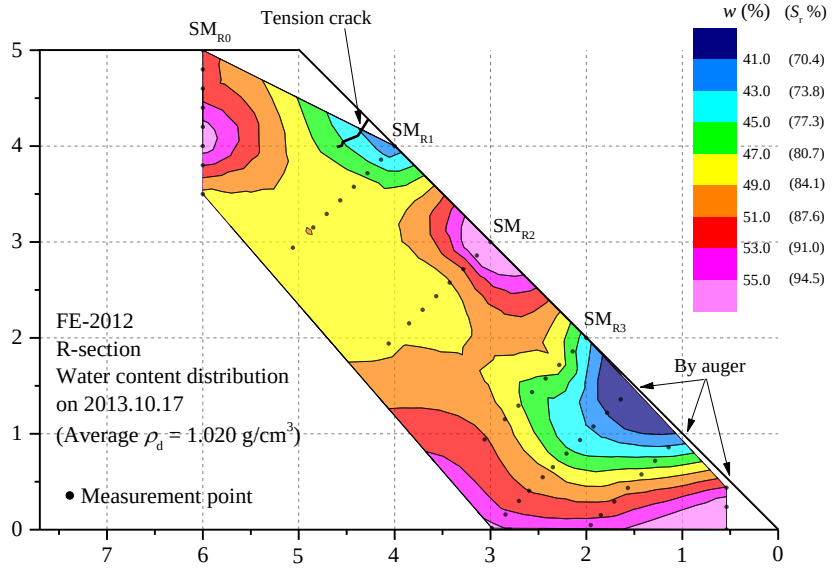

(b) R-section

Figures 5.4.4 Water content distributions at slope failure on 2013.10.17

5.5 Discussion on reasonable design and management for volcanic soil embankments in cold regions

In this thesis, simulating the geotechnical problems that would occur in cold regions such as Hokkaido, the effects of compaction conditions at construction, freeze-thaw sequence and particle crushing on the mechanical characteristics of compacted soil materials have been revealed by means of the laboratory element tests. In addition, a series of in-situ monitoring tests has been conducted with the full-scale embankment constructed by the same soil material as used for the laboratory tests until the embankment leads to slope failure after freeze-thaw period. In this section, possible problems to occur resulting from the above will be discussed with summarizing the testing results.

Let us first discuss the liquefaction strengths of the compacted I soil and Komaoka volcanic soils, i.e., K soil and $K_{original}$, with comparing those of some soils actually liquefied in past earthquake cases. Figures 5.5.1 (a) and (b) exhibit the liquefaction strengths to cause *DA* = 5 % shown in the present study with those of Niigata sand (Ishihara et al. 1978) and reclaimed lands in Port island and Rokko island in Hyogo prefecture (Zen and Yamazaki 1996) and some volcanic soils deposited in Hokkaido (Miura et al. 2003 and Yagi et al. 2005), respectively. The present results correspond to the liquefaction curves for I soil (D_{cc} = 91.7 %), K soil (D_{cc} = 92.5 %) and $K_{original}$ (D_{cc} = 93.1 %) that was sampled with the thin-wall sampler as explained in *CHAPTER 4*, which are all compacted in the optima ($0.9 < w_i/w_{opt} < 1.1$). Ishihara et al. (1978) conducted the liquefaction test using Niigata sand sampled at the Shinano river site by the in-situ freezing method, which were liquefied in Niigata earthquake (1964). Their results are shown in Figure 5.5.1 (a) on the basis of the relative density (Drc = 20 ~ 40 %, 40 ~ 60 %, 60 % ~). Zen and Yamazaki (1996) also adopted the in-situ freezing method for the sands, Masado (decomposed granite soil) that led to liquefaction at Port island and Rokko island by Hanshin earthquake (1995) to examine the liquefaction behavior. First, regarding the liquefaction strength of $K_{original}$ sampled in-situ from the embankment, FE-2012, the strength seems

to be consistent with those of the reconstituted specimen at the similar degree of compaction using K soil and I soil. Furthermore, it could be understood that the sands in Port and Rokko islands have similar liquefaction strengths to the above compacted soils, which means even the compacted embankment can be liquefied by the same strong motion of Hanshin earthquake if the soil meets the condition required for the liquefaction phenomenon, i.e., saturation of soil. Then, as observed in Figures 5.4.4, because FE-2012 was partially saturated at the degree of saturation around 95 %, the volcanic soil embankment should be considered as one of the structure that has liquefaction potential to cause. From Figure 5.5.1 (a), however, the Niigata sands have clearly lower liquefaction strength even at the higher relative density over 60 %. On the other hand, as shown in Figure 5.5.1 (b), Miura et al. (2003) and Yagi et al. (2005) also performed the liquefaction test using Hokkaido volcanic soil specimens reconstituted in their laboratory, which were controlled at the individual in-situ densities. According to Yagi et al. (2005), the liquefaction damage that widespread was confirmed at Sapporo and Kitami by the 2003 Tokachi-oki Earthquake in Hokkaido. From the figure, the relatively-similar liquefaction strength among the present study and the results of MORI, TOMIKAWA and NAKASHIBETSU volcanic soils can be recognized. However, the looser volcanic soils using SAPPORO and KITAMI tend to be readily liquefied compared with the above, while the liquefaction strengths can increase with increasing the relative densities. Thus, when comparing the past liquefaction cases that occurred in Japan, it may be concluded that the compacted embankment can be liquefied if the conditions permit such as strong motion input into the embankment and sufficient saturation. In addition, it is apparent that some factors such as higher molding water content (*see* Figure 5.1.12), freeze-thawing (*see* Figure 5.2.20) and finer fraction increasing over F_c = 30 % (*see* Figure 5.3.7) can act on the embankment as the factor to reduce the liquefaction strength more or less from the discussion in *CHAPTER 5*.

Keeping the liquefaction potential of compacted embankments in mind as discussed above, Figure

5.5.2 shows the relation between the compaction conditions and mechanical properties under the conditions mentioned in *5.1, CHAPTER 5*. In the section, the results of cyclic and monotonic compression tests, bender element test and permeability test were shown, and those indicated that not only the degree of compaction D_c but also the molding water content could influence the mechanical characteristics for I soil and K soil. The soils were significantly improved in terms of strength and stiffness, and the permeability became lower, as those soils was more densely compacted at the D_c range of 90 to 100 %, which are shown by (b') comparing with (b) in the figure. In addition, even at the same degree of compaction, the soil compacted dry of optimum (a) shows higher cyclic strength, lower q_{max} at ε_a = 15 % and higher permeability, but the wetter molding water content (c) has the converse influences against the above mechanical properties. Then, the fact that the relation between cyclic and monotonic compression strength with the molding water content contradicts is considered to result from the difference in dilatancy behavior at certain strain levels as discussed before. Some researchers have proposed the difference of pore size distribution or of soil particle arrangement as the causes for such effect of molding water content (Lambe 1958a, Juang and Holtz 1986, Ahmed et al. 1974 and Watabe et al. 2000 and Yokohama et al. 2012), but those do not lead to an uniform opinion so far because of the difficulty to identify the microscopic structure of compacted soils and no unified methodology. Apart from such microscopic structure, when the difference of molding water content has a non-negligible effect on the mechanical properties, it is apparent that such effect of water content at compaction should be incorporated in designing and constructing embankments. Then, as shown in *5.3 CHAPTER 5*, although the effect of molding water content appears depending on the finer content at compaction, in the next paragraph, that will be discussed with combining the present compaction control for some embankments.

In order to discuss the effect of finer content on the above relation between the compaction conditions and liquefaction strength, the typical compaction controls for dyke embankment (Japan

Institute of Country-ology and Engineering 2009) and road embankment (Japan Road Association 2010) will be reviewed here with Table 5.5.1. As shown in the table, the mechanical performance for the compacted earth structures are usually evaluated by the degree of compaction, air content or degree of saturation throughout construction. According to the table, the three parameters are distinguished and adopted for the adequate compaction control based on the finer content F_c. Then, for the dyke embankment, when the F_c value ranges from 25 % to 50 % (sandy soil) or over 50 % (cohesive soil), the air content control is separately employed; that is, the air content v_a is controlled at less than 15 % or 10 %. On the other hand, for the road embankment, in such cases as the compaction degree control cannot be satisfied, the air content or degree of saturation controls are recommended. According to Japan Institute of Country-ology and Engineering 2009 and Japan Road Association 2010, the above thought is based on the fact that replacing air void with water after compaction inhibits significant settlement due to further increment of void water. Figure 5.5.3 describes the above compaction control applied to Komaoka volcanic soils different in the finer content, i.e., K soil, $K_{1.9}$, $K_{17.4}$ and $K_{48.2}$, and I soil with taking the compaction curve and some constant air content curves of K soil as an example. When following the above compaction control, K soil, $K_{48.2}$ and I soil, which contain the F_c value over 30 %, could be controlled by the air content v_a. Then, for example, if discussing the liquefaction strength at the degree of compaction of 90 %, the water content at compaction required to satisfy v_a less than 15 % (or 10 %) reaches around 1.2 or more in w_i/w_{opt}. As elaborated in *5.3 CHAPTER 5*, for those soils, because the further increment of water content at the wetter condition prior to compaction deteriorates the liquefaction strength, it is concerned that the compaction conditions exhibited by (b) or (c) in Figure 5.5.3 would act disadvantageously in terms of the liquefaction strength compared with that of (a) located at the optimum. Therefore, as shown by (b') in the figure, it can be emphasized that decreasing the air content should be attributed to increasing the degree of compaction to keep higher liquefaction

resistance.

Next, let us discuss the present study using Komaoka volcanic soils in terms of the particle crushability. Simulating crushable soils such as Komaoka volcanic soil, Figure 5.5.4 illustrates the compaction planes that transition depending on the finer content F_c (%); i.e., the compaction planes are expanded to 3-dimension related with the F_c value. First, from the compaction test results explained in *CHAPTER 3*, the optimum water content w_{opt} decreases and the maximum dry density ρ_{dmax} increases, as the F_c value becomes higher, even under the same compactive effort (*see* Figures 3.2.7). Therefore, the relations of F_c with w_{opt} and ρ_{dmax} in Figure 5.5.4 projected on the w-F_c and ρ_d-F_c planes schematically give the compaction properties shown in Figures 3.2.7. The trend indicates quite an important potential on compacting the crushable volcanic soils. That is, because the ρ_{dmax} value becomes higher with increasing the F_c value, when such an external factor as compaction causes the constitutive particle crushing, the degree of compaction for the crushable soil could be possibly overestimated. Then, as explained in Figures 5.3.12, while the cyclic strength tends to increase with increasing the finer fraction and dry density until the F_c value reaches around 30 %, the relation shifts to decreasing behavior of the cyclic strength over 30 % in F_c. Therefore, when the particle breakage occurs at the F_c value over 30 %, the liquefaction strength could not always become higher, even though the apparent degree of compaction increases.

On the other hand, as shown in Figure 5.5.4, this study reveals that the optimum water content decreases with the finer fractions increasing. The fact implies, regarding the water content at compaction w_i, that it could be supposed that the w_i value transitions relatively to the wetter side of optimum with the soil crushed and densified, even though the water content does not change throughout. For example, those transitions are expressed as the solid arrows of (a) to (d), (b) to (e) and (c) to (f) in Figure 5.5.4. Then, in the cases of K soil and $K_{48.2}$, which have the F_c values higher than 30 %, because the cyclic strength tends to decrease as the molding water content becomes higher,

the increase of finer fractions due to particle crushing is considered to act for decreasing the cyclic strength within the corresponding F_c range. Therefore, when the original compaction condition to satisfy an desired mechanical performance of an embankment is determined as shown by "(I)" in the figure, it may be moved to the "adequate compaction condition (III)" to obtain the same mechanical performance as desired before particle crushing. Then, as expressed by the path of (c) to (f), a possible change is that the compacted crushable soil under the original compaction condition does not always meet the adequate compaction condition after particle crushing. If considering such case, the compaction condition should be modified to "(IV)" in the figure, where both compaction conditions before and after particle crushing are overlapping. That is, the compaction condition would be required at relatively-dry side of optimum.

As discussed in *5.3.3*, the change in cyclic strength due to the increment of finer fractions could differ depending on whether or not the water content changes throughout. That is, when the increase in finer content with densification occurs with the water content increasing as shown by the dashed arrows of (a) to (e) and (b) to (f) in Figure 5.5.4, it results in either less increase or more decrease in the cyclic strength, comparing with the cases of no change in the water content, (a) to (d) and (b) to (e). However, the particle crushing and corresponding densification behavior possibly occur with the water content decreasing, as represented by the dotted arrows of (b) to (d) and (c) to (e) in the figure, although it was not discussed before. Then, it is clear that the increase in finer fractions and density has an opposite effect on change in the cyclic strength as could be understood in Figure 5.3.13.

The increase of finer fractions due to particle crushing is not necessarily caused with densification. As indicated by the solid arrow of (a) to (b) in Figure 5.5.5, it can occur with a soil swelled in a certain case, i.e., freeze-thawing. According to the results of freeze-thawing tests discussed in *5.2*, the K soil specimens led to the more amounts of dilation and particle breakage after freeze-thaw sequence,

when those were compacted more densely. In such cases, it could be supposed that K soil should be exposed to the multiple influences of freeze-thawing and the relative change of compaction condition due to particle crushing, and those factors mutually stimulate the deterioration of cyclic strength.

The above discussion regarding the effect of finer content change, however, is on the basis of the cyclic shear behavior, and needless to say, the appropriate compaction condition must be determined upon examining, in addition, the monotonic shear strength, compressibility and permeability etc. Furthermore, although the particle crushing phenomenon has been discussed in terms of the increment of finer content in this study, the particle breakage should be caused in different ways depending on the external factors, i.e., compaction, consolidation, shearing and freeze-thawing. Therefore, the individual evaluation or discussion will be fundamentally required for the breakthrough of mechanical properties of crushable soils.

In this study, the individual effects of compaction condition, freeze-thawing and finer fraction were examined by some laboratory element tests. In-situ embankments in Hokkaido, however, are considered variously and complexly exposed to the above factors. In order to prevent human damage involved in the rainfall-induced slope failure of earth structures, therefore, how to manage the structures and to evaluate the potential risk of failure throughout in-service period have been discussed. Kawamura and Miura (2013a) conducted a series of laboratory model tests, and clarified that the initial water content w_0 (%) at construction of the specimens simulating volcanic soil embankments is likely to have a unique relation with the water content at failure w_f (%) due to artificial rainfall as shown in Figure 5.5.6 (revision of Kawamura and Miura 2013a). It is noted, however, that the relationship can be significantly affected by whether the soil is exposed to freeze-thaw sequence as well as the laboratory element tests (Ishikawa and Miura 2011 and Matsumura et al. 2013). In this figure, the relation of w_0 versus w_f obtained from the in-situ monitoring test of FE-2012 is additionally demonstrated, and then it could be understood that the laboratory model test results agree well with the

in-situ monitoring results. The fact indicates the high applicability of simulating the risk of slope failure from the water contents. In addition, because of the simplicity of in-situ observing the water content and the higher validity comparing with the rainfall intensity and pore pressure as mentioned in Figure 5.4.3, the water content could be a promising index to evaluate the risk of slope failure.

In this section, some possible problems about volcanic soil embankments in cold regions taken through this study have been discussed. Generally speaking, such earth structures as embankment are regarded as the structures that increase the geotechnical stability due to consolidation progressing with the time passing after construction, unlike the other construction materials; concrete and steel. Volcanic soil embankments in cold regions, however, are enforced to experience annual freeze-thaw sequence and particle crushing resulting from the stress history that can deteriorate the mechanical performance, in addition to heavy rain and earthquake. Thus, the crushable volcanic soils depositing in cold regions such as Hokkaido are considered very complicated materials. This study has been focused on the limited mechanical properties of the volcanic soil that can vary attributed to compaction condition, freeze-thaw sequence and finer content, but for the volcanic soil embankment, a comprehensive discussion will be required that enables evaluating and managing not only the mechanical performance but also its change with time throughout the whole period from construction to possible failure.

Through a series of laboratory and in-situ tests in this study, on the other hand, the author strongly feels the limitation of present compaction control and that there is room to improve how to evaluate mechanical performance of embankments. First, while the slight difference of degree of compaction D_c, even within 10 % over 90 % in D_c, has the significant influences on the mechanical characteristics as can be recognized from the laboratory test results, the in-situ density cannot be strictly controlled and the values of degree of compaction widely scatter to some extent. Furthermore, because the natural water content often tends to be higher than optimum water contents

in Japan as well as that of I soil, which corresponds to 1.26 in w_i/w_{opt}, it could be understood that controlling water content prior to compaction may spend unreasonable cost and time. Keeping in mind the above, therefore, in order to evaluate the in-situ mechanical performance of embankments, it should be associated with some parameter related directly to those such as shear resistance and stiffness and permeability etc., unlike the density parameter, i.e., degree of compaction. For the above purpose, various approaches could be required, that is, what parameter is available to evaluate the mechanical performance of in-situ earth structures, how the parameter can be in-situ measured and the relationship between laboratory and in-situ evaluations. Thus, controlling some mechanical parameters during construction would enable embankments to be more uniform and stable in terms of mechanical evaluation.

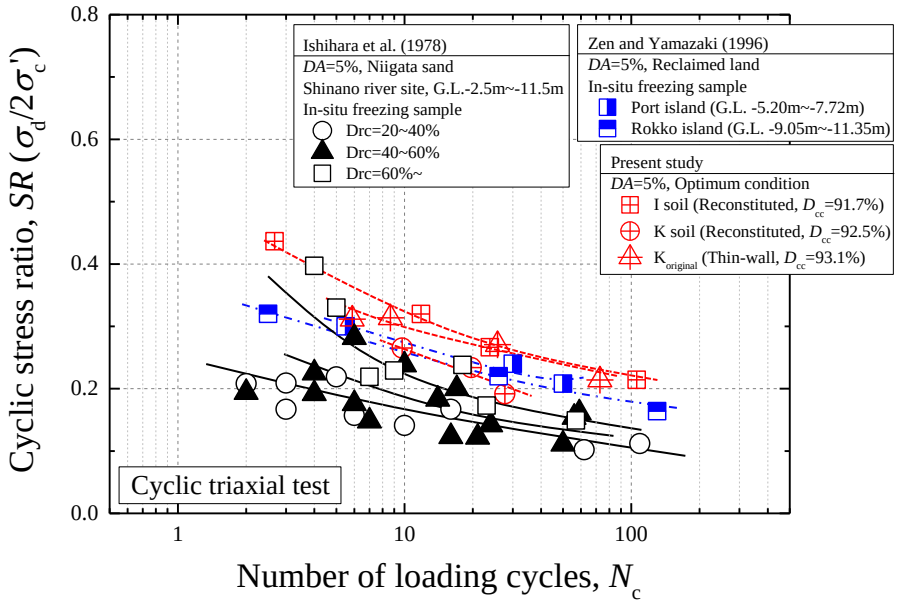

(a) Niigata sand and Masado in Port and Rokko islands

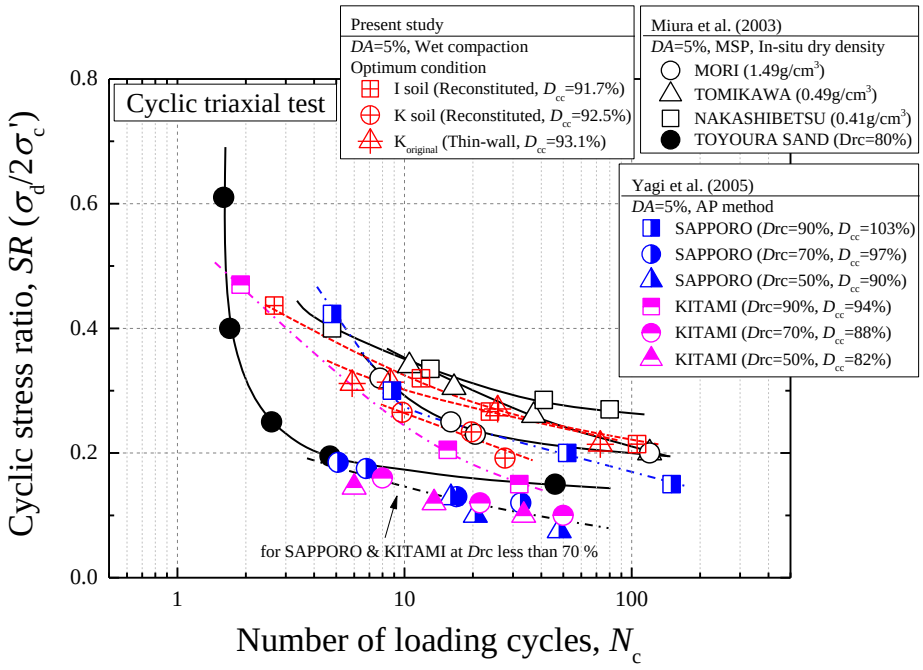

(b) Volcanic soils deposited in Hokkaido

Figures 5.5.1 Liquefaction strength of Komaoka volcanic soils compared with some sands liquefied in Japan

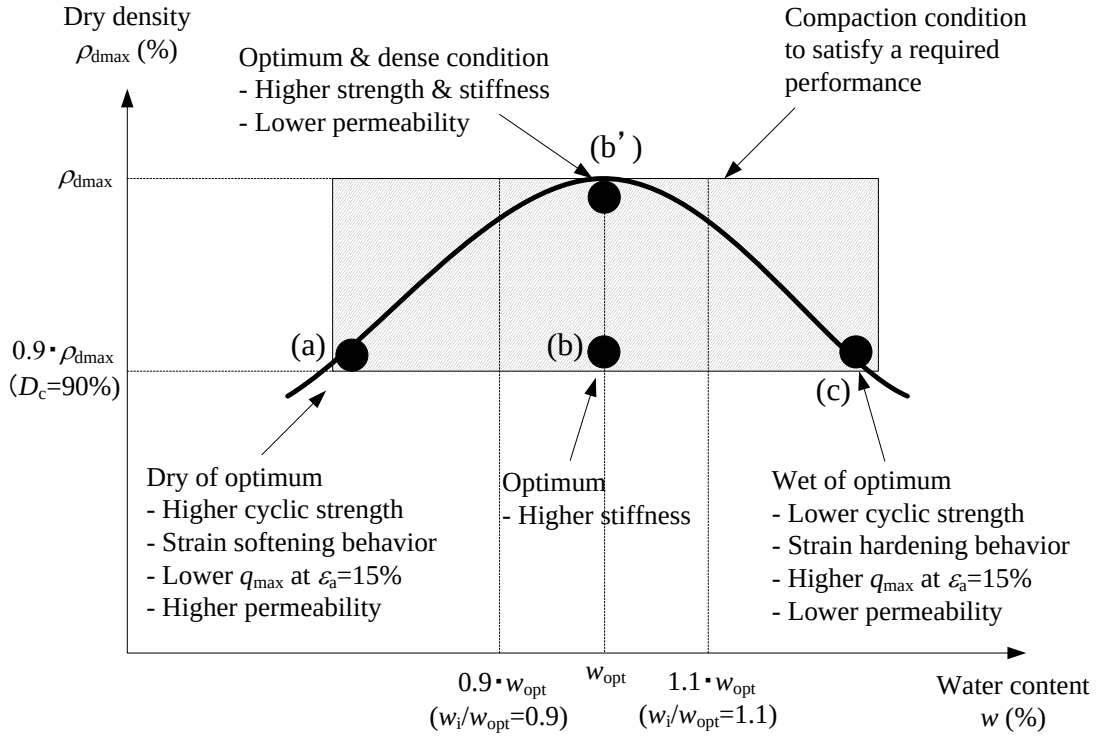

Figure 5.5.2 Mechanical properties of compacted soils at variable compaction conditions

Table 5.5.1 Compaction controls for dyke embankment and road embankment
(Japan Institute of Country-ology and Engineering 2009 and Japan Road Association 2010)

Compaction control	Dyke embankment	Road embankment*[1]
Degree of compaction	w_n: acceptable for trafficability over w_{opt} $D_c \geqq 90\%$ in average and $D_c \geqq 80\%$ at minimum	w_n: w_{opt} or acceptable for trafficability $D_c \geqq 90\%$
Air content	w_n: acceptable for trafficability over w_{opt} Sandy soil ($25\% \leqq F_c \leqq 50\%$); $v_a \leqq 15\%$ Cohesive soil; $2\% < v_a \leqq 10\%$	w_n: w_{opt} or acceptable for trafficability Sandy soil; ($2\% <$) $v_a \leqq 15\%$ Cohesive soil; ($2\% <$) $v_a \leqq 10\%$
Degree of saturation	w_n: acceptable for trafficability over w_{opt} $85\% \leqq S_r \leqq 95\%$	w_n: w_{opt} or acceptable for trafficability $85\% \leqq S_r \leqq 95\%$

*[1] Filled up ground and A,B method for compaction

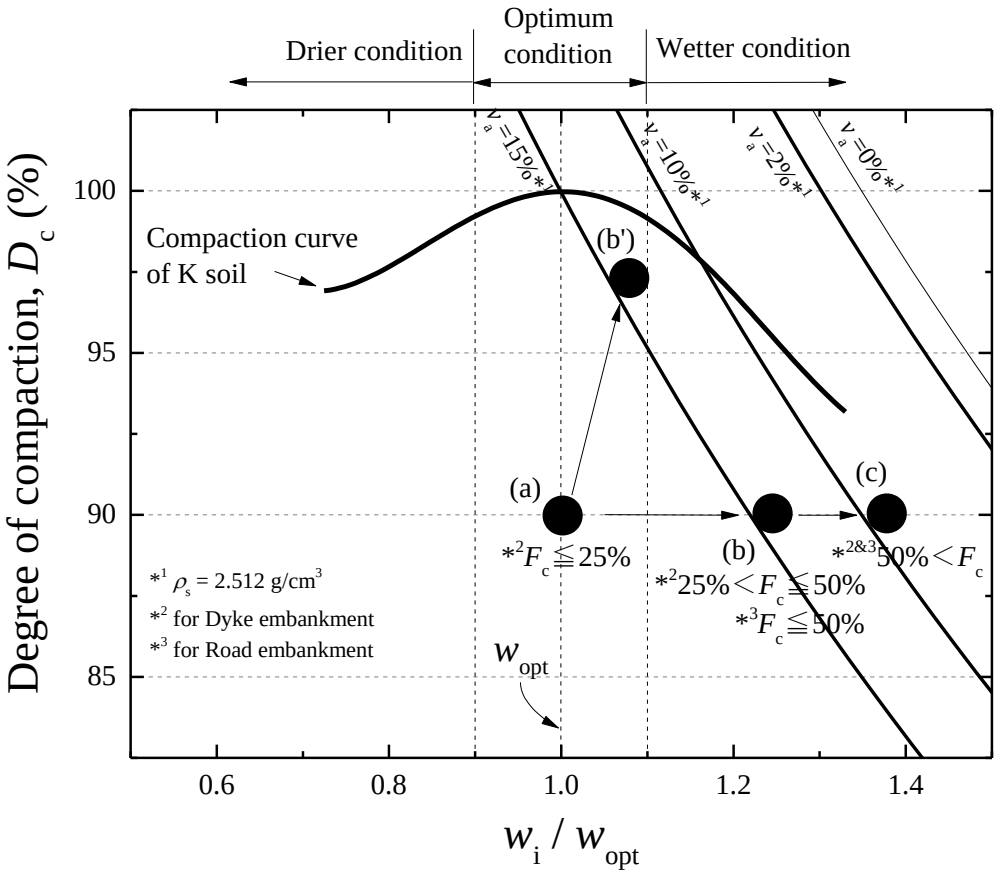

Figure 5.5.3 Compaction controls by air content for Komaoka volcanic soils and I soil

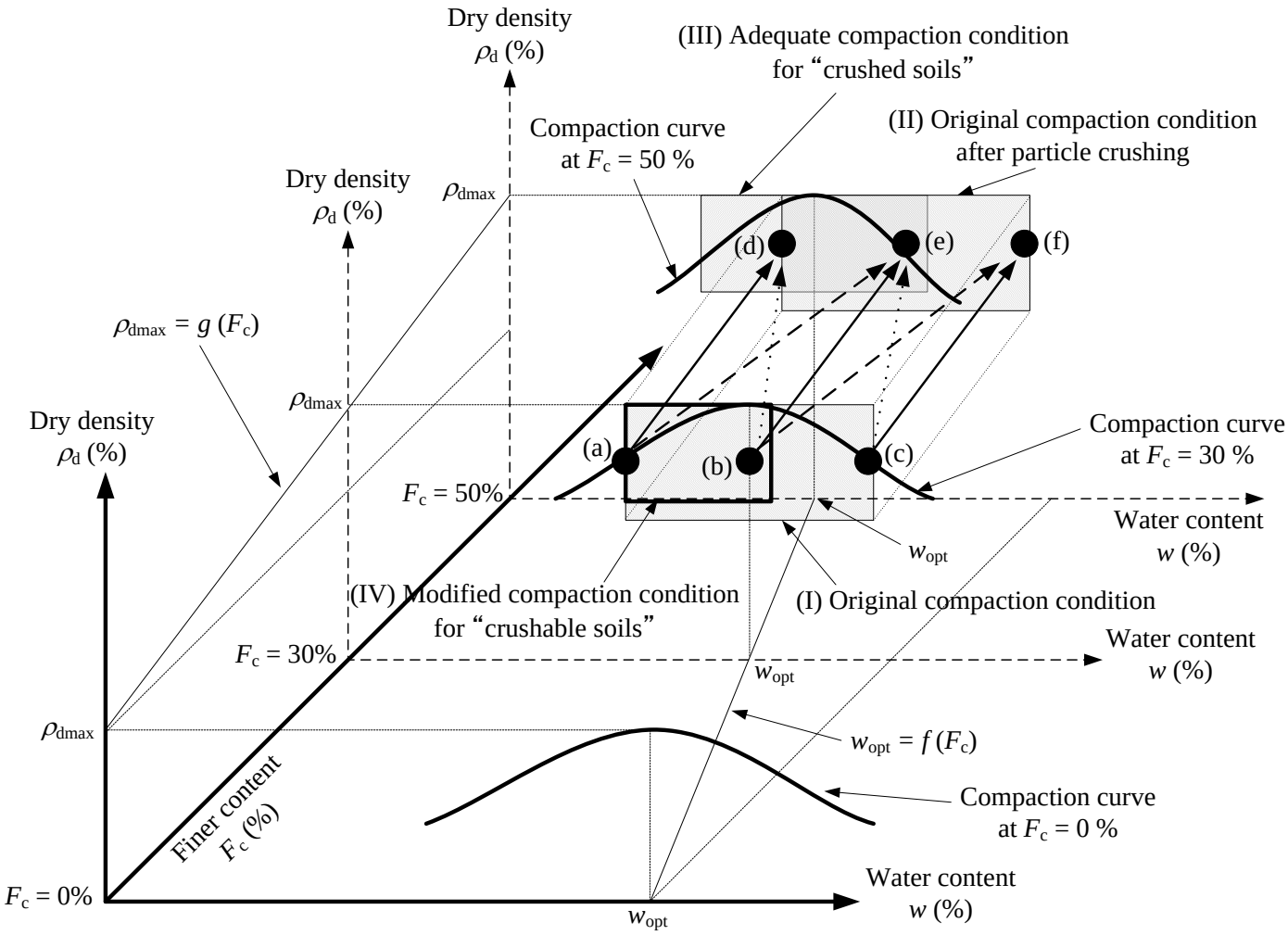

Figure 5.5.4 Change in mechanical properties of compacted soils due to increase in finer content and a concept of compaction control for crushable volcanic soil

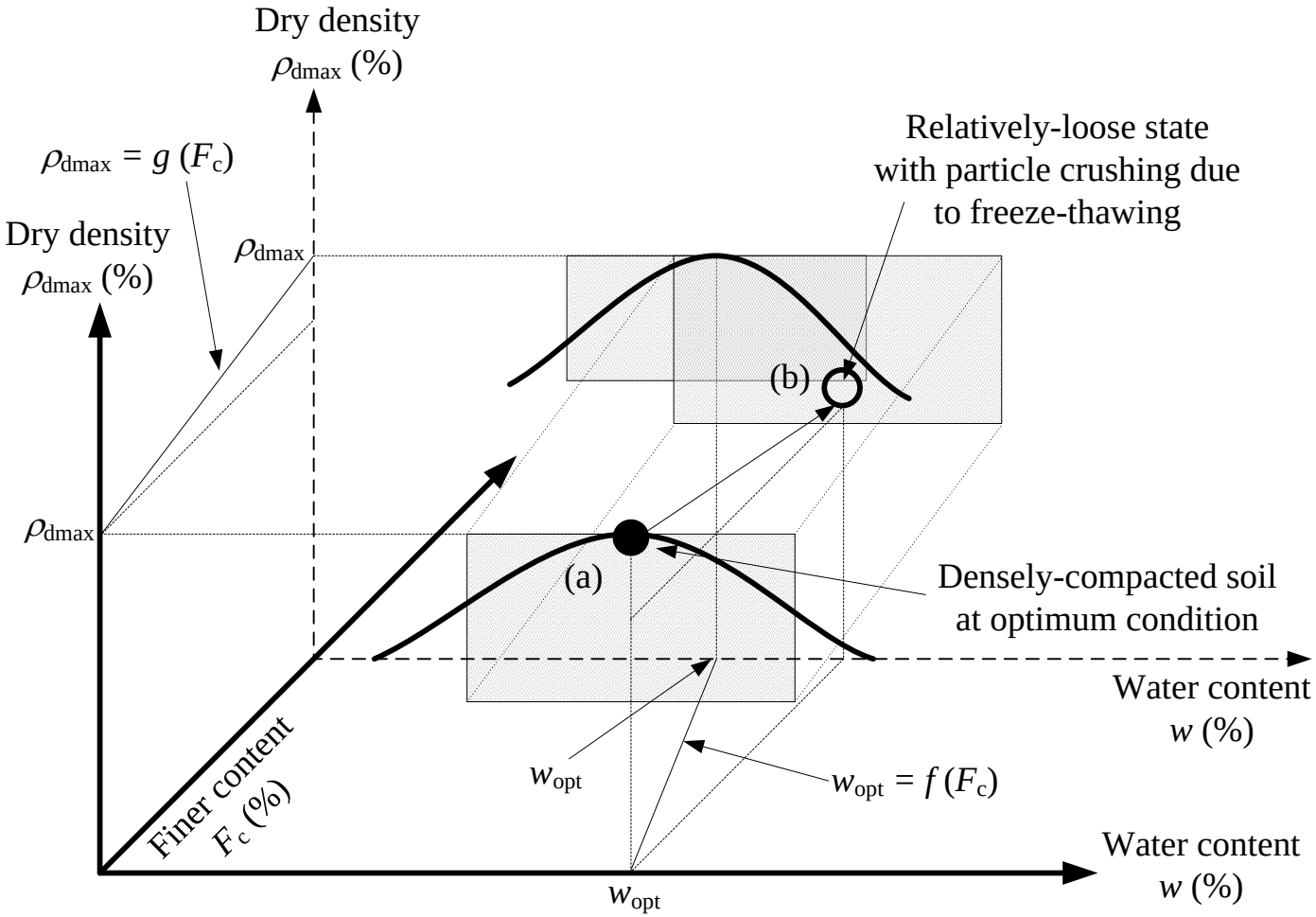

Figure 5.5.5 Change in mechanical properties of crushable volcanic soil subjected to freezing and thawing

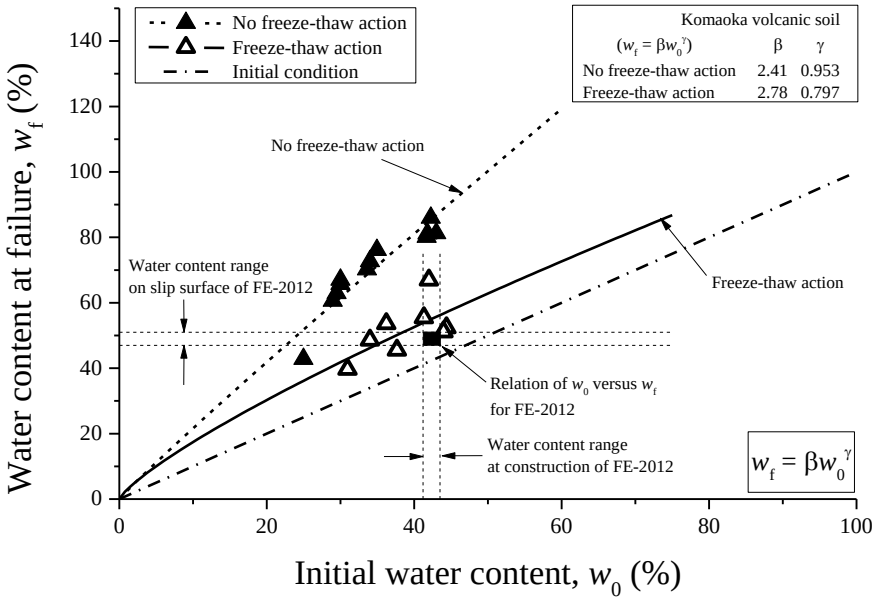

Figure 5.5.6 Relations of initial water content versus water content at failure for Komaoka volcanic soil with or without freeze-thaw sequence

CHAPTER 6 CONCLUSIONS

On the basis of the limited experimental data obtained from a series of laboratory tests and the in-situ monitoring investigation, the following conclusions may be drawn.

The results of the study on the effect of compaction conditions such as dry density, molding water content on some mechanical properties are summarized as follows:

(1) The cyclic strength behavior significantly differs depending on the compaction conditions. The increase in degree of compaction leads to the significant increase of the cyclic strength, and such behavior becomes remarkable under the drier condition than the optimum water content. Furthermore, from the relations of the cyclic strength with the molding water content, the peak cyclic strength appears at the drier condition, and the cyclic strength is reduced to a significant extent with the molding water content higher. The difference in excess pore water pressure behavior during the cyclic loading could be considered as a possible reason for the above strength behavior.

(2) The undrained triaxial compression tests were conducted using I soil and K soil specimens compacted under various compaction conditions. From the testing results, it could be seen that the stress-strain curves and the excess pore water pressure behavior were obviously different in each compaction condition. That is, the specimens showed the typical strain softening behavior at the drier condition, but in contrast the definite peak strength could not be found at the wetter condition until the axial strain reached about 15 % as seen on the strain hardening behavior. Then, in particular, the excess pore water pressure of the specimens at the wetter condition tends strongly to

fluctuate during the monotonic loading, and those show the stronger dilative behavior around at the end of loading. Focusing on the effect of degree of compaction, on the other hand, the remarkable strength increase could be recognized with the specimens compacted more densely.

(3) It could be seen that the shear modulus and the permeability were strongly susceptible to the compaction conditions, and the increase in degree of compaction led to the stiffer and low-permeable soil structures. In addition, such behavior varied depending on the molding water content.

(4) The above mechanical characteristics and its change triggered by compaction agreed qualitatively to both I soil and K soil. In addition, such behavior may be attributed to the difference in soil fabrics built in various compaction conditions, because the soil fabrics were considered to remain throughout the testing procedure to a certain degree without losing due to saturation and consolidation based on little difference in volume change behavior.

From the results of a series of cyclic triaxial tests on K soil specimens with or without freeze-thaw sequence, the following conclusions were derived;

(1) The cyclic triaxial apparatus capable of simulating freeze-thaw sequence, desired moisture state and cyclic loading was newly developed. It can cause the specimen to freeze and thaw one-dimensionally in the triaxial cell, controlling the temperatures of the cap, pedestal and cell water independently.

(2) Freeze-thaw sequence causes volume change with water supply and drainage and particle breakage, and each behavior differs depending on the initial degree of compaction D_{ci}. K soil densely compacted tends to swell more significantly with absorbing water due to freezing, and the specimen remains in dilation even after thawed and consolidated. At lower degree of compaction than 90 %, however, the specimen causes less dilation with drainage due to freezing, and it shrinks after thawed and consolidated.

(3) Freeze-thaw sequence causes the stronger negative dilatancy behavior of K soil specimens with the excess pore water pressure higher during cyclic loading. Consequently, it leads to the reduction of cyclic shear strength for K soil densely compacted at D_{ci}=97.0 %. Then, the cyclic stress ratio to cause DA=5 % with the number of loading cycles N_c of 20, SR_{20}, drops to around 70 % due to freeze-thaw sequence compared with the non-frozen specimens.

(4) Freeze-thawing triggers change in cyclic deformation behavior. The deformation of the frozen specimens tends to continue constantly to evolve as the loading cycle increases, while that of the non-frozen specimens seems to increase exponentially as soon as the Δu value reaches 95 % of σ_c'. In addition, anisotropic behavior in liquefying changes due to freeze-thaw sequence.

(5) The effect of freeze-thawing on cyclic shear characteristics varies depending on the initial degree of compaction D_{ci}. That is, such effects of freeze-thawing as mentioned above can reduce at the lower degree of compaction.

The effect of finer fractions on the relations between cyclic strength and compaction conditions was examined using four Komaoka volcanic soils gradation-controlled in advance (K soil, $K_{1.9}$, $K_{17.4}$ and $K_{48.2}$). The results may be concluded as follows;

(1) From the experimental results on K soil and $K_{48.2}$, which have the finer content higher than 30 %, the effect of the molding water content on the cyclic strength becomes remarkable even if the specimens are compacted at the similar degrees of compaction. Then, the maximum cyclic strengths appear under the drier conditions, and those tend to decrease with the molding water content higher. On the other hand, $K_{1.9}$ and $K_{17.4}$ have the unique relations between the cyclic strength and the degree of compaction regardless of the target molding water content.

(2) The correlations of the cyclic strength with the compactive effort tend to be a unique and positive for each soil material unlike the relations with the degree of compaction and molding water content.

(3) The change behavior of the cyclic strength due to particle crushing with densification differs depending on the finer content at cyclic loading. The cyclic strength tends to increase with the particle crushing and densification progressing at the finer content lower than about 30 %. In contrast, the cyclic strength has the negative correlation with the increment of finer content and densification at the finer content over 30 %. In addition, the above behavior is considered to be also affected by the water content at the particle breakage and densification.

From the results of the in-situ monitoring and failure tests of the full-scale embankment constructed by Komaoka volcanic soil, the following conclusions are summarized.

(1) In freeze-thaw period, the embankment is exposed to freeze-thawing from the surface, and drying progresses below the freezing line with the suction increased.

(2) In snowmelt season and rainfall, the rapid increase of water content and pore pressure are confirmed with the inflow of water.

(3) The slope failure of embankment was caused by the water supply, simulating the inflow of snowmelt. Because heavier rainfall event and little suction had been long observed while the water content had been constantly increasing before the slope failure, the water content can be expected as a promising index to evaluate the risk of slope failure.

TABLE OF OFTEN USED SYMBOLS

$\dot{\varepsilon}_a$	=	Loading rate in compression triaxial test (%/min)
AEV	=	Air entry value (kPa)
A_c	=	Area of specimen after consolidation
CPT	=	Cone penetration test
CS	=	Cut slope constructed in 2011
CU test	=	Consolidated undrained test
D_{50}	=	Mean grain size (mm)
DA	=	Double amplitude axial strain in cyclic triaxial test (%)
D_c	=	Degree of compaction (%)
D_{ci}	=	Initial degree of compaction (%)
D_m	=	Compaction mold diameter (mm)
D_{max}	=	Maximum grain size (mm)
D_s	=	Specimen diameter (mm)
FE-2011	=	Full-scale embankment constructed in 2011
FE-2012	=	Full-scale embankment constructed in 2012
F_c	=	Finer content (% <75μm)
F_c'	=	Finer content after shearing (%)
G_{BE}	=	Shear modulus examined by bender element test (MPa)
H_c	=	Specimen height after consolidation (mm)
H_i	=	Specimen height before freezing (mm)

H_m = Compaction mold height (mm)

H_s = Specimen height after compaction (mm)

I soil = Sandy silt sampled in Chiyoda district, Ikeda-cho, Hokkaido

I_p = Plasticity index

JGS = The Japanese Geotechnical Society

JSCE = Japanese society of civil engineering

$K_{original}$ = Shikotsu pumice flow deposit with the original grain size distribution sampled in Komaoka district, Makomanai, Hokkaido

K_0 = Coefficient of earth pressure at rest

$K_{1.9}$ = K soil with the controlled grain size distribution of F_c = 1.9 %

$K_{17.4}$ = K soil with the controlled grain size distribution of F_c = 17.4 %

$K_{48.2}$ = K soil with the controlled grain size distribution of F_c = 48.2 %

Ksoil = Shikotsu pumice flow deposit with the cut grain size distribution (< 9.5 mm) sampled in Komaoka district, Makomanai, Hokkaido

L_{BE} = Distance between two bender elements in a specimen

L_a = Length of the section with water supply holes in a water supply pipe (mm)

L_b = Length of the section with no water supply hole in a water supply pipe (mm)

L_c = Diameter of a water supply pipe (mm)

N value = Number of blows by SPT

NP = Non plastic soil

N_c = Number of loading cycles

N_l = Numbers of compaction layers

SCP = Seismic cone penetration test

SPT = Standard penetration test

SR = Cyclic stress ratio defined as $\sigma_d/2\sigma_c$'

SR_{10} = Cyclic stress ratio to cause desired DA with $N_c = 10$

SR_{20} = Cyclic stress ratio to cause desired DA with $N_c = 20$

SWCC = Soil-water characteristics curve

Spfl = Shikotsu pumice flow deposit

S_r = Degree of saturation (%)

U_c = Uniformity coefficient

V_f = Freezing velocity (mm/hr)

V_m = Compaction mold volume

V_s = Shear wave velocity (m/s)

V_{sc} = Volume of coarse fractions

V_{sf} = Volume of finer fractions

V_v = Volume of void

WEV = Water entry value (kPa)

a_b = Area of double-tube burette (A)

e = Void ratio

e_g = Granular void ratio

f = Frequency of cyclic loads (Hz)

i = Hydraulic gradient

k = Permeability coefficient at temperature of 15 °C (m/s)

k_T = Permeability coefficient at given temperature of T °C (m/s)

p' = Effective mean principal stress, $(\sigma_1' + 2\sigma_3')$ / 3 (kPa)

q_{max} = Peak deviator stress at ε_a less than 15 % (kPa)

s = Matric suction (kPa)

u_a = Pore air pressure (kPa)

u_w = Pore water pressure (kPa)

w_L = Liquid limit (%)

w_P = Plastic limit (%)

w_f = Water content at failure (%)

w_i, w_0 = Water content at compaction, molding water content (%)

w_n = Natural water content (%)

w_{opt} = Optimum water content obtained from laboratory compaction test (%)

x_i = Content percentage of soil particles that have ρ_{si}

ΔF_c = Increment of finer particle (%)

ΔH_f = Maximum amount of axial displacement induced by freezing

ΔL = Water head difference in permeability test

ΔL_1 = Water head difference of two burette before percolation in permeability test

ΔL_2 = Water head difference of two burette after percolation in permeability test

ΔV = Drainage during freezing and thawing (ml)

Δt_{BE} = Travelling time of shear wave

Δt_f = Required time to cause the corresponding ΔH_f value

E = Compaction energy ratio, the number of blows in compacting the specimens normalized by 75 times

ε_a = Axial strain (%)

$\varepsilon_{a\ comp.}$ = Axial strain at compression side in cyclic triaxial test (%)

$\varepsilon_{a\ ext.}$ = Axial strain at extension side in cyclic triaxial test (%)

ε_{af} = Axial strain where the q_{max} value appears (%)

ε_f = Freezing expansion rate, $\Delta H_f/H_i$ (%)

ε_r = Radial strain

η_{15} = Viscosity coefficient of water at temperatures of 15 °C

η_T = Viscosity coefficient of water at temperatures of given T °C

θ_w = Volumetric moisture content (%)

ρ_{di} = Initial dry density after compaction (g/cm^3)

ρ_{dmax} = Maximum dry density obtained from compaction test (g/cm^3)

ρ_s = Soil particle density (g/cm^3)

ρ_{si} = Soil particle density of each grain size range (i = 1 ~ 8) (g/cm^3)

ρ_w = Density of water (g/cm^3)

σ = Total stress (kPa)

σ_a' = Effective axial stress (kPa)

σ_c' = Effective confining (or consolidation) pressure (or stress) (kPa)

σ_d = Deviator stress (kPa)

σ_{net} = Net stress (kPa)

σ_r' = Effective radial stress (kPa)

APPENDIX

Cyclic triaxial test results to examine the effect of compaction condition

Soil material	Compaction condition	w_i (%)	w_i/w_{opt}	ρ_{di} (g/cm^3)	D_{ci} (%)	ρ_{dc} (g/cm^3)	D_{cc} (%)	Ave. w_i	Ave. D_{cc}	N_c		SR
										DA =1%	DA =5%	
I soil	Opt	27.4	1.10	1.414	97.8	1.425	98.6	26.2	96.9	17.2	38.2	0.320
		25.7	1.03	1.395	96.5	1.397	96.6			2.8	9.7	0.419
		25.6	1.02	1.381	95.5	1.386	95.8			15.7	34.7	0.375
		26.0	1.04	1.387	95.9	1.400	96.8			23.4	37.7	0.407
		25.5	1.02	1.313	90.8	1.325	91.6	25.9	91.7	0.71	2.7	0.436
		25.6	1.02	1.331	92.1	1.338	92.5			16.77	23.8	0.266
		25.4	1.01	1.318	91.1	1.322	91.4			7.8	11.8	0.320
		27.3	1.09	1.310	90.6	1.317	91.1			97.9	105.7	0.214
		23.3	0.93	1.280	88.5	1.288	89.1	23.4	88.2	3.8	4.7	0.264
		23.7	0.95	1.269	87.8	1.277	88.3			4.8	6.7	0.266
		23.1	0.92	1.252	86.6	1.260	87.1			28.9	31.8	0.214
	Dry	19.1	0.77	1.380	95.4	1.384	95.7	19.1	95.7	22.8	38.7	0.429
		19.0	0.76	1.376	95.1	1.380	95.5			7.7	14.7	0.484
		19.2	0.77	1.382	95.6	1.387	95.9			3.7	12.8	0.516
		20.5	0.82	1.334	92.3	1.339	92.6	20.1	92.7	27.8	34.8	0.321
		19.4	0.77	1.311	90.7	1.315	90.9			18.9	30.7	0.375
		20.3	0.81	1.363	94.2	1.368	94.6			5.8	13.8	0.451
		20.0	0.80	1.278	88.4	1.285	88.8	20.4	88.8	3.8	5.7	0.309
		20.9	0.84	1.280	88.5	1.285	88.9			8.7	11.7	0.297
		20.3	0.81	1.276	88.2	1.284	88.8			11.7	13.7	0.254
		16.0	0.64	1.350	93.4	1.357	93.9	15.2	92.9	97.8	115.7	0.322
		14.7	0.59	1.319	91.2	1.321	91.3			0.8	1.7	0.531
		15.0	0.60	1.350	93.4	1.353	93.6			2.8	6.7	0.460
	Wet	28.3	1.13	1.402	96.9	1.412	97.7	28.1	96.7	22.8	41.7	0.267
		28.2	1.13	1.379	95.4	1.380	95.5			0.7	1.7	0.567
		27.7	1.11	1.396	96.5	1.402	96.9			198.4	242.7	0.258
		27.7	1.11	1.338	92.6	1.343	92.9	28.4	92.9	9.8	19.7	0.298
		27.8	1.11	1.352	93.5	1.343	92.9			52.9	68.8	0.268
		29.7	1.19	1.334	92.3	1.343	92.9			3.9	8.6	0.313

Cyclic triaxial test results to examine the effect of compaction condition

Soil material	Compaction condition *1	Compaction condition *2	w_i (%)	w_i/w_{opt}	ρ_{di} (g/cm^3)	D_{ci} (%)	ρ_{dc} (g/cm^3)	D_{cc} (%)	Ave. w_i	Ave. D_{cc}	N_c DA=1%	N_c DA=5%	SR
K soil	Opt	(IV)	43.3	1.07	1.061	100.2	1.058	99.9	43.5	99.5	22.8	38.7	0.300
			43.3	1.07	1.047	98.9	1.055	99.6			8.8	18.7	0.376
			44.1	1.09	1.042	98.4	1.049	99.1			3.7	15.7	0.456
		(I)	41.5	1.03	1.045	98.7	1.048	98.9	41.3	98.6	7.8	19.8	0.318
			41.2	1.02	1.037	98.0	1.040	98.2			3.7	11.7	0.422
			41.2	1.02	1.037	98.0	1.045	98.6			34.3	53.7	0.268
		(I)	40.8	1.01	1.002	94.6	1.008	95.2	40.5	94.3	4.8	15.7	0.350
			40.6	1.00	0.995	93.9	1.000	94.5			5.8	14.7	0.317
			40.2	0.99	0.995	94.0	1.000	94.4			9.7	18.8	0.265
			40.2	0.99	0.980	92.6	0.987	93.2			9.8	19.8	0.238
		(IV)	43.5	1.07	0.968	91.4	0.973	91.9	43.4	92.5	5.8	9.8	0.265
			43.5	1.07	0.978	92.4	0.987	93.2			12.8	19.7	0.234
			43.4	1.07	0.972	91.8	0.980	92.6			20.8	27.7	0.192
	Dry	(II)	33.4	0.82	1.045	98.7	1.051	99.2	33.2	99.5	19.9	37.8	0.321
			33.0	0.82	1.049	99.0	1.054	99.5			10.8	27.8	0.400
			33.2	0.82	1.049	99.1	1.055	99.7			2.8	15.7	0.500
		(II)	34.5	0.85	1.010	95.3	1.017	96.0	34.1	96.2	16.7	25.7	0.267
			34.2	0.84	1.022	96.5	1.031	97.3			11.8	21.7	0.321
			33.5	0.83	1.004	94.8	1.009	95.3			3.7	9.6	0.423
		(II)	32.7	0.81	0.936	88.4	0.946	89.4	32.7	89.3	8.7	12.7	0.210
			33.1	0.82	0.940	88.7	0.946	89.3			29.8	33.8	0.161
			32.4	0.80	0.937	88.5	0.944	89.2			3.7	5.7	0.256
		(III)	28.2	0.70	1.002	94.6	0.989	93.4	28.5	94.7	6.7	13.7	0.264
			28.6	0.71	1.014	95.7	1.020	96.3			45.8	58.7	0.214
			28.6	0.71	0.993	93.8	1.000	94.4			7.7	14.7	0.319
	Wet	(IV)	46.7	1.15	1.065	100.5	1.072	101.2	46.6	100.2	10.7	26.7	0.264
			46.4	1.15	1.051	99.2	1.054	99.5			4.7	16.7	0.316
			46.6	1.15	1.052	99.3	1.057	99.8			3.7	15.8	0.393
		(IV)	47.3	1.17	1.020	96.3	1.026	96.9	46.4	95.4	12.9	26.7	0.266
			46.6	1.15	0.990	93.5	0.996	94.0			2.8	8.7	0.374
			45.3	1.12	1.003	94.7	1.010	95.3			6.7	11.7	0.319
		(IV)	48.4	1.20	0.973	91.9	0.979	92.4	48.0	91.1	20.8	28.7	0.213
			47.3	1.17	0.954	90.1	0.962	90.8			3.8	6.7	0.254
			48.2	1.19	0.947	89.5	0.954	90.1			9.7	13.7	0.237

*1 Classification for compaction condition based on w_i/w_{opt} (*see* Figure 5.3.4)

*2 Classification for compaction condition based on w_i (*see* Figure 5.3.10)

Undrained consolidation triaxial compression test results to examine the effect of compaction condition

Soil material	Compaction condition	w_i (%)	w_i/w_{opt}	ρ_{di} (g/cm^3)	D_{ci} (%)	ρ_{dc} (g/cm^3)	D_{cc} (%)	σ_c' (kPa)	q_{max} (kPa) ($\varepsilon_a \leq 15\%$)	ε_{af} (%)
I soil	Opt	25.0	1.00	1.277	88.3	1.281	88.6	50	105.7	3.0
		25.0	1.00	1.436	99.3	1.440	99.6	50	509.6	7.1
		25.2	1.01	1.398	96.7	1.401	96.9	50	381.4	7.6
		27.0	1.08	1.426	98.6	1.434	99.1	100	452.7	10.4
		27.0	1.08	1.354	93.7	1.374	95.1	100	186.6	15.3
		25.0	1.00	1.288	89.1	1.317	91.1	100	116.2	3.5
		25.0	1.00	1.440	99.6	1.447	100.1	100	490.6	8.6
		25.0	1.00	1.412	97.6	1.419	98.1	100	449.2	9.0
		24.3	0.97	1.294	89.5	1.319	91.2	150	163.5	3.6
		25.0	1.00	1.475	102.0	1.490	103.0	150	734.0	14.9
		24.1	0.96	1.398	96.7	1.408	97.4	150	421.6	5.9
		26.2	1.05	1.406	97.2	1.429	98.8	150	608.7	10.4
	Dry	14.9	0.60	1.336	92.4	1.336	92.4	50	143.7	1.5
		13.4	0.54	1.390	96.2	1.420	98.2	50	189.1	2.9
		13.6	0.55	1.385	95.7	1.396	96.5	100	238.2	2.2
		18.8	0.75	1.338	92.5	1.340	92.6	150	234.3	1.9
		13.5	0.54	1.424	98.5	1.436	99.3	150	316.4	2.4
	Wet	31.3	1.25	1.272	88.0	1.301	89.9	50	145.0	15.4
		29.7	1.19	1.337	92.5	1.332	92.1	150	398.5	14.4

Soil material	Compaction condition	w_i (%)	w_i/w_{opt}	ρ_{di} (g/cm^3)	D_{ci} (%)	ρ_{dc} (g/cm^3)	D_{cc} (%)	σ_c' (kPa)	q_{max} (kPa) ($\varepsilon_a \leq 15\%$)	ε_{af} (%)
K soil	Opt	36.6	0.90	1.052	99.4	1.053	99.5	50	582.2	5.3
		41.7	1.03	1.006	95.0	1.007	95.1	100	560.7	7.3
		41.2	1.02	1.071	101.1	1.072	101.2	150	625.8	8.9
	Dry	36.2	0.89	1.107	104.5	1.108	104.7	50	636.5	7.9
		28.0	0.69	1.069	100.9	1.067	100.8	50	401.2	7.1
		31.4	0.78	0.997	94.1	1.000	94.4	50	463.4	7.9
		25.6	0.63	1.038	98.0	1.038	98.0	150	507.9	6.6
	Wet	49.7	1.23	1.023	96.6	1.025	96.8	50	464.5	12.7
		45.8	1.13	0.979	92.4	0.980	92.5	50	262.9	8.6
		50.2	1.24	1.054	99.5	1.064	100.5	100	709.1	14.2
		49.9	1.23	1.062	100.3	1.066	100.7	150	665.9	15.0

Bender element test results to examine the effect of compaction condition

Soil material	Compaction condition	w_i (%)	w_i/w_{opt}	ρ_{di} (g/cm^3)	D_{ci} (%)	ρ_{dc} (g/cm^3)	D_{cc} (%)	G_{BE} (MPa)	V_s (m/s)
I soil	Opt	24.1	0.96	1.158	80.1	1.185	82.0	13.2	87.4
		24.4	0.98	1.256	86.9	1.293	89.4	18.9	108.4
		24.9	1.00	1.287	89.0	1.290	89.2	19.6	104.7
		24.2	0.97	1.376	95.2	1.380	95.4	31.1	134.6
		24.8	0.99	1.428	98.8	1.430	98.9	30.1	129.9
		24.7	0.99	1.446	100.0	1.450	100.3	35.4	140.0
		23.4	0.94	1.309	90.5	1.313	90.8	20.3	111.9
		27.4	1.10	1.374	95.0	1.376	95.2	31.1	133.2
		27.3	1.09	1.390	96.1	1.393	96.3	37.0	144.4
	Dry	15.5	0.62	1.338	92.5	1.343	92.9	19.4	111.8
		17.6	0.70	1.406	97.2	1.412	97.6	26.3	125.8
		17.3	0.69	1.373	95.0	1.367	94.5	30.1	137.0
	Wet	28.2	1.13	1.401	96.9	1.407	97.3	38.8	146.7

Soil material	Compaction condition	w_i (%)	w_i/w_{opt}	ρ_{di} (g/cm^3)	D_{ci} (%)	ρ_{dc} (g/cm^3)	D_{cc} (%)	G_{BE} (MPa)	V_s (m/s)
K soil	Opt	40.3	1.00	1.116	105.4	1.120	105.7	31.2	140.9
		40.6	1.00	0.970	91.6	0.971	91.7	16.0	108.3
		40.0	0.99	1.003	94.7	1.004	94.8	27.3	164.5
	Dry	32.1	0.79	0.987	93.2	0.989	93.4	11.5	93.8
		31.2	0.77	1.002	94.6	1.005	94.9	11.8	94.7
		28.4	0.70	1.038	98.0	1.041	98.3	8.9	81.7
	Wet	47.9	1.18	1.025	96.8	1.027	97.0	16.1	102.9

Permeability test results to examine the effect of compaction condition

Soil material	Compaction condition	w_i (%)	w_i/w_{opt}	ρ_{di} (g/cm^3)	D_{ci} (%)	ρ_{dc} (g/cm^3)	D_{cc} (%)	k_{15} (m/s)
I soil	Opt	25.0	1.00	1.346	93.1	1.350	93.4	6.6E-07
		25.0	1.00	1.277	88.3	1.284	88.8	1.6E-06
		27.0	1.08	1.411	97.6	1.416	97.9	8.2E-08
		25.0	1.00	1.379	95.4	1.385	95.7	2.1E-07
		25.0	1.00	1.4	96.8	1.404	97.1	7.6E-08
	Dry	18.0	0.72	1.382	95.6	1.389	96.0	3.2E-07
		20.0	0.80	1.342	92.8	1.351	93.5	7.5E-07
	Wet	28.7	1.15	1.369	94.7	1.374	95.0	2.1E-07

Soil material	Compaction condition	w_i (%)	w_i/w_{opt}	ρ_{di} (g/cm^3)	D_{ci} (%)	ρ_{dc} (g/cm^3)	D_{cc} (%)	k_{15} (m/s)
K soil	Opt	41.3	1.02	1.058	99.9	1.059	100.0	3.1E-06
		41.2	1.02	1.010	95.4	1.013	95.6	5.1E-06
		41.0	1.01	0.971	91.7	0.978	92.3	9.7E-06
		43.9	1.08	1.060	100.1	1.070	101.0	2.0E-06
		40.1	0.99	0.952	89.9	0.956	90.2	1.8E-05
		38.9	0.96	1.013	95.7	1.016	95.9	7.6E-06
	Dry	30.4	0.75	1.017	96.0	1.017	96.1	7.7E-06
		36.0	0.89	1.047	98.9	1.053	99.4	4.5E-06
		30.3	0.75	1.001	94.5	1.003	94.7	1.4E-05
	Wet	48.1	1.19	1.040	98.2	1.043	98.5	1.3E-06
		49.5	1.22	1.070	101.0	1.076	101.6	6.2E-07

Cyclic triaxial test results to examine the effect of freeze-thawing

Soil material	Testing condition	w_i (%)	ρ_{di} (g/cm^3)	D_{ci} (%)	ρ_{dc} (g/cm^3)	D_{cc} (%)	Ave. w_i	Ave. ρ_{di}	Ave. D_{ci}	ε_{af} (%)	N_c		*SR*
											DA =1%	*DA* =5%	
K soil	Freeze-thawing test	40.6	1.037	97.9	1.015	95.9	39.9	1.027	97.0	6.1	2.6	17.9	0.329
		38.1	1.058	99.9	1.041	98.3				4.9	1.7	8.7	0.385
		40.7	1.009	95.3	0.988	93.3				4.3	9.8	28.9	0.255
		40.2	1.005	94.9	0.993	93.8				6.0	0.7	5.7	0.470
		39.4	0.996	94.0	0.992	93.7	39.2	0.994	93.9	3.9	4.8	17.7	0.272
		39.0	0.997	94.2	0.986	93.1				3.2	0.7	7.8	0.409
		39.3	0.990	93.5	0.986	93.1				4.6	13.8	32.8	0.219
		38.9	0.939	88.6	0.946	89.3	39.2	0.940	88.8	2.6	7.5	13.8	0.237
		39.6	0.941	88.9	0.942	88.9				3.1	24.8	31.8	0.182
		39.2	0.940	88.8	0.940	88.8				2.9	2.9	6.7	0.307
	Non-freezing test	41.6	1.019	96.2	1.018	96.2	40.9	1.019	96.3	-	8.8	30.1	0.389
		41.7	1.018	96.1	1.018	96.2				-	3.8	20.0	0.464
		41.6	1.012	95.5	1.010	95.4				-	49.0	75.6	0.260
		38.9	1.029	97.1	1.033	97.5				-	18.8	38.8	0.327
		39.5	0.975	92.1	0.977	92.2	39.4	0.978	92.4	-	6.8	17.0	0.321
		39.8	0.973	91.8	0.971	91.7				-	2.7	11.9	0.371
		38.8	0.987	93.2	0.988	93.3				-	22.1	35.3	0.258
		38.1	0.937	88.5	0.935	88.3	39.0	0.935	88.3	-	163.4	172.5	0.158
		39.3	0.936	88.3	0.942	88.9				-	8.7	12.7	0.229
		39.3	0.936	88.4	0.942	88.9				-	30.8	37.7	0.180
		39.2	0.933	88.1	0.939	88.7				-	1.7	4.9	0.323

Cyclic triaxial test results to examine the effect of finer content

Soil material	Compaction condition *1	Compaction condition *2	w_i (%)	w_i/w_{opt}	ρ_{di} (g/cm^3)	D_{ci} (%)	ρ_{dc} (g/cm^3)	D_{cc} (%)	Ave. w_i	Ave. ρ_{dc}	Ave. D_{cc}	E	N_c DA =1%	N_c DA =5%	SR
$K_{1.9}$	Opt	(I)	37.8	1.01	0.933	90.5	0.940	91.3	37.7	0.942	91.4	0.32	7.7	11.7	0.263
			37.5	1.00	0.931	90.4	0.941	91.4				0.32	3.7	7.6	0.311
			37.8	1.01	0.935	90.8	0.943	91.6				0.32	26.8	31.7	0.181
			37.4	1.00	0.989	96.0	0.998	96.9				0.64	14.7	23.7	0.266
			37.7	1.01	0.987	95.8	0.997	96.8	37.7	0.995	96.6	0.64	35.8	45.8	0.214
			38.0	1.01	0.985	95.6	0.992	96.3				0.64	7.7	15.7	0.317
	Dry	(III)	29.5	0.79	0.927	90.0	0.935	90.7	29.2	0.942	91.5	0.32	39.7	44.7	0.160
			29.1	0.78	0.936	90.9	0.944	91.6				0.32	5.7	8.7	0.262
			29.0	0.77	0.940	91.3	0.948	92.1				0.32	12.8	16.7	0.209
			28.3	0.76	1.007	97.7	1.013	98.3				0.88	17.8	28.7	0.267
			28.5	0.76	1.013	98.3	1.020	99.0	28.8	1.014	98.5	0.88	9.8	20.7	0.319
			29.1	0.78	1.023	99.3	1.029	99.9				0.88	6.8	18.8	0.371
			29.3	0.78	0.989	96.1	0.996	96.7				0.88	29.8	41.8	0.213
	Wet	(IV)	45.5	1.21	0.946	91.8	0.955	92.7	46.1	0.939	91.1	0.32	6.7	11.8	0.263
			46.2	1.23	0.917	89.0	0.925	89.8				0.32	32.9	38.7	0.181
			46.6	1.24	0.924	89.7	0.936	90.9				0.32	4.5	8.6	0.293
			45.3	1.21	1.007	97.8	1.013	98.4				0.64	22.9	36.8	0.267
			43.8	1.17	1.017	98.7	1.025	99.6	44.6	1.011	98.2	0.64	3.7	12.8	0.372
			44.8	1.19	0.990	96.1	0.994	96.5				0.64	9.7	18.7	0.318

*1 Classification for compaction condition based on w_i/w_{opt} (*see* Figure 5.3.4)

*2 Classification for compaction condition based on w_i (*see* Figure 5.3.10)

Cyclic triaxial test results to examine the effect of finer content

Soil material	Compaction condition *1	Compaction condition *2	w_i (%)	w_i/w_{opt}	ρ_{di} (g/cm^3)	D_{ci} (%)	ρ_{dc} (g/cm^3)	D_{cc} (%)	Ave. w_i	Ave. ρ_{dc}	Ave. D_{cc}	E	N_c DA =1%	N_c DA =5%	SR
$K_{17.4}$	Opt	(I)	39.6	1.06	0.962	92.2	0.971	93.0	38.9	0.970	92.9	0.32	7.8	14.7	0.265
			38.6	1.03	0.963	92.3	0.972	93.1				0.32	3.7	6.6	0.314
			38.5	1.03	0.957	91.7	0.966	92.5				0.32	19.7	25.7	0.192
		(I)	40.5	1.08	1.038	99.4	1.046	100.2	39.9	1.052	100.8	0.64	12.7	23.7	0.321
			39.5	1.05	1.040	99.6	1.046	100.2				0.64	17.7	27.7	0.267
			39.6	1.06	1.058	101.3	1.064	101.9				0.64	43.8	58.7	0.214
	Dry	(II)	34.0	0.91	1.039	99.5	1.046	100.2	33.8	1.044	100.0	0.64	11.7	21.7	0.321
			33.3	0.89	1.041	99.7	1.048	100.4				0.64	12.9	22.7	0.266
			34.0	0.91	1.030	98.6	1.038	99.4				0.64	2.8	10.7	0.430
		(II)	32.3	0.86	0.979	93.8	0.988	94.6	32.2	0.978	93.7	0.32	8.8	14.7	0.266
			33.0	0.88	0.957	91.7	0.964	92.4				0.32	16.8	20.9	0.191
			31.4	0.84	0.975	93.3	0.983	94.2				0.32	1.7	4.7	0.374
	Wet	(IV)	44.8	1.19	0.961	92.1	0.971	93.0	45.3	0.977	93.6	0.32	19.7	25.7	0.213
			46.4	1.24	0.965	92.4	0.974	93.3				0.32	10.7	16.7	0.265
			45.1	1.20	0.983	94.2	0.992	95.0				0.32	83.8	94.8	0.161
			45.0	1.20	0.970	92.9	0.971	93.0				0.32	4.9	10.7	0.318
		(IV)	43.8	1.17	1.018	97.6	1.026	98.3	43.5	1.030	98.7	0.64	21.9	33.7	0.267
			43.1	1.15	1.017	97.4	1.026	98.3				0.64	10.7	19.7	0.321
			43.5	1.16	1.032	98.8	1.039	99.5				0.64	3.7	13.7	0.428

*1 Classification for compaction condition based on w_i/w_{opt} (*see* Figure 5.3.4)

*2 Classification for compaction condition based on w_i (*see* Figure 5.3.10)

Cyclic triaxial test results to examine the effect of finer content

Soil material	Compaction condition *1	Compaction condition *2	w_i (%)	w_i/w_{opt}	ρ_{di} (g/cm^3)	D_{ci} (%)	ρ_{dc} (g/cm^3)	D_{cc} (%)	Ave. w_i	Ave. ρ_{dc}	Ave. D_{cc}	E	N_c DA =1%	N_c DA =5%	SR
$K_{48.2}$	Opt		34.8	1.06	1.131	100.5	1.139	101.2				0.64	9.8	18.7	0.320
		(II)	34.4	1.05	1.131	100.6	1.137	101.1	34.4	1.142	101.5	0.64	5.7	12.7	0.408
			33.9	1.04	1.144	101.7	1.151	102.3				0.64	19.8	29.7	0.234
			34.1	1.04	1.083	96.2	1.090	96.9				0.32	6.8	10.7	0.264
		(II)	37.0	1.13	1.096	97.4	1.103	98.1	34.9	1.090	96.9	0.32	18.8	22.7	0.192
			33.5	1.02	1.076	95.6	1.076	95.6				0.32	1.8	3.7	0.327
	Dry		26.7	0.82	1.093	97.1	1.101	97.9				0.64	11.7	16.7	0.266
		(III)	26.6	0.81	1.087	96.7	1.093	97.2	26.6	1.093	97.2	0.64	22.9	28.7	0.213
			26.6	0.81	1.080	96.0	1.086	96.6				0.64	3.9	7.7	0.314
			26.1	0.80	1.130	100.4	1.135	100.9				1.00	25.8	34.7	0.267
		(III)	25.6	0.78	1.125	100.0	1.130	100.5	25.8	1.130	100.5	1.00	12.9	21.7	0.320
			25.8	0.79	1.116	99.2	1.125	100.0				1.00	3.7	9.7	0.420
			19.4	0.59	1.108	98.5	1.115	99.1				0.64	29.7	33.7	0.192
		-	19.5	0.60	1.103	98.1	1.109	98.5	19.3	1.111	98.7	0.64	7.8	11.7	0.266
			18.9	0.58	1.102	98.0	1.109	98.6				0.64	4.7	6.6	0.316
	Wet		39.1	1.20	1.127	100.2	1.132	100.6				0.40	3.7	8.7	0.312
		(I)	40.8	1.25	1.114	99.0	1.120	99.6	39.3	1.130	100.4	0.40	12.8	18.7	0.212
			38.1	1.16	1.127	100.1	1.136	101.0				0.40	16.8	22.7	0.185
			41.0	1.25	1.087	96.6	1.096	97.4				0.16	2.8	5.6	0.288
		(I)	41.1	1.26	1.073	95.4	1.079	95.9	40.6	1.088	96.7	0.16	10.7	13.7	0.189
			40.6	1.24	1.082	96.2	1.098	97.6				0.16	12.8	15.9	0.191
			39.8	1.22	1.070	95.1	1.080	96.0				0.16	26.9	30.7	0.149

*1 Classification for compaction condition based on w_i/w_{opt} (*see* Figure 5.3.4)

*2 Classification for compaction condition based on w_i (*see* Figure 5.3.10)

Cyclic triaxial test results using the in-situ specimens sampled from the embankment, FE-2012

Soil material	Sampling number*	Compaction condition	w_i (%)	w_i/w_{opt}	ρ_{di} (g/cm^3)	D_{ci} (%)	ρ_{dc} (g/cm^3)	D_{cc} (%)	Ave. w_i	Ave. D_{cc}	N_c DA =1%	N_c DA =5%	SR
$K_{original}$	No.1	Opt	42.2	1.04	0.963	91.0	0.978	92.3	43.1	93.1	3.7	5.9	0.311
	No.2		42.3	1.05	0.985	93.0	1.004	94.8			4.7	8.7	0.314
	No.3		44.0	1.09	0.980	92.5	0.991	93.5			16.8	25.7	0.271
	No.4		43.8	1.08	0.952	89.9	0.970	91.6			62.9	72.7	0.214

* *see* Figure 4.2.8

ACKNOWLEDGEMENT

The author would like to express his profound gratitude to Professor Seiichi Miura of Hokkaido University who has continuously guided and encouraged him throughout till this day. The author also wishes to make a cordial acknowledgment to Professor Tatsuya Ishikawa, Professor Hiroyuki Tanaka and Professor Shunji Kanie of Hokkaido University for their review and helpful advice given in completing the thesis. The author is deeply grateful to Associate Professor Shima Kawamura of Muroran Institute of Technology and Assistant Professor Shoji Yokohama of Hokkaido University for their support and valuable discussion.

The author would like to emphasize that the present study has been supported by many colleagues in Laboratory of Analytical Geomechanics of Hokkaido University and Soil mechanics and Foundations Engineering Laboratory of Muroran Institute of Technology. Mr. Inam Aasim and Ms. Zhang Yuan have given helpful advices about various things and they were the author's good English teachers. The experimental work in the study has been mainly supported by Messrs. Shintaro Izumi, Keisuke Ito, Yuta Hosono, Ryohei Takada, Asuka Kudo, Hiroshi Minami and Naotoshi Iwamura. Although there are many laboratory members else to be introduced, who have supported the author, he would like to thank all for their support and cooperation.

The author also would like to express his gratitude to Associate Professor Satoshi Nishimura of Hokkaido University for his advice and encouragement.

REFERENCES

1) Ahmed, S., Lovell, W. C. and Diamond, S. (1974) : Pore sizes and strength of compacted clay, *Proc. of ASCE*, Vol.100, No.GT4, pp.407-425.

2) Alonso, E. E., Pinyol, M. N. and Gens, A. (2013) : Compacted soil behaviour: initial state, structure and constitutive modelling, *Géotechnique*, Vol.63, No.6, pp.463-478.

3) Asonuma, T., Miura, S., Yagi, K. and Tanaka, H. (2002) : Dynamic deformation characteristics of volcanic soils and their evaluation methods, *J. of Geotech. Engrg.*, JSCE, No.708/III-59, pp.161-173 (in Japanese).

4) Benson, H. C. and Daniel, E. D. (1990) : Influence of clods on hydraulic conductivity of compacted clay, *J. of Geotech. Engrg., ASCE*, Vol.116, No.8, pp.1231-1248.

5) Benson, H. C. and Othman, A. M. (1993) : Hydraulic conductivity of compacted clay frozen and thawed in situ, *J. of Geotech. Engrg.*, ASCE, Vol.119, No.2, pp.1083-1097.

6) Danjo, T., Sako, K., Fukagawa, R., Sakai, N., Iwasa, N. and Quang, M. N. (2012) : Verification on the process of rainfall-induced surface failure from rainfall intensity, unsaturated seepage and deformation results, *J. of Geotech. Engrg.*, JSCE, Vol.68, No.3, pp.508-525 (in Japanese).

7) Eigenbrod, D. K. (1996) : Effects of cyclic freezing and thawing on volume changes and permeabilities of soft fine-grained soils, *Can. Geotech. J.*, Vol.33, No.4, pp.529-537.

8) Fredlund, G. D. and Rahardjo, H. (1993) : Soil mechanics for unsaturated soils.

9) Goto, S. (1993) : Influence of a freeze and thaw cycle on liquefaction resistance of sandy soils, *Soils and Foundations*, Vol.33, No.4, pp.148-158.

10) Goto, S., Suzuki, Y., Nishio, S. and Oh-oka H. (1992) : Mechanical properties of undisturbed Tone-river gravel obtained by in-situ freezing method, *Soils and Foundations*, Vol.32, No.3, pp.15-25.

11) Haruyama, M. (1973) : Geological, physical, and mechanical properties of “Shirasu” and its engineering classification, *Soils and Foundations*, Vol.13, No.3, pp.45-60.

12) Hata, Y. and Ichii, K. (2011) : Seismic response analysis of a slope to consider the effect of the rainfall, *J. of the Jpn. Landslide Soc*., Vol.48, No.4 (in Japanese).

13) Hatanaka, M., Sugimoto, M. and Suzuki, Y. (1985) : Liquefaction resistance of two alluvial volcanic soils sampled by in situ freezing, *Soils and Foundations*, Vol.25, No.3, pp.49-63.

14) Heitor, A., Indraratna, B. and Rujikiatkamjorn, C. (2013) : Laboratory study of small-strain behavior of a compacted silty sand, *Can. Geotech. J.*, Vol.50, No.2, pp.179-188.

15) Hokkaido branch of the Japanese Geotechnical Society (2010) : Volcanic soil for geo-engineer ~ geotechnical characteristics, design, construction and disaster case ~ (in Japanese).

16) Hwang, D., Yanagisawa, E. and Sugano, T. (1993) : Shear characteristics of silt containing sand, *J. of Geotech. Engrg*., JSCE, No.463/III-22, pp.25-33 (in Japanese).

17) Ichii, K. (2005) : Experimental study on seismic resistance reduction of embankment due to rainfall, *J. of eq. Engrg,*. JSCE, vol.28, No.188 (in Japanese).

18) Investigation group of Japanese society of civil engineering for damage due to the 2011 off the Pacific coast of Tohoku Earthquake (2011) : Immediate investigation report of earthquake-induced damage, JSCE (in Japanese).

19) Iseda, T. and Mizuno, M. (1971) : Study on compressibility of compacted soil, *J. of Geotech. Engrg.*, JSCE, No.188, pp.45-52 (in Japanese).

20) Ishihara, K., Silver, M. L. and Kitagawa, H. (1978) : Cyclic strengths of undisturbed sands obtained by large diameter sampling, *Soils and Foundations*, Vol.18, No.4, pp.61-76.

21) Ishikawa, T. and Miura, S. (2011) : Influence of freeze-thaw action on deformation-strength characteristics and particle crushability of volcanic coarse-grained soils, *Soils and Foundations*, Vol.51, No.5, pp.785-799.

22) Iwasaki, T., Shimizu, N., Masunari, T., Sato, W., Haraguchi, K. and Oshima, H. (2012) : GPS automatic displacement monitoring system for safety management of slopes, *Jour. Japan Soc. Eng. Geol.*, Vol.52, No.6, pp.256-264 (in Japanese).

23) JGS 0111-2009 (2009) : Test method for density of soil particles, Standards of the Japanese Geotechnical Society (in Japanese).

24) JGS 0131-2009 (2009) : Test method for particle size distribution of soils, Standards of the Japanese Geotechnical Society (in Japanese).

25) JGS 0141-2009 (2009) : Test method for liquid limit and plastic limit of soils, Standards of the Japanese Geotechnical Society (in Japanese).

26) JGS 0151-2009 (2009) : Test method for water retentivity of soils, Standards of the Japanese Geotechnical Society (in Japanese).

27) JGS 0161-2009 (2009) : Test method for minimum and maximum densities of sands, Standards of the Japanese Geotechnical Society (in Japanese).

28) JGS 0711-2009 (2009) : Test method for soil compaction using a rammer, Standards of the Japanese Geotechnical Society (in Japanese).

29) Japan Institute of Country-ology and Engineering (2009) : Construction manual for dyke embankment, Chapter 3 (in Japanese).

30) Japan Road Association (2010) : Manual for earth structure - Outline of road construction, Japan Road Association (in Japanese).

31) Jotisankasa, A., Coop, M. and Ridley, A. (2009) : The mechanical behaviour of an unsaturated compacted silty clay, *Géotechnique*, Vol.59, No.5, pp.415-428.

32) Juang, H. C. and Holtz, D. R. (1986) : Fabric, pore size distribution, and permeability of sandy soils, *J. of Geotech. Engrg., ASCE*, Vol.112, No.9, pp.855-868.

33) Kamei, T. and Enomoto, M. (1994) : Wetting-induced collapse behaviour of compacted silty

soil, *J. of Geotech. Engrg., JSCE*, No.505/III-29, pp.97-103 (in Japanese).

34) Kato, S. (1998) : Deformation characteristics of a compacted clay in collapse under isotropic stress state and its shear deformation after collapse, *J. of Geotech. Engrg.*, JSCE, No.596/III-43, pp.271-281 (in Japanese).

35) Kawaguchi, T., Mitachi, T., Shibuya, S. and Sano Y. (2001) : Evaluation of elastic shear modulus G in laboratory bender element test, *JSCE*, No.694/III-57, pp.195-207 (in Japanese).

36) Kawajiri, S., Kawaguchi, T., Shibuya, S. and Takahashi, M. (2011) : Effects of moulding water content and compaction method on deformation and strength characteristics of compacted soil, *J. of Geotech. Engrg.*, JSCE, Vol.67, No.4, pp.532-543 (in Japanese).

37) Kawamura, S. and Miura, S. (2013a) : Rainfall-induced failures of volcanic slopes subjected to freezing and thawing, *Soils and Foundations*, Vol.53, No.3, pp.443-461.

38) Kawamura, S. and Miura, S. (2013b) : Failures of volcanic slopes in cold regions and its prediction, *Proc*., The Third Italian Workshop on Landslides (peer reviewing).

39) Kawamura, S., Miura, S., Ishikawa, T. and Yokohama, S. (2010) : Rainfall-induced failure of unsaturated volcanic slope subjected to freeze-thaw action and its mechanism, *J. of Geotech. Engrg.*, JSCE, Vol.66, No.3, pp.577-594 (in Japanese).

40) Kawamura, S., Miura, S., Yokohama, S., Kudo, A. and Kaiya, N. (2013) : Field monitoring of embankment constructed by volcanic soil and its evaluation, Stability and Performance of Slopes and Embankments III, GeoCongress2013, *ASCE-Geotechnical Special Publication*, No.231, pp.373-382.

41) Kazama, M., Miura, S., Yagi, K., Unno, T., Suzuki. T., and Ito, Y. (2006a) : Volcanic soil - its characteristics and design-construction 6. Case study in volcanic soil grounds, *TSUCHI-TO-KISO*, JGS, Vol.54, No.2, pp.45-54 (in Japanese).

42) Kazama, M., Takamura, H., Unno, T., Sento, N. and Uzuoka, R. (2006b) : Liquefaction

mechanism of unsaturated volcanic sandy soils, , *J. of Geotech. Engrg.*, JSCE, Vol.62, No.2, pp.546-561 (in Japanese).

43) Kim, H. W., and Daniel, E. D. (1992) : Effects of freezing in hydraulic conductivity of compacted clay, *J. of Geotech. Engrg.*, ASCE, Vol.118, No.7, pp.1083-1097.

44) Kimoto, S., Oka, F., Fukutani, J., Yabuki, T. and Nakashima, K. (2011) : Monotonic and cyclic behavior of unsaturated sandy soil under drained and fully undrained conditions, *Soils and Foundations*, Vol.51, No.4, pp.663-681.

45) Kitamura, R., Sako, K., Kato, S., Mizushima, T. and Imanishi, H. (2007) : Soil tank test on seepage and failure behaviors of Shirasu slope during rainfall, *Japanese Geotech. J.*, JGS, Vol.2, No.3, pp.149-168 (in Japanese).

46) Kiyohara, Y. and Kazama, M. (2008) : Field monitoring of rainfall infiltration in model embankments composed of volcanic sandy soils, *J. of Geotech. Engrg.*, JSCE, Vol.64, No.3, pp.519-531 (in Japanese).

47) Konrad, -M. J. (2010) : Hydraulic conductivity changes of a low-plasticity till subjected to freeze-thaw cycles, *Géotechnique*, Vol.60, No.9, pp.679-690.

48) Kudo, A. (2013) : Damage and restoration for slope failure in Route 230, *Geotech. Engrg. Magazine*, JGS, Vol.61, No.3, Ser.No.662, pp.30-31 (in Japanese).

49) Kudo, A., Miura, S., Kawamura, S., Yokohama, S., Matsumura, S. and Kaiya, N. (2012) : Mechanical behavior of embankment constructed by volcanic coarse grained soil based on field monitoring data, *Technical report*, Hokkaido branch of the Japanese geotechnical society, Vol.52, pp.193-198 (in Japanese)

50) Kuwano, J., Sapkota, B. K., Hashizume, H. and Takahara, K. (1993) : Liquefaction characteristics of sand containing fines, *TSUCHI-TO-KISO*, JGS, Vol.41, No.7, pp.23-28 (in Japanese).

51) Lambe, T. W. (1958a) : The structure of compacted clay, *Proc. of ASCE*, Vol.84, No.SM2, pp.1654-1-1654-34.

52) Lambe, T. W. (1958b) : The engineering behavior of compacted clay, *Proc. of ASCE*, Vol.84, No.SM2, pp.1655-1-1655-35.

53) Liu, N. and Mitchell, K. J. (2006) : Influence of nonplastic fines on shear wave velocity-based assessment of liquefaction, *J. of Geotech. and Geoenviron. Eng.*, ASCE, Vol.132, No.8, pp.1091-1097.

54) Magistris, De S. F. and Tatsuoka, F. (2004) Effects of moulding water content on the stress-strain behaviour of a compacted silty sand, *Soils and Foundations*, Vol.44, No.2, pp.85-101.

55) Matsumura, S., Miura, S. and Yokohama, S. (2012) : Effects of compaction conditions on cyclic undrained shear properties of sandy-silt soils and its evaluation, *J. of Geotech. Engrg.*, JSCE, Vol.68, No.4, pp.597-609 (in Japanese).

56) Matsumura, S., Miura, S., Yokohama, S. and Minami, H. (2013) : Evaluation of cyclic shear strength of volcanic soil embankment with freeze-thaw action, Technical report, JGS conference, No.48, pp.513-514 (in Japanese).

58) Miki, K. (1997) : Introduction of geology for geotechnique, Kajima Institute Publishing Co., Ltd., chapter 2, pp.49 (in Japanese).

59) Mitchell, K. J., Hooper, R. D. and Campanella, G. R. (1965) : Permeability of compacted clay, *Proc. of ASCE*, Vol.91, No.SM4, pp.41-65.

60) Miura, S. and Toki, S. (1984) : Anisotropy in mechanical properties and its simulation of sands sampled from natural deposits, *Soils and Foundations*, Vol.24, No.3, pp.69-84.

61) Miura, S. and Yagi, K. (1997) : Particle breakage of volcanic coarse-grained soils and its evaluation, *J. of Geotech. Engrg.*, JSCE, No.561/III-38, pp.257-269 (in Japanese).

62) Miura, S., Ohgiya, O. and Masumura, K. (1990) : Membrane penetration and reducing method in cyclic undrained triaxial test on granular materials, Technical report, JGS conference, No.25, pp.753-754 (in Japanese).

63) Miura, S., Yagi, K. and Kawamura, S. (1996a) : Static and cyclic shear behavior and particle crushing of volcanic coarse grained soils in Hokkaido, *J. of Geotech. Engrg.*, JSCE, No.547/III-36, pp.159-170 (in Japanese).

64) Miura, S., Yagi, K. and Kawamura, S. (1996b) : Effect of stress history on cyclic undrained deformation-strength characteristics of volcanic coarse-grained soils, *J. of Geotech. Engrg.*, JSCE, No.547/III-36, pp.221-229 (in Japanese).

65) Miura, S., Yagi, K., Asonuma, T. (2003) : Deformation-strength evaluation of crushable volcanic soils by laboratory and in-situ testing, *Soils and Foundations*, Vol.43, No.4, pp.47-57.

66) Miyaura, M, Nakata, T., Kimura, M. and Yokohama, S. (2011) : Evaluation of permeability of volcanic ground for suitability of snow dump site, *Technical report*, Hokkaido branch of the Japanese geotechnical society, Vol.51, pp.221-228 (in Japanese).

67) Mori, T., Chiba, T., Uzuoka, R. and Kazama, M. () : The relationship between change of soil moisture resulted from rainfalls and seismic response characteristics in the valley fill ground, *J. of Japan Assoc. for Eq. Eng.*, Vol.10, No.4 (in Japanese).

68) Nakamura, D., Suzuki, T., Goto, T., Kim, H., Ito, Y. and Yamashita, S. (2011) : Changes in the permeability coefficient and the void ratio of compacted soil by the effect of freeze-thaw cycles, *J. of Geotech. Engrg.*, JSCE, Vol.67, No.2, pp.264-275 (in Japanese).

57) Nakamura, S., Higuchi, S., Sawada, S. and Yoshida, N. (2010) : Effect of moisture condition on failure characteristics of embankment based on centrifuge shaking table test, *J. of Geotech. Engrg.*, JSCE, Vol.66, No.2, pp.446-456 (in Japanese).

69) Nakata, T. and Miura, S. (2007) : Change in void structure due to particle breakage of volcanic

coarse-grained soil and its evaluation, *J. of Geotech. Engrg.*, JSCE, Vol.63, No.1, pp.224-236 (in Japanese).

70) Obihiro Development and Construction Department (2010) : River development project for the riverine system of the Tokachi river, Hokkaido Development Bureau, Ministry of Land, Infrastructure, Transport and Tourism, available at <http://www.ob.hkd.mlit.go.jp/hp/kakusyu/houshin-seibi/pdf/keikaku.pdf>

71) Oda, M. (1972) : Initial fabrics and their relations to mechanical properties of granular material, *Soils and Foundations*, Vol.12, No.1, pp.17-36.

72) Ohta, H., Itoh, M., Ishiguro, T. and Yonetani, S. (1991) : Precompaction pressure and strength of compacted cohesive soils, *J. of Geotech. Engrg.*, JSCE, No.436/III-16, pp.27-36 (in Japanese).

73) Ono, T., Kodama, D. and Kato, T. (2003) : The properties of normally and overconsolidated clay after freezing and thawing history, *J. of Geotech. Engrg.*, JSCE, No.743/III-64, pp.47-57 (in Japanese).

74) Panayides, S., Rouainia, M. and Wood, M. D. (2012) : Influence of degradation of structure on the behaviour of a full-scale embankment, *Can. Geotech. J.*, Vol.49, No.3, pp.344-356.

75) Rad, S. N. and Clough, W. G. (1984) : New procedure for saturating sand specimens, *J. of Geotech. Engrg.*, ASCE, Vol.110, No.9, pp. 1205-1218.

76) Sahaphol, T. and Miura, S. (2005) : Shear moduli of volcanic soils, *Soil Dynamics and Earthquake Engineering*, Vol.25, No.2, pp.157-165.

77) Sasaki, Y. (1980) : Earthquake damages of river dykes, *TSUCHI-TO-KISO*, JGS, Vol.28, No.8, pp.25-30 (in Japanese).

78) Sasaki, Y. (2012) : Liquefaction of embankment on peat ground, JICE, report, vol.16, No.9, pp.90-101 (in Japanese).

79) Sato, M., Oda, M., Kazama, H. and Ozeki, K. (1997) : Fundamental study on the effect of fines on liquefaction strength of reclaimed ground, *J. of Geotech. Engrg.*, JSCE, No.561/III-38, pp.271-282 (in Japanese).

80) Seed, H. B. and Chan, C. K. (1959) : Structure and strength characteristics of compacted clays, *Proc. of ASCE*, Vol.85, No.SM5, pp.87-128.

81) Seed, H. B., Singh, S. Chan, C. K. and Vilela, F. T. (1982) : Considerations in undisturbed sampling of sands, *Proc. of ASCE*, Vol.108, No.GT2, pp.265-283.

82) Seed, H. B., Woodward, J. R. and Lundgren, R. (1962) : Prediction of swelling potential for compacted clays, *Proc. of ASCE*, Vol.88, No.SM3, pp.53-87.

83) Singh, S., Seed, H. B. and Chan, C. K. (1982) : Undisturbed sampling of saturated sands by freezing, *Proc. of ASCE*, Vol.108, No.GT2, pp.247-264.

84) Sivakumar, V., Kodikara, J., O'hagan, R., Hughes, D., Cairns, P. and Mckinley, D. J. (2013) : Effects of confining pressure and water content on performance of unsaturated compacted clay under repeated loading, *Géotechnique*, Vol.63, No.8, pp.628-640.

85) Takada, M., Kitamura, R. and Kitada, T. (1997) : Estimation of geotechnical properties of alluvial secondary Shirasu ground, *J. of Geotech. Engrg.*, JSCE, No.561/III-38, pp.237-244 (in Japanese).

86) Takada, M., Kitamura, R., Kitada, T. and Tomiyama, T. (1999) : Dynamic properties of alluvial secondary Shirasu ground and its liquefaction potential, *J. of Geotech. Engrg.*, JSCE No.631/III-48, pp.61-69 (in Japanese).

87) Takada, M., Matsumoto, I. and Kitamura, R. (2001) : A consideration on mechanical properties of primary Shirasu ground, *J. of Geotech. Engrg.*, JSCE, No.694/III-57, pp.343-348 (in Japanese).

88) Takada, N., Kinoshita, T. and Shinozaki, W. (1986) : On the instability of compacted gravelly

soils under submerged conditions, *TSUCHI-TO-KISO*, JGS, Vol.34, No.5, pp.63-68 (in Japanese).

89) The Japanese Geotechnical Society (2006) : Mechanism of slope failure due to heavy rain and its hazard prediction, JGS, Chapter 3, pp.35-48 (in Japanese).

90) The Japanese Geotechnical Society (2009a) : For preventing ground disasters due to earthquake, heavy rain and flood ~ Proposal from geotechnique ~ , JGS, 2.3, pp.131-179 (in Japanese).

91) The Japanese Geotechnical Society (2009b) : Volcanic coarse-grained soil, Test for unusual soils,, Japanese standards and explanations of laboratory tests of geomaterials Vol.8, Chapter 4, pp.988-1006 (in Japanese).

92) The Japanese Geotechnical Society (2013) : Investigation for heavy rain in Akita and Iwate on August 2013, JGS, available at <https://www.jiban.or.jp/images/H25-8akitaiwatesaigaichosahokoku.pdf> (in Japanese).

93) The Japanese society of civil engineering and the Japanese Geotechnical Society (2013) : Investigation report for disaster due to heavy rain in Yamaguchi and Shimane, JSCE and JGS, available at <https://www.jiban.or.jp/images/file/H25-7yamaguchishimanegouusaigai_130917v2.pdf> (in Japanese).

94) Thevanayagam, S., Shenthan, T., Mohan, S., and Liang, J. (2002) : Undrained fragility of clean sands, silty sands and sandy silts, *J. of Geotech. and Geoenviron. Eng.*, ASCE, Vol.128, No.10, pp.849-859.

95) Viklander, P. (1998) : Permeability and volume changes in till due to cyclic freeze/thaw, *Can. Geotech. J.*, Vol.35, No.3, pp.471-477.

96) Walberg, C. F. (1978) : Freezing and cyclic triaxial behavior of sands, *Proc. of ASCE*, Vol.104, No.GT5, pp.667-671.

97) Watabe, Y., Leroueil, S. and Bihan, Le -P. J. (2000) : Influence of compaction conditions on pore-size distribution and saturated hydraulic conductivity of a glacial till, *Can. Geotech. J.*, Vol.37, No.6, pp.1184-1194.

98) Yagi, K. and Miura, S. (2001) : Effect of particle-crushed fines on cyclic undrained shear behavior of volcanic coarse-grained soils, *J. of Geotech. Engrg.*, JSCE, No.694/III-57, pp.305-317 (in Japanese).

99) Yagi, K., Miura, S. and Shihikawa, K. (2005) : Liquefaction strength of pyroclastic flow deposits damaged by the 2003 Tokachi-Oki Earthquake, Technical report, JGS conference, No.40, pp.2175-2176 (in Japanese).

100) Yajima, J., Numata, Y. and Nakase, A. (1999) : A study on liquefaction strength evaluation methods and liquefaction properties of fine containing sand, *J. of Geotech. Engrg.*, JSCE, No.624/III-47, pp.113-122 (in Japanese).

101) Yajima, Y., Sasaki, Y. and Kurahashi, T. (2008) : Analysis of disaster features using slope disaster database of natural roads, *Jour. Japan Soc. Eng. Geol.*, Vol.48, No.6, pp.304-311 (in Japanese).

102) Yamaguchi, A., Yoshida, N. and Tobita, Y. (2012) : Sand boils along the Naruse river and the Yoshida river by the 2011 Tohoku-region Pacific Coast Earthquake, *Japanese Geotech. J.*, JGS, Vol.7, No.1, pp.243-251 (in Japanese).

103) Yamaguchi, H. and Ikenaga, H. (1992) : Pore structures of compacted soils, *J. of Geotech. Engrg.*, JSCE, No.448/III-19, pp.35-44 (in Japanese).

104) Yamaki, M., Miura, S. and Yokohama, S. (2009) : Effect of freeze-thaw sequence on deformation properties of crushable volcanic soil, *J. of Geotech. Engrg.*, JSCE, Vol.65, No.1, pp.321-333 (in Japanese).

105) Yokohama, S., Miura, S. and Matsumura, S. (2012) : Effect of compaction condition on

strength, permeability and shear modulus of sandy silt as embankment material, *J. of Geotech. Engrg.*, JSCE, Vol.68, No.2, pp.422-432 (in Japanese).

106) Yoshimi, Y., Hatanaka, M. and Oh-oka, H. (1978) : Undisturbed sampling of saturated sands by freezing, *Soils and Foundations*, Vol.18, No.3, pp.59-73.

107) Zen, K. and Yamazaki, H. (1996) : Liquefaction characteristics of Masado (decomposed granite soil) used for reclaimed land, *TSUCHI-TO-KISO*, JGS, Vol.44, No.2, pp.60-63 (in Japanese).

108) Zwanenburg, C., Haan, Den. J. E., Kruse, M. A. G. and Koelewijn, R. A. (2012) : Failure of a trial embankment on peat in Booneschans, the Netherlands, *Géotechnique*, Vol.62, No.6, pp.479-490.